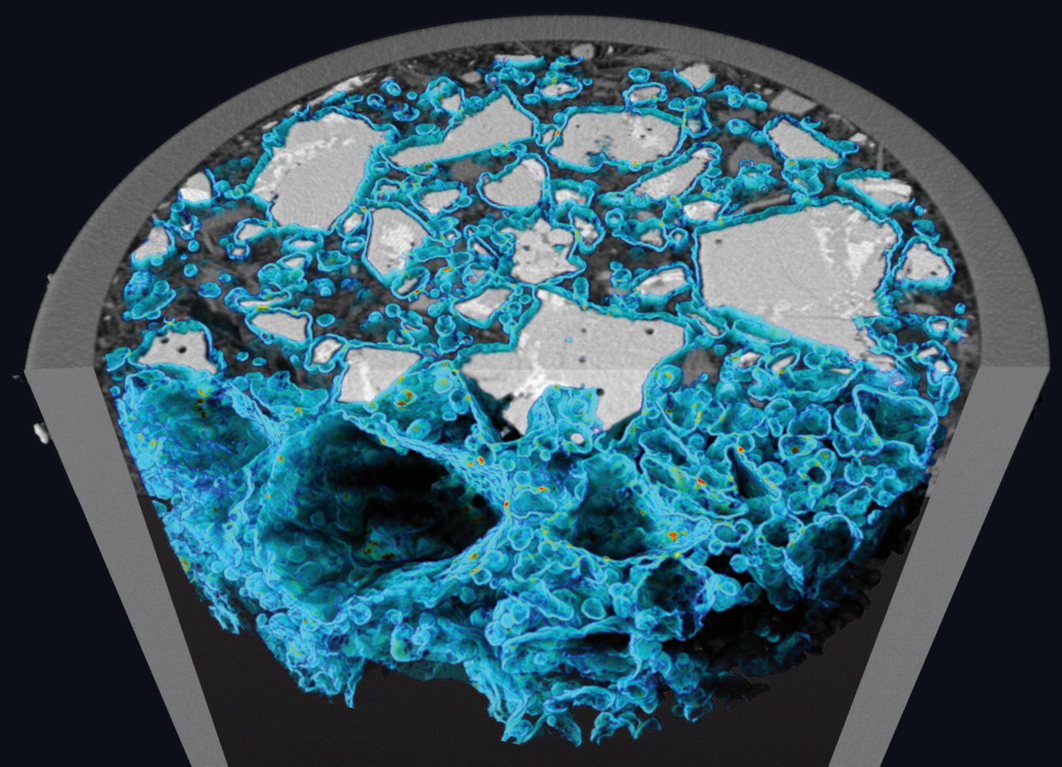

2023

ADVANCED QUANTITATIVE SYNCHROTRON X-RAY IMAGING OF CEMENT MICRO- AND MESO- STRUCTURES

Tesis doctoral por compendio de publicaciones

Shiva Shirani Tak Abi

TESIS DOCTORAL

POR COMPENDIO DE PUBLICACIONES

Facultad de Ciencias

Departmento de Química Inorgánica, Cristalografía y Mineralogía

Programa de doctorado :

"Química y Tecnologías Químicas, Materiales y Nanotecnología"

UNIVERSIDAD DE MÁLAGA

ADVANCED QUANTITATIVE SYNCHROTRON X-RAY IMAGING OF CEMENT MICRO- AND MESO-STRUCTURES

Shiva Shirani Tak Abi

Directores

Prof. Miguel Ángel García Aranda

Dra. Ana María Cuesta García

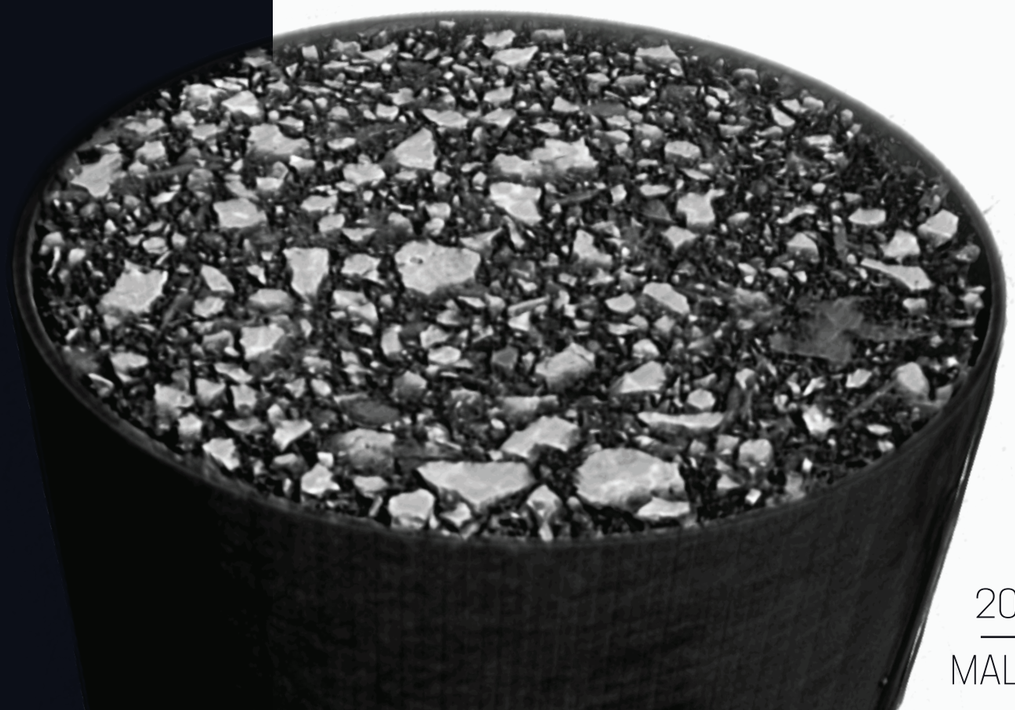

2023

MALAGA

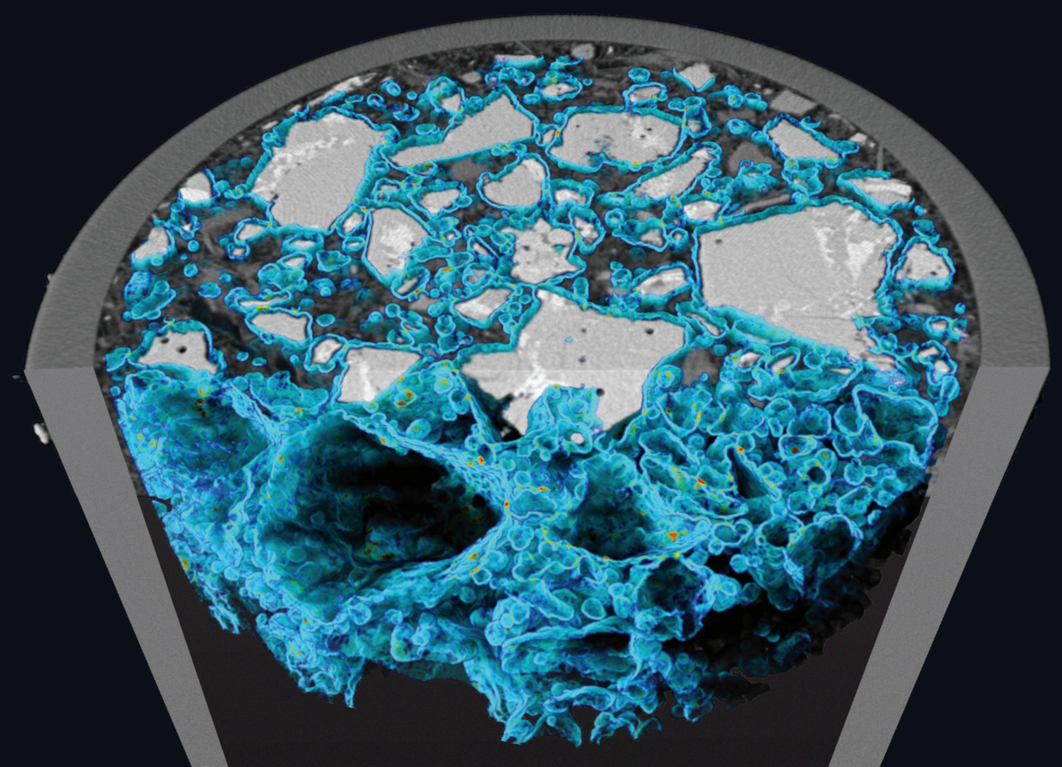

2023

ADVANCED QUANTITATIVE SYNCHROTRON X-RAY IMAGING OF CEMENT MICRO- AND MESO- STRUCTURES
Doctoral thesis by compendium of publications

Shiva Shirani Tak Abi

DOCTORAL THESIS
BY COMPENDIUM OF PUBLICATIONS

Faculty of Science
Department of Inorganic Chemistry, Crystallography and Mineralogy

Doctoral program:
"Chemistry and ChemicalTechnologies, Materials and Nanotechnology"

UNIVERSIDAD DE MÁLAGA

ADVANCED QUANTITATIVE SYNCHROTRON X-RAY IMAGING OF CEMENT MICRO- AND MESO-STRUCTURES

Shiva Shirani Tak Abi

Supervised by
Prof. Miguel Angel Garcia Aranda
Dr. Ana Maria Cuesta Garcia

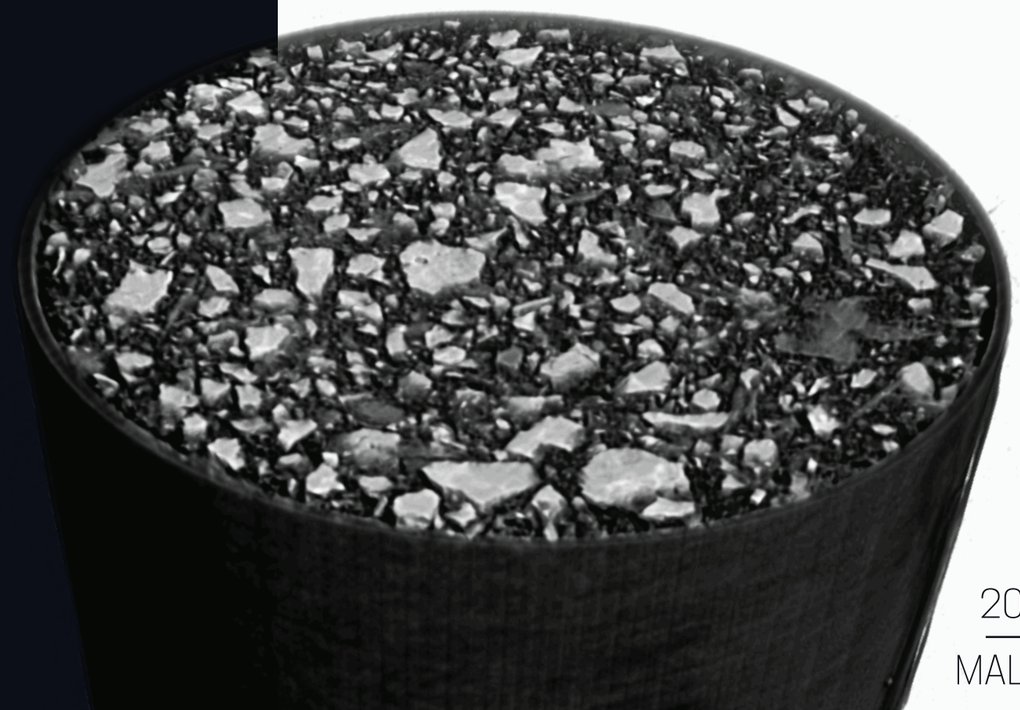

2023
MALAGA

AUTORA: Shiva Shirani Tak Abi

https://orcid.org/0000-0001-6877-7375

EDITA: Publicaciones y Divulgación Científica. Universidad de Málaga

DECLARACIÓN DE AUTORÍA Y ORIGINALIDAD DE LA TESIS PRESENTADA PARA OBTENER EL TÍTULO DE DOCTOR

Dª. SHIVA SHIRANI TAK ABI, estudiante del programa de doctorado en QUÍMICA Y TECNOLOGÍAS QUÍMICAS, MATERIALES Y NANOTECNOLOGÍA de la Universidad de Málaga, autor de la tesis presentada para la obtención del título de doctor por la Universidad de Málaga, titulada: **ADVANCED QUANTITATIVE SYNCHROTRON X-RAY IMAGING OF CEMENT MICRO- AND MESO- STRUCTURES.**

Realizado bajo la tutorización de MIGUEL ÁNGEL GARCÍA ARANDA y dirección de MIGUEL ÁNGEL GARCÍA ARANDA y ANA MARÍA CUESTA GARCÍA.

DECLARO QUE:

La tesis doctoral presentada es una obra original que no infringe los derechos de propiedad intelectual ni los derechos de propiedad industrial u otros, conforme el ordenamiento jurídico vigente (Real Decreto Legislativo 1/1996, de 12 de abril, por el que se aprueba el texto refundido de la Ley de Propiedad Intelectual, regularizando, aclarando y armonizando las disposiciones legales vigentes sobre la materia), modificado por la Ley 2/2019, de 1 de marzo.

Igualmente asumo, ante a la Universidad de Málaga y ante cualquier otra instancia, la responsabilidad que pudiera derivarse en caso de plagio de contenidos en la tesis doctoral presentada, conforme al ordenamiento jurídico vigente.

En Málaga, a 12 de SEPTIEMBRE de 2023

Fdo.: SHIVA SHIRANI TAK ABI Doctorando	Fdo.: MIGUEL ÁNGEL GARCÍA ARANDA Tutor
Fdo.: MIGUEL ÁNGEL GARCÍA ARANDA y ANA MARÍA CUESTA GARCÍA Directores de tesis	

Edificio Pabellón de Gobierno. Campus El Ejido 29071
Tel. 952 13 10 28/ 952 13 14 61/ 952 13 71 10
Email: doctorado@uma.es

El Prof. MIGUEL ÁNGEL GARCÍA ARANDA, Catedrático de Universidad, y la Dra. ANA MARÍA CUESTA GARCÍA, Investigadora Postdoctoral, en la Universidad de Málaga

HACEN CONSTAR:
Que la tesis doctoral presentada por compendio de publicaciones, titulada: **ADVANCED QUANTITATIVE SYNCHROTRON X-RAY IMAGING OF CEMENT MICRO- AND MESO- STRUCTURES**, ha sido realizada por Dª. SHIVA SHIRANI TAK ABI bajo la tutorización y dirección del Prof. MIGUEL ÁNGEL GARCÍA ARANDA, y la dirección de la Dra. ANA MARÍA CUESTA GARCÍA.

AUTORIZAMOS:
En cumplimiento de la legislación vigente, a su trámite y presentación para la obtención del grado de Doctor en el Programa de Doctorado de la Universidad de Málaga de QUÍMICA Y TECNOLOGÍAS QUÍMICAS. MATERIALES Y NANOTECNOLOGÍA por parte del interesado. Además, informamos que las publicaciones en coautoría que la avalan no han sido utilizadas en tesis anteriores.

En Málaga, a 12 de septiembre de 2023

Tutor:

Fdo. Miguel Ángel García Aranda

Directores:

Fdo. Miguel Ángel García Aranda

Fdo. Ana María Cuesta García

UNIVERSIDAD DE MÁLAGA

Advanced quantitative synchrotron X-ray imaging of cement micro- and meso- structures

Memoria presentada para optar al título de:

Doctor en Química y Tecnologías Químicas. Materiales y Nanotecnología

Mención Internacional

En Málaga, a 12 de SEPTIEMBRE de 2023

Doctorando:

Fdo: Shiva Shirani Tak Abi

Directores:

Fdo: Miguel Ángel García Aranda
Catedrático Química Inorgánica
Universidad de Málaga

Fdo: Ana María Cuesta García
Investigadora Postdoctoral
Universidad de Málaga

Facultad de Ciencias
Departamento de Química Inorgánica, Cristalografía y Mineralogía

TESIS DOCTORAL
por compendio de publicaciones
Universidad de Málaga

Facultad de Ciencias, Departamento de Química Inorgánica, Cristalografía y Mineralogía

Programa de doctorado : Química y Tecnologías Químicas, Materiales y Nanotecnología

Shiva Shirani Tak Abi

Advanced quantitative synchrotron X-ray imaging of cement micro- and meso- structures

---

Directores
Prof. Miguel Ángel García Aranda
Dra. Ana María Cuesta García

DOCTORAL THESIS
by compendium of publications
University of Malaga

Faculty of Science, Department of Inorganic Chemistry, Crystallography and Mineralogy

Doctoral program : Chemistry and Chemical Technologies, Materials and Nanotechnology

Shiva Shirani Tak Abi

Advanced quantitative synchrotron X-ray imaging of cement micro- and meso- structures

---

Prof. Miguel Ángel García Aranda **Supervisor**
Dr. Ana María Cuesta García **Co-supervisor**

*"**X-rays** have unlocked a world of possibilities, bridging the gap between the invisible and the visible, and allowing us to probe the hidden wonders of **nature**."*

*- **Marie Curie***

Acknowledgements

I would like to start by expressing my sincere gratitude to my supervisor, Prof. Miguel Angel Garcia Aranda, who has been a constant source of support and guidance throughout my adventure in synchrotron and X-ray imaging. From the very beginning, Miguel encouraged me to go beyond my perceived limits because he saw my potential. His mentorship has greatly influenced my academic and professional development over a span of about 8 years (from the early days of my master's when I started to become interested in tomography). I sincerely appreciate his constant confidence in my abilities.

I would like to express my deep gratitude to Dr. Ana Maria Cuesta Garcia, my co-supervisor, for all her tremendous efforts in handling administrative tasks and providing guidance when needed. I would like to thank the entire Cement Science group, as well as my friends and colleagues in the Faculty of Science at the University of Malaga (UMA), who have supported me in this academic endeavour. The opportunity to be a member of such a remarkable community makes me grateful.

I'm also grateful for the opportunity to work with and learn from the outstanding X-ray imaging scientists I've met over the years and since my Master's. My understanding of the subject has been greatly influenced by their knowledge, willingness to share it and collaborative nature, which has also enhanced the quality of my study.
In honour of my late supervisor at the European Synchrotron Radiation Facility (ESRF) in France, Dr. Claudio Ferrero, I would like to express my sincere gratitude for the significant influence he has had on my academic career. I promise Claudio that I will continue to work on synchrotron X-ray imaging. Five years have passed since his death, but his lessons and his unwavering belief in my abilities still speak to me. Although he is no longer physically here, I often wonder how he would feel about the progress I have made. I think his smile would be radiant if he could see the results of my work.
I would like to express my deep appreciation to Dr. Emmanuel Brun, who was the first to teach me image analysis and whose software package was the first image analysis software I worked with years ago, alongside Claudio. He has been a valuable mentor, a close friend and a constant source of encouragement over the years.
My sincere thanks go to Dr. Alexander Rack, who was my first synchrotron tomography supervisor at ID19 of ESRF (first during the OpenSESAME fellowship in my Master's degree). And I am very grateful for the opportunity to have worked with him again during my PhD.

I would like to express my sincere thanks to the cSAXS group at the Swiss Light Source (SLS) at the Paul Scherrer Institute (PSI) in Switzerland: Dr. Ana Diaz, Dr. Mirko Holler, Dr. Pavel Trtik and Dr. Manuel Guizar-Sicairos for their important help and support. In particular, I would like to thank Ana Diaz for her excellent supervision of the experimental setup and data handling. My research path has benefited greatly from

her advice and knowledge, and I am truly grateful for her outstanding mentorship. She gave me the confidence to carry out ptychography experiments on my own, and her assistance made the procedure easy and effective.

Apart from the fact that this thesis has been awarded by Formación de Personal Investigador (FPI) Competition Grant from the Spanish Ministry of Science and Innovation for 4 years, I'm also grateful that during this PhD I have been able to win awards such as "Jim Elliott" and grants such as "EXCITE" from the European Union's Horizon Research and Innovation Programme.

I would like to express my sincere gratitude to the ToScA (Tomography for Scientific Advancement) team in the United Kingdom: Dr. Farah Ahmed, Prof. Graham Davis, Dr. Jay Warnett and Prof. Richard Johnston for the incredible opportunity they have given me through the "International Jim Elliott Award" for X-ray tomography research.

To each and every colleague at the ESRF, thank you for your expertise and sharing of knowledge. The whole ID19 and ID16A team, Dr. Peter Cloetens and Dr. Julio Cesar da Silva.

I would like to express my sincere acknowledgement to the software teams who have generously provided me with their invaluable software packages. I would like to thank the Dragonfly team in Montreal, Canada and Prof. Anton du Plessis. I would also like to thank the IPSDK team in Grenoble, France. Their software package played a crucial role in my thesis.

I would like to express my deepest gratitude to Prof. Veerle Cnudde for accepting me as an international PhD student at the University of Ghent (UGent). I would also like to thank Prof. Matthieu Boone for his guidance during the in-situ experiment at the UGCT. I would like to thank the EXCITE network for awarding my experiments in Ghent and I would like to acknowledge the invaluable help of Dr. Laurenz Schroer.

I would like to express my sincere gratitude to all the science communication groups associated with Lightsources and the wider Lightsources community that I have had the privilege of working with over the years. I am immensely grateful for the opportunity to work with these science communication groups. And to the science-loving followers on social media who have encouraged me to talk about my research and share science content with others, providing me with a platform to share my research, insights and scientific discoveries with a wider audience.

I would like to express my heartfelt appreciation to my old classmate and best friend, Rayhane, for being an exceptional friend and indispensable companion throughout my PhD journey, even though she lives far away from me in another country. Her willingness to lend an ear and provide insightful advice has been invaluable. She has been a trusted confidante,

always ready to listen attentively and offer valuable advice.

My sincere thanks go to my parents and my brother, Chavosh, for their everlasting love and support throughout my journey. Their support and understanding has been crucial in my quest for knowledge, as moving to another country to pursue a scientific career and fulfil the dream of becoming a scientist is a big decision. I am extremely fortunate to have all my family members - near and far - in my life who have supported me with advice, love and a listening ear. It is because of your support that I have the strength to push boundaries, see new possibilities and work towards my scientific goals and dreams.
My heart swelled with eagerness as I composed each sentence of this thesis, anticipating the moment when I would hold my newborn twin nephew and niece (my dearest "Tabaar" and "Diyar") in my arms. This thesis serves as a symbol of the love that drives me forward and the immense joy I will feel when I finally meet them for the first time.

To My Lovely Family ♥

Contents

Special Terms

1D . . . one-Dimensional
2D . . . two-Dimensional
3D . . . three-Dimensional
4D . . . four-Dimensional

A# . . . Article number
Abs. . . . Absorption
AFm . . . Monosulfate
AFt . . . Ettringite
ART . . . Algebraic Reconstruction Techniques

BC . . . Belite Cement
BM . . . Bending Magnet
BW . . . Bounded Water

c . . . speed of light
C_2S . . . Dicalcium Silicate (Belite)
C_3A . . . Tricalcium Aluminate
C_3S . . . Tricalcium Silicate (Alite)
C_4AF . . . Tetracalcium AluminoFerrite (Ferrite)
CA . . . Calcium Aluminate
CAC . . . Calcium Aluminate Cement
CART . . . Classification and Regression Tree
C-A-S-H . . . Calcium Aluminate Silicate Hydrate
$C\underline{C}$ . . . Calcite
CCD . . . Charge Coupled Devices
CDI . . . Coherent Diffractive Imaging
CH . . . Calcium Hydroxide (Portlandite)
CM . . . cement
CMOS . . . Complementary Metal-Oxide-Semiconductor
CO_2 . . . Carbon dioxide
CPU . . . Central Processing Unit
cSAXS . . . Coherent Small-Angle X-ray Scattering
C-S-H . . . Calcium Silicate Hydrate
CT . . . Computed Tomography
CTF . . . Contrast Transfer Function
CXRO . . . Center of X-ray Optics

$D_{v,50}$ . . . Median particle size by volume
DOH . . . Degree of Hydration
DQE . . . Detective Quantum Efficiency

DR . . . . . Dynamic Range
DRAMA . . . . . Dynamic Row-Action Maximum-likelihood Algorithm
DTA . . . . . Differential Thermal Analysis
DTG . . . . . Derived ThermoGravimetric

E . . . . . Energy
EBS . . . . . Extremely Brilliant Source
EIGER . . . . . Extremly hIGh rate detEctoR
ESRF . . . . . European Synchrotron Radiation Facility
eV . . . . . electron Volt

f . . . . . frequency
FBP . . . . . Filtered Back-Projection
FDK . . . . . Feldkamp Davis and Kress algorithm
FEL . . . . . Free Electron Laser
FOV . . . . . Field of View
FPD . . . . . Flat Panel Detector
FRC . . . . . Fourier Ring Correlation
FSC . . . . . Fourier Shell Correlation
FW . . . . . Free Water
FWHM . . . . . Full Width Half Maximum

GPU . . . . . Graphics Processing Unit
GSAS . . . . . General Structure Analysis System
GSH . . . . . GreyScale Histogram
GT . . . . . Global Thresholding
Gyp . . . . . Gypsum

h . . . . . Planck's constant
HP . . . . . Hydrate Product

I . . . . . measured Intensity of the X-ray beam
ID . . . . . Inserting Device
ILST . . . . . Iterative Least-Squares Technique
IPSDK . . . . . Image Processing Software Development Kit

LaB_6 . . . . . Lanthanum hexaBoride
Lab-μCT . . . . . Laboratory X-ray Computed microTomography
LC^3 . . . . . Limestone Calcined Clay Cement
LinAc . . . . . Linear Accelerator
LS . . . . . Limestone
LXRPD . . . . . Laboratory X-Ray Powder Diffraction

MAS-NMR . . . . . Magic Angle Spinning Nuclear Magnetic Resonance
MIP . . . . . Mercury Intrusion Porosimetry
MK . . . . . Metakaolinite
ML . . . . . Machine Learning
MLEM . . . . . Maximum-Likelihood Expectation Maximization
Mo . . . . . Molybdenum
MoBI . . . . . Modulation Based Imaging
MTF . . . . . Modulation Transfer Function

NMR . . . . . Nuclear Magnetic Resonance

OPC . . . . . Ordinary Portland Cement
ORS . . . . . Object Research Systems
OSEM . . . . . Ordered Subset Expectation Maximization

Pag. . . . . Paganin
PBI . . . . . Propagation Based Imaging
PC . . . . . Portland Cement
PCE . . . . . Polycarboxylate Ether
PCI . . . . . Phase-Contrast Imaging
PSD . . . . . Particle Size Distribution
PSF . . . . . Point Spread Function
PSI . . . . . Paul Scherrer Institute
PXCT . . . . . Ptychographic X-ray Computed Tomography

RAM . . . . . Random Access Memory
RAMLA . . . . . Row Action Maximum Likelihood Algorithm
RF . . . . . RadioFrequency
ROI . . . . . Region of Interest
RQPA . . . . . Rietveld Quantitative Phase Analysis
RT . . . . . Room Temperature

SCM . . . . . Supplementary Cementitious Material
SIRT . . . . . Simultaneous Iterative Reconstruction Technique
SLS . . . . . Swiss Light Source
SNR . . . . . Signal-to-Noise Ratio
STFT . . . . . Short-Time Fourier Transform
Syn-μCT . . . . . Synchrotron X-ray Computed microTomography

TAM . . . . . Thermal Activity Monitor
TGA . . . . . ThermoGravimetric Analysis

TIE . . . . . Transport-of-Intensity Equation
TW . . . . . Total Water

UCP . . . . . Unreacted Cement Particles

VOI . . . . . Volume of Interest

w/b . . . . . water-to-binder ratio
w/c . . . . . water-to-cement ratio
wt . . . . . weight

XCT . . . . . X-ray Computed Tomography
XRF . . . . . X-Ray Fluorescence

Z . . . . . atomic number

Cement Nomenclature

Table 1: Cement Nomenclature

$A = Al_2O_3$
$C = CaO$
$\underline{C} = CO_2$
$F = Fe_2O_3$
$H = H_2O$
$K = K_2O$
$M = MgO$
$N = Na_2O$
$S = SiO_2$
$\underline{S} = SO_3$

Table 2: Overview of common compounds and formula abbreviations in cement science.

Name	Cement abbreviation	Formula	Oxides
Anhydrite	$C\underline{S}$	$CaSO_4$	$CaO.SO_3$
Bassanite	$C\underline{S}H_{0.5}$	$CaSO_4.0.5H_2O$	$CaO.SO_3.0.5H_2O$
Calcite	$C\underline{C}$	$CaCO_3$	$CaO.CO_2$
Calcium Aluminate	CA	$CaAl_2O_4$	$CaO.Al_2O_3$
Dicalcium Aluminate Hydrate	C_2AH_8	$Ca_2Al(OH)_6[Al(OH)_4.3H_2O]$	$2CaO.Al_2O_3.8H_2O$
Dicalcium Silicate (Belite)	C_2S	Ca_2SiO_4	$2CaO.SiO_2$
Ettringite (AFt)	$C_6A\underline{S}_3H_{32}$	$Ca_6Al_2(OH)_{12}(SO_4)_3.26H_2O$	$6CaO.Al_2O_3.3SO_3.32H_2O$
Gibbsite	AH_3	$2Al(OH)_3$	$Al_2O_3.3H_2O$
Gypsum	$C\underline{S}H_2$	$CaSO_4.2H_2O$	$CaO.SO_3.2H_2O$
Hemicarbo-aluminate (Hc)	$C_4A\underline{C}H_{11}$	$Ca_2Al(OH)_6(CO_3)_{0.25}$ $OH_{0.5}\cdot 2H_2O$	$4CaO.Al_2O_3.CO_2.11H_2O$
Hydrogarnet	C_3AH_6	$Ca_3Al_2(OH)_{12}$	$3CaO.Al_2O_3.6H_2O$
Iron Hydroxide	FH_3	$2Fe(OH)_3$	$Fe_2O_3.3H_2O$
Iron (Siliceous) Hydrogarnet	$C_3A_{0.5}F_{0.5}SH_4$	$Ca_3(Al_{0.5}Fe_{0.5})_2(SiO_4)(OH)_8$	$3CaO.0.5Al_2O_3.0.5Fe_2O_3.$ $SiO_2.4H_2O$
Mayenite	$C_{12}A_7$	$Ca_{12}Al_{14}O_{33}$	$12CaO.7Al_2O_3$
Metakaolinite	AS_2	$Al_2Si_2O_7$	$Al_2O_3.2Si_2O_2$
Monocarbo-aluminate (Mc)	$C_4A\underline{C}_{0.5}H_{12}$	$Ca_2Al(OH)_6(CO_3)_{0.5}\cdot 2H_2O$	$4CaO.Al_2O_3.0.5CO_2.12H_2O$
Monosulfate (AFm)	$C_4A\underline{S}H_{12}$	$Ca_4Al_2(OH)_{12}(SO_4).6H_2O$	$4CaO.Al_2O_3.SO_3.12H_2O$
Portlandite	CH	$Ca(OH)_2$	$CaO.H_2O$
Siliceous Hydrogarnet	C_3ASH_4	$Ca_3Al_2(SiO_4)(OH)_8$	$3CaO.Al_2O_3.SiO_2.4H_2O$
Stratlingite	C_2ASH_8	$Ca_2Al(OH)_6[AlSiO_2$ $(OH)_4.3H_2O]$	$2CaO.Al_2O_3.SiO_2.8H_2O$
Tetracalcium Aluminoferrite	C_4AF	$Ca_4Al_2Fe_2O_{10}$	$4CaO.Al_2O_3.Fe_2O_3$
Tricalcium Aluminate	C_3A	$Ca_3Al_2O_6$	$3CaO.Al_2O_3$
Tricalcium Silicate (Alite)	C_3S	Ca_3SiO_5	$3CaO.SiO_2$

Summary *

Portland cement is the most common type of cement used. Portland cement (PC) is made by heating limestone with other phases such as clay and sand in a kiln at high temperature. Portland cement (PC) is produced at a rate of around 4 billion tonnes per year, making it the main ingredient in the production of concrete, the second most widely used substance after fresh water.
Despite its ubiquitous use, PC is a controversial material because of its enormous environmental impact. On average, the production of one tonne of Portland clinker releases approximately 0.9 tonnes of CO_2 into the environment, including emissions from limestone crushing and fuel combustion. This accounts for around 7% of total anthropogenic CO_2 emissions and also emits chemicals and particles that can cause health problems.
Cement hydration is a complex process influenced by a number of factors such as chemical composition, particle size and environmental conditions. Accurate microstructural investigation at different length scales remains a challenge in cement hydration research. The carbon footprint of cement is also being reduced by substituting clinker with calcined clay and calcite for instance in Limestone Calcined Clay Cements (LC^3). When SCMs are added to cement mixes, pozzolanic reactions occur which help to decrease capillary porosity.

The first chapter of this dissertation provides the background to the study by giving an overview of the materials, experimental procedures and imaging modalities used. It begins with a description of the history and applications of different types of cement and then moves on to the growth of imaging technologies in the sector. The chapter then delves into a comprehensive review of characteristic tests and X-ray imaging techniques, focusing on synchrotron and laboratory imaging, absorption imaging and phase contrast. Due to the multidisciplinary nature of the thesis, this introductory chapter is divided into three sections: cements, X-ray imaging and X-ray imaging of cements. The chapter also provides an overview of the consumables, equipment and sample preparation procedures used in the study.

The objectives of the thesis are outlined in the second chapter and are essentially to create a methodology and optimise sample preparation for quantitative analysis of cementitious materials using X-ray based imaging. Emphasis is placed on data analysis for synchrotron-based imaging and comparisons with laboratory-based systems. While the emphasis is on X-ray imaging, other laboratory techniques are used to confirm the results. Three imaging modalities are reviewed and contrasted, namely synchrotron X-ray computed microtomography, ptychographic X-ray computed nanotomography and laboratory X-ray computed microtomography.

The third chapter brings together the derived papers from the thesis into

* Note: A minimum of 3000 words is required by the University of Malaga normative.

a single coherent piece.
Because of the environmental impact of Portland Cement (PC) production and the demand for more environmentally friendly alternatives. The production of PC is a significant contributor to CO_2 emissions and emits hazardous gases and particles. One option to reduce the CO_2 is supplementary cementitious materials (SCM) and the other option is to use active Belite Cements (BCs), which have lower CO_2 emissions and other benefits such as lower energy consumption and longer service life. However, due to their lower reactivity, BCs require more grinding energy and faster cooling rates.

The first paper investigates the hydration behaviour of Limestone Calcined Clay Cements using synchrotron and laboratory X-ray microtomography to study microstructural characteristics and capillary porosity variations. The second study investigates the hydration properties of Belite Cements at different curing temperatures using techniques such as laboratory X-ray powder diffraction analysis, thermal analysis and synchrotron X-ray microtomography. The third paper uses hard X-ray ptychographic nanotomography to study the hydration of Calcium Aluminate Cements and the formation of secondary water porosity. The fourth paper uses near-field ptychographic nanotomography to visualise the early stages of Portland Cement hydration, providing insights into dissolution and precipitation processes. Finally, the fifth paper presents a new methodology for studying the hydration process of cement pastes in situ, combining laboratory X-ray powder diffraction (LXRPD) and microtomography (CT). To avoid self-drying, the pastes are injected into a thicker capillary (compared to the rest of the work in this thesis) and measurements are taken at the same location as the hydrating paste.
The aim of Article 1 (A#1) is to investigate the hydration behaviour of Limestone Calcined Clay Cements (LC^3). Microporosity and capillary porosity are investigated using synchrotron and laboratory X-ray microtomography. The study shows that while X-ray microtomography is useful in detecting these properties, it has limitations in assessing porosity below the spatial resolution of the imaging technique. Various samples are given to illustrate the application of X-ray microtomography to the study of LC^3 binders.
Furthermore, this study fits into our larger goal of directly measuring metakaolinite (MK) and limestone reactivities using coupled X-ray imaging and diffraction. This cannot be achieved by diffraction alone as various amorphous phases disappear (at least free water and MK) and form (at least C-S-H gel from alite, C-A-S-H gel from pozzolanic reaction and iron siliceous hydrogarnet amorphous phase from ferrite hydration). The use of Rietveld refinement of laboratory X-ray powder diffraction (LXRPD) in conjunction with laboratory CT is being investigated. We conclude in this work that for synchrotron microtomographic studies, a minimal sample-to-detector propagation distance enhances the contrast in Paganin reconstructed datasets. This experimental setup and data processing approach produces tomograms in which calcite can be separated from the other components.

Article 2 (A#2) deals with Belite Cements (BCs), which have the potential to be more environmentally friendly binders than typical Portland

Cements (PCs). The second article investigates the effect of curing temperature on the hydration process of Belite Cement in comparison with Portland Cement. The aim of the study is to improve knowledge of the behaviour of Belite cement under different curing conditions and to provide insights into its potential use in construction. The hydration properties of BCs at different curing temperatures (20, 40 and 60 °C) are investigated and compared with those of PC. Methods used in this project include Rietveld phase analysis, thermal analysis, calorimetry, silicon MAS-NMR, mercury intrusion porosimetry and synchrotron X-ray microtomography.
We exploit the coherence properties of synchrotron X-rays by positioning the detector a few millimetres away from the sample, resulting in edge enhancement, commonly known as X-ray phase contrast, but without numerous fringes that could compromise quantitative analysis. Two data sets, "Absorption" and "Paganin", were reconstructed from a single propagation-based tomographic data acquisition.
Several analyses were carried out by inspecting the greyscale histograms and showing the volume percentage evolution of each component for these *ex situ* samples hydration stages. The results indicate that the improved mechanical performance of BCs at moderate curing temperatures is mainly due to a higher degree of belite reaction and reduced porosity coarsening.
In other words, the research in Article 2 (A#2) looks at the changes in hydration behaviour and microstructure between BCs and PCs at different hardening temperatures. In contrast to PCs, BCs have been shown to increase in compressive strength with increasing temperature. To corroborate these findings and compare the microstructural changes, the study used high-resolution synchrotron X-ray microtomography. By providing insight into the different behaviour of BCs and PCs, the results could lead to the production of more sustainable concretes.

Calcium Aluminate Cements (CAC) offer high early strength, chemical resistance and low temperature workability. They are often used as additives in complex building formulations, acid attack resistance, rapid repair materials and refractory concretes. However, CACs are not recommended for general structural applications due to their susceptibility to misuse. The main hydraulic phase of CACs is monocalcium aluminate (CA), which undergoes temperature-dependent hydration processes. CA-hydrate conversion reactions result in the formation of denser hydrates and the release of secondary water, leading to the development of porosity in the binders. High water-to-cement ratios and low cement concentrations contribute to durability problems and building collapse. There are two knowledge gaps: the mass densities and water contents of aluminium hydroxide gels, and the microstructural effects of conversion processes.
In Article 3 (A#3), synchrotron ptychographic nanotomography X-ray imaging, a high-resolution imaging technique, is proposed to study the conversion reactions and characterise the porosity growth in CACs. In this project, we have used ptychographic nanotomography to study CA hydration and to understand the evolution of water porosity during conversion chemical reactions, which has a significant impact on the mechanical strength and durability of CACs. By being able to distinguish air and water porosity with ptychography imaging modality, we segmented

the secondary water porosity of CAC sample in 3D. This is a proof of the appeared secondary water content by increasing temperature in CAC conversion processes. Initial data analysis show secondary porosity with typical pore diameters of around 140 nm. The research reports on the mass densities of the resulting $Al(OH)_3$ gels and explores the implications of the data for durability predictions. The resulting mass densities for samples hydrated at 4, 20 and 50 °C are 1.94, 1.98 and 2.23 g/cm^3 respectively, assuming that the gels have an $Al(OH)_3$ composition.

The Nature Communications paper (Article 4 (A#4)) focuses on the use of sophisticated combined X-ray imaging techniques to analyse the early stages of cement hydration. Cement hydration describes the chemical processes that occur when water combines with cement, resulting in the formation of solid compounds and the hardening of the material.
Starting with the initial *in situ* mixing of cement powder with water, the experimental setup involved the analysis of cement samples at different stages of hydration. The samples were studied over time, allowing us to record the dynamic changes occurring within the cement matrix.
To gain a thorough understanding of the hydration process, we used a cutting-edge imaging technique called 4D nanoimaging. This method combines X-ray tomography with time-resolved imaging, allowing high-resolution visualisation of cement structures in three dimensions and over time. We were able to follow the growth of the cement microstructure (such as etch-pit development, anhydrous grain dissolution) and gain insight into the underlying chemical events by taking images at regular intervals.
The fourth paper deals with the difficulty of understanding cement dissolution and precipitation processes at an early stage. We used near-field ptychographic nanotomography to visualise the hydration of commercial Portland cement in a capillary. From this work and after 19 hours, a porous C-S-H gel shell with a thickness of 500 nm develops around the alite grains, containing a water gap of 490 nm of thickness in average. The dissolution rates of small and large alite grains are studied and the formation of etch-pits is shown. Complementary laboratory and synchrotron microtomography measurements are used to analyse particle size distributions over time, and the potential of 4D nanoimaging for understanding dissolution-precipitation processes is highlighted.
4D nanoimaging sheds light on the mechanisms involved in the formation of C-S-H gel, providing critical insights into its evolution. Alite particles smaller than 3 μm are completely hydrated within 19 hours, resulting in a spatial dissolution rate of 100 nm/h in the acceleration period. The largest size of Hadley grains found here agrees well with previous studies (at 24 hours), which show a maximum size of 5 μm with shells of 500 nm. From the data analysis in the deceleration period, 19h to 47h, the measured alite dissolution rate was 25nm/h. As a result, there appears to be a 3-4 fold difference in the spatial dissolution rate of small alite grains during acceleration versus large alite grains during deceleration. The measured electron densities for the different components have been compared with the theoretical values. For instance, the measued electron density for "Portlandite" at 19 h and 93 h were 0.62 $eÅ^{-3}$ and 0.651 $eÅ^{-3}$, which is lower than the 0.69 $eÅ^{-3}$ theoretical value. This lower value may be due to a partial volume effect, as there is more water in the early stages of hydration that can be occluded within the segmented volumes.

This water can not be distinguished due to the attained spatial resolution, close to 250 nm. Understanding the evolution of pore structures is critical because it affects cement properties such as permeability and mechanical strength. The 4D ptychographic nanoimaging approach can also reveal pore patterns within the cement matrix and distinguish between water and air porosity. During the hydration process, we see the formation and distribution of pores and also the conversion of water porosity to air porosity and densification.

In all of the articles the step by step image analysis is discussed and based on the modality of the imaging, we are able to segment the cement phases between 3 to 7 components. Ptychographic X-ray Computed Tomography's great spatial resolution and strong contrast allowed us to classified the components into seven groups. For instance, the spatial resolution for the "Near-field Ptychography" of Article 4 (A#4) was in the range of 250 nm.

In the same vein, Article 5 (A#5) discusses the difficulties in understanding the hydration process of Portland Cement (PC) at different length scales. Accurate analytical methods are required to understand the hydration processes. The ability to correctly analyse unaltered microstructures at different length scales is not well established for PCs. Article 5 (A#5) study focuses on the *in situ* measurement of PC hydration using laboratory X-ray techniques: X-ray microtomography (CT) and X-ray powder diffraction. While X-ray powder diffraction has been widely used for quantitative phase analysis of crystalline components, accurate CT analysis of hydrated components and microstructures remains challenging.
Article 5 (A#5), proposes a novel and accurate method for analysing cement hydration using *in situ* laboratory microtomography and X-ray powder diffraction methods that do not require sample conditioning and where data analysis can be automated (in the future). The use of thick capillaries is critical to prevent the paste from drying out, so the investigation focuses on a Portland cement paste injected into 2.0 mm capillaries with a water-to-cement ratio (w/c) of 0.50. To ensure accuracy and consistency, all measurements are taken from the same area of the hydrating capillary.
This study extends the *in situ* research described in Article 4 (A#4), which used ptychographic synchrotron nanotomography, now with laboratory microCT to assess PC hydration at an early stage. In addition to using LXRPD and CT to investigate the hydration of a PC, further *ex situ* samples are prepared for accuracy validation using thermal analysis and calorimetry. The proposed *in situ* technique is shown to be accurate and provides the basis for future applications to more complex hydrating binders, including the ultimate goal: the hydration of PC-SCMs blends.

These publications, taken together, contribute to a better knowledge of the hydration behaviour and microstructures of different types of cementitious materials using advanced imaging techniques. It provides useful insights into the performance and properties of these materials, as well as the advantages and disadvantages of different imaging techniques for studying their properties.

The fourth chapter is the general discussion section, in which the results of these papers are not repeated but an integrative approach is developed by inspecting the spatial resolution, contrast and segmentation details of all these works. The research implications are addressed in relation to the study objectives and the data are critically analysed in the context of the field. Any unexpected or contradictory findings are discussed and explained when possible, and ways of revisiting the findings are suggested and implemented. This in-depth discussion is intended to broaden awareness of the challenges of the thesis topic, generate fresh ideas and set the framework for research into X-ray imaging of cementitious materials.

The discussion focuses on the idea of resolution, which can be divided into three types: temporal resolution, spatial resolution and contrast resolution. Apart from Fourier Shell Correlation (FSC), a commonly used criterion for measuring spatial resolution, which has been criticised for its reliance on a threshold, variations in grey level/electron density and interface edge sharpness are employed to determine spatial resolution in a unified and general way for hydrating cements. All imaging setups used in the investigation of this thesis used the same type of glass capillary with air surrounding the mounted specimen. The method for measuring interface sharpness is described here and the results of several approaches to get a sense of spatial resolution are summarised in a complete table including key acquisition parameters. Several measurements are averaged and different cases are presented in figures.

The different parameters of the acquisition setups of the different imaging modalities are discussed and the possible advantages and disadvantages are pointed out. The Field of View (FOV) of the scans and its impact on the imaging modalities used and the shape of the capillaries in different studies is illustrated, as well as how this affects data acquisition.

In addition, the section discusses contrast resolution in X-ray imaging. We illustrate this by employing the grey values (or electron densities in ptychotomography) histograms, It is clear that a larger number of narrow peaks indicate a better contrast. In other words, a better ability to distinguish between different components. The phase contrast approach, which uses refraction information in addition to absorption, allows greater differentiation of components in a sample. The different imaging modalities used in the study allow different stages of cement samples to be distinguished to different degrees. The acquisition times for each modality are different, with ptychography providing superior contrast and spatial resolution but taking longer to scan. Another limitation is sample thickness, as different modalities require different sample thicknesses for effective data processing. For instance, algorithms for near-field ptychographic nanotomography currently fail to reconstruct tomograms for samples thicker than 250 microns.

The importance of contrast is highlighted in the quantitative analysis and segmentation of complex cementitious materials. The use of methods such as the Paganin filter in phase-contrast mode can enhance specific components, but may affect quantitative analysis based on the histogram. The high spatial coherence of synchrotron radiation is used to enhance contrast and identify phase boundaries in phase retrieval techniques such as propagation-based phase contrast and ptychography.

Furthermore, the difference between the delta and beta data sets that can be derived from the ptychography modality is shown.

We discussed how we have used our knowledge of synchrotron imaging for *in situ* imaging in laboratory X-ray imaging and combined it with complementary studies. This was achieved by using an optimised sample preparation procedure and consistent data analysis. During the ptychography scans, the position of the capillaries was precisely preserved and data realignment was investigated. A custom-designed sample holder was developed for the laboratory. In addition, the Lab-μCT followed the approach of the synchrotron phase-contrast beamline sample mounting, which is a mark on the sample holder to limit variability in the initial incidence angle position.

A section of the discussion chapter is also dedicated to a detailed description of the segmentation approaches used in this thesis, namely Global Thresholding and Machine Learning.
We explain the application of Machine Learning (ML) in the field of X-ray imaging and data processing, with particular emphasis on its use in the analysis of cementitious materials. In the discussion, we describe the three types of machine learning: unsupervised learning, supervised learning and semi-supervised learning. We highlight the importance of supervised learning models, which rely on labelled data to provide superior results, and which are used in this thesis. It also discusses decision trees, which were the first learning algorithms used in machine learning. It describes how decision trees categorise data at each node based on multiple criteria. Bagging is a technique that combines different algorithms trained on subsets of data to increase accuracy. The Random Forest approach, an extension of bagging that incorporates "feature randomness" to produce more diverse and less correlated decision trees, is also described. We emphasise the importance of training data in ML algorithms, and the need for it to represent the full range of changes and situations observed in research. The quality and variety of input data is critical for good predictions, but low resolution, noisy or poorly labelled data can lead to errors. Deep learning issues such as the need for large amounts of RAM and GPU power are noted, especially when working with cement samples. The limitations of obtaining annotated training data are also highlighted, as is the use of random forest as an alternative. The influence of the partial volume effect on threshold segmentation and quantitative analysis is also discussed. The importance of ML in correcting for these effects and improving quantitative measurement accuracy is highlighted. A comparison of Global Thresholding (GT) and Machine Learning (ML) for *in situ* laboratory testing is given, with a focus on Hydrate Product (HP) and Unhydrated Cement Particles (UCP) contents.

The fifth chapter of the dissertation contains a brief overview and conclusion. It summarises the aims of the study, the methodology used and the main conclusions drawn from the investigations. The chapter also discusses the implications of the findings and offers future directions for study. This chapter concludes the thesis by highlighting the relevance of the work and its contributions to the field of cementitious materials investigation using X-ray imaging. The sixth chapter is the Spanish translation of the previous one.

The seventh chapter is the collection of Supplementary Information for the papers presented in the third chapter.

Resumen (Spanish summary)[†]

El cemento Portland es el tipo de cemento más utilizado. El cemento Portland se fabrica calentando piedra caliza con otras fases, como arcilla y arena, en un horno a alta temperatura.
El cemento Portland se produce a razón de unos 4.000 millones de toneladas al año, lo que lo convierte en el principal componente en la producción de hormigón, el segundo producto más utilizado después del agua dulce.
A pesar de su uso omnipresente, el cemento Portland es un material controvertido por su enorme impacto ambiental. Por término medio, la producción de una tonelada de clínker Portland libera aproximadamente 0,9 toneladas de CO_2 al medio ambiente, incluidas las emisiones procedentes de la trituración de la piedra caliza y la combustión del combustible. Esto representa alrededor del 7% de las emisiones antropogénicas totales de CO_2 a la atmósfera y también emite sustancias químicas y partículas que pueden causar problemas de salud. La hidratación del cemento es un proceso complejo en el que influyen varios factores, como la composición química, el tamaño de las partículas y las condiciones ambientales. Hacer una investigación microestructural con precisión a diferentes escalas de longitud sigue siendo un reto en la investigación de la hidratación del cemento. La huella de carbono del cemento también se está reduciendo mediante la sustitución del clinker con arcilla calcinada y calcita, como los cementos de arcilla calcinada con piedra caliza (LC^3). Cuando se añaden materiales cementantes suplementarios a las mezclas de cemento, se producen reacciones puzolánicas que contribuyen a disminuir la porosidad capilar.
El primer capítulo de esta tesis proporciona los antecedentes del estudio ofreciendo una visión general de los materiales, los procedimientos experimentales y las técnicas de obtención de imágenes utilizadas. Comienza con una descripción de la historia y las aplicaciones de los distintos tipos de cemento para pasar después al crecimiento que han tenido las tecnologías de obtención de imágenes en el sector. A continuación, el capítulo se adentra en una revisión exhaustiva de los ensayos característicos y las técnicas de obtención de imágenes de rayos X, centrándose en las imágenes de sincrotrón y de laboratorio, las imágenes de absorción y el contraste de fases. Debido al carácter multidisciplinar de la tesis, este capítulo introductorio se divide en tres secciones: cementos, técnicas de imagen de rayos-X y técnicas de imagen de rayos-X de cementos. El capítulo también ofrece una visión general de los consumibles, el equipo y los procedimientos de preparación de muestras utilizados en el estudio.

Los objetivos de la tesis se esbozan en el segundo capítulo y consisten esencialmente en crear una metodología y optimizar la preparación de muestras para el análisis cuantitativo de materiales del cemento mediante imágenes basadas en rayos X. Se hace hincapié en el análisis de datos con imágenes de sincrotrón y comparaciones con sistemas basados en laboratorio. Aunque se hace hincapié en las imágenes de rayos X, se

[†] Note: The abbreviations used in the Spanish summary and Spanish conclusion are the same as those used in the English, which are listed in the "Spatial Terms" section.

utilizan otras técnicas de laboratorio para confirmar los resultados. Se revisan y contrastan tres modalidades de obtención de imágenes, la microtomografía computarizada de rayos X de sincrotrón, la pticongrafía tomográfica de rayos-x computerizada (PXCT) y la microtomografía computarizada de rayos X de laboratorio.

El tercer capítulo reúne los trabajos derivados de la tesis en una sola pieza siguiendo una coherencia. Debido al impacto ambiental de la producción de cemento Portland se necesitan alternativas más respetuosas con el medio ambiente. La producción de cemento Portland contribuye significativamente a las emisiones de CO_2 y emite gases y partículas peligrosas. Una opción para reducir el CO_2 son los materiales cementantes suplementarios y la otra opción es utilizar cementos belíticos activados, que tienen menores emisiones de CO_2 y otras ventajas como un menor consumo de energía y una vida útil más larga. Sin embargo, debido a su menor reactividad, los cementos belíticos requieren más energía de molienda y velocidades de enfriamiento más rápidas.

El primer trabajo investiga el comportamiento de hidratación de los cementos de arcilla calcinada con caliza utilizando microtomografía de rayos X de sincrotrón y de laboratorio para estudiar las características microestructurales y las variaciones de porosidad capilar. El segundo estudio investiga las propiedades de hidratación de los cementos belíticos a diferentes temperaturas de curado utilizando técnicas como el análisis de difracción de polvo de rayos X de laboratorio, el análisis térmico y la microtomografía de rayos X de sincrotrón. El tercer trabajo utiliza nanotomografía pictográfica de rayos X duros para estudiar la hidratación de los cementos de aluminato cálcico y la formación de porosidad de agua secundaria. El cuarto artículo utiliza la pticotomografía de campo cercano para visualizar las primeras etapas de la hidratación del cemento Portland, proporcionando información sobre los procesos de disolución y precipitación. Por último, el quinto artículo presenta una nueva metodología para estudiar de forma *in situ* el proceso de hidratación de las pastas de cemento, combinando la difracción de rayos X en polvo de laboratorio y la microtomografía. Para evitar el autosecado, las pastas se inyectan en un capilar más grueso (en comparación con el resto de los trabajos de esta tesis) y las mediciones se realizan en el mismo lugar donde se hidrata la pasta.

El objetivo del artículo 1 (A#1) es investigar el comportamiento de hidratación de los cementos de arcilla calcinada caliza (LC^3). La microporosidad y la porosidad capilar se investigan utilizando microtomografía de rayos X de sincrotrón y de laboratorio. El estudio muestra que, aunque la microtomografía de rayos X es útil para detectar estas propiedades, tiene limitaciones para evaluar la porosidad por debajo de la resolución espacial de la técnica de imagen. Se presentan varias muestras para ilustrar la aplicación de la microtomografía de rayos X al estudio de los cementos LC^3. Además, este estudio encaja en nuestro objetivo final de medir directamente las reactividades del metacaolín y la caliza utilizando imágenes de rayos X y difracción de forma conjunta. Esto no puede lograrse únicamente mediante difracción, ya que varias fases amorfas desaparecen con el tiempo (al menos agua libre y metacaolín) y se forman (al menos

gel C-S-H de alita, gel C-A-S-H de la reacción puzolánica y fase amorfa de hidrogranate silíceo de hierro de la hidratación de ferrita). Se está investigando el uso del afinamiento Rietveld de la difracción de polvo de rayos X de laboratorio junto con la tomografía computarizada de laboratorio. Concluimos en este trabajo que para los estudios microtomográficos de sincrotrón, una distancia mínima de propagación muestra-detector mejora el contraste en los conjuntos de datos reconstruidos con Paganin. Esta configuración experimental y el enfoque de procesamiento de datos producen tomogramas en los que la calcita se puede separar de los otros componentes.

El artículo 2 (A#2) trata de los cementos belíticos, que tienen el potencial de ser aglutinantes más respetuosos con el medio ambiente que los típicos cementos Portland. El segundo artículo investiga el efecto de la temperatura de curado en el proceso de hidratación de los cementos belíticos en comparación con el cemento Portland. El objetivo del estudio es mejorar el conocimiento del comportamiento de los cementos belíticos en diferentes condiciones de curado y aportar ideas sobre su posible uso en la construcción. Se han investigado las propiedades de hidratación de los cementos belíticos a diferentes temperaturas de curado (20, 40 y 60 °C) y se han comparado con las del cemento Portland. Los métodos utilizados en este proyecto incluyen el análisis de fases de Rietveld, el análisis térmico, la calorimetría, MAS-NMR de silicio, la porosimetría por intrusión de mercurio y la microtomografía de rayos X de sincrotrón. Aprovechamos las propiedades de coherencia de los rayos X de sincrotrón colocando el detector a pocos milímetros de la muestra, lo que da lugar a un realce de los bordes, comúnmente conocido como contraste de fase de rayos X, pero sin numerosas franjas que pudieran comprometer el análisis cuantitativo. Se reconstruyeron dos conjuntos de datos, "Absorción" y "Paganin", a partir de una única adquisición de datos tomográficos basados en la propagación. Se han realizado varios análisis inspeccionando los histogramas de escala de grises y mostrando la evolución del porcentaje de volumen de cada componente para estas etapas de hidratación de las muestras ex situ. Los resultados indican que la mejora de las prestaciones mecánicas de los cementos belíticos a temperaturas de curado moderadas se debe principalmente a un mayor grado de reacción de la belita y a un contenido reducido de poros gruesos.
En otras palabras, la investigación del artículo 2 (A#2) examina los cambios en el comportamiento de hidratación y la microestructura entre los cementos belíticos y los cementos Portland a diferentes temperaturas de endurecimiento. A diferencia de los cementos Portland, se ha demostrado que los cementos belíticos aumentan su resistencia a la compresión al aumentar la temperatura. Para corroborar estos resultados y comparar los cambios microestructurales, en este estudio se utilizó la microtomografía de rayos X de sincrotrón de alta resolución. Una vez conocida la información sobre los diferentes comportamientos de los cementos belíticos y Portland, los resultados obtenidos podrían conducir a la producción de hormigones más sostenibles.

Los cementos de aluminato cálcico ofrecen una alta resistencia inicial, resistencia química y trabajabilidad a bajas temperaturas. Suelen utilizarse como aditivos en formulaciones complejas de construcción, resistencia al

ataque ácido, materiales de reparación rápida y hormigones refractarios. Sin embargo, los cementos de aluminato cálcico no se recomiendan para aplicaciones estructurales generales debido a la posibilidad de ser usados de forma incorrecta. La principal fase hidráulica de los cementos de aluminato cálcico es el aluminato monocálcico, que experimenta procesos de hidratación dependientes de la temperatura. Las reacciones de conversión aluminato monocálcico-hidrato dan lugar a la formación de hidratos más densos y a la liberación de agua secundaria, lo que conduce al desarrollo de porosidad en las pastas de cemento. Las altas relaciones agua-cemento y las bajas concentraciones de cemento contribuyen a los problemas de durabilidad y al colapso de los edificios. Existen dos lagunas de conocimiento: las densidades de masa y los contenidos de agua de los geles de hidróxido de aluminio, y los efectos microestructurales de los procesos de conversión.

En el artículo 3 (A#3), se propone la pticotomografía de campo lejano, una técnica de imagen de alta resolución, para estudiar las reacciones de conversión y caracterizar el crecimiento de la porosidad en los cementos de aluminato cálcico. En este proyecto, hemos utilizado la pticotomografía para estudiar la hidratación del aluminato monocálcico y comprender la evolución de la porosidad del agua durante las reacciones químicas de conversión, lo cual tiene un impacto significativo en la resistencia mecánica y la durabilidad de los cementos de aluminato cálcico. Al ser capaces de distinguir la porosidad del aire y del agua con la modalidad de imagen de pticotomografía, segmentamos la porosidad secundaria del agua de la muestra de cemento de aluminato de calcio en 3D. Esto es una prueba del contenido de agua secundaria que aparece al aumentar la temperatura en los procesos de conversión del cemento de aluminato de calcio. Los primeros análisis de datos muestran una porosidad secundaria con diámetros de poro típicos de unos 140 nm. Esta investigación reporta las densidades de masa de los geles de $Al(OH)_3$ resultantes y explora las implicaciones de los datos para las predicciones de durabilidad. Las densidades másicas resultantes para las muestras hidratadas a 4, 20 y 50 °C son de 1.94, 1.98 y 2.23 g/cm^3 respectivamente, suponiendo que los geles tienen una composición química de $Al(OH)_3$.

El artículo de Nature Communications (artículo 4 (A#4)) se centra en el uso de técnicas sofisticadas que combinan las imágenes de rayos-X para analizar las primeras etapas de la hidratación del cemento. La hidratación del cemento describe los procesos químicos que se producen cuando el agua se combina con el cemento, dando lugar a la formación de compuestos sólidos y al endurecimiento del material.

Partiendo de la mezcla inicial cuando se mezcla de forma *in situ* el cemento en polvo con el agua, el montaje experimental da lugar al análisis de muestras de cemento en distintas fases de hidratación. Las muestras se estudiaron a lo largo del tiempo, lo que permitió registrar los cambios dinámicos que se producían dentro de la matriz de cemento.

Para comprender a fondo el proceso de hidratación, utilizamos una técnica de imagen de vanguardia denominada nanoimagen en 4D. Este método combina la tomografía de rayos X con la obtención de imágenes con resolución temporal, lo que permite una visualización de alta resolución de las estructuras del cemento en tres dimensiones y a lo largo del tiempo. Se ha podido seguir el crecimiento de la microestructura del cemento (como el desarrollo de la fosa, la disolución de granos anhidros)

y se han comprendido mejor los procesos químicos subyacentes tomando imágenes a intervalos regulares.
El cuarto artículo aborda la dificultad de comprender los procesos de disolución y precipitación del cemento a edades tempranas. Utilizamos pticotomografía de campo cercano para visualizar la hidratación de cemento Portland comercial en un capilar. En este estudio se ha observado que al cabo de 19 horas, se desarrolla alrededor de los granos de alita una envoltura porosa de gel C-S-H (silicato cálcico hidratado) con un espesor de 500 nm, que contiene un hueco de agua de 490 nm de espesor de media. Se estudian también las velocidades de disolución de los granos de alita pequeños y grandes y se muestra la formación de "etch-pits". Se utilizan medidas complementarias de laboratorio y de microtomografía sincrotrón para analizar la distribución del tamaño de las partículas a lo largo del tiempo, y se pone de relieve el potencial de la técnica de nanoimagen en 4D para comprender los procesos de disolución-precipitación. La técnica de nanoimagen en 4D da detalles sobre los mecanismos implicados en la formación del gel de C-S-H, proporcionando una visión crítica de su evolución. Las partículas de alita menores de 3 μm se hidratan completamente en un plazo de 19 horas, lo que da lugar a una velocidad de disolución espacial de 100 nm/h en el periodo de aceleración. El mayor tamaño de los granos de Hadley encontrados aquí concuerda bien con estudios anteriores (a las 24 horas), que muestran un tamaño máximo de 5 μm con carcasas de 500 nm. A partir del análisis de los datos en el período de desaceleración, de 19h a 47h, la velocidad de disolución de la alita fue de 25 nm/h. Como resultado, parece haber una diferencia de 3-4 veces en la velocidad de disolución espacial de los granos de alita pequeños durante la aceleración frente a los granos de alita grandes durante la deceleración.
Las densidades de electrones medidas para los distintos componentes se han comparado con los valores teóricos. Por ejemplo, la densidad de electrones medida para la "Portlandita" a las 19 h y 93 h fue de 0.62 e$Å^{-3}$ y 0.651 e$Å^{-3}$, que es inferior al valor teórico de 0.69 e$Å^{-3}$. Este valor inferior puede deberse a un efecto de volumen parcial, ya que hay más agua en las primeras edades de hidratación que puede quedar ocluida dentro de los volumenes segmentados. Esta agua no se puede distinguir debido a la resolución espacial que es cercana a 250 nm.
Comprender la evolución de las estructuras de poros es fundamental porque afecta a las propiedades del cemento, así como a la permeabilidad y la resistencia mecánica. El enfoque de la técnica de nanoimagen en 4D también puede mostrar patrones de poros dentro de la matriz de cemento y distinguir entre porosidad de agua y de aire. Durante el proceso de hidratación, vemos la formación y distribución de los poros y también la conversión de la porosidad del agua en porosidad del aire y su densificación.

En todos los artículos se analiza paso a paso el análisis de la imagen y se discute basándonos en la modalidad de la imagen, de esta forma somos capaces de segmentar las fases del cemento en bloques de entre 3 y 7 componentes. La gran resolución espacial y el fuerte contraste de PXCT nos permitieron clasificar los componentes del cemento en siete grupos. Por ejemplo, la resolución espacial para la "Pticotomografía de campo cercano" del artículo 4 (A#4) se situó en el rango de los 250 nm.

En la misma línea, el artículo 5 (A#5) analiza las dificultades para comprender el proceso de hidratación del cemento Portland a diferentes escalas de longitud. Se necesitan métodos analíticos precisos para comprender los procesos de hidratación. La capacidad de analizar correctamente las microestructuras inalteradas a diferentes escalas de longitud no está bien establecida para los cementos Portland. El estudio del artículo 5 (A#5) se centra en la medición *in situ* de la hidratación del cemento Portland mediante técnicas de rayos X de laboratorio: Microtomografía de rayos X y difracción de polvo de rayos X. Mientras que la difracción de polvo de rayos X ha sido ampliamente utilizada para el análisis cuantitativo de fases de componentes cristalinos, hacer un análisis preciso por tomografía computarizada de componentes hidratados y microestructuras sigue siendo un reto. El artículo 5 (A#5), propone un método novedoso y preciso para analizar la hidratación del cemento de forma *in situ* utiizando métodos como son la microtomografía de laboratorio y difracción de rayos X en polvo que no requieren acondicionamiento de la muestra y en el que el análisis de datos podría automatizarse (en el futuro). El uso de capilares gruesos es crítico para evitar que la pasta se seque, por lo que la investigación se centra en una pasta de cemento Portland inyectada en capilares de 2.0 mm con una relación agua-cemento de 0.50. Para garantizar la precisión y la coherencia, todas las mediciones se realizan en la misma zona del capilar hidratado.
Este estudio amplía la investigación *in situ* descrita en el artículo 4 (A#4), que utiliza pticotomografía, ahora con microCT de laboratorio para evaluar la hidratación del cemento Portland a edades tempranas. Además de utilizar la difracción de polvo de rayos X de laboratorio y la tomografía computarizada para investigar la hidratación del cemento Portland, se preparan otras muestras *ex situ* para validar la precisión mediante otras técnicas como el análisis térmico y calorimetría. La técnica *in situ* propuesta demuestra ser precisa y sienta las bases para ser aplicada en el futuro a pastas de cementos más complejas, incluido el objetivo final: la hidratación de mezclas PC-SCMs.

Estas publicaciones, en su conjunto, contribuyen a un mejor conocimiento del comportamiento de la hidratación y de las microestructuras de distintos tipos de materiales del cemento mediante técnicas avanzadas que permiten obtener imágenes de rayos-X. Estas metodologías aportan información útil sobre el comportamiento y las propiedades de estos materiales, así como sobre las ventajas e inconvenientes de las distintas técnicas de imagen para estudiar sus propiedades.

El cuarto capítulo es la sección de discusión general, en la que no se repiten los resultados de estos trabajos, sino que se desarrolla un enfoque integrador inspeccionando los detalles de resolución espacial, contraste y segmentación de todos los trabajos en conjunto. Se abordan las implicaciones de la investigación en relación con los objetivos del estudio y se analizan críticamente los datos en el contexto del campo de estudio. En la medida de lo posible, se discuten y explican las conclusiones inesperadas o contradictorias y se sugieren y aplican formas de revisarlas. Esta discusión profunda tiene por objeto ampliar la conciencia de los retos relacionados con la temática de la tesis, para generar nuevas ideas y establecer el marco para la investigación usando imágenes de

rayos X en materiales del cemento. La discusión se centra en la idea de resolución, que puede dividirse en tres tipos: resolución temporal, resolución espacial y resolución de contraste. Se ha usado la metodología de "Fourier Shell Correlation", un criterio comúnmente utilizado para medir la resolución espacial, a pesar de haber sido criticado por su dependencia de un umbral, las variaciones en el nivel de grises/densidad de electrones y la nitidez del borde de la interfaz para determinar la resolución espacial de una manera unificada y general para los cementos hidratados. Todas las metodologías usando técnicas de imagen utilizadas en la investigación de esta tesis utilizaron el mismo tipo de capilar de vidrio con aire rodeando la muestra. El método para medir la nitidez de la interfaz se describe aquí y los resultados de varios enfoques para obtener una idea de la resolución espacial se resumen en una tabla completa que incluye los parámetros clave para la adquisición de datos. Se calcula la media de varias mediciones y se presentan diferentes casos en las correspondientes figuras.

Se discuten los diferentes parámetros de las configuraciones de adquisición de las distintas modalidades de obtención de imágenes y se señalan las posibles ventajas e inconvenientes. Se ilustra el campo de visión de las exploraciones y su repercusión en las modalidades de obtención de imágenes utilizadas y la forma de los capilares en diferentes estudios, así como el modo en que esto afecta a la adquisición de datos.

Además, en esta sección también se analiza la resolución de contraste en las imágenes de rayos X. Ilustramos esto empleando los histogramas de valores de grises (o densidades electrónicas en pticotomografía), Está claro que un mayor número de picos estrechos indica un mejor contraste. En otras palabras, una mayor capacidad para distinguir entre los distintos componentes. El enfoque de contraste de fase, que utiliza información de refracción además de la absorción, permite una mayor diferenciación de los componentes dentro de una misma. Las distintas modalidades de imagen utilizadas en el estudio permiten distinguir en distinto grado los diferentes componentes de las muestras de cemento. Los tiempos de adquisición de cada modalidad son diferentes, y la pticografía proporciona un contraste y una resolución espacial superiores, pero con tiempos de escaneo superiores. Otra limitación es el grosor de la muestra, ya que las distintas modalidades requieren grosores de muestra diferentes para un procesamiento eficaz de los datos. Por ejemplo, los algoritmos de la nanotomografía pictográfica de campo cercano no son capaces de reconstruir tomogramas de muestras de más de 250 micras de grosor.

Se destaca la importancia del contraste en el análisis cuantitativo y la segmentación de sistemas cementantes complejos. El uso de métodos como el filtro Paganin en modo de contraste de fase puede realzar componentes específicos, pero puede afectar al análisis cuantitativo basado en el histograma. La alta coherencia espacial de la radiación sincrotrón se utiliza para mejorar el contraste e identificar los límites de fase en técnicas de recuperación de fase como el contraste de fase basado en la propagación y la pticotomografía.

Además, se muestra la diferencia entre los conjuntos de datos delta y beta que pueden derivarse de la modalidad de pticotomografía.

Se discute también como se ha aplicado el conocimiento disponible sobre las metodologías de imagen con radiación sincrotrón para aplicarlo a imagenes obtenidas con rayos-X de laboratorio y lo hemos combinado

con estudios complementarios. Esto se consiguió utilizando un procedimiento de preparación de muestras optimizado y un análisis de datos coherente. Durante las medidas de pticotomografía, se preservó con precisión la posición de los capilares y se investigó la realineación de los datos. Se desarrolló un portamuestras a medida para las medidas de laboratorio. Además, para realizar la microtomografía de laboratorio se siguió un enfoque similar al usado para el montaje de las muestra en la línea de haz de contraste de fase de sincrotrón, que consiste en hacer una marca en el portamuestras para limitar la variabilidad en la posición del ángulo de incidencia inicial.

También se dedica una sección del capítulo de discusión a la descripción detallada de los enfoques de segmentación utilizados en esta tesis, "Global Thresholding" (usando las varaciones en las escalas de grises) y "Machine learning" (que usa inteligencia artificial).
Se explica la aplicación del Machine Learning en el campo de las técnicas de imágenes de rayos X y el procesamiento de datos, con especial énfasis en su uso en el análisis de materiales del cemento. En la discusión, describimos los tres tipos de aprendizaje automático: aprendizaje no supervisado, aprendizaje supervisado y aprendizaje semisupervisado. Destacamos la importancia de los modelos de aprendizaje supervisado, que se basan en datos etiquetados para proporcionar resultados superiores, y que se utilizan en esta tesis.
También se habla de los árboles de decisión, que fueron los primeros algoritmos de aprendizaje utilizados en el aprendizaje automático. Describe cómo los árboles de decisión categorizan los datos en cada nodo basándose en múltiples criterios. "Bagging" es una técnica que combina distintos algoritmos entrenados en subconjuntos de datos para aumentar la precisión. También se describe el método Random Forest, una extensión del "Bagging" que incorpora la "aleatoriedad de características" para producir árboles de decisión más diversos y menos correlacionados. Destacamos la importancia de los datos de entrenamiento en los algoritmos de aprendizaje automático y la necesidad de que representen toda la gama de cambios y situaciones observados en la investigación. La calidad y variedad de los datos de entrada es fundamental para obtener buenas predicciones, pero cuando los datos son de baja resolución, ruidosos o mal etiquetados pueden dar lugar a errores. Se señalan problemas de aprendizaje como la necesidad de usar un ordenador con alta memoria RAM y potencia de GPU, especialmente cuando se trabaja con muestras de cemento. También se destacan las limitaciones de obtener datos de entrenamiento anotados, así como el uso de "Random Forest" como alternativa. También se analiza la influencia del efecto de volumen parcial en la segmentación usando Global Thresholding y el análisis cuantitativo. Se destaca la importancia del aprendizaje automático para corregir estos efectos y mejorar la precisión de las mediciones cuantitativas. Se ofrece una comparación entre "Global Thresholding" y "Machine Learning" para ensayos de laboratorio in situ, centrándose en el contenido de partículas de cemento hidratadas y no hidratadas.

El quinto capítulo de la tesis contiene un breve resumen y una conclusión. En él se resumen los objetivos del estudio, la metodología empleada y las principales conclusiones extraídas de las investigaciones. En este capítulo

también se analizan las implicaciones de los resultados y se ofrecen futuras líneas de estudio. Este capítulo concluye la tesis destacando la relevancia del trabajo y sus contribuciones al campo de la investigación de materiales del cemento analizados mediante técnicas de imágenes de rayos X. El sexto capítulo es la traducción al español del anterior.
El séptimo capítulo es la recopilación de la información complementaria de los artículos presentados en el tercer capítulo.

Introduction 1

The goal of this chapter is to contextualize the materials and samples in this thesis, as well as to define the experimental methodologies and imaging modalities used. Then we will look at the history and application of various types of cement, as well as the evolution of the most widely used imaging methods. Finally, we will go over each used characteristic test analysis and X-ray imaging in greater detail, introducing Synchrotron and Laboratory imaging, absorption imaging, and phase contrast.

As this thesis topic is in an interdisciplinary field, the introductory chapter (first chapter) of the thesis is divided into three main sections: 1.1) Introduction to cements and 1.2) Introduction to X-ray imaging and 1.3) Introduction to X-ray imaging of cements.

The first chapter of this manuscript is fully devoted to describing the context of this study. Firstly, the principal materials and pieces of equipment needed for monitoring cement hydration and achieving its quantitative analysis are introduced. In addition, the sample preparation step-by-step schematic and physical instruments of each method are presented.

1.1 Introduction to cements

Many types of cement are used in the construction industry. Population growth is one of the main drivers of demand for housing and infrastructure, which has led to increased cement production. Cement may be primarily used to bind together different building materials such as bricks, stones and concrete blocks to create strong, durable and long-lasting structures, but today we can see other uses in everyday life, even in decoration and jewellery design.
The increase of these usages and the impact on global warming and climate changes drive and motivate the similar type of research studies of this manuscript. Some of the most frequent cements used in the scientific research of this thesis are as follows:

1.1.1 Portland Cement (PC)

The ordinary type of cement that is used for most of the applications is Portland. Portland Cement (PC) is created by heating limestone with additional phases such as clay and sand in a kiln at roughly 1500°C (H. F. Taylor et al. 1997). The resultant material, known as clinker, is crushed into a fine powder and combined with a quantity of a soluble sulfate source (such as gypsum) to produce the commonly used PC.

The worldwide production of Portland Cement (PC) is approximately 4 billion tons per year (K. L. Scrivener, John, and Gartner 2018), making it the main component for manufacturing concrete (H. F. Taylor et al. 1997), which is the second most widely used material after fresh water. Despite its widespread use, PC is a highly debated material due to its

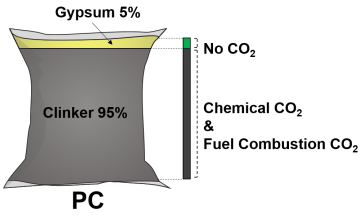

Figure 1.1: PC contents.

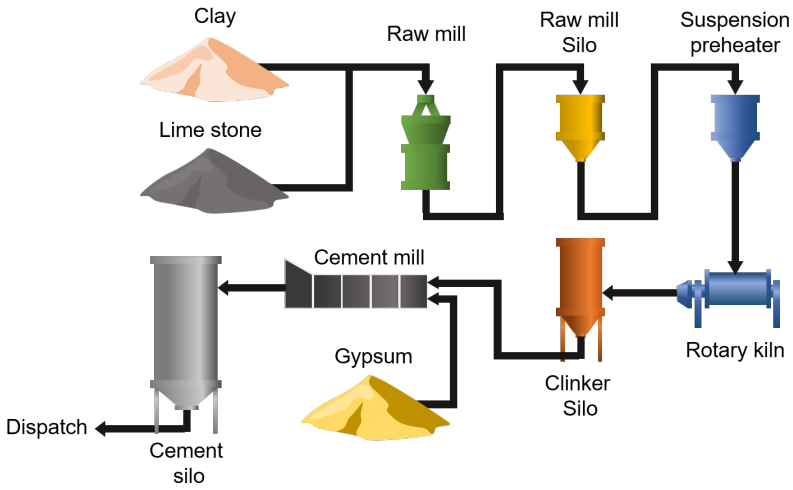

Figure 1.2: Cement production process.

significant environmental impact. On average, the production of one ton of Portland clinker results in the emission of around 0.9 tons of CO_2 into the atmosphere (Initiative 2009), including emissions from limestone decomposition and burning fuel (K. L. Scrivener, John, and Gartner 2018), (See Figure 1.2). This accounts for around 7% of the total anthropogenic CO_2 emissions (Barcelo et al. 2014) and also releases gases and particles that can cause health problems (Miller and Moore 2020). This is the main reason why we are focusing on cement imaging in this thesis, which is the best approach to understanding the evolution and reactions at the micro- and nano-scale, which can help to go further for the proposal of alternative and eco-cement. In cement science, this type of cement is also known as Ordinary Portland Cement (OPC).

1.1.2 Belite Cement (BC)

As can be deduced from the name of this type of cement, it has a higher proportion of the initial belite phase in it, see Table 1.1. Belite Cement (BC) could be a more sustainable binder than Portland Cement (PC) (Ana Cuesta, Ayuela, and M. A. Aranda 2021). One way to reduce the CO_2 footprint of cements is to use active BCs (Miller and Myers 2019, Barcelo et al. 2014, Van Vliet et al. 2012, Chatterjee 1996). Reduced limestone requirements with lower associated CO_2 emissions, lower maximum kiln operating temperature and longer service life are some of the motivations for using BC.

1.1.3 Limestone Calcined Clay Cement (LC^3)

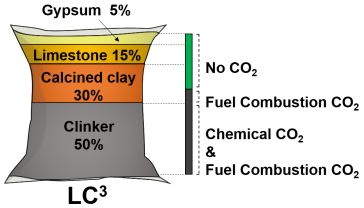

Figure 1.3: LC^3 contents.

The use of Supplementary Cementitious Materials (SCM) is another popular option for reducing the CO_2 footprint of concretes and mortars. These compounds are used as partial clinker replacements or independently in the concrete mixer. (Juenger, Snellings, and S. A. Bernal 2019, Skibsted and Snellings 2019, John et al. 2018, Juenger and Siddique 2015, Lothenbach, K. Scrivener, and Hooton 2011). One innovative and ecological alternative to traditional PC is Limestone Calcined Clay Cement (LC^3) (K. Scrivener, Martirena, et al. 2018, K. Scrivener, Avet, et al. 2018, Zunino and K. Scrivener 2021). LC^3 is a type of cement made from a combination

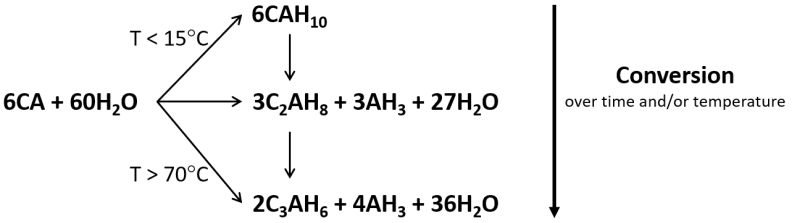

Figure 1.4: CAC conversion.

of limestone (LS), Calcined Clay and gypsum, as it shown in Figure 1.3. It has been established that LC^3-50 is made by replacing 45% of clinker with limestone and calcined clay, resulting in a 40% reduction in CO_2 emissions.

1.1.4 Calcium Aluminate Cement (CAC)

After the First World War, high-alumina cement was widely used in the United Kingdom because of its higher aluminium oxide concentration than PC (Pöllmann 2012). A special form of non-Portland cement is Calcium Aluminate Cement (CAC) (K. Scrivener and Capmas 2003), which is used in a wide variety of applications such as industrial floor and castable refractory concrete (Bayoux 1990, Lee et al. 2001, Adams and Ideker 2017). CAC is a type of hydraulic binder produced from the combination of limestone (LS) and bauxite with more than 40wt% of monocalcium aluminate as the main component. CAC can also include mayenite, gehelenite, grossite, ferrite among others. Due to the great variety in chemical composition, they can be classified in different categories (Pöllmann 2012). These expensive cements offer unique properties such as good chemical resistance, high early strength development and low-temperature workability. However, CAC is now banned in many countries for general structural purposes due to the transformation of calcium aluminate hydrate, which has led to building collapses in concretes with high water content. The conversion equations of the CAC as a function of temperature (K. L. Scrivener, Cabiron, and Letourneux 1999) is shown in Figure 1.4.

1.1.5 Cement phases and components

Cementitious materials react with added water, forming hydration products on the surface of the cement particles/grains and expanding into the previously water-filled region (Mindess 2019).

Cement is made by a complex chemical process in which basic materials such as limestone, clay and sand interact with heat and other additives. Depending on the exact circumstances and materials used, this process can produce a wide variety of different phases, both crystalline and amorphous. The exact content and structure of these phases can vary depending on the type of cement and the manufacturing conditions. The amount and arrangement of these phases in cement can have a major influence on the properties and performance of the material.

1.1.5.1 Crystalline phases

Crystalline phases in cement are those that have a regular, repeating atomic structure, similar to that of a crystal. For instance, the main crystalline phases of a Portland clinker are: alite, belite, tricalcium aluminate and ferrite. As for the hydration products, the main crystalline phases are mainly Portlandite (CH) and ettringite (AFt). Some hydrated phases of calcium aluminate can also be crystallised. For example, AFm-type phases (monosulfate, hemicarbonate and monocarbonate).

Each of the cement types described above has its own initial phase proportions, called crystallines, which also influence and differ its reactions, hydrated components or conversion.
A typical grey **Portland** clinker (the CEM type-I used in this thesis) mineralogical composition is close to 65 wt% of alite (C_3S), 10 wt% of belite (C_2S), 15 wt% of ferrite (C_4AF), 5 wt% of tricalcium aluminate (C_3A) and 5 wt% of other minor content phases.
Belite clinker generally contains the same components with the reversed percentage amount of alite and belite.
Studied blended **LC**^{3} in these research contained 52 wt% of PC, 30 wt% of the calcined clay (FC-35), 15 wt% of LS, and 3 wt% of Gypsum (Table1.1).

Table 1.1: Overview of mineralogical composition of each cement type.

	Cement Type		
Phase	PC	BC	LC^3
Alite (C_3S)	65 wt%	10 wt%	34 wt%
Belite (C_2S)	10 wt%	65 wt%	5 wt%
Ferrite (C_4AF)	15 wt%	15 wt%	8 wt%
Tricalcium Aluminate (C_3A)	5 wt%	5 wt%	3 wt%
Limestone (LS)	-	-	15 wt%
Metakaolinite (MK)	-	-	30 wt
Gypsum (Gyp)	-	-	3 wt%
minors	5 wt%	5 wt%	2 wt%

1.1.5.2 Amorphous phases

The structure of amorphous phases lacks long range order. These phases often contain a range of glassy materials, such as silica glass, as well as a number of other amorphous compounds, such as C-S-H, which is the most important phase in cement as it is responsible for the strength and durability of the material and considered as the primary amorphous gel hydration product with holes known as gel pores. In fact, C-S-H gel is nanocrystalline with local order related to clino-tobermorite (Cuesta, Zea-Garcia, et al. 2018, Cuesta, Santacruz, et al. 2021). However, the particles are plenty of defects and they are smaller than about 4 nm. Moreover, C-A-S-H type gels, from the pozzolanic reaction, may have smaller local order. Pair distribution functions studies, in addition to other techniques, are being employed to get more insights (Garg et al. 2019).

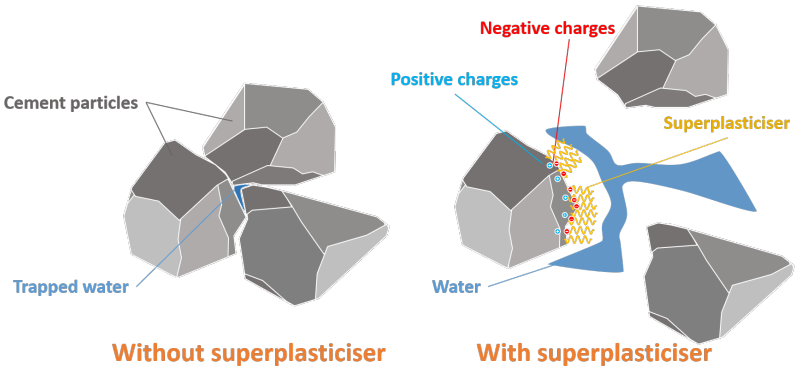

Figure 1.5: Superplasticizer effect.

1.1.6 Admixtures

Chemical admixtures are important in cements, and most significant technological advances in concrete technology have been achieved through the introduction of novel materials (Mehta 1999).

Admixtures are commonly used to enhance the mechanical strength of cementitious materials, such as "superplasticisers" (by improving the particle dispersion, homogeneity and hence flowability, and reducing the water demand), and “accelerators” (also called strength enhancement admixtures).

1.1.6.1 Superplasticiser

The intermolecular forces between cement particles can vary depending on surface chemistry, particle size, particle shape, the presence of additional additives or impurities in the cement mix, and so on. It is possible to modify/optimize the particle-particle interactions in cementitious systems and achieve desirable properties such as strength, durability and workability by carefully managing these parameters (R. J. Flatt 2004). Water-reducing admixtures (superplasticizers) are therefore used to improve the workability of the cement mix. Among them, Polycarboxylate ether-based superplasticizers (PCE) show improved results (e.g. workability at low dosages) compared with others. Around 40 years ago, in 1981, Dr. Tsuyoshi Hirata invented them in the laboratories of Nippon Shokubai in Osaka, Japan (Lei, Hirata, and Plank 2022). They are mainly formed by i) a backbone with anionic groups (main chain), and ii) organic side chains (R. Flatt and Schober 2012), See Figure 1.5.

The anions from the backbone of the PCE are adsorbed onto the surface of the cement particles and hydration phases (mainly ettringite) (Sha et al. 2020); in a lower amount, PCE can also be adsorbed onto the anhydrous cement particles through calcium cations in cement pore solution (Lei, Palacios, et al. 2022). Then, the side chains of the PCE will produce steric repulsion, which is the main responsible for the dispersion (Sha et al. 2020, Lei, Palacios, et al. 2022). The adsorption of PCE allows the particles to move more freely in the mixing process, resulting in improved workability and lower viscosity.

1.1.6.2 Accelerators

To overcome the slow cement hydration, some chemical accelerators can be used to speed up the reactions. Cement accelerators are chemical additives used to accelerate the cement hydration process, or the chemical reaction that happens between cement and water to produce a solid matrix. During the mixing stage, these accelerators can be added to the cement mixture. These chemicals work by promoting the dissolution of specific cement compounds in water. In fact, the mechanisms of traditional accelerators such as $CaCl_2$ has never been fully established. There are indications that it could yield a more permeable C-S-H gel that permits faster ion/water diffusion but it also modifies calcium supersaturation respect to C-S-H gel and portlandite. On the other hand, most modern accelerators are based on C-S-H nucleation seeding. This procedure affects the rates of hydration of different phases, not only alite, and product precipitation pathways. Moreover, strength enhancement does not need to arise from clinker hydration phase acceleration but it also may come from moving the C-S-H precipitation from the surfaces of the clinker grains towards the capillary porosity. Here, imaging methods has a very clear advantage although high spatial resolution, better than 300 nm, and very good contrast-to-noise ratios (to distinguish between different hydrates) are needed. This increased dissolution rate allows a faster reaction between the cement and water, resulting in faster hydration and setting times. (Cuesta, Morales-Cantero, et al. 2023)

1.1.7 Sample holders and containers

Figure 1.6: Glass capillary.

According to the well-known Debye-Scherrer method, all prepared cement pastes are tested for X-ray analysis in "Mark-tubes made of borosilicate glass" from Hilgenberg (Germany), Figure 1.6, which allowed in this thesis to compare dual X-ray diffraction and X-ray imaging experiments and also allowed to prepare samples for different required imaging Field of View (FOV). These tubes have a funnel to facilitate paste insertion, storage and, in some techniques, sample mounting.

There are also some brass connectors/adaptors from Huber (Germany) that would used normally in the synchrotron facilities and laboratories for mounting the sample, Figure 1.7. In this thesis also a customized sample holder for the development of laboratory X-ray analysis and imaging has been made (would be discussed in chapter 4 of this thesis).

1.1.8 Methodologies

Figure 1.7: Brass holder.

In this section, we will discuss all the methods that allowed us to obtain the results of this thesis and the X-ray imaging, which is the main purpose of this manuscript would be discussed in the next section as it needs detailed description. (see section 1.2).

1.1.8.1 Laboratory X-Ray Powder Diffraction (LXRPD)

Laboratory X-Ray Powder Diffraction (LXRPD) is a commonly used analytical method for identifying the crystal structure and associated

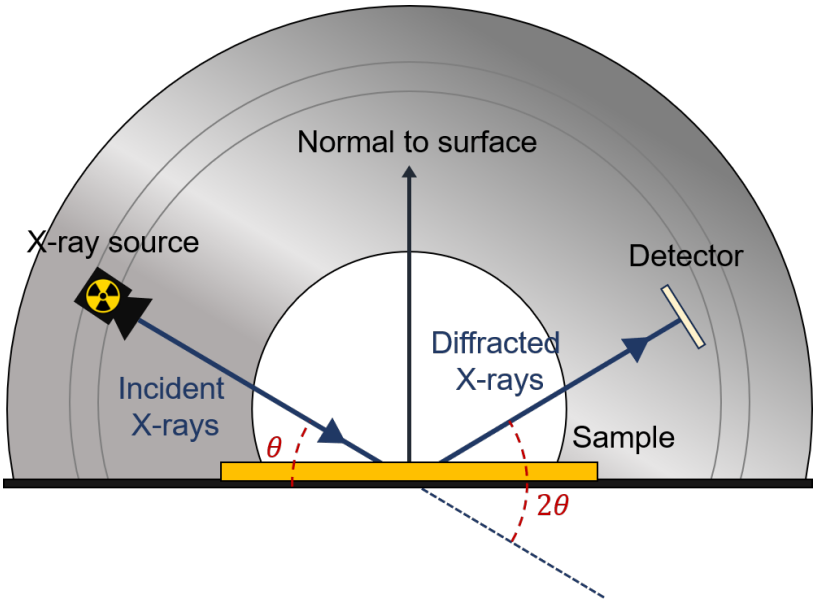

Figure 1.8: Schematic XRD setup.

characteristics of materials. LXRPD involves directing an X-ray beam over a powdered sample and analyzing the diffraction pattern that results. The diffraction pattern is a succession of peaks that correspond to interplanar distances along specific directions within the crystal lattice. The crystal structure and other features of the sample can be determined by evaluating the angles and intensities of these peaks.

Instrumental setups The LXRPD apparatus is made of various parts, including an X-ray source, a monochromator, a sample holder assembly, and a detector. The X-ray source produces an X-ray beam, which is collimated and directed at the sample by a slit according to the sample size/thickness. The monochromator picks an X-ray wavelength to improve the resolution of the diffraction pattern and the detector captures the diffraction pattern created by the sample. The LXRPD data collection procedure generally consists of multiple steps. First, the sample is ground into a fine powder and placed on a sample holder. The holder is then put in the LXRPD equipment, which directs an X-ray beam onto the sample. The X-rays interact with the atoms in the sample, creating a diffraction pattern that is detected and recorded.

Figure 1.9: Anti-scatter slit.

In this thesis, most of the LXRPD studies were collected on a D8 ADVANCE diffractometer (Bruker AXS) using strictly monochromatic Mo-Kα_1 radiation (λ=0.7093 Å) The incident beam was formed by a primary monochromator with a focusing mirror and a 2 mm anti-scatter slit, as it is shown in Figure 1.9. Moreover, 2.5°Soller slits were used for the incident and transmitted beams. An EIGER detector (from DECTRIS, Baden, Switzerland) was used which is optimised for Mo anodes. This was used with an aperture of 4 × 21 degrees, working in VDO mode. Data collection was performed from 3 to 35°(2θ) for around 2 h.

Figure 1.10: D8 ADVANCE tool (Bruker).

Analyzing method The Rietveld technique is an extremely effective tool for evaluating LXRPD data. It employs a least-squares refinement process identify sample's mineralogical composition and related characteristics. The process entails comparing the experimental diffraction pattern to a theoretical pattern generated from a hypothesized crystal structure.

By iteratively tweaking the model parameters until the theoretical and experimental patterns coincide, the crystal structure is refined and fitted. This refining process comprises modifying the crystal structure model's parameters such as atomic orientations, etc. Several key steps are involved in the Rietveld Quantitative Phase Analysis (RQPA). First, a preliminary model of the crystal structure based on prior knowledge or data is proposed. Following that, the General Structure Analysis System (GSAS) software package (Von Dreele and Larson 2004) is used to calculate the theoretical diffraction pattern for the proposed crystal structure and for quantitative phase analysis. The theoretical and experimental patterns are then compared, and the crystal structure parameters are repeatedly modified until the theoretical and experimental patterns agree. The phase abundance or weight fraction of each required/existing phase in the sample is computed using the improved parameters once the Rietveld refinement procedure is complete. Each phase's weight fraction is determined as the ratio of the integrated peak areas of the associated diffraction peaks. Because of the known amount of internal standard material in the sample, absolute quantitative analysis of each phase is possible. Further insights about the internal standard method can be obtained in (De La Torre, Bruque, and Aranda 2001, Meier, Anderson, and Verryn 2012).

1.1.8.2 X-Ray Fluorescence (XRF)

X-Ray Fluorescence (XRF) is an analytical technique that utilizes the interaction between X-rays and matter to determine the elemental composition of a sample. It works on the premise that when a sample is exposed to high energy X-rays, the atoms in the sample absorb the energy and emit characteristic fluorescent X-rays.

The XRF data collection and analysis procedures are as follows:

1. Excitation: When the sample is exposed to an X-ray beam and the high-energy X-rays from an X-ray tube interact with the sample atoms, causing inner-shell electron displacement (called Photoelectric effect).
2. Fluorescence: These displaced electrons leave vacancies in the inner electron shells. Outer-shell electrons move to these lower energy levels to stabilize themselves, emitting fluorescent X-rays at specific energies typical of the elements present in the sample.
3. Detection: Then by a detector, such as a scintillation counter or a solid-state detector, is then used to detect and measure the emitted X-rays. The detector measures the intensity and energy of the fluorescent X-rays.
4. Output: Since different elements have different X-ray emission energies, the energy of the observed X-rays correlates with the elemental composition of the sample. The elemental composition of the sample can be identified by comparing the energy of the observed X-rays with a known database of X-ray energies for different elements.

In this thesis, the elemental composition of the cements was measured by XRF using an ARL ADVANT'XP+ (Thermo Fisher) equipment.

Figure 1.11: Calorimetry sample preparation.

1.1.8.3 Particle Size Distribution (PSD)

Particle Size Distribution (PSD) is commonly measured by grain/particle size analysis, which involves quantifying and measuring the sizes of the cement particles in the sample. Particle size analysis methods can include laser diffraction, sedimentation and microscopy. The PSD of cement not only affects the energy consumption of the grinding process, but also the properties of the final cementitious materials. For example, one of the characteristics used to define PSD is Median particle size by volume, $D_{v,50}$. This reflects the particle size (in volume) at which 50% of them are bigger and 50% are smaller. In this thesis, Particle Size Distribution (PSD) was measured by laser diffraction. BC was measured in a MasterSizerS equipment (Malvern Panalytical), located in Madrid, and provided with a wet chamber. BC powders were previously dispersed in isopropanol using an ultrasonic bath. PC powders were measured in a Mastersizer 3000 (Malvern Panalytical), located in Málaga, using a dry chamber (Aero S).

Figure 1.12: Calorimetry ampule locating.

1.1.8.4 Isothermal calorimetry

Isothermal calorimetry is a technique for measuring the heat released during chemical reactions or processes that take place at a constant required temperature. It allows real-time monitoring of the heat of hydration in cement research. It involves placing a cement paste in a special calorimeter with precise temperature control and monitors the heat flow produced by the paste as the cement hydrates over time.

In this thesis, isothermal calorimetry tests were carried out in an eight-channel Thermal Activity Monitor (TAM) equipment using glass ampoules, see Figure 1.13. Outside the calorimeter, the paste was prepared by mixing the cements with water and stirring for 1 minute manually, followed by 1 minute using a vortex mixer. The pastes were homogenized before being placed in ampoules and subsequently within the calorimeter, as shown in Figure 1.11 and Figure 1.12. Based on the needed investigations at the desired temperatures, heat flow curves were collected for up to 7 days, beginning after 45 minutes of mixing for temperature stabilization.

Figure 1.13: TAM-AIR.

1.1.8.5 Thermal Analysis (TA)

When the cement paste is heated, it undergoes a continuous series of degradation processes that are more or less irreversible. The thermal degradation of cement paste is studied using thermogravimetric analysis (TGA) and derived thermogravimetric analysis (DTG) curves (Alarcon-Ruiz et al. 2005).

Differential Thermal Analysis (DTA) is a technique used to study the thermal behaviour of materials. It involves measuring the temperature difference between a sample and a known reference material as they are heated. In the case of cement science, DTA can provide useful information on cement thermal properties and behaviour, particularly during the hydration process and at different ages. This means that a cement sample is heated at a controlled rate while a reference sample, which does not undergo chemical changes under the same conditions, is used for comparison. The heat flow into or out of the sample and reference material is monitored as the temperature changes. Afterwards, The DTA curve is formed by plotting the differential temperature between the sample and the reference material as a function of temperature. This curve shows typical peaks, troughs and other characteristics that correlate with various heat events and reactions occurring within the cement.

In this thesis, Differential Thermal Analysis (DTA) and Thermogravimetric Analysis (TGA) measurements for the cement pastes were performed in an SDT-Q600 analyzer from TA instruments from New Castle, USA. For almost all the samples the data were taken from both hydration-arrested and non-arrested specimens. The temperature is varied from Room Temperature (RT) to 1000°C at a heating rate of 10°C/min in open platinum crucibles under synthetic air flow. Then the weighed loss from RT to 550°C is assigned as chemically Bounded Water (BW) and the weighed loss from 550 to 1000°C is considered as CO_2. From here, the Free Water (FW) content, can be calculated for each paste by using these equations for Total Water (TW) and the Bounded Water (BW):

$$BW = \frac{(BW_{TGA} \times CM)}{(100 - BW_{TGA})} \tag{1.1}$$

$$FW = TW - BW \tag{1.2}$$

CM refers to "cement" amount in wt%,

It should be noted that the BW content is significantly underestimated as the water released from the C-S-H gel above 550°C is not calculated. Cement pastes contain limestone and it is difficult to distinguish between the two sources of mass loss at 550°C.

1.1.8.6 Nuclear Magnetic Resonance (NMR)

Nuclear Magnetic Resonance (NMR) is a technique that exploits the properties and behaviour of atomic nuclei within a magnetic field to assess the local chemical environment of a given chemical species. It is based on the idea that some atomic nuclei have a property known as

"spin", which produces a magnetic moment. Compared to conventional NMR spectroscopy, Magic Angle Spinning Nuclear Magnetic Resonance (MAS-NMR) spectroscopy has significant advantages. MAS-NMR can dramatically minimise line broadening and improve spectral resolution by spinning the sample at the magic angle, allowing more accurate detection of chemical shifts and detailed identification of molecular structures in solids. The process includes the following steps:

1. Sample: A solid-state powdered cement is put into a nonmagnetic rotor and spun at high speeds.
2. Magic angle: The rotor containing the sample is inserted into the NMR spectrometer and spun at a specific angle relative to the magnetic field, often at 54.7 degrees, which helps to average out the dipolar interactions between atomic nuclei in the sample, resulting in increased spectral resolution.
3. Radiofrequency: A radiofrequency (RF) pulse is applied to the sample, causing the nuclei to switch between energy levels. The resulting NMR signals are detected by a radiofrequency coil or antenna that surrounds the rotating sample.
4. Spectrum: The collected NMR signals are converted into a spectrum showing their frequency and strength. The spectrum contains information about the chemical changes and dynamics of the nuclei in the sample.

In this thesis, ^{29}Si MAS-NMR (Magic Angle Spinning Nuclear Magnetic Resonance) spectra were recorded at RT on a Bruker AVIII HD 600 NMR spectrometer (field strength of 14.1 T) at 156.4 MHz. The chemical shift was referenced to an external solution of tetramethylsilane.

1.1.8.7 Mercury Intrusion Porosimetry (MIP)

The pore size distribution and other pore-related properties of porous materials are determined using Mercury Intrusion Porosimetry (MIP). Since the 1970s (Winslow and Diamond 1970), MIP has become one of the most widely used techniques for investigating pore structure in cement-based materials. It involves the controlled introduction of mercury into the pores of a sample, allowing analysis of pore shape and volume. MIP can provide a better understanding of the porosity characteristics of cementitious materials which is critical in determining the strength and likelihood of cracking or deterioration in cement-based structures.

The process of conducting MIP on cement samples involves the following steps:

1. Sample preparation: To ensure reliable porosity readings, a tiny fraction of the hardened cement is dried.
2. Saturation: The sample is placed in the MIP, which is then filled with mercury. The pressure applied allows the mercury to penetrate the pores of the sample, ensuring saturation and complete filling of the accessible pores.
3. Pressure and intrusion: The pressure is gradually increased, forcing the mercury to infiltrate further into the tiny pores of the sample. At each pressure step, the infiltration volume is measured, providing information on the volume of mercury that has entered the pores.

4. Volume measurement: Once the required pressure has been reached, the pressure is gradually reduced, allowing the mercury to extrude from the pores of the cement. The volume of mercury expelled is measured, which corresponds to the volume of mercury penetrated and is proportional to the pore volume of the cement sample.
5. Derived data: Pore-related metrics such as pore size distribution, porosity volume, etc. are calculated from the observed intrusion and extrusion volumes. These values provide information about the pore structure and connectivity of the cement sample.

Proper characterisation of the pore and microstructure is crucial to gain fundamental knowledge of material behaviour and to develop methodologies for proper material design, and MIP is a typical approach for common cementitious systems (Das et al. 2015).

In this thesis, pore entry size distributions were measured on crushed cylindrical samples 1 cm in diameter and 1.5 cm in height. The pastes were measured 28 days after hydration and also stopped three days before MIP measurements by immersing the fragments in isopropanol. The pastes were then dried to constant weight by gentle heating at 40°C for approximately 5 days. The applied pressure by the intrusion porosimeter was from 0 to 206 MPa.

1.1.8.8 Rheology

The study of the flow and deformation behavior of matter is known as "Rheology". It is needed an understanding of the physical properties and flow characteristics of cement pastes, mortars and concretes and how they react to applied pressures or stresses. Several parameters, such as the amount of cement, water and admixtures, etc., influence the rheological properties of cementitious materials. Understanding their rheological behavior and controlling the viscosity, yield stress, and the evolution with time, is critical to optimizing various elements of mortars/concrete production as it affects the strength, performance and durability of the hardened mortars/concrete structure (Banfill et al. 2003).

Figure 1.14: VTiQ AIR tool (Thermo Scientific Haake).

In this thesis, for being able to fill the small glass capillaries for the appropriate imaging Field of View (FOV) some rheology tests were perform on cement pastes to optimize the amount of superplasticiser for having a compact/homogeneous filled thin capillary. For that, a rheometer (Model VTiQ AIR, Thermo Scientific Haake, Karlsruhe, Germany), with a serrated concentric cylinder sensor (CC38/Ti/SE), was used (paste volume was 30.8 mL). Flow curves (controlled rate measurements), were measured between 2 and 150 s^{-1}, for a total of 17 ramps. From there, the shear rate was decreased to 2 following the same ramp times. Prior to the measurements, the pastes were pre-sheared at the maximum shear rate for 30 s and kept at 0 s^{-1} for 5 s, inside the equipment.

1.2 Introduction to X-ray imaging

X-rays are a form of electromagnetic radiation with a wavelength between 10^{-8} and 10^{-12} meters, corresponding to an energy range of 100 eV to 100 keV, see figure 1.15. Electromagnetic radiation carries energy

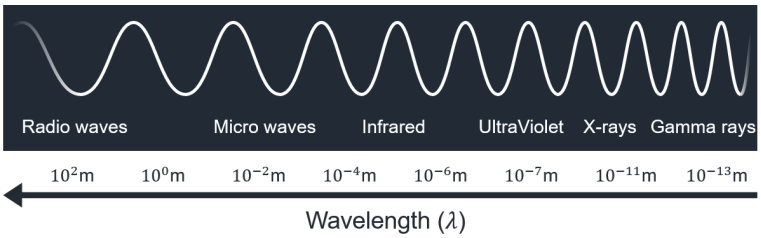

Figure 1.15: X-ray range wavelength.

through space in the form of waves and photons. Radiation is categorised according to its wavelength λ_{photon}, which is the length of one cycle of the wave. The wavelength can alternatively be represented by the frequency f_{photon} and the speed of propagation of the wave, i.e. the speed of light c ($\approx 2.99792 \times 10^5$ ms^{-1}).

$$\lambda_{photon} = \frac{c}{f_{photon}} \tag{1.3}$$

The energy is directly related to the wavelength or the frequency of the photon and is given by the electron volt [eV] unit.

$$E_{photon} = \frac{hc}{\lambda_{photon}} = f_{photon} h \tag{1.4}$$

h refers to Planck's constant ($\approx 6.626069 \times 10^{-34}$ J s).

Definition: Electronvolt

An electronvolt (eV) corresponds to the energy gained by a resting electron of charge $e = 1.6 \times 10^{-19}$C when an electric potential of 1 V is applied in vacuum.
$1eV = 1.6 \times 10^{-19} J$.

In this thesis, for the calculation of the X-ray attenuation length and to continue our quantitative analysis derived from these basic equations described, accessible databases have been used, for example, from the Center of X-ray Optics (CXRO) (Henke, Krachenberg, and Lyons 1993).

X-rays, like visible light, lose energy as they pass through different materials. The energy loss is determined by the absorption behaviour of the material. The primary concept of classical X-ray imaging is absorption, which causes energy loss. In general, X-ray radiography quantifies the amount of energy lost. Because this loss differs for the different materials, we can see a certain contrast in the image. For example, a radiograph shows high intensities (whitish color) for air (porosity) and lower intensities (greyish color) where the X-rays have passed through material components, see Figure 1.16 which shows an "absorption" radiograph of our cement paste in a glass capillary containing air bubbles (air pores), the image taken by Xradia Versa laboratory instrument from Zeiss company. Because of their high energy, X-rays can pass through materials without being much absorbed. X-ray energy varies from about 0.1 keV to several MeV, with a practical limit of 120 keV in medical imaging. X-rays are divided into two types: soft X-rays with energies between 0.1 and 10 keV, which are mainly used for diffraction analysis of thin samples, and hard X-rays with energies between 10 and 120 keV, which are used for imaging

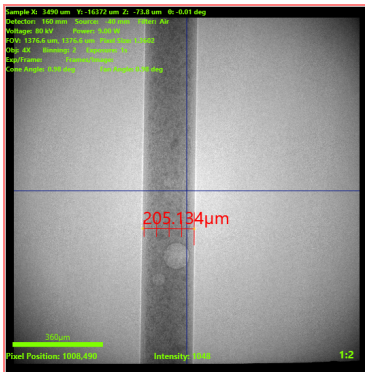

Figure 1.16: Cement paste absorption radiograph.

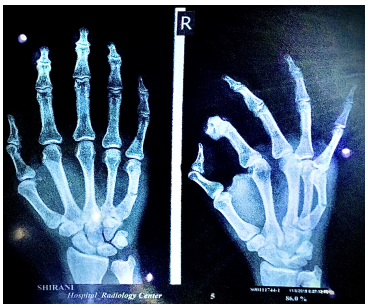

Figure 1.17: Showing fracture of the skeletal system in X-ray radiographic image.

thicker materials. It should be noted that the absorbed is directly related to the dose delivered to the sample during an acquisition.

X-ray was discovered in 1895 by Wilhelm Conrad Röntgen in Würzburg, Germany. His experiment focused on investigating the effects of cathode-ray tubes (Crookes tubes) until he discovered that this gadget generated a type of radiation, which he called these unknown radiations " X-rays". He subsequently noticed that these rays were very penetrating and were attenuated according to the density of the materials through which they passed. The use of these X-rays for biomedical purposes rapidly expanded, and in 1901 he was awarded the first Nobel Prize in Physics for his groundbreaking discovery. It was immediately recognised that X-rays held enormous promise for medical imaging. By the time the First World War broke out, the technology was so advanced that Marie Curie developed mobile X-ray machines that were sent to the battlefields.

This resulted two types of examinations: One was radiography, which provides a simple projection of the imaged organs; like Figure 1.17 that shows taken "attenuation" radiographs of my brother's hand inspired by one of the first X-rays images that Wilhelm Röntgen took from his wife's hand. In this case, the high attenuation coefficient of bone compared to surrounding tissue provides good contrast and allows fractures to be identified and graded. In this thesis, initial "absorption" radiography of the filled paste capillary is used as a method to check the fullness of the sample and to avoid large pores in the scanning region before real experiments, as shown in Figure 1.16.

And the second examination was fluoroscopy, which provides a dynamic version of these projections and whose discovery led to significant developments in the use of X-rays for imaging, namely Computed Tomography (CT). The word "tomos" has its origins in the ancient Greek word for "slice" or " section". This approach uses 2D projections collected from all directions to create a 3D image of the body. This method is primarily based on the use of Radon's theorem, which was established in 1917, but was not applied to X-ray imaging until 1973 because it required both the digitization of 2D projections and computers capable of calculating tomographic reconstructions. The transition from analogue recording on photographic film to digital recording on electronic cards, together with the development of the computing power of computers, has made this progress possible. Even today, many years later, the application of complicated algorithms for quantitative analysis, complex deep learning models and volume visualisation of these tomography images requires appropriate characteristics of the computers and workstations.

1.2.1 X-ray interactions

When X-rays go through matter, three important interactions can occur: interactions with atomic electrons, interactions with nucleons, and interactions with electric fields associated with atomic electrons and nuclei. When an X-ray photon hits a material, it is in contact with a large number of atoms that make up that material. This means based on the probability of each of the interactions which are specified by its cross-sections, one of these transmission, compton scattering, photoelectric absorption, pair production and rayleigh scattering may happen. These cross-sections

contribute to the linear attenuation coefficient (μ), which depends on the energy of the radiation (E) and the atomic number (Z) of the material. As a result, X-ray photons undergo either total absorption, elastic scattering, or inelastic scattering. In its basic configuration, the interaction employed for X-ray imaging consists of a decrease in radiation intensity, which is nothing more than a decrease in the number of photons arriving at the detector. Attenuation is the term used to describe this process and it is caused by a variety of physical processes, such as a change in photon count, photon direction, or photon energy.
According to Lambert-Beer's law, when a monochromatic X-ray beam passes a homogeneous object with absorption or attenuation coefficient , the measured intensity I is proportional to the intersection length of the object x and the ray:

$$I = I_0.e^{-\mu x} \tag{1.5}$$

The fractional transmitted intensity I/I_0 is used in X-ray CT to measure a large number of beam paths through the object. The logarithm of this ratio is used as an input to reconstruction methods to obtain a collection of line integrals.

1.2.2 X-ray detection

For converting these X-rays to an actual image, detection methods are required. Unlike traditional X-ray films, which use X-rays directly to affect the chemical properties of the X-ray film material, most current detection systems convert X-rays into light and then into electrons. Which makes the detector a fundamental member of the experimental setup. There are several types of X-ray detectors, and choosing the best one is a balancing act between the needs of the experiment and the advantages of different technical solutions. The following standard parameters are used to compare different detectors:

1. **Spatial resolution** : The ability of the detector to determine the position of arriving photons.
2. **Noise** : fluctuations in the detected signal from various elements that limit the minimum detectable signal level. Key sources of noise include photon noise (statistical fluctuations in the number of photons) and dark noise (fluctuations in the signal with no incident radiation).
3. **Temporal resolution** : the detector's capacity to establish the photons' time of arrival.
4. **Wavelength range** : determined by the lowest energy required to cause an event (long limit) and the transmission of the detector's window or coating (short limit).
5. **Dynamic range** : the ratio of the greatest observable signal before saturation impacts the detector's intrinsic noise. High count rates cause non-linear response and missing events, resulting in saturation.
6. **Detective Quantum Efficiency (DQE)** : the ratio of signal output to noise output squared divided by the ratio of signal input to noise input squared, which is related to item 2, above.

7. **Environmental requirements** : Any specific requirements for the detector's proper operation, such as shielding, cooling, high vacuum.

Detectors can be categorized into different types: photon counters, flat detectors and gas detectors. The most common detector in X-ray imaging is the flat detector. X-rays are converted into electrical charge by direct or indirect means. **"Indirect flat detector"** consists of a photodetector array and a scintillator layer: X-rays are converted into light and then absorbed by a scintillator material to create high-energy electrons, producing electrical charge. Then generate a large number of electron-hole pairs. These pairs recombine to produce photons in the visible range, which are then converted to electric charge by a photodiode. The most common medical imaging device, including mammography machines, and computed tomography (CT) scanners (technique used in this thesis) uses an indirect flat detector. The alternative for the indirect Flat Panel Detectors (FPD) are direct flat Charge Coupled Devices (CCD) and Complementary Metal-Oxide-Semiconductor (CMOS) detectors. Although indirect detectors have the advantage of having very small pixels, only a few micrometres in size, the conversion process in the scintillator reduces the accuracy with which the position of the incident photon can be identified. This is due to the fact that before they reached the chip's conversion region, the re-emitted photons dispersed throughout the material. The Full Width Half Maximum (FWHM) of the measured signal in response to a point source is defined as the Point Spread Function (PSF), which is used to describe this loss of precision. The detected image is often slightly blurred as a result of its typical Gaussian shape.

A common quality measure for imaging is the signal-to-noise ratio (SNR).

A single projection image does not retain all spatial information, as it merely shows something akin to "shadows" of the imaged objects.

1.2.3 Reconstruction and data processing

The first step of the acquisition consists in reconstructing the acquired data. Since projections from a single sample in a few directions are not sufficient to determine the spatial distribution of structures within the object, it must be irradiated from all angles. The task of estimating the spatial structure of an object from its projections is known as **Image reconstruction** in Computed Tomography (CT). In mathematics, this is known as an inverse problem, and it requires techniques from physics, mathematics, and computer science. Because of the inverse problem, the spatial distribution of the attenuating objects is unknown and must be inferred using a series of observed projections. Allen MacLeod Cormack and Sir Godfrey Hounsfield, who received the Nobel Prize in medicine in 1979 for their pioneering work, were the first to apply this approach to medical computed tomography.

1.2.3.1 Fourier Slice theorem

Conventional reconstruction techniques rely on the Fourier slice theorem which directly links the Fourier transform of a projection and the Fourier

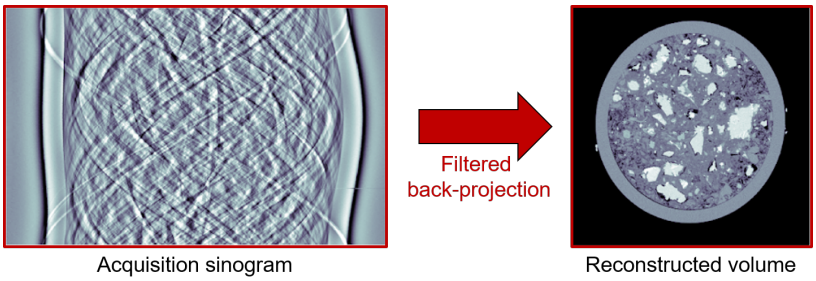

Figure 1.18: Filtered Back-Projection and Reconstruction

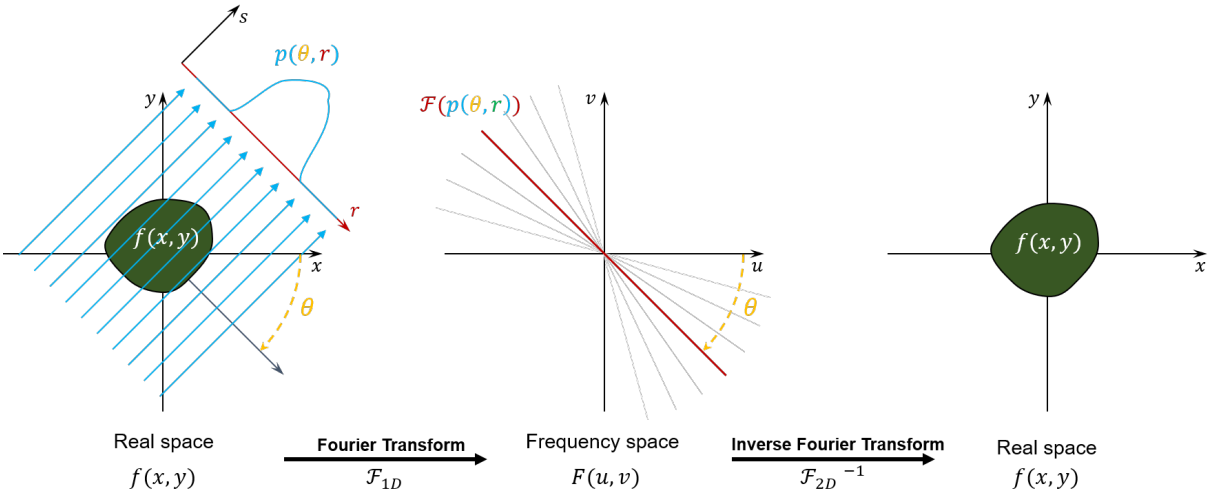

Figure 1.19: Principle of the Fourier Slice theorem

space of the sample distribution. Indeed, as shown in Figure 1.19, by acquiring projections from angles varying between 0 and π, we can fill the Fourier space of the sample distribution. The θ angle acquisition resolution is of main importance as low frequencies density is higher than high frequencies. As a consequence, low frequencies must be filtered when computing the real space result.

1.2.3.2 Filtered back-projection

Practically, the number of projections acquired for reconstruction is finite. Thus, the Fourier slice theorem only gives us an approximation of the real sample distribution. Kak and Slaney proposed in (Kak and Slaney 2001) a Filtered Back-Projection (FBP) technique, also known as convolution reconstruction algorithm, that would help overcome this limitation and is now widely used in today's CT systems. This method consists in filtering low frequencies using a high-pass filter, followed by a backward projection step. This approach can be applied to non-parallel beam geometries such as fan-beam and cone-beam. Corrective factors are integrated to take into account the divergence of the beam (see Figure 1.18). Feldkamp proposed a Filtered Back-Projection approach for this type of reconstruction in (Feldkamp, L. C. Davis, and Kress 1984) (FDK algorithm). Many other approaches are also used, (Grass, Köhler, and Proksa 2000; Katsevich 2003; H. Kudo and Saito 1991; G. Wang et al. 1993; Yan and Leahy 1992) but not as widely as the FDK algorithm.

1.2.3.3 Iterative reconstructions

Iterative approaches were proposed before FBP reconstuction methods, when Gordon et al. introduced ART (Algebraic Reconstruction Techniques) in (Gordon, Bender, and Herman 1970) to reconstruct cross sections of samples. The main limitation that prevented its development at the time was the unsufficient computational power. Their principle consisted in solving a system of equations iteratively, determining the values of each unknown (each pixel of the reconstructed image) as a function of numerous equations (acquired projections). For example, an acquisition performed with 100 projections on 180 degrees using a 1D detector of 100 pixels wide gives us 100*100 equations with 100×100 unknowns (corresponding to the pixels of the reconstructed 2D section). The ART method consists in linearly solving this system and was improved many times since (SIRT Gilbert 1972, ILST Goitein 1971, conjugate gradient Reid 1971...). Other methods were also proposed, using a statistical approach, consisting in solving this kind of system by maximizing a likelihood function (MLEM Dempster, Laird, and work(s): 1977, OSEM Hudson and Larkin 1994, DRAMA Browne and Pierro 1996, RAMLATanaka and Hiroyuki Kudo 2003). The main advantage of the statistical approach is the lower requirements in terms of number of projections but its main drawback is its higher computational cost. The iterative reconstruction approaches are widely used in the nuclear imaging field.

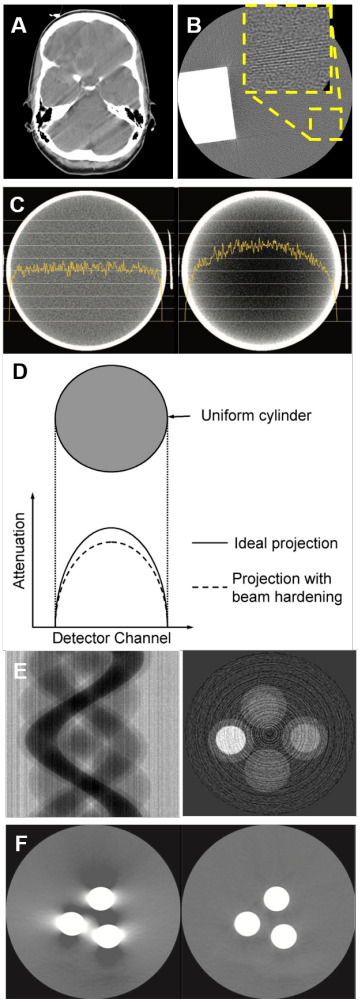

Figure 1.20: Computed tomography common Artifacts. A: Motion artifacts. B: Undersampling artifacts. C: Beam Hardening. D: Beam Hardening principle. E: Ring artifacts. F: Partial Volume. Adapted from (Barrett and Keat 2004; Eldib et al. 2017).

1.2.4 Artifacts

Aside from the limitations that all imaging systems have in common, the most well-known ones include spatial resolution, contrast ratio, and noise. Similar to noise, artifacts are image degradations that also find their source in physical effects during the scan. However, the difference to noise is that when a scan is repeated using the exact same object and scan parameters, artifacts are reproduced exactly whereas noise effects will change based on a probabilistic scheme. By designing and configuring appropriate equipment, performing experiments and using mathematical processing, artifacts can be reduced (G. Davis and Elliott 2006). Here we point some of the artifacts:

1. **Motion Artifacts** : In general, it assumed that the anatomy in the reconstructed slice would not change during the data acquisition. However, if the change in attenuation coefficient over time is taken into account, the problem of reconstructing images with a continuously changing data set arises. To solve this problem, the main objective of CT scanner designers is to speed up data collection, particularly at time scales associated with anatomical and physiological motion. Multi-slice scanners that operate in sub-second time frames are currently available.
2. **Beam-Hardening Artifacts** : When the produced X-ray spectrum is polychromatic which is the case with conventional X-ray tubes, beam-hardening artifacts can appear in the reconstruction. When a broadband spectrum of X-ray energy passes through an object, the spectrum changes due to the variable attenuation of different frequency bands, which varies according to the particular attenuation coefficients of the material. The wavelength-dependent interaction

of the X-rays with the target material and the path length are two things that determine radiation attenuation. Soft X-ray beams are generally more strongly absorbed than hard X-ray beams, resulting in hardening of the X-ray spectrum and corresponding image error. A common correction method used in almost all CT scanners is to filter the soft radiation near the source before it reaches the sample.

3. **Ring Artifacts** : These are electronic artifacts known as ring artifacts. Small errors in the detector pixel values persist throughout the CT acquisition, causing ring-shaped and semicircular distortions in the back projection.
   These errors are caused by variations in defects in the optical coupling system, fluctuations in the X-ray beam and instability in the monochromator crystal for synchrotron sources. If the X-ray beam was absolutely steady during CT and the detector response was linear for each pixel, standard dark current and flat field correction techniques would be sufficient to correct for these inhomogeneities and remove the artifacts. However, because the detector response, dark current and experimental conditions change with location and time, typical correction methods are unable to compensate for these intensity variations over the full dynamic range, and alternative approaches must be used to correct for these artifacts.
4. **Partial-Volume Artifacts** : Sharp edges in the detail of an object can expose the resolution limitations of a detection system. The boundary will often not coincide perfectly with the edge between two detector components, causing the X-ray energy to be averaged across the width of the detector, resulting in blurring. This discrepancy causes artifacts in the reconstructed image, which appear as streaks along the backprojection path. Because backprojections from other directions cannot reliably fix the erroneous value projected over the entire image, partial volume artefacts appear as ghost lines, especially from straight object boundaries. Beam collimation can be fine-tuned to reduce these artifacts.
5. **Sampling Artifact** : It is critical to follow Shannon's sampling theorem in computed tomography for avoiding these types of artifacts which applies to both axial slice reconstruction and 3D data display via slice stacking. Aliasing artifacts can occur when a signal is subsampled.
6. **Scatter Artifacts** : No particular interaction affects the intensity of the direct beam path measured by a detector element. However, detectors positioned out of the direct line of sight may be affected by specific interactions, particularly in locations with highly absorbing objects where the recorded values may be distorted by scattered radiation. The scattered X-rays can account for a large proportion of the total signal, and in projection directions with heavily absorbing objects, the desired signal can become extremely weak, resulting in inconsistencies within the filtered back projection and streak artifacts.

1.2.5 X-ray sources and instruments

The deceleration of charged particles can produce X-rays. In electron impact generators, radiation is produced by slowing down a high-energy

electron as it enters a metal anode. A linear accelerator can also be used to generate X-rays.

1.2.5.1 From conventional to laboratory X-ray tube

There are different types of X-ray tubes, from the first experimental Crookes tube, Coolidge tube (Figure 1.21), rotating anode tube to the developed microfocus X-ray tube. Some X-ray examinations require very high resolution images and therefore require X-ray tubes that can produce very small focal spot sizes. For example, the Bruker, Figure 1.22, has a nanofocus X-ray tube.

Following up the classical Röntgen mechanism, an X-ray tube is used to generate X-rays, consisting of a vacuum tube containing an anode and a cathode as shown in Figure 1.21. This cathode is made of thoriated tungsten, similar to a conventional incandescent lamp. When a potential difference is applied between the cathode and the anode, the temperature of the filament rises above 2400K, allowing electrons to escape by thermionic emission. These electrons are focused onto an anode target using a cup-shaped electrode known as a Wehnelt cylinder. This means the kinetic energy of emitted electrons directly depends on the acceleration voltage applied between the cathode and the anode.

There are two possibilities when electrons reach the anode:

1. **Bremsstrahlung radiation**: Electrons arriving at the anode are diffracted and decelerated by the Coulomb fields of the anode atoms. According to Maxwell's equations, approximately 1% of the kinetic energy of electrons is transformed into heat and expelled as radiation. These released radiations are known as "Bremsstrahlung" (from the German words "bremsen", meaning to brake, and "Strahlung", meaning radiation.). The energy of the released photons then fluctuates depending on the degree of the interaction with the nuclei.
2. **Characteristics radiation**: When an electron from the K-shell of an anode atom collides with a fast electron, it is knocked out. As a result, the atom is ionised and an electron from one of the higher shells (with a lower binding energy) fills the vacant space in the K-shell. This process is accompanied by the emission of an energy photon equal to the energy difference between the two shells. This process produces "characteristic peaks" in the emission spectrum of the source (Figure 1.21). These electrons can make multiple contacts with the atoms of the target, emitting many photons in the process. They are eventually transported out of the tube through a beryllium window.

It is also important to take into account the fact that lower energy photons are more likely to be absorbed by matter. To overcome this problem and avoiding beam-hardening artifacts, low energy photons are filtered by metal filters positioned at the output of the source. These filters, which are usually flat and from 0.1 to a few millimetres thick, explain the shape of the spectrum at low energies. The material and thickness of the filters are usually determined by the type of source used, the acceleration voltage and the object being photographed. The electron flux is proportional to the current flowing through the tube and its maximum value is determined by the thermal capacity of the anode. In fact, under

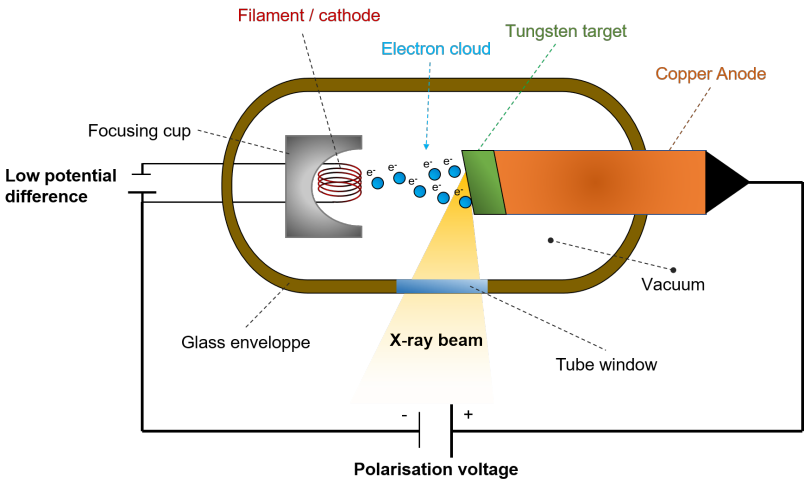

Figure 1.21: Schematic of cathode X-ray tube.

most circumstances, the energy output of X-ray photons is very low, as approximately 99% of the energy is dissipated as heat, leading to significant overheating concerns. To address this issue, rotating anodes have been used to reduce the scattered heat load by allowing part of the anode to cool before being bombarded with electrons again. New X-ray tubes have been developed to overcome the thermal limitations of traditional sources by replacing rotating anodes with liquid metal beam alternatives (Hemberg, Otendal, and Hertz 2003).

Laboratory X-ray scanners (from Zeiss and Bruker company) that have been used in this thesis use these kinds of X-ray tubes. The Bruker SKYSCAN 2214 uses the latest generation open type X-ray source. True spatial resolution is less than 500 nm, X-ray energy up to 160 keV and source power up to 16 W. The source is virtually maintenance free. The SKYSCAN 2214 has an open-type (pumped) nanofocus X-ray source with a diamond window. It generates an X-ray beam with a peak energy ranging from 20 kV to 160 kV and is equipped with two types of cathodes. The tungsten (W) cathodes function in the complete range of accelerating voltages up to 160 kV and provide a spot size of 800 nm. Lanthanum hexaboride (LaB_6) cathodes can be utilised to accelerate voltages ranging from 20 kV to 100 kV and generate an X-ray beam spot size of less than 500 nm for the highest resolution in imaging and 3D reconstruction. The JIMA resolution pattern showed that 500 nm structures can be resolved. Modern laboratory X-ray tubes provide various advantages over traditional X-ray tubes, including increased X-ray output, improved heat dissipation, higher resolution imaging, and increased flexibility and control. These advancements have increased the versatility and effectiveness of X-ray technology in a wide range of laboratory and industrial applications.

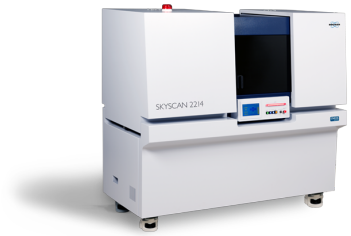

Figure 1.22: SKYSCAN 2214 tool (Bruker).

Figure 1.23: Xradia Versa tool (Zeiss).

1.2.5.2 Synchrotron sources

In the middle of the 20th century, synchrotron radiations were discovered which allowed access to much more intense X-ray sources than conventional ones. They were discovered in a linear accelerator at the General Electric Research Laboratory when Langmuir noticed that accelerated electrons were missing energy that was emitted as radiation: synchrotron

radiation. These X-ray sources are based on the same principle: acceleration of particles to relativistic speeds. In order to do this, they are first accelerated using a linear accelerator or "LinAc" until they reach the MeV energy range. Then, they are sent into a booster ring that increases their energy to the GeV range. The particles are finally sent into a storage ring where they are accelerated by RF electric fields. They follow a quasi-circular trajectory thanks to bending magnets of a few Tesla magnetic field perpendicular to the trajectory. Everytime they lose a part of their energy which they regain it thanks to the RF electric fields. According to Maxwell's equations, since these particles do not follow a uniform rectilinear trajectory, they emit electromagnetic radiation perpendicular to their speed: the "synchrotron light".

This synchrotron light has the following characteristics (Mobilio and Meneghini 2015):

1. High intensity and highly collimated,
2. Emitted in very short pulses, (less than a nano-second, which enables time resolved studies),
3. Tunable (wavelength selection),
4. Highly polarized (linear and circular),
5. A very wide and continuous spectral range (infrared to hard X-rays),

Inserting devices can be found periodically on the straight portions of the storage ring (ID). They make the particles oscillate perpendicularly to their trajectory and emit more intense synchrotron light. A higher critical energy can be reach thanks to these IDs. The number of oscillations caused by the structure also allows to increase the intensity of the emitted radiation. IDs are divided in two types: undulators and wigglers. They have an equivalent role and their difference is the ratio K between the wiggling angle α and the natural aperture angle of the synchrotron $1/\gamma$:

$$K = \alpha\gamma \tag{1.6}$$

When $K << 1$, the ID is an undulator. In this case, interference occurs between the radiations emitted at different points and are added coherently. This allows to reach a spectral brightness much higher than wigglers, by several orders of magnitude. When $K >> 1$, the contributions to the radiation of each period of field add up incoherently which makes it possible to increase the critical energy, thus giving a broad energy spectrum. This kind of ID corresponds to wigglers. Hence, the main differences between these two IDs are: brightness, coherence and beam energy spectrum.

In this thesis, imaging synchrotron experiments were performed at Swiss Light Source (SLS) in Paul Scherrer Institute (PSI) in Villigen, Switzerland. And also at the European Synchrotron Radiation Facility (ESRF) in Grenoble, France. After its upgrade in 2020 to an extremely bright source (ESRF-EBS), ESRF operated a fourth-generation electron storage ring. Intense X-ray beams were produced by 6.04 GeV relativistic electrons passing through the inserts located along the 844 m long storage ring and collected by one of the 44 beamlines in operation. More precisely, they were performed on the **Microtomography** beamline **ID19** which setup is shown later in the Figure 1.26 . This beamline can work in the energy range 6 to 250 keV, but most of the experiments are performed in the 19-35 keV range.

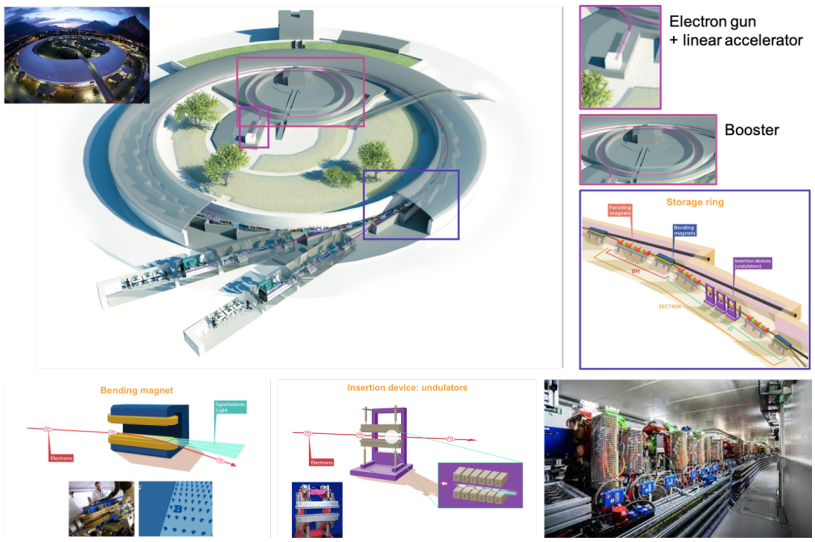

Figure 1.24: Principle of a synchrotron source and its accelerators, Bending Magnets (BM) and undulator.

The SLS operated a third-generation electron storage ring. Intense X-ray beams were produced by 2.4 GeV relativistic electrons passing through the inserts located along the 288 m long storage ring and collected by one of the 16 beamlines in operation. More precisely, the experiments were performed on the **Coherent Small-Angle X-Ray Scattering** beamline called **X12SA-cSAXS** and **Tomographic Microscopy and Coherent Radiology Experiments** beamline called **X02DA-TOMCAT** imaging beamlines which setups are shown later in the Figure 1.28 and Figure 1.27.

The cSAXS beamline is optimized to perform small-angle X-ray scattering and high-resolution X-ray microscopy in the energy range between 4.4 and 17.9 keV. Typical techniques include 2D and 3D ptychography, a microscopy technique with spatial resolution in the tens of nanometers, 2D and 3D scanning SAXS, with spatial resolution down to 5 micron, and time-resolved SAXS. Ptychography can be additionally used to characterize X-ray optics.

The TOMCAT beamline provides X-ray tomographic microscopy endstations for the non-destructive, high-resolution, quantitative volumetric investigations of a large variety of samples. Absorption-based and phase contrast imaging are routinely performed with isotropic voxel sizes ranging from 0.16 to 11 μm. In addition, the hard X-ray full-field microscope setup delivers a pixel size of 65 nm for microscopic samples (75x75 μm^2 field-of-view). Typical acquisition times are on the order of seconds to a few minutes and dynamic processes can be followed in 4D (3D space + time) for extended time periods with sub-second temporal resolution using the ultra-fast endstation. The scientific activity at the beamline focuses on the development of tools, both instrumentation and algorithms, for tomographic X-ray imaging exploiting synchrotron light. This includes the design and construction of ultra-fast data acquisition systems to provide dynamic investigation of rapidly evolving (*in situ*, *operando* or *in vivo*) processes, the development of imaging techniques exploiting complementary contrasts (absorption, phase and dark field) as well as the visualization and quantification of complex 3D-microstructures in biological and innovative materials.

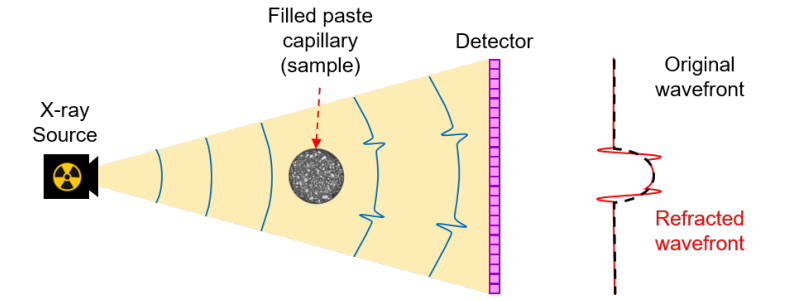

Figure 1.25: Schema of a propagation-based phase contrast imaging system with an X-ray source, cement paste capillary and detector.

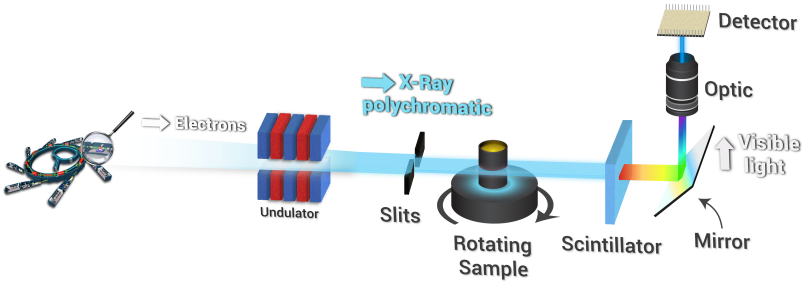

Figure 1.26: Schema of ID19 setup.

1.2.6 X-ray imaging techniques and modalities

1.2.6.1 Phase-Contrast

In 1965, Bonse and Hart (Bonse and Hart 1965) applied phase-contrast to X-rays, which was then only used with visible light. These methods have been developed thanks to the 3rd generation synchrotron sources, because of their extreme brightness and their high spatial and temporal coherence.

Its principle consists in retrieving both informations of absorption and phase from an attenuation image. It thus reveals much more information on the imaged sample compared to the native attenuation image. Although the early work of Bonse and Hart employed a crystal interferometer, there are many different Phase-Contrast Imaging (PCI) techniques available today:

1. Propagation Based Imaging (PBI)
2. Modulation Based Imaging (MoBI)
3. Analyser Based Imaging
4. Crystal Interferometry
5. Grating Based Imaging
6. Edge Illumination

A review of these methods can be found in (Bravin, Coan, and Suortti 2013). Among all these techniques, we used propagation-based techniques that use the free-space propagation of a coherent X-ray beam to retrieve phase information, see Figure 1.25. After passing through the sample, the wavefront of the partly-coherent beam is distorted. The great propagation distance between the sample and the detector helps us detect the Fresnel diffraction fringes caused by the multiple interfaces in the sample (Cloetens et al. 1996). Low-attenuation samples (such as PMMA) become visible thanks to enhanced edges. They would otherwise not be seen in the image. This type of acquisition is only possible thanks to the high spatial coherence available at the synchrotron. The computational methods to recover phase information from the acquired projections are

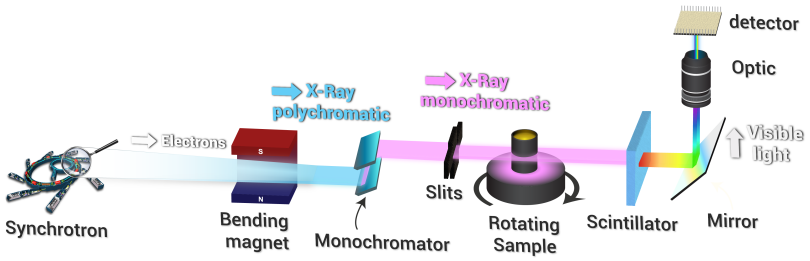

Figure 1.27: Schema of TOMCAT setup.

multiple. Most of them are based on the transport-of-intensity equation (TIE) or the contrast transfer function (CTF). For example, the method consists in acquiring images at several distances to recover this phase information. However, some assumptions allow the recovery of this information from a single acquisition by making the strong assumption that the sample is composed of a single element. In the case of the acquisitions done in this thesis, the non-iterative phase retrieval method **Paganin** prevails (Paganin et al. 2002).

1.2.6.2 Ptychography

It was 54 years ago, in 1969, that Walter Hoppe first introduced ptychography (Walter Hoppe 1969), and later, after 13 years, he returned to his idea in 1982 (Hoppe et al. 1982), as computers became more capable and powerful. This means that it was only about half a century later that this thesis began to use a fairly new technique in the field of cement imaging.

Ptychography etymological roots are in ancient Greek (a fold + to write), but it has also been cited because convolution in reciprocal space is a key component of the original technique, and convolution is commonly called "Faltung" in German (folding). There may be a connection between the two (Guizar-Sicairos and Thibault 2021). Ptychography has evolved into a lensless microscopy technology that uses computational reconstructions to replace image-forming optics. This means it does not require well-corrected high optics and its resolution is not limited by the illumination spot size.

In principle, restricted by the maximum diffraction angle at which intensities can be measured with sufficient statistics. This makes it experimentally advantageous compared to scanning probe microscopy and holography, which require near-perfect optics. The spatial structure of the illumination probe influences the information encoded in a ptychogram. Ptychograms are a collection of intensity measurements used to reconstruct a signal's frequency content. Without this structure, transverse shifts in the sample have no effect on the measured intensities, and both the dependence of the ptychogram on the spatial coordinate and the encoded information disappear. Methods have been developed to introduce structure and wavefront aberrations into illumination beams to enhance the spatial structure of the illumination.

Hoppe's idea was to retrieve the structure of a crystal by illuminating it with a coherent electron beam and measuring the far-field intensity distribution. Bragg peaks appear when a periodic structure is illuminated with a homogeneous coherent field, and the complex wave fields of

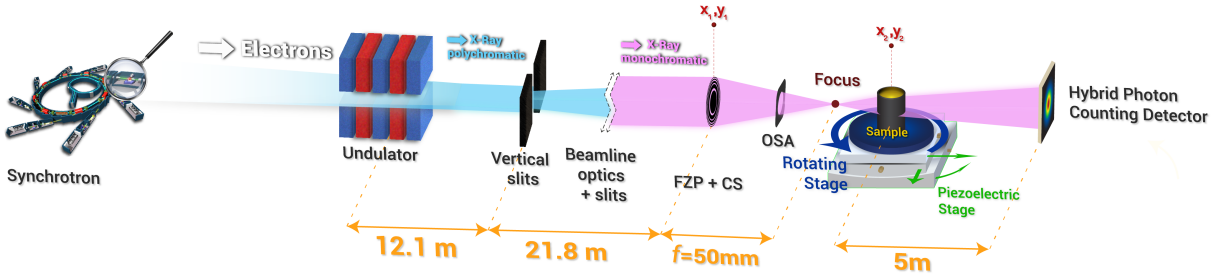

Figure 1.28: Schema of cSAXS for near-field Ptychography setup.

these peaks are needed to reconstruct the real-space structure by Fourier synthesis. The phase problem is the impossibility of measuring these phases directly and the difficulty of retrieving them by indirect means. He realized that if the beam was small enough, the Fourier transform would be comparable to the spacing between the Bragg peaks, and the convolution would broaden these peaks enough to overlap and interfere with each other. This created a beat pattern in the overlap region from which the phases of the peaks could be extracted.
Ten years later, in 1992, John Rodenburg and Richard Bates formalized the mathematics linking the reconstruction of ptychograms in real space to their spatial frequency description (Rodenburg and Bates 1992). They showed that a ptychogram is a convolution of the Wigner distributions of the probe and object, and outlined a unique and direct reconstruction method for arbitrary objects by deconvolution. This procedure also provided an avenue for further analysis, such as statistical noise propagation.

Spectrograms and ptychograms are two-dimensional representations of the variation of a frequency spectrum over time. Spectrograms represent a one-dimensional sound with one axis being time and the other being frequency, while ptychograms have both spatial and spatial-frequency axes. Audio signal processing uses the Short-Time Fourier Transform (STFT) to create audio spectrograms. In ptychograms, the illumination probe acts as a spatial rather than a temporal slider. The measured far-field signal represents the spatial frequencies locally present in the object, albeit convolved with the Fourier transform of the probe. The problem of ptychography reconstruction is mathematically closely related to that of recovering a signal from its STFT. Ptychography requires a probe with significant spatial structure and a broad spatial spectrum, and its phase retrieval procedure decouples the contributions of the object and the probe. Iterative phase retrieval algorithms have been introduced to ptychography, allowing data sets to be reconstructed without the small sampling steps of the Wigner method. Ptychogram sampling in real space can be done with step sizes much larger than the resolution, as long as the illuminated regions have sufficient overlap.

Meanwhile, from the other side in early 1972, two electron microscopists Ralph Gerchberg and Owen Saxton began investigating iterative phase retrieval methods based on the recently established Fast Fourier Transform algorithm (Gerchberg 1972). Later in 1978, James Fienup introduced the hybrid input-output algorithm to reconstruct an object from its Fourier transform, using limited a priori information to impose constraints in real and reciprocal space (Fienup 1978). His algorithm was used in 1999 to demonstrate Coherent Diffractive Imaging (CDI), which uses X-rays to

visualize non-periodic objects (Miao et al. 1999). It has limitations, such as limited size and uniform illumination, but is important for imaging with X-ray Free Electron Lasers (FEL) and for Bragg coherent diffraction imaging in synchrotrons.

Later In 2004, Helen Faulkner and Rodenburg showed that ptychographic reconstructions could be obtained within an iterative phase retrieval framework, bringing the technique to its modern form. They retained the original experimental procedure of aiming a spatially bound probe at different transverse positions relative to the object, but applied constraints in real and reciprocal space until they converged on a solution. They filed a patent that year claiming broad coverage of iterative methods applied to ptychography. The proactive protection of the patent by its current owner has influenced the free exchange of algorithmic tools.

Ptychographic reconstructions benefit from the simultaneous constraints of multiple diffraction patterns and robustness to noise, removing ambiguities and providing additional information to resolve ambiguities and aid phase retrieval.

1.3 Introduction to X-ray imaging of cements

Initially, computed tomography was intended for medical purposes. The application of X-ray computed tomography to cementitious materials really took off at the beginning of the 21st century, although one of the first applications in this cement science field dates back to the late 1970s (Morgan et al. 1979, Morgan et al. 1980). None of the techniques described in section 1.1.8) Methodologies, provide information on the spatial distribution of sample components/constituents or a 3D visualisation of its microstructure.

X-ray imaging provides an unprecedented window into the formation of mineral fractures, the tortuosity of oil and gas core plugs and their fluid flow (Kakouie et al. 2021) down to a few microns, as well as the connectivity of the porous network (Bernal, Shirani, et al. 2021) and the alteration of the cementitious matrix due to various chemical degradation processes.

The multiscale microstructure of cementitious materials is recognised to have a major impact on their macroscopic characteristics. However, the sample preparation required by previous *ex situ* methods (explained in section 1.1.8) such as cutting, grinding, polishing or high vacuum testing, often has irreversible effects on the microstructure of cement-based materials.
Before starting an imaging experiment, it is necessary to get a sense of the expected contrast between our cementitious sample phases/components and the total transmission through our sample. As mentioned in section 1.2, microCT experiments typically have an energy range of 10 keV to 100 keV. The choice of energy depends on the imaging setup and the resolution we need to achieve. In this thesis we have chosen an energy between 6 and 20 keV for the synchrotron imaging modalities. For this reason, chapter 4 Figure 4.5 includes a provided graph showing the linear attenuation coefficient as a function of photon energy for all the

components that we encountered in the cement-based samples of this thesis.

In general, the application of CT to cementitious materials can be divided into two main groups: one is the application that considers microstructural changes over time (such as cracks, hydration, etc). Another is the type of application that considers only one image of the sample (ignoring possible microstructural evolution). Below is a categorisation of these types of observations and an indication of the studies that have been carried out in recent years in the field of cement science.

1.3.1 Time-invariant observation

This refers to the static microstructural state of the sample, where the microstructure remains unchanged or shows no change with time, or perhaps the changes are not of interest in these studies. For some of these investigations, porosity is usually the key phase. The contrast between the air and the hydrated components can distinguish crack propagation and pore connectivity, which can lead to tortuosity calculations.

For example for Pore Size Distribution (PSD) in porous network concrete (Rifai et al. 2018, Leite and Monteiro 2016), 3D-visualization of pore structure (Wei et al. 2013) or bubble size distributions (She et al. 2018) in foamed concrete, study PC grains pores (Ferrari et al. 2017), investigate local porosity in various w/c ratios (Wan and Xu 2014), porosity distribution (Kashani et al. 2017) or porosity variation (Lanzón et al. 2012, Lanzón et al. 2015) or pore detection and effective pore network (Schaefer et al. 2018) , or porosity analysis in mortars with different minerals (Murugan et al. 2016, Pilehvar et al. 2017, Awoyera et al. 2017), or chemicals (Olawuyi and Boshoff 2017, Pyatina et al. 2016, Viejo et al. 2016) or even novel binders (Rattanasak and Kendall 2005, Das et al. 2015, Long et al. 2018, Kupwade-Patil et al. 2018), 3D model of the pores of concrete with added nanoparticles (Niewiadomski, Stefaniuk, and Hoła 2017), and pore-scale modelling of aerated cement pastes (Melo, Aguilar, and Olivares 2014).

In addition to performing this type of pore segmentation, lower energy around 20 keV energy were used for pore connectivity (Bossa et al. 2015, Schock et al. 2016, Karim and Krabbenhoft 2010, Koster, Hannawald, and Brameshuber 2006) and tortuosity (Provis, Myers, et al. 2012, Promentilla, Takafumi Sugiyama, et al. 2008, Promentilla, Sugiyama, et al. 2009, Schabowicz et al. 2016) across the pores.

1.3.2 Time-resolved microstructural evolution

This refers to the dynamic changes in the microstructure of a cement-based material that occur over time.
Monitoring the hydration process is one of the applications that can be studied in time-resolved mode. It can be considered as 4D imaging, but may not be an *in situ* sample preparation to scan in a single exact volume due to possible limitations such as limited beamtime shifts, etc. (This is discussed in the chapter 4, also the *in situ* 4D imaging is discussed in the

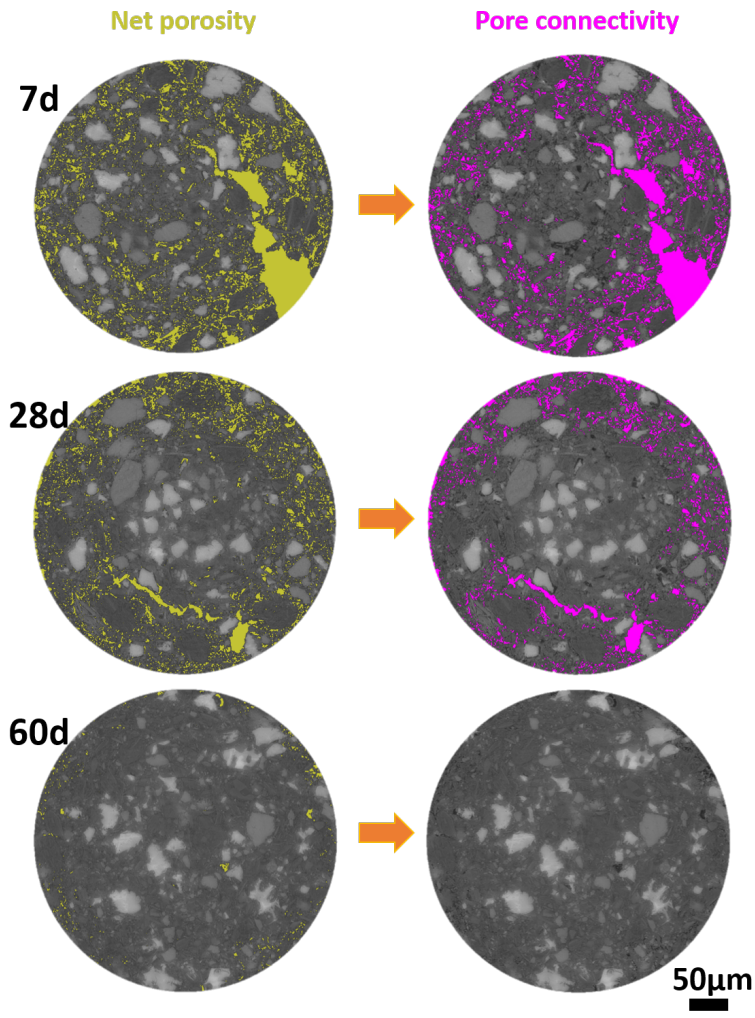

Figure 1.29: LC^3 pore connectivity and self-healing.

section 1.3.4 " *in situ* 4D imaging of cement hydration", below.)

For example, in Article 2 (A#2) in section 3.2, we studied PC and BC in different hydration ages (3, 7 and 28 days) and curing temperatures. Also, in another parallel project in our research group, we followed the LC^3 hydration over time (7, 28 and 60 days) and monitored the pore connectivity and self-healing of this type of eco-cement in different samples (Bernal, Shirani, et al. 2021), see Figure 1.29. Both of these projects can be described as *ex situ* 4D imaging, because the evolution/changes are tracked in different samples with the same type of filled material (enclosed in a glass capillary) and with different hydration ages.

In order to assess the overall performance and durability of cementitious materials, it is necessary to understand and characterise the pore connectivity in such materials. The pore connectivity analysis in Figure 1.29 was performed to distinguish between open pores (connected to the surface of the sample VOI) and closed pores (separated and isolated) at the available spatial resolution. It is well known that pore connectivity depends upon the spatial resolution with better data yielding larger connected porosities. The process involves first segmenting the porosity phase (net porosity) and then calculating the connected components

in the labelled phase. In this study, the two approaches of 6-connected components (connectivity on the voxel faces) and 26-connected components (connectivity on the corners) to determine whether two voxels are linked were performed using Dragonfly (Object Research Systems (ORS)) software. From the total porosity volume percentage (net porosity), 92, 78 and 9% of the pores were found to be connected for 7, 28 and 60 days LC^3 eco-cement paste samples, respectively (see Figure 1.29) for the attained spatial resolution in the range of 550nm.

There are also other dynamic studies such as morphological features in the first 60 days of hydration by focusing on the reacting anhydrous cement grains and porosity (Gallucci et al. 2007), monitoring pore structure development (Zhu et al. 2018), tracking plaster hydration (Adrien et al. 2016), corrosion and the formation of cracks in embedded reinforced concrete (Dong et al. 2017, Michel et al. 2011, Šavija et al. 2015), microscale characterisation of alkali-silica reaction morphological and crystallographic features by a combination of synchrotron CT and diffraction (Marinoni et al. 2015).

1.3.3 Nano-tomography of cement-based materials

Most of these studies and investigations carried out at the micro-scale can be obtained at the nano-scale, if it is of interest, by moving to the other local tomography, nanoCT and ptychography modalities. The adaptation of the appropriate FOV and optimised spatial resolution for each acquisition setup is essential.

In the nanoscale and submicron resolution there are a number of studies in the cement field. First soft X-ray synchrotron nanoCT (Brisard et al. 2012) was used, later on C-S-H (Bae, R. Taylor, et al. 2015) and ancient Roman concrete (Jackson et al. 2013). This was paralleled by the pioneering use of hard X-ray nanoCT to characterise the 3D pore structure (Provis, Rose, et al. 2011).

The first research on ptychographic imaging of cements using hard X-rays was published by Trtik et al. (Trtik et al. 2013). Silva et al. then carried out a detailed investigation of 3D nanoCT using ptychography to assess the spatially resolved mass density and water content of C-S-H in a cement paste (Silva et al. 2015) the technique we used in this thesis for quantitative analysis based on the electron densities of the cement components (see chapter 3). This approach has previously been used by our research group to characterise the chemistry and mass density of aluminium hydroxide gel in eco-cements (Cuesta, De la Torre, et al. 2017a), and to study the disentanglement of nanocrystalline phases in Portland cement paste (Cuesta et al. 2019).

1.3.4 *In situ* 4D imaging of cement hydration

Unlike other *ex situ* methods in section 1.1.8, X-ray computed tomography can work *in situ* on samples with minimal and rapid sample preparation,

making hydration studies more feasible and with less errors due to sample preparation artifacts.
Monitoring the hydration process of cementitious materials may be difficult, but it is one the most desirable application of dynamic X-ray imaging in this thesis, besides calculating the amount of reacted initial anhydrous grains, monitoring porosity, etch-pit evolutions, etc. (see chapter 3). Our recent developments in time-resolved experiments have achieved monitoring of PC hydration, see Article 4 (A#4) in section 3.4.

The act of matching relevant VOIs in more than two 3D image stacks of the sample is known as **"image registration"** and has also been used in the reduction of unreacted particles and air filling during 28 days hydration steps studies (L. Wang et al. 2014) and is an important step in the interpretation of this type of *in situ* dynamic dataset. Registration was performed and adjusted based on imaging modalities for all *in situ* studies in this thesis. The full description of how this has been done for the Lab-μCT, Syn-μCT and PXCT modalities is explained in the Supplementary Information of Article 4 (A#4) in section 7.3.

Some other recent *in situ* studies include: *in situ* hydration of PC with different w/c ratios (Parisatto et al. 2015), tricalcium silicate pastes hydration (Bae, Kanematsu, et al. 2016, Moradian et al. 2017, Geng et al. 2018), direct measurements of 3D microstructure and chemistry of C_3S hydration (Hu, Aboustait, et al. 2016a, Hu, Aboustait, et al. 2016b), C_3S grain dissolution (X. Li, Hu, Robertson, Ley, De Andrade, et al. 2023), the *in situ* hydration of Ye'elimite (Cuesta, De la Torre, et al. 2017b), 3D dynamics of the cement paste hardening by dark-field tomography (Prade et al. 2016), chemical composition changes during PC hydration by multi-scale observation (Moradian et al. 2019), An automated motion correction computation method for cementitious pastes (Vigor et al. 2020), *in situ* monitoring of plaster setting (Seiller et al. 2021), *in-operando* coupled X-ray and neutron tomography of a concrete sample heated at moderate temperatures (Sleiman et al. 2021), early hydration of blended cements (Poirier et al. 2022).

Vigor et al. monitored the transformation of a liquid paste into a solid on a sub-minute time scale and took into account corrections for sample movement. During the induction step, a layer becomes visible on the surface of the grains that is different in density from the bulk of the cement grains. In this study, the following measurements were made: the chemical and physical processes of PC hardening, the development of a fluid-filled pore network surrounding the cement grains, the strengthening of the hydrate phases surrounding the grains, the density gradient within the microstructure and the solidification of the structure into a hardened porous matrix (Vigor et al. 2022).

It is quite challenging to make dynamic observations in real-time (following the sample changes in the order of seconds). The fast imaging technique allows a real-time type of observation. Fast tomography was used to analyse the spatial behaviour of monoclinic tricalcium silicate from the first few seconds to one hour after hydration (X. Li, Hu, Robertson, Ley, and Xiao 2023).
This very recent paper by X. Li et al, describes research using rapid

X-ray nanoCT to directly observe the dissolution process of C_3S particles. As tricalcium silicate is a fundamental component of cement and its dissolution behaviour is critical in regulating the reactivity and strength development of cementitious materials. However, due to its fast reaction and tiny particle size, the dissolution process of C_3S particles is difficult and complicated to track directly.

They immersed C_3S particles in a solution and continuously monitored their hydration using nanoCT scans at different time intervals, allowing them to gain a thorough grasp of the hydration kinetics. The results of the study indicated a stepwise dissolution process of the particles, starting with the reaction of the surface layers and progressing to the core. They found that the dissolution process was heterogeneous, with differences in dissolution rates and patterns between different particles.

The study also investigated the effect of several parameters on dissolution kinetics, such as C_3S particle size and solution composition. They found that higher solution alkalinity and smaller particle size increased the dissolution rate.

Objectives 2

In this chapter, we will discuss the objectives of this thesis, which will allow us to obtain the results of the following chapters.

The aim of this thesis is to develop a methodology and optimize the sample preparation for the quantitative analysis of cementitious materials using X-ray based imaging for the monitoring of cement hydration. We will focus on the data analysis of the synchrotron based imaging and compare the results with the laboratory based device.

In this thesis we have focused on the use of X-ray imaging for the study of cementitious materials. Other complementary laboratory tests have been used to confirm or invalidate the results obtained with X-ray imaging.

We will address three imaging modalities for this purpose: Synchrotron X-ray computed microtomography (Syn-μCT), Ptychographic X-ray computed tomography (PXCT) and Laboratory X-ray computed microtomography (Lab-μCT) and compare them with other laboratory measurements.

The specific aims can be described as follows:

1. **To develop a precise methodology for the study of cement** : Most of the previous methods of studying cement require the sample to be altered in order to characterise it, but we have developed a step-by-step method of studying cement hydration in a non-destructive way that is also more accurate.
2. **To optimise sample preparation** : Depending on the required study and the structure size order to be studied, sample preparation should be optimised to be ready for X-ray imaging. we have proposed a sample preparation pipeline that works with most of X-ray imaging and diffraction modalities and can be compared with other laboratory initial characterizations.
3. **Multicontrast imaging modalities** : We have combined multi-contrast imaging modalities and show the use and order of detail of each in the hydration domain.
4. **Appropriate spatial resolution** : We also showed the appropriate spatial resolution for each cement study and its limitations in each modality.
5. ***In situ* cement hydration evolution** : We proposed an approach that would allow us to study hydration in exactly the same sample, rather than tracking hydration in different samples, which is much less accurate.
6. **Image analysis approaches pipelines** : proposing treatments for the both threshold-based and Machine-Learning based data analysis for gaining the required outputs.
7. **Quantitative data analysis** : For the first time, particles and the nano-features during cement hydration are tracked in 4D with the appropriate details and the order of size and rate for each change during hydration.

8. **Accuracy in combined techniques** : Due to optimised sample preparation, it is possible to perform both X-ray imaging and X-ray diffraction and also show the agreed result of each technique.

Articles section 3

In this chapter, all the derived papers from this thesis are gathered.

This chapter contains a comprehensive collection of papers resulting from this PhD research. These papers represent the culmination of my research to date and highlight key findings and contributions to the field. Each paper focuses on a specific component of the research topic, using a variety of experimental procedures and analytical techniques. The resulting papers have undergone thorough peer review and have been accepted for publication in prestigious scientific journals. This chapter provides an overview of the main objectives, methodology and key results of each publication, illustrating their combined importance in advancing our understanding in the different research areas.

3.1 Article 1 (A#1): X-ray microtomographic studies of LC^3 and related binders

Shiva Shirani, Cinthya Redondo-Soto, Isabel M. R. Bernal, Ana Cuesta, Isabel Santa-cruz, Angeles G. De la Torre, Inés R. Salcedo, Margie P. Olbinado and Miguel A. G. Aranda,* Proceeding of Calcined Clay for Sustainable Concrete **2022** Conference

Abstract:

Limestone calcined clay cements are being widely researched and they are starting to find field applications. Most chemical hydration reactions and their durability features are being reported. However, due to the large variability in the mineralogy and textural properties of the clays, it is important to have a wide portfolio of techniques to understand their hydration behavior. Here, we contribute to the LC^3 hydration understanding by using synchrotron and laboratory X-ray microtomography (μCT). On the one hand, μCT allows determining microstructural features like microporosity (mainly amount, size(s) and connectivities). However, porosity can only be measured for sizes larger than the attained spatial resolution, usually 1-2 μm at best. Therefore, only a fraction of capillary porosity is currently being measured by even synchrotron μCT where currently the best true spatial resolution is ~1 μm. On the other hand, and for in situ experiments, where the same capillary is measured with time, μCT has the potential to follow the volume decrease (i.e. reaction/hydration) of amorphous phases like metakaolin. For synchrotron μCT measurements, the detector can be placed at a certain distance from the samples (here 5.5 mm) and phase-propagation increases the visibility between components with similar attenuations to the X-rays. The Paganin phase retrieval algorithm resulted in augmented contrast. Here several preliminary examples of the use of μCT in LC^3 related binders are reported and discussed.

3.2 Article 2 (A#2): Influence of curing temperature on belite cement hydration: A comparative study with Portland cement

Shirani, S., Cuesta, A., Morales-Cantero, A., Angeles, G., Olbinado, M. P., & Aranda, M. A. (**2021**). Influence of curing temperature on belite cement hydration: A comparative study with Portland cement. Cement and Concrete Research, 147, 106499.

DOI: 10.1016/j.cemconres.2021.106499

Abstract:

Belite cements (BCs) could be a more sustainable binder than Portland cements (PCs) but adequate knowledge of the hydration features has still to be built. In particular, the mild curing hydration temperature effects have been extensively studied for PCs but not for BCs. This research was triggered by a previous work reporting improved mechanical strengths of BCs at higher curing temperatures. Here, we report the hydration characteristics of a BC at 20, 40 and 60 °C and compared to those of a typical PC. We have corroborated previous findings and used a multi-technique approach including Rietveld phase analysis, thermal analysis, calorimetry, silicon MAS-NMR, mercury intrusion porosimetry and chiefly synchrotron X-ray microtomography, to thoroughly understand the different behavior. In a nutshell, the improved mechanical performances at mild curing temperatures for BCs are mainly due to a much larger belite degree of reaction, with lower porosity coarsening of belite cements also playing a role.

3.3 Article 3 (A#3): Calcium aluminate cement conversion analysed by ptychographic nanotomography

Shirani, S., Cuesta, A., De la Torre, A. G., Diaz, A., Trtik, P., Holler, M., & Aranda, M. A. G. (**2020**). Calcium aluminate cement conversion analysed by ptychographic nanotomography. Cement and Concrete Research, 137, 106201.

DOI: 10.1016/j.cemconres.2020.106201

Abstract:

Calcium aluminate cements are used for special applications but are nowadays banned for general structural purposes due to the calcium aluminate hydrate conversion, that has led, for concretes fabricated with high water contents, to building collapses. The stoichiometries of these conversion chemical reactions are relatively well established but the consequences in porosity, key to predict durability, were unknown. Here, we have used hard X-ray ptychographic nanotomography to study the hydration of $CaAl_2O_4$ at different temperatures and chiefly, at 4 °C and then at 50 °C to provoke conversion similar to field conditions. The mass densities of the resulting $Al(OH)_3$ gels were 1.94, 1.98 and 2.23 g/cm^3, for samples hydrated at 4, 20 and 50 °C, respectively. These values are lower than that of gibbsite, 2.42 g/cm^3. Above all, this 3D imaging technique has allowed measuring the secondary water porosity developed in the conversion, which has an average pore dimension close to 140 nm.

3.4 Article 4 (A#4): 4D nanoimaging of early age cement hydration

nature communications

Article

https://doi.org/10.1038/s41467-023-38380-1

4D nanoimaging of early age cement hydration

Received: 18 November 2022

Accepted: 26 April 2023

Published online: 08 May 2023

Check for updates

Shiva Shirani[1], Ana Cuesta[1], Alejandro Morales-Cantero[1], Isabel Santacruz[1], Ana Diaz[2], Pavel Trtik[3], Mirko Holler[2], Alexander Rack[4], Bratislav Lukic[4], Emmanuel Brun[5], Inés R. Salcedo[6] & Miguel A. G. Aranda[1]

Despite a century of research, our understanding of cement dissolution and precipitation processes at early ages is very limited. This is due to the lack of methods that can image these processes with enough spatial resolution, contrast and field of view. Here, we adapt near-field ptychographic nanotomography to in situ visualise the hydration of commercial Portland cement in a record-thick capillary. At 19 h, porous C-S-H gel shell, thickness of 500 nm, covers every alite grain enclosing a water gap. The spatial dissolution rate of small alite grains in the acceleration period, ~100 nm/h, is approximately four times faster than that of large alite grains in the deceleration stage, ~25 nm/h. Etch-pit development has also been mapped out. This work is complemented by laboratory and synchrotron microtomographies, allowing to measure the particle size distributions with time. 4D nanoimaging will allow mechanistically study dissolution-precipitation processes including the roles of accelerators and superplasticizers.

Portland concrete is the world's largest fabricated commodity, ~20 billion tonnes/yr. The enormous production of Portland cement (PC), ~4 billion tonnes/yr, results in ~2.7 billion tonnes/yr of CO_2 emissions[1]. Therefore, there are many attempts to decrease the cement CO_2 footprint[1,2]. In order to rationally design approaches to decrease the embodied carbon content of binders, maintaining the performances, cement hydration understanding is key. Unfortunately, there are many unanswered questions[3] regarding the complex dissolution and precipitation processes that lead the setting and early hardening of cements[4].

The hydration of PC can be divided into five periods[3], see Fig. 1b. Stage-I is the initial dissolution (first minutes); stage-II is the low activity, induction, period (some hours); stage-III is the acceleration (several hours until the maximum of the heat flow trace); stage-IV is the deceleration (tens of hours); and stage-V is the diffusion-controlled hydration (months to years). There was a strong debate about the mechanism responsible of the induction period. However, it is now accepted that it is the dissolution controlled by undersaturation[5] and not the protective membrane theory. Conversely, there is no agreement in the mechanism(s) to explain the transition from acceleration to deceleration, when there is a degree of hydration of just 10-20% and plenty of space for the hydrates to grow. The most advanced theories, recently discussed[6], are based on heterogeneous nucleation and growth within confined regions taking into account the initial particle size distributions[7], for instance, see the reaction zone hypothesis[8]. There are alternatives[9] like the needle model[6] where alite, the most abundant component of PC, hydrates[10,11] to yield nonstoichiometric calcium-silicate-hydrate (C-S-H) gel[12], which nucleates and grows as needles. Neither the dissolution of small grains, nor water diffusion, nor etch-pits coalescence, nor C-S-H gel impingement –alone– can currently explain the transition from the acceleration to the deceleration periods[3]. The factors affecting the C-S-H gel growth in these two periods, III and IV, are not known. Moreover, the role of etch-pits[13] needs to be better understood as well as the consequences of the spatial gap which opens between the dissolving (inward) alite grains and the growing (mainly

[1]Departamento de Química Inorgánica, Cristalografía y Mineralogía, Universidad de Málaga, 29071 Málaga, Spain. [2]Laboratory for Macromolecules and Bioimaging, Paul Scherrer Institut, 5232 Villigen PSI, Switzerland. [3]Laboratory for Neutron Scattering and Imaging, Paul Scherrer Institut, 5232 Villigen PSI, Switzerland. [4]ESRF-The European Synchrotron, 71 Rue des Martyrs, 38000 Grenoble, France. [5]Université Grenoble Alpes, Inserm UA7 STROBE, 38000 Grenoble, France. [6]Servicios Centrales de Apoyo a la Investigación, Universidad de Málaga, 29071 Málaga, Spain. e-mail: g_aranda@uma.es

https://doi.org/10.1038/s41467-023-38380-1

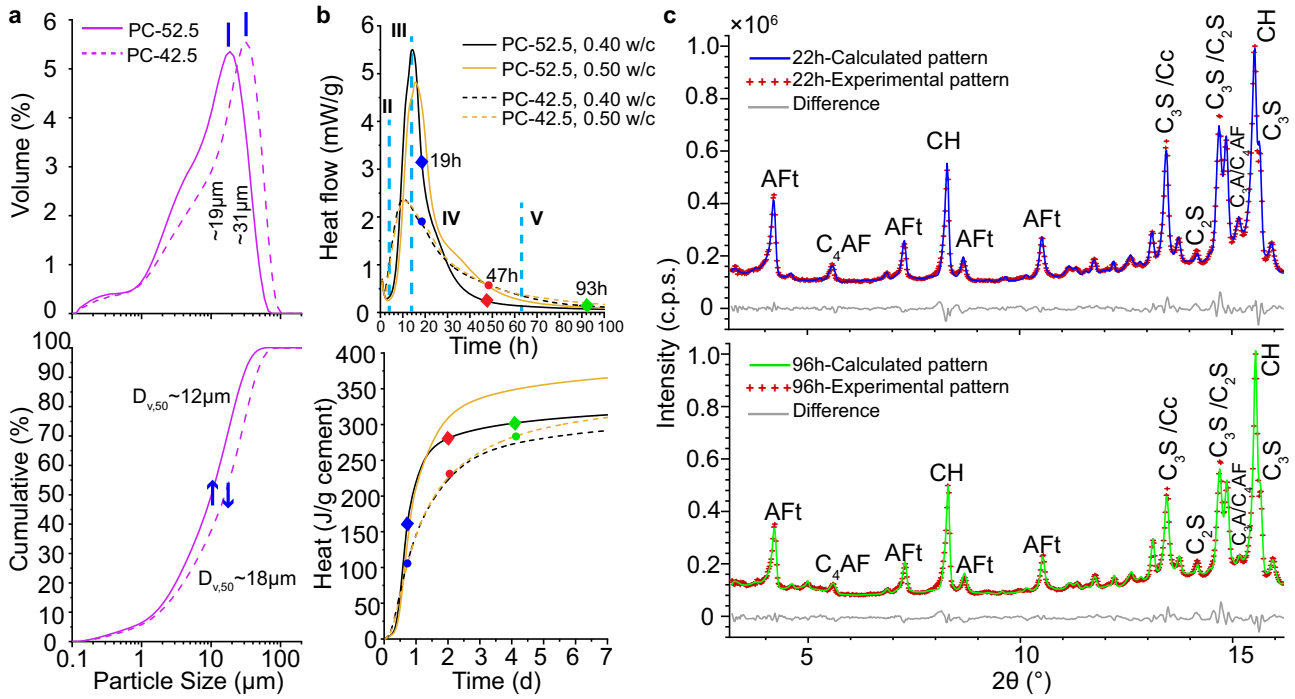

Fig. 1 | Initial characterization of the employed Portland cements. a Textural analysis of the two cements: PC-52.5 and PC-42.5, with Blaine values of 409 and 368 m^2kg^{-1}, respectively. (top) Particle size distributions, (bottom) cumulative volume variation as measured by laser scattering. **b** Isothermal calorimetric study, T = 25 °C, for the cement pastes prepared with w/c values of 0.50 and 0.40, referenced to 1 g of anhydrous cement. (Top) Heat flow curves (where the typical hydration stages are sketched), (bottom) cumulative heat traces for the two cements. **c** Laboratory Rietveld plots (MoKα_1 radiation, λ = 0.7093 Å) for PC-52.5 paste, w/c = 0.40, within a capillary of 1 mm of diameter. The main diffraction peaks are labelled with the contributing crystalline component by using the cement notation: tetracalcium aluminoferrite (C_4AF), belite (C_2S), alite (C_3S), tricalcium aluminate (C_3A), calcite (Cc), portlandite (CH) and ettringite (AFt). (Top) Pattern collected at 22 h, (bottom) pattern collected at 96 h of hydration.

outward) C-S-H gel[14,15]. Finally, the density evolution of the C-S-H gel shells is also unknown.

On the one hand, in situ laboratory[16] and synchrotron[17] powder diffraction allow following the phase development with time. These studies yield volume-averaged information which misses any spatial feature like particle size dependence. On the other hand, electron microscopy (EM) techniques yield very valuable information, with high spatial resolution, but they only give snapshots, as the experimental conditions are not compatible with the hydration in relevant conditions. In situ tomography[18,19] can contribute to filling this gap. In cements, modelling[20] and microstructural characterization methods[21] acknowledge the growing importance of X-ray microtomography (µCT) in their different modalities[22]. Moreover, µCT is being widely used[23] and in particular to follow in situ 4D (3D + time) some specific features of cement hydration[24–33]. In the last three years, important advances have been reported including: i) the automated correction for the movement of suspended particles at very early ages[34] which allowed to follow in situ PC hydration after water mixing[35]; ii) to follow the fast dissolution of plaster and the precipitation of gypsum[36]; iii) the simultaneous use of neutron and laboratory X-ray tomographies for in situ studying the microstructural changes of PC mortars on moderate heating[37]; and iv) the measurement of alite particle dissolution using fast synchrotron nano X-ray computed tomography[38,39]. However, none of these 4D imaging works combine the stringent four requirements needed for carrying out relevant contributions to the understanding of the mechanism(s) of Portland cement hydration at early ages: (i) water to cement mass ratio (w/c) close to 0.50, (ii) submicrometer spatial resolution, (iii) good contrast to be able to identify the different evolving components (more than eight), and (iv) relatively large scanned volume to allow hydration to progress with appropriate particle sampling, the particle sizes of commercial PCs have $D_{v,50}$∈10-20 µm. In particular, hard X-ray synchrotron microtomography has not the required submicrometer spatial resolution neither sufficient component contrast[35,40], hard X-ray synchrotron nanotomography has not the required contrast between the components to be able to classify the hydrates[38,39] and soft X-ray synchrotron nanotomography has the contrast but it requires very large w/c ratios and very small fields of view which does not allow the hydrates to growth in relevant condition (i.e. confined space with low water-cement ratios)[32].

So far, ptychographic X-ray computed tomography (PXCT)[41], which merges scanning X-ray microscopy and coherent diffraction imaging[42–44], met the first three requirements. Hence, it was applied to several binders within capillaries of ~40 µm of diameter[45,46] using a photon energy of 6.2 keV. The second study[46] provided valuable information about C-S-H gel hydrated for 5 months: an average stoichiometry of $(CaO)_{1.80}(SiO_2)(H_2O)_{3.96}$ with a mass density of 2.11 gcm^{-3} and an electron density of 0.64 $e^-Å^{-3}$. Moreover, it allowed quantifying a 6.4 vol% of a second amorphous component, iron-siliceous hydrogarnet, with 2.52 gcm^{-3} and 0.76 $e^-Å^{-3}$. Here, we have used PXCT in near-field configuration[44,47] to acquire data in a record-thick capillary of ~160 µm, employing a higher photon energy, 8.93 keV. This configuration, and the iterative algorithms that allowed the reconstructions[44], now meet simultaneously the four stringent requirements with current data collections of 3-4 h allowing 4D measurements of spatially resolved data during the first four days of cement hydration. On the one hand, the relatively slow overall acquisition time is the main limitation of this work, but this is expected to improve, see last section. On the other hand, the excellent spatial resolution and contrast of ptychographic nanotomography gave quantitative values of relevant parameters in the dissolution-precipitation processes like alite spatial dissolution rates

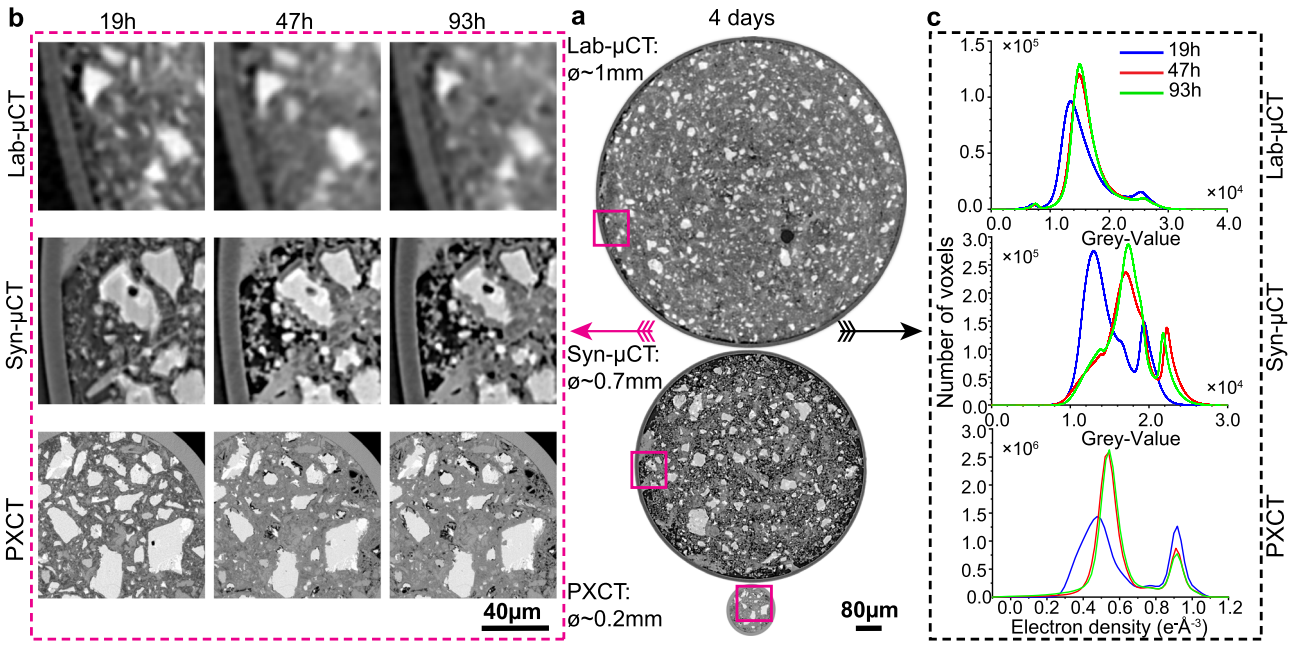

Fig. 2 | In situ multicontrast X-ray tomographic studies of cement hydration. **a** Selected orthoslices for the three imaging approaches. (Top) Attenuation-contrast laboratory data (Lab-μCT) for a PC-52.5 paste with w/c = 0.40. (Middle) Inline propagation-based phase-contrast synchrotron data (Syn-μCT) for a PC-42.5 paste with w/c = 0.50 [phases retrieved by using the Paganin algorithm[51]], (bottom) Quantitative phase-contrast, phases retrieved by near-field PXCT for a PC-52.5 paste scanning a region with w/c~0.40. The thicknesses of the capillaries are given. **b** Enlarged views for the three approaches, at the three hydration ages, to qualitatively illustrate the quality of the data (contrast and spatial resolution). Clinker minerals are seen as whitish particles, porosity as darkish regions, and hydrates have intermediate grey tones. **c** Histograms for the different tomographic studies and hydration times. The histograms were obtained by computing the largest possible volumes without including the glass capillary walls.

and etch-pit growth rate. These values can help to test the above described models.

Result and discussion

Initial cement analysis and cement hydration study

Two commercial PCs have been used and their laboratory X-ray powder diffraction (LXRPD) patterns were analysed by the Rietveld method, see Fig. S1. The elemental and mineralogical analyses are given in Tables S1 and S2, respectively. As reported in Table S2, the anhydrous cements are mixtures with more than eight crystalline phases. The cements have very similar elemental and mineralogical compositions but differ in their textural properties, see Fig. 1a and Table S3. The specific surface areas for PC-52.5 and PC-42.5 were 2.27 and 1.25 m^2g^{-1}, respectively. PC-52.5, with finer particles $D_{v,50}$~12 μm, was used for the PXCT study in order to have more hydrating particles in the analysed volume. It is noted that, in a very recent nanotomographic study[7], researchers milled alite very extensively, all particles<10 μm, in order to fit them within a small field of view (FOV) of ~50 μm. PC-52.5 was used for the PXCT and laboratory μCT imaging studies and the additional laboratory characterization. PC-42.5, with slightly larger average particle size, was used for the synchrotron μCT imaging study.

The calorimetric study, see Fig. 1b, gave the hydration kinetic features at the relevant w/c ratios of 0.50 and 0.40. Table S4 reports the cumulative heat at the hydration times where the imaging data were acquired. Moreover, it also lists the degree of hydration (DoH) at those times to be used as a reference in the imaging studies; for a detailed explanation of this type of calculation, see ref. 48. As expected, PC-52.5 releases more heat than PC-42.5, mainly because of its finesse. The DoH at the maxima of the heat flow peaks were 19% and 10% for PC-52.5 and PC-42.5, respectively. These values are well-known[3,49,50] but they cannot be explained by current models.

Figure 1c displays the LXRPD Rietveld fits for hydrating PC-52.5 taken in the same capillary where the Lab-μCT imaging study was carried out. The in situ LXRPD data were analysed by the Rietveld method resulting in the quantitative phase analyses reported in Table S5. From these data, the DoHs of the different clinker phases are derived at 22, 50 and 96 h of hydration, also used as reference.

In situ X-ray tomographic studies of cement hydration

Two additional in situ X-ray imaging studies were carried out to place the results of the PXCT nanoimaging in context. Emphasis is placed on the accuracy of the results that can only be estimated by comparison. The FOVs were cylinders. Figure 2a displays one orthoslice for each work: (i) Lab-μCT for PC-52.5-w/c = 0.40, FOV = 1200×940 μm (ϕ×L); (ii) Syn-μCT for PC-42.5-w/c = 0.50, FOV = 800 × 1190 μm; and (iii) PXCT for PC-52.5-w/c~0.40, FOV = 186 × 30 μm. Syn-μCT data has a larger w/c value, showing higher porosity (the darkish micro-regions) see the central panel in Fig. 2a. The nominal w/c mass ratio employed to fill the PXCT narrow capillary, 200 μm of nominal diameter, was 0.50, see methods. However, it is very difficult to accurately control the w/c ratio in very thin capillaries. Therefore, the w/c ratio of the scanned volume for the PXCT measurement was measured as previously published[46] and detailed in a subsection of the S.I. The w/c ratio of the scanned volume in the PXCT study was 0.41.

Figure 2b shows enlarged views to illustrate the evolution of the different components and the spatial resolutions. The PXCT study has a much higher resolution and contrast at the expense of a smaller FOV. A minor artefact can be seen in the Syn-μCT data as some borders have grey-values too white. This is a common feature for inline propagation-based data that cannot be fully corrected with the employed Paganin algorithm[51]. Figure 2c shows the histogram evolutions with time. At 19 h (blue traces), there is plenty of free water, which displaces the main peak toward smaller grey-values/electron densities. As hydration progresses, and as expected, the main peak in the histograms densifies and the amount of clinker components decreases. The histogram evolutions for the same cement paste from Lab-μCT and PXCT, see corresponding panels in Fig. 2c, were very similar giving confidence to

Article https://doi.org/10.1038/s41467-023-38380-1

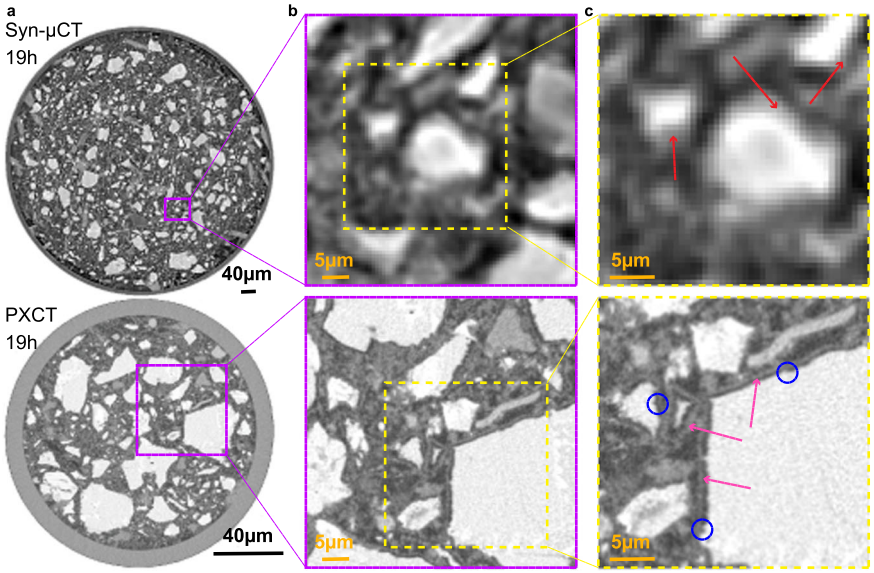

Fig. 3 | Comparison of phase-contrast synchrotron tomography and ptychographic X-ray computed tomography. a Selected orthoslices at 19 h for (top) Syn-µCT [voxel size: 650 nm, total scanned volume: 5.25 10^8 µm^3, overall acquisition time: 5 min], and (bottom) PXCT [voxel size: 186.64 nm, total scanned volume: 8.15 10^5 µm^3, overall acquisition time: 3 h, 55 min]. **b** Enlarged views of the highlighted regions (purple squares) in **a**, in order to illustrate the level of detail that can be observed with these imaging modalities. Every voxel in Syn-µCT image starts to be evident. **c** Further enlarged views to illustrate the maximum level of detail that can be observed. (Top) The Syn-µCT image shows whitish particles (anhydrous cement particles) surrounded by hydrates (greyish voxels) which are highlighted by red arrows. (Bottom) The PXCT data, at the same magnification, shows a much higher level of detail. The C-S-H gel shells surrounding the alite particles are clearly visible (pink arrows). There is a water gap between the shell and the alite grain due to the inward dissolution of alite. Moreover, etch-pits on the surfaces of the alite particles are also visible (blue circles). The highest spatial resolution and better contrast of PXCT data allow visualizing submicrometre features of the dissolution-precipitation processes which are not visible in propagation-based Syn-µCT. Conversely, propagation-based Syn-µCT permits to scan much larger volumes in much smaller acquisition times, showing the complementary nature of both techniques.

the relevancy of the nanoimaging results in spite of the limited amount of volume scanned to have submicrometer resolution. The grey-values in the Lab-µCT study, see Fig. 2c (top panel), are related to the attenuation coefficients of the components in this PC-52.5 paste, but the relationship is not quantitative due to the polychromatic nature of the employed radiation. Conversely, the electron density values obtained for the same paste by PXCT are quantitative. Therefore, the grey scales in the Lab-CT and the electron densities in the PXCT datasets cannot be directly related as they derived from the imaginary and the real part of the refractive index of every component.

The spatial resolution was characterised by two approaches as recently reported[52]. The procedures are thoroughly detailed in Supplementary Information (SI). On the one hand, the spatial resolution can be determined by the edge sharpness across selected interfaces. A point spread function (PSF) used to determine the spatial resolution of the images as ISO/TS 24597 defines the Gaussian radius of the PSF as the resolution, which equals a change between 25%–75% grey value along the studied interfaces[38]. The spatial resolutions, determined by this approach, were 250(25) nm, 264(25) nm, 272(34) nm, 748(19) nm and 2.21(17) µm, for PXCT-19h, PXCT-47h, PXCT-93h, Syn-µCT and Lab-µCT datasets, respectively. As examples of this procedure, Figs. S2–S4 display line profiles of sharp interfaces between high (i.e. alite) and low density (i.e. porosity) components within the capillaries. On the other hand, Fourier-shell-correlation (FSC)[53] has also been employed to estimate spatial resolution. Figs. S5–S7 displays the FSC traces for the three imaging modalities. The agreement between both approaches is satisfactory for Syn-µCT and Lab-µCT, but not for PXCT. The worse spatial resolution estimated by FSC for PXCT is very likely due to the low number of projections, i.e. 420, which make the subtomograms employed in the FSC calculation severely undersampled. Moreover, Fig. 3 compares the level of details that can be obtained with Syn-µCT and PXCT at 19 h of hydration. The latter shows the C-S-H gel shell and a porosity gap between the shell and the dissolving alite particle that it is not observed in the Syn-µCT data because the lack of spatial resolution and contrast.

4D nanoimaging of cement hydration

In situ near-field PXCT data were taken as detailed in methods. To ensure the relevance of the results, the scanned volumes were assessed. Firstly, the w/c ratio was 0.41(2), as determined from the absorption data[46], see Table S6. This w/c value is fully consistent with the obtained degrees of hydration. Secondly, possible signatures of radiation damage were explored. The mean electron density values of the whole sample were 0.600, 0.599 and 0.591 e$^-$Å^{-3}, for the 19, 47 and 93 h datasets, respectively. The spatial resolution from FSC was 470 and 500 nm, for the 47 and 93 h data, respectively. Hence, radiation damage cannot be discarded but it is small, if any. Thirdly, seven sets of components within the tomograms were identified: air, water, AFt/C-S-H gel/others, CH, Cc, C_3A/C_3S/C_2S and C_4AF, using the electron density and the absorption data in the bivariate plots, see Figs. S8 and S9. The calculated electron density and attenuation length values are given in Table S7, and Fig. S10 displays the histogram evolution in logarithm scale. The differences between the theoretical electron densities and the measured ones are mainly due to partial volume effects. For instance, portlandite, i.e. $Ca(OH)_2$, has a theoretical electron density value of 0.69 e$^-$Å^{-3}. The measured values at 19 and 93 h were 0.62(2) and 0.651(5) e$^-$Å^{-3}, see Table S7. These numbers are 6-10% smaller than the theoretical one, with the difference being higher than the errors of the measurements, which are estimated in 2-3%[46,54]. This difference is very likely due to the presence of residual water porosity below the spatial resolution of the measurements, which we refer to partial volume effects. It should be noted that individual C-S-H nanoparticles have sizes close to 5 nm[12,55] much smaller than the spatial resolution of this work, i.e. ~250 nm. Therefore, the C-S-H regions analysed here very likely contain other components like gel and capillary water porosities and interspersed calcium hydroxide. It should also be noted

https://doi.org/10.1038/s41467-023-38380-1

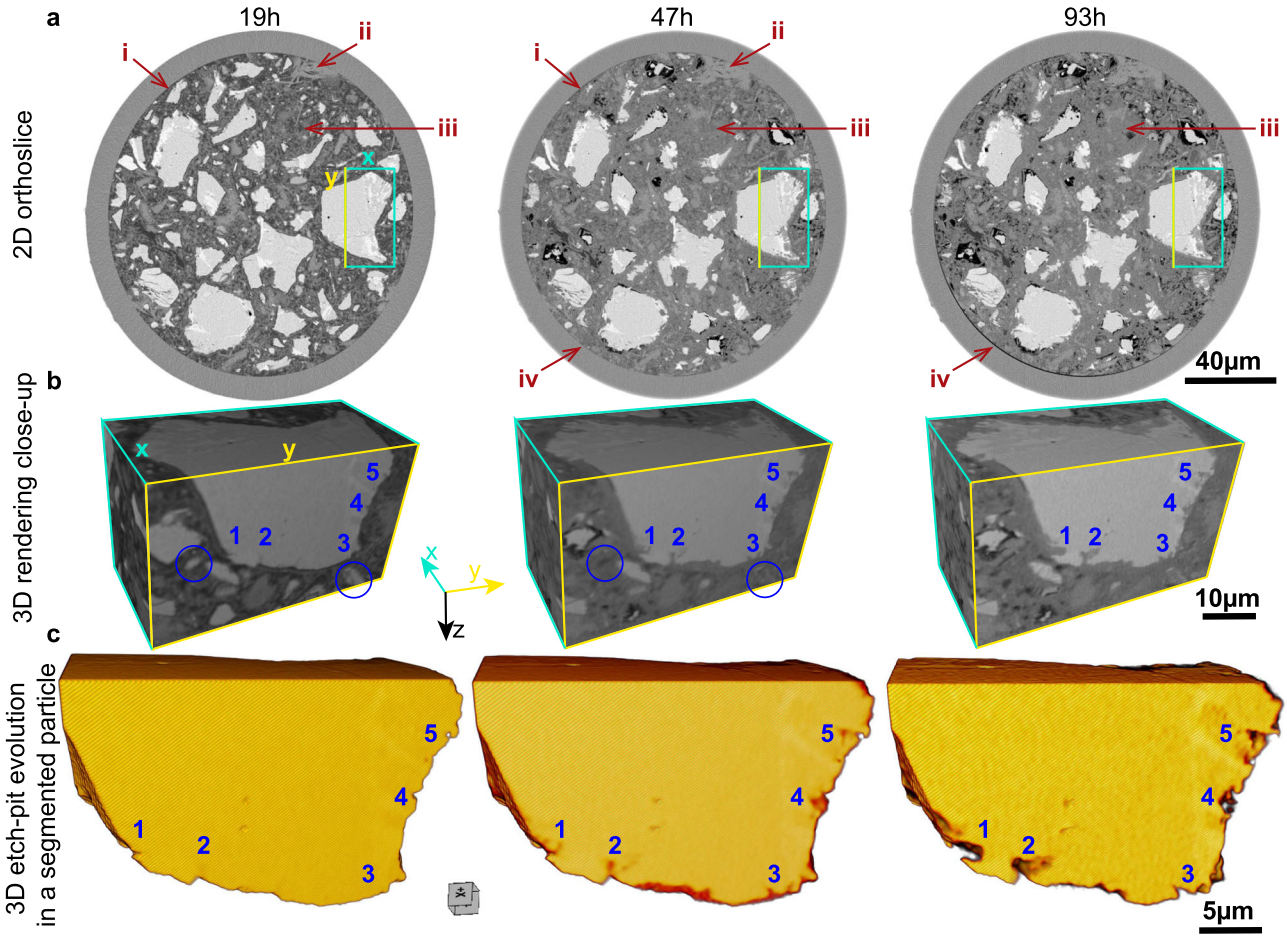

Fig. 4 | 4D nanoimaging study highlighting the etch-pit evolution. a PXCT orthoslices at the studied hydration ages showing the evolution of the PC-52.5-w/c~0.40 paste which includes: i) dissolution of cement particles, ii) portlandite growth, iii) C-S-H gel densification at 2 and 4 days, and iv) chemical shrinkage. Examples of these features are labelled with red arrows. **b** 3D rendering of a volume including a fraction of large alite particle highlighted in **a**, to show the evolution of five selected etch-pits, which are labelled. These images also show the full reaction of small alite particles, featured with blue circles. These 3D rendered views do not show exactly the electron densities as they are affected by visualization features like the lighting source. **c** 3D representation of the segmented particle, shown in the previous panels, to highlight the evolution of the etch-pits. It is noted that three branches within etch-pit #1 at 47 h coalesce at 93 h of hydration which may mean a reduction in surface with hydration time.

that the employed stoichiometry for C-S-H gel, i.e. $(CaO)_{1.80}(SiO_2)(H_2O)_{4.0}$[56,57], is an assumption and slightly smaller Ca/Si ratios, ~1.70, have also been reported[12,58]. On the other hand, ettringite and portlandite particles have larger sizes, usually ranging 1-5 μm[3], and they can be imaged in the present work. In any case, partial volume effect (the presence of components contributing below the spatial resolution of the measurements) is always taking place in cement pastes as some hydrates may have quite small particle sizes[17].

The crux of our results is the 4D submicrometer features of cement hydration, see Figs. 4 to 6. Supplementary Movie 1 also shows a summary of the main findings. It is underlined that PXCT readily distinguishes air and water porosities because of their difference in electron densities, 0 and 0.33 e·Å^{-3}, respectively; when the phase retrieval is carried out quantitatively[54]. The paste evolution is displayed in Fig. 4a, showing a partly reacted binder plenty of capillary water at 19 h. The main change from 19 to 47 h is the large consumption of capillary water (dark-grey regions in Fig. 4a-19h) and the densification of C-S-H gel. The main evolution from 47 to 93 h is the appearance of chemical shrinkage, evidenced by the development of many air-containing (black) regions. Importantly, Fig. 4c and Figs. S11–S12 show the evolution of etch-pits with time, including etch-pit coalescence, which contributes, in addition to the consumption of small alite particles, to the decrease of specific surfaces in the deceleration period. The etch-pit growth rate was estimated, as detailed in SI, from the analysis of 27 dissolving regions in five alite grains. The resulting rate, between 19 and 47 h, was 41(29) nm/h. The etch-pit growth rate between 47 and 93 h was slower with a large variability, 7(8) nm/h, showing that the water diffusion is already limiting hydration. The large variability in the growth rates of the etch-pits is highlighted in Fig. S13. Etch-pits at very early ages, i.e. 2-4 h, were imaged by EM with sizes of ~15 nm[59] which is out of in situ PXCT capabilities.

Chiefly, the spatial dissolution rate of alite was determined from the study of the surface evolution of selected particles, see Fig. 5a and Figs. S14–S19, as examples. C_2S particles were identified and excluded from this analysis, because they do not have C-S-H shells at 19 h of hydration. C_3A particles were also recognised and discarded because of their smaller electron density values, i.e. ~0.91 e·Å^{-3}, 5% lower than that of alite. From 22 measurements along different surfaces, the dissolution rate between 19 and 47 h was 25(14) nm/h. This value compares well with 36 nm/h from the reaction zone model[8] but poorly with 84 nm/h obtained from the same dataset by using the boundary nucleation and growth model[60]. Moreover, this spatial dissolution rate can also be estimated from the segmentation results presented in the next subsection. Based on the quantitative analysis derived from Machine Learning (ML) segmentation of the PXCT datasets (for the C_3S/C_2S class, dark brown colour code in the 3D visualization of Fig. 7),

Article https://doi.org/10.1038/s41467-023-38380-1

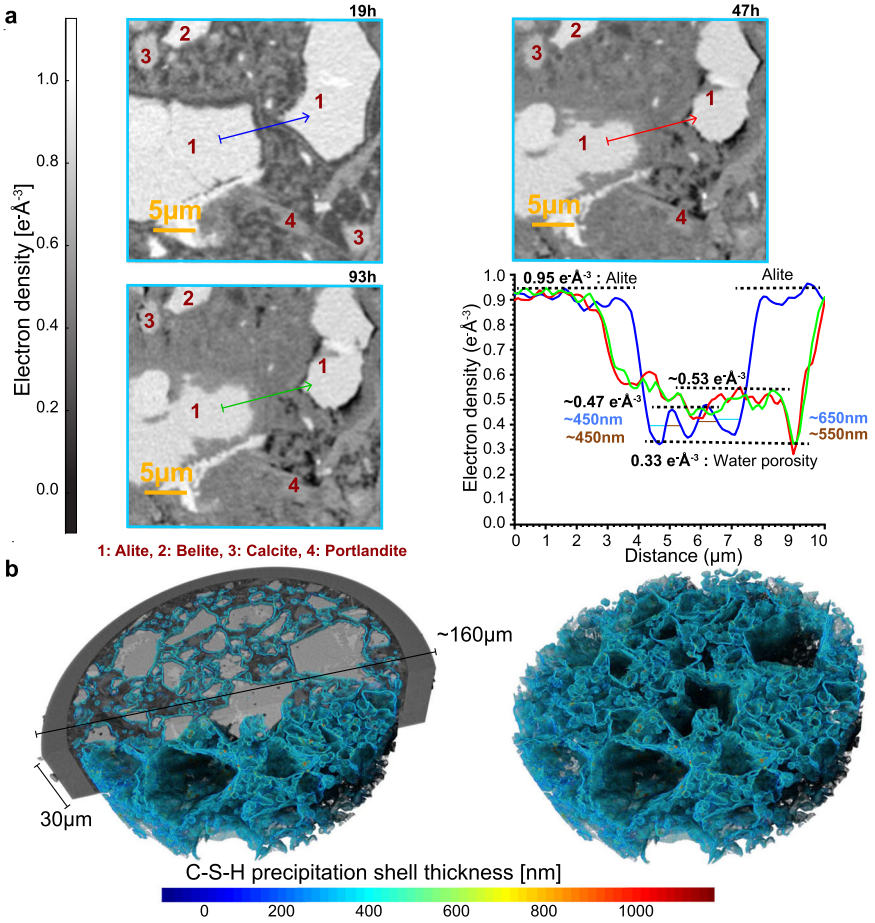

Fig. 5 | C-S-H gel shells and their evolution. a Selected 2D views of the PXCT data. The fourth panel displays the electron density profiles corresponding to the straight lines in the previous plots. At 19 h, the C-S-H shell covers every alite particle. The line profile at 19 h, blue trace in the fourth panel, shows water porosity (gap) between the alite particle and its shells. For these two particles, the shells have a thickness of ~550 nm and an electron density of ~0.47 $e^-Å^{-3}$. This C-S-H densifies at 2 days to ~0.53 $e^-Å^{-3}$. The alite particles partly dissolve and air porosity starts to develop (black regions). **b** 3D rendered views of the ML segmented C-S-H gel shells with the colour signalling its thickness for the 19 h tomogram. (left) View superimposing the C-S-H shells to half of the studied capillary. (Right) 3D view of the segmented C-S-H shells.

it is possible to derive an average spatial dissolution rate. Mathematical morphology tools were used to retrieve the outer layer of the segmented grains at 19 and 47 h. Subsequently, the average distance between these outer layers was computed for each grain, giving a mean value of 1.92 pixels (i.e. ~13 nm/h). This value is smaller than that obtained from the analysis performed in 2D slices for alite, 25 nm/h. However, it should be noted that in the segmentation calculation, alite and belite were classified together and therefore, the obtained spatial dissolution rate is underestimated as belite does not dissolve at early ages. Table S5, Rietveld analysis results, indicates that the amount of belite is half of that of alite during this stage. Therefore, the spatial dissolution rate can be corrected. The alite spatial dissolution rate should be close to 13/0.67 or 19 nm/h. This value agrees relatively well with 25 nm/h, obtained from 22 measurements in 2D slices, given the number of approximations which took place for both calculations.

The analysis of the 12 largest Hadley grains (hollow-shell microstructure, see Fig. 6a, b and larger view at Fig. S20)[14,15,61,62] gave 2.6(3) μm of size. Here, their time-evolution can be followed and it is noted that hollow regions are filled with water at 19 and 47 h but dried at 93 h, see Fig. 6a, directly evidencing the water diffusion through the C-S-H shells. Additionally, the analysis of the 15 smallest alite particles leaving an unhydrated, very small, core gave an average particle size of 3.4(5) μm. Therefore, it is concluded that alite particles smaller than ~3.0 μm are fully hydrated in the 4-19 h range, leading to a spatial dissolution rate of ~100 nm/h. The largest size of the Hadley grains found here agrees well with previous works[61,62] (at 24 h) reporting a maximum size of 5.0 μm with shells of 500 nm. Hence, it seems to be a 3-4 fold difference between the spatial dissolution rate of small alite grains in the acceleration period and that of large alite grains in the deceleration stage.

Figure 5a and Figs. S14–S17 show views detailing the hydration of alite particles and showing the C-S-H gel shells that surround all alite grains enclosing a gap. Similar plots containing belite particles, Figs. S18–S19, did not show gaps, as expected. C-S-H shells on alite have been extensively analysed by EM[6,14,15,61,63], but here their electron density and spatial evolutions can be followed. The C-S-H shells for these two alite particles, Fig. 5a, have ~0.47 $e^-Å^{-3}$ which increases to ~0.53 $e^-Å^{-3}$ at 47 h. This means a very low mass density shell. For instance, ettringite, a phase with 32 crystallization water molecules has ~0.56 $e^-Å^{-3}$, and mature C-S-H gel, with $(CaO)_{1.8}(SiO_2)(H_2O)_{4.0}$ composition, i.e. including gel pore water, had 0.64 $e^-Å^{-3}$ [46]. As this result is critical for discarding diffusion as the mechanism for the deceleration period, a larger study was carried out. 20 shells were analysed giving 0.51(4) $e^-Å^{-3}$ and 500(120) nm, for the average electron density and thickness, respectively. Moreover, this study also yields the average width of the gap, 490(140) nm. At 24 h, the thickness of the shells and gaps were reported as ~500 and ~300 nm from EM[62]. Moreover, a gap of 490 nm developed in 15 h, time between the end of the induction period and the first nanoimaging measurement, which means an alite spatial dissolution rate of ~33 nm/h. Therefore, the dissolution rates of

Article https://doi.org/10.1038/s41467-023-38380-1

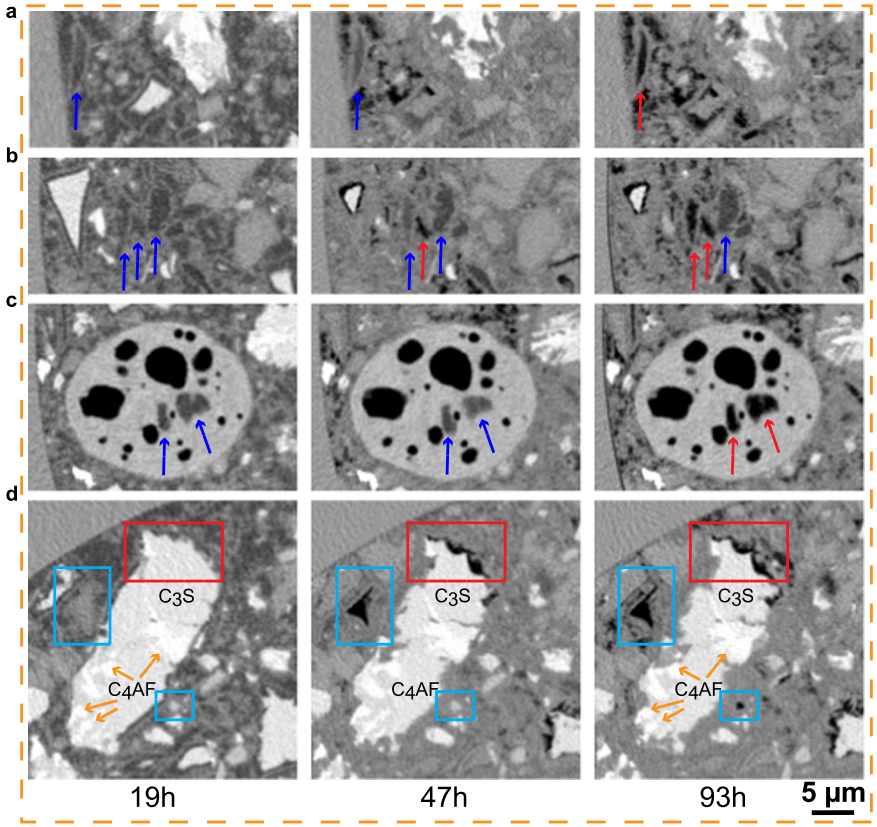

Fig. 6 | Hydration time evolution of selected nano-features directly visualised by near field PXCT. a Hollow-shell microstructure, also known as Hadley grain. The Hadley grains are fully hydrated small alite particles that contain a void within the original boundary of the anhydrous grain. The hollow regions are filled with water at 19 and 47 h (blue arrows) but dried at 93 h (red arrow) directly evidencing the porosity of the C-S-H shells. **b** Evolution of water porosity (dark-grey) to air porosity (black). It is noted that at 47 h, a tiny pore of about 1 µm size is already dried, but being very close to two larger water-filled pores, of sizes larger than 2 µm. This observation remarks the heterogeneity in cement hydration. It can be deduced that the relative humidity is not constant, at a given time, through the sample. This is due to a set of factors including the barriers to water diffusion and the crystallization/precipitation of different hydrates with quite different water contents, for instance ettringite and portlandite. **c** Evolution of water porosity inside a calcite grain, if connected to the surface. This calcite comes very likely from the limestone addition to the Portland cement as quantified in the anhydrous material, see Table S2. **d** Evolution of alite dissolution (hydration) which stops at the C_4AF intergrown regions, highlighted by brown arrows. Moreover, alite hydration also stops as soon as air porosity (pore drying) develops on the surfaces of the anhydrous grains, see red rectangles. This panel also illustrates that (recently precipitated) hydrates can dissolve, see blue rectangles.

large and small alite grains differ at least three-fold, which should be considered for modelling. To further study the C-S-H shells, the components were segmented by ML as described in methods following the procedure summarized in Fig. S21. Subsequently, the C-S-H shells were segmented as detailed in Fig. S22. The results of the C-S-H shell segmentation are presented in Fig. 5b with a relatively constant shell size of ~450 nm. The Supplementary Movie 2 displays a full picture of the segmented shells. Fig. S23 shows a 2D comparison of the raw data and the resulting segmented shells yielding a reasonable good agreement.

Finally, Fig. 6 shows interesting (directly-observed) *nano-features*. Figure 6a, b exhibit the water diffusion through the C-S-H shells for some Hadley grains between 19 and 93 h of hydration. Larger regions are shown in Figs. S20 and S24, respectively. Figure 6c displays the water porosity evolution within a calcite particle evidencing that some small pore regions, 2-3 µm in size, were water filled at 19 and 47 h and dried at 93 h, see also Fig. S25. This observation directly explains the indirect result of water transport within limestone grains obtained by X-ray dark-field tomography[30]. Figure 6d, larger view in Fig. S26, shows how hydration progresses along the surface of an alite particle but it stops at C_4AF intergrown regions, evidencing the importance of alkanolamines at early ages as accelerators[64]. Moreover, Fig. 6d also illustrates that C-S-H gel can dissolve to leave a dry capillary pore. Fig. S27 presents at 47 h the full dissolution of a grain of a size of 4 µm at 19 h. This implies a very large dissolution rate, >75 nm/h, which is likely C_3A.

Segmentations of the X-ray tomographies

Figure 7a displays orthoslices of the trained models overlaid on the three raw datasets and Fig. 7b shows the time evolution of the segmented components. For the PXCT study, the average electron densities and the segmented volumes are reported in Table S8. Moreover, Fig. S28 displays the evolution of the segmented water capillary porosity. It seems that at 19 h, the free water is preferentially located close to the walls of the capillary. This could be related to the 'wall effect' well known in mortars and concretes, where the cement paste content (water and fine cement particles) is slightly higher near the wall of the container respect to the larger aggregate particles which are preferentially arranged towards the centre. This feature, and its implications in the interfacial transition zone, has been extensively studied by numerous techniques, including synchrotron microtomography, see for example[65]. For cement pastes, higher porosity near the capillary wall has been observed by synchrotron microtomography[24]. For a water-rich alite paste, wall effect was clearly observed by PXCT where the resulting C-S-H gel had higher water content near the capillary wall[66]. In order to quantitatively study this feature, the scanned capillary was divided into two volumes, a central cylinder with half of the

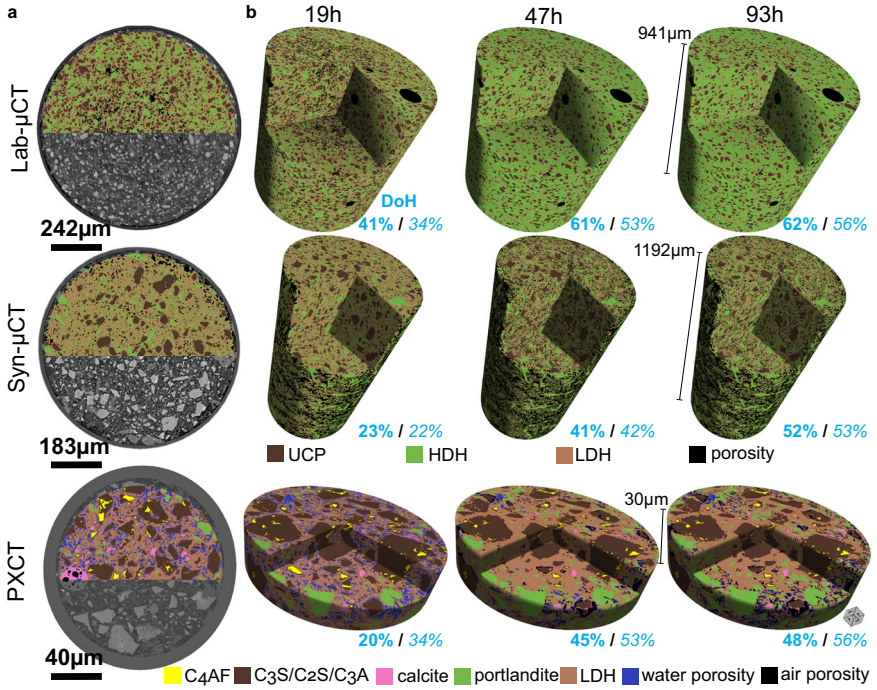

Fig. 7 | ML training and segmentation results for the three datasets with different contrast mechanisms. a ML trained models overlaid on the three raw datasets. **b** 3D rendering of the segmented volumes at the three studied hydration ages. The DoH values determined from microtomography (bold) are compared to the ones from calorimetry (italics). The number of quantified components in the Lab-µCT and Syn-µCT datasets are four: i) porosity (air and water), ii) LDH (low-density hydrates: mainly C-S-H gel and ettringite), iii) HDH (high-density hydrates: mainly portlandite and calcite), and iv) UCP (anhydrous cement particles: all unreacted clinker phases). The number of quantified components in the PXCT datasets is seven: i) air porosity, ii) water porosity, iii) LDH (low-density hydrates: mainly C-S-H gel and ettringite), iv) portlandite, v) calcite, vi) $C_3A/C_3S/C_2S$, and vii) C_4AF. It is noted that with the quality of the data reported in this study (spatial resolution and electron density contrast), it is not possible to disentangle low-density from high-density C-S-H.

radius and the outer region up to the glass capillary wall. The mean electron densities were computed, but the voxels with electron density smaller than 0.24 $e^-Å^{-3}$, air porosity, were not included in order to minimise any bias due to the shrinkage/pore drying. The results for the centre volume were 0.614, 0.618 and 0.617 $e^-Å^{-3}$ for the 19, 47 and 94 h datasets, respectively. The corresponding mean electron density values for the outer region were 0.608, 0.610 and 0.601 $e^-Å^{-3}$. The 1% difference between the two regions at 19 h is quite small but not negligible. Hence, the degree of hydration could slightly be a function of the horizontal position of the particles.

The amount of anhydrous components, together with the initial values, allow determining the DoH from the three imaging studies which are reported in Table S9 and summarised in Fig. 7b. Table S9 also gives the DoH from calorimetry and LXRPD as references. The agreement for Syn-µCT is noteworthy likely due to the large volume probed and the relatively good spatial resolution. The DoHs from Lab-µCT are overestimated probably due to the relatively poor spatial resolution and contrast, which do not allow us to quantify the anhydrous particles smaller than ~3 µm. Finally, PXCT yields underestimated values for the DoH likely due to the limited scanned volume.

Importantly, the high resolution and excellent contrast of the PXCT study allowed us to track down the individual hydration evolution of 1407 particles with connected anhydrous volume, at 19 h, of 1 $µm^3$ or larger. For this particle tracking statistical study, they were arbitrarily classified into four groups having connected volumes ($µm^3$) of $1.0 \geq vol_1 > 27.0 \geq vol_2 > 216.0 \geq vol_3 > 1000.0 \geq vol_4$. A rough estimation of their sizes in µm could be $\sqrt[3]{(vol)}$ or $1.0 \geq size_1 > 3.0 \geq size_2 > 6.0 \geq size_3 > 10.0 \geq size_4$. The groups contained 1117, 204, 61 and 20 particles, respectively. The corresponding volume percentages with respect to the overall anhydrous cement particle volume at this hydration age, were 5.4, 12.9, 21.5 and 60.2%. It is not possible to calculate the DoH of these groups at 19 h because there are no reference values at t_0. The degree of reaction, between 47 and 19 h, was 69.4%, 59.3%, 37.2% and 15.9% for the groups classified as vol_1, vol_2, vol_3 and vol_4, respectively, and they account for 12.9, 26.4, 27.7 and 33.0% of the total dissolved volume. In other words, the twenty particles of vol_4 group has a degree of reaction of 15.9% but it accounts for 33% of the dissolved volume in that period. A similar study can be carried out between 93 and 47 h. The degree of reaction during this period decreased to 14.7%, 11.6%, 6.7% and 3.6% for the corresponding groups. In terms of dissolved volume percentage in this period, the values are 6.8, 16.9, 25.3 and 51.0%, respectively. This simple analysis shows that 51% of the observed reaction during this diffusion-limited period is due to the 20 largest particles as they account for a very large fraction of the volume. The strong decrease of hydration rate in this time range is in line with a diffusion controlled hydration stage.

Finally, Fig. 8a displays the hydration evolution of the segmented anhydrous cement particles. It is readily visible that smaller particles dissolve faster than larger ones. Moreover, the segmentation output allows us to classify the particles and to follow their volumes and cumulative volumes, see Fig. 8b. The cumulative volume results for Lab-µCT and PXCT are very similar and in agreement with the expected DoH from calorimetry showing a large variation between 19 and 47 h and a small variation at 93 h. Moreover, the hydration of PC-42.5 is slower because of their larger average particle sizes, with similar DoH variation between the two studied time intervals, see Fig. 8b, in full agreement with their calorimetric traces, see Fig. 1b. This reflects a good accuracy of the obtained results. Finally, it should be noted that the scanned length in the vertical direction, 30 µm, for PXCT is limited taking into account that some alite grains with sizes of 20 µm, or slightly larger, are present in PC cements. This was mitigated by imaging 160 µm in the transversal direction. This type of experiment will benefit from imaging cylindrical volumes with 60-100 µm of height. However, with the current experimental procedure, this would lead to

https://doi.org/10.1038/s41467-023-38380-1

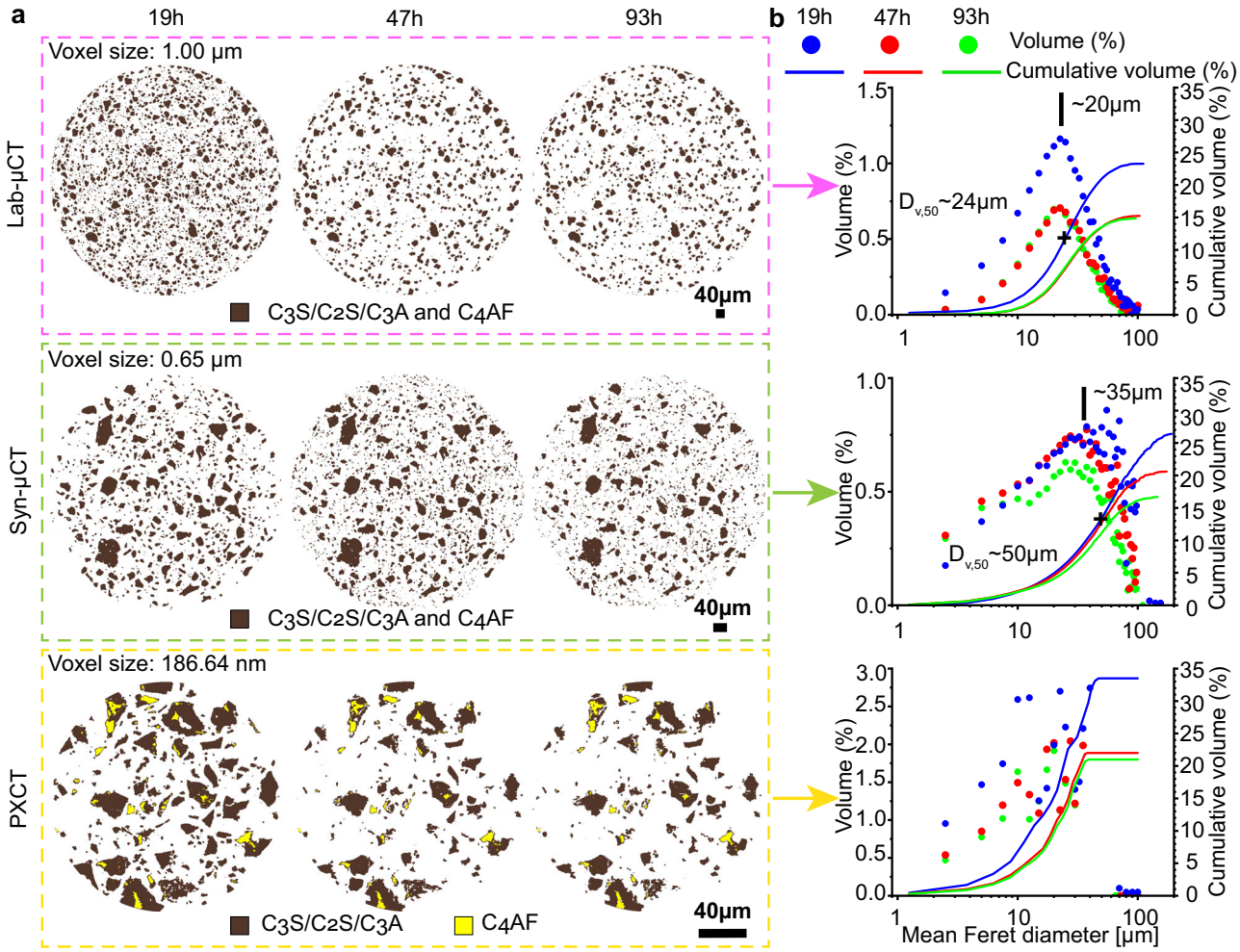

Fig. 8 | Hydration study as a function of time and cement particle sizes. a 2D views of the segmented anhydrous cement particles as a function of time. PXCT data shows that C_4AF hydrates little up to 93 h. This is likely due to the low w/c ratio in the scanned volume and its slow hydration rate. **b** Volumes and cumulative volumes for the anhydrous cement particles as a function of the particle size, represented in logarithmic scale for easy comparison with Fig. 1. The particle sizes are computed as the mean Feret diameter frequency which measures object size along directions. The particles are represented grouped in sets of 2.5 microns, i.e. 0-2.5, 2.5-5.0 µm, etc. The maximum and $D_{v,50}$ values for the Lab-µCT and Syn-µCT are given in the panels. These data are scattered for PXCT because the limited height of the studied cylinder yields a poor representative elementary volume for this feature.

acquisition times larger than 7-9 h and therefore changes due to hydration could take place during an acquisition. Procedures for faster data collection are being explored and they are discussed below.

The hydration of PC, in relevant conditions, has been measured with very high spatial resolution, i.e. 250 nm, and contrast. As expected but not directly measured so far, the hydration of Portland cement at 1 day or earlier is dominated by the small particles, smaller than 3 µm, and the hydration after 3 days is very much dependent of the large alite particles, larger than about 10 µm. The nanoimaging work shows the C-S-H gel shells surrounding every alite grain which does not preclude diffusion. The measured alite spatial dissolution rates, ~100 nm/h for small grains in the acceleration period and ~25 nm/h for large particles in the deceleration stage impose constraints on the cement hydration models. The alite etch-pit growth rate between 19 and 47 h has been estimated as ~40 nm/h, which decreases to ~7 nm/h in the 47 to 93 h interval. Moreover, etch-pit coalescence, the merging of different branches, has also been visually observed. However, better spatial resolution is required for a thorough etch-pit growth rate quantification. The configuration employed here already allows studying the roles of admixtures (accelerators, retarders, superplasticizers, etc.) by measuring C-S-H shell density, C-S-H gel spatial distribution and alite spatial dissolution and etch-pit growth rates. For instance, it would be possible to measure if the acceleration produced by $CaCl_2$ is due to a lower density of the C-S-H shells (higher water diffusion) or if it is mainly due to higher calcium supersaturation.

The current spatial resolution of in situ near-field PXCT, i.e. ~250 nm, could be improved by increasing the number of projections, without larger acquisition times. Moreover, so far the time resolution is modest, i.e. 3-4 h for a complete tomogram, but this is expected to improve in fourth-generation synchrotron sources with tailored beamlines for ptychography. Time resolutions of ~1 h will open the way to accurately study the processes in the acceleration period. However, in these cases, radiation damage could be an issue if the total dose is not kept low. Higher time resolution does not necessarily imply higher doses and therefore possibly larger radiation damage. For instance, sparsity techniques could be coupled to PXCT in order to decrease the overall acquisition time for the whole series by as much as 90%, as recently reported[67]. Another approach could be to use machine learning/deep learning for denoising of datasets collected with much less X-ray dose[68]. On the other hand, gamma irradiation of Portland pastes, mortars and concretes is known to produce water radiolysis finally leading to H_2 microbubbles and calcium peroxide, $CaO_2{\cdot}8H_2O$[69]. Therefore, the signatures of these species should be monitored for studies with high X-ray doses. Higher spatial resolution

and shorter acquisition times will allow to thoroughly study the acceleration stage which will be beneficial to rationally design new accelerator admixtures with the final aim of developing low carbon cements with competitive mechanical strengths and durability performances. Moreover, dissolution-precipitation processes with moderate reaction rates take place also in several other fields like geochemistry or biomaterials, which could benefit from the reported investigation.

Methods

Material provenance and initial characterization

Two different types of commercial cement were used: a CEM I 52.5 R (PC-52.5) and a CEM I 42.5 R (PC-42.5) which conform to EN 197–1. The full characterization of these anhydrous materials is performed with X-ray Fluorescence (XRF) and Laboratory X-ray Powder Diffraction (LXRPD) using the Rietveld Method, see Fig. S1 and Tables S1, S2. Moreover, a polycarboxylate ether (PCE) superplasticiser, containing 35 wt% of the active matter, was employed to efficiently fill the very narrow capillaries required for the PXCT nanoimaging study. The characterisation of this PCE has been recently reported[70].

Textural analysis

The textural characterization was carried out in dry conditions. Particle size distribution (PSD) data were measured by laser diffraction in a MasterSizer 3000 equipment (Malvern). Specific surface areas were determined by N_2 adsorption isotherms in ASAP 2420 equipment (Micromeritics, USA). The air permeabilities were measured with the Blaine fineness apparatus (Controls) according to EN 196–6. The density of the samples was measured with a helium Pycnometer (Accupyc II 1320 Pycnometer, Micromeritics). The resulting data are reported in Table S3.

Isothermal calorimetry

The pastes were prepared using the PC-52.5 and PC-42.5 and with w/c mass ratios of 0.40 and 0.50, respectively. For PC-52.5, 0.43 wt% (by weight of cement) of PCE was used. Water and superplasticizer were mixed by magnetic stirring for 1 min. Then, the cement was mixed with the water/suspension and shaken, for 1 min manually and 1 min with a laboratory vortex mixer. Finally, the pastes were introduced into the glass ampoules. The calorimetric data were taken in an eight-channel Thermal Activity Monitor (TAM) instrument. Data were collected for up to 7 days at 25 °C and at 20 °C and for PC-52.5 and PC-42.5, respectively. The first 45 min were required for the thermal stabilization of the system. The employed conditions mimic the ones used for the imaging studies.

Laboratory X-ray Powder Diffraction (LXRPD) and Data Analysis

The same paste prepared for the calorimetry measurement (PC-52.5-w/c = 0.40) was used to fill the capillaries of ~1 mm in diameter. LXRPD measurements were collected on a D8 ADVANCE diffractometer (Bruker AXS) using strictly monochromatic Mo-Kα_1 radiation (λ = 0.7093 Å). This diffractometer is located at SCAI, University of Malaga. The incident beam was formed by a primary monochromator with a focusing mirror and a 2 mm anti-scatter slit. Moreover, 2.5° Soller slits were used for the incident and transmitted beams. An EIGER detector (from DECTRIS, Baden, Switzerland) was used which is optimised for Mo anodes. This was used with an aperture of 4 × 21 degrees, working in VDO mode. Data collection was performed from 3 to 35° (2θ) for 2 h and 10 min. Rietveld quantitative phase analysis was performed with GSAS software.

Laboratory X-ray computed microtomography experiment (Lab-μCT)

Lab-μCT experiments were carried out at ~25 °C for the same capillary used in the LXRPD data collection and scanning the same region with time. Lab-μCT experiment was performed on a SKYSCAN 2214 (Bruker) scanner at SCAI, University of Malaga. Images were obtained using an X-ray tube with a LaB_6 source filament and employing a 0.25 mm Al foil to minimise the beam hardening effect. This source was operated at 55 kV and 130 μA. The CCD3 detector with a physical pixel size of 17.427 μm was set in a middle position with a source-to-detector distance of 315.449 mm and a source-to-sample distance of 9.051 mm which yielded a voxel size of 1.00 μm (binning 2 × 2). Finally, the projections were acquired every 0.22° over 360° with a total of 1637 projections per tomogram and using an exposure time of 1.9 s. This results in an overall recording time of 3.5 h per dataset. Image reconstruction of the CTs was carried out using Bruker NRecon software (version 2.1.0.1) and by applying Gaussian smoothing and beam hardening correction.

Because Lab-μCT and LXRPD data were acquired in the same capillary, but not in the same equipment, the description of the timing is important. Lab-μCT data were collected from 17.5 h until 21.0 h, using cement-water mixing time as the reference. This dataset is labelled as 19 h. Then, the capillary was transfer to the diffractometer, in the same room, and the LXRPD data were taken from 21 h 15 min to 23 h 25 min. This dataset is labelled as 22 h. The data collections at 47 h and 93 h followed the same protocol but it is less important at these hydration ages, as the kinetics are slower.

Synchrotron X-ray computed microtomography experiment (Syn-μCT)

PC-42.5 with a w/c ratio of 0.50 was used to prepare the paste for this experiment and PCE was not required. The paste was manually mixed for 3.5 min and then introduced in a capillary of ~0.7 mm of diameter. Inline propagation-based phase-contrast microtomographic data were acquired at ID19 beamline of the European Synchrotron (ESRF) in Grenoble, France. The measurements were performed at 21.5 °C, temperature of the experimental hutch, using a photon energy of 19 keV. The distance between the sample and the detector was 15 mm. The total time to record a full tomogram was 6 min with 0.05 s exposure time. 6000 projection angles were acquired over a 360 degree tomographic scan. For reconstructions, Paganin phase retrieval of the projections was performed[51]. The resulting voxel size was 0.65 μm. Further experimental details are given in the SI.

Near-field ptychographic X-ray computed tomography (PXCT)

The paste employed for the in situ nanoimaging study was PC-52.5 with a nominal w/c ratio of 0.50 and 0.43 wt% of PCE. The suspension was mixed with a mechanical stirrer at 800 rpm for 3.5 min and then introduced in a glass capillary of 200 μm of nominal diameter. Near-field PXCT data were taken at the cSAXS beamline of the Swiss Light Source (SLS) at the Paul Scherrer Institute (PSI), Villigen, Switzerland. Near-field ptychography[47] is a variant of X-ray ptychography[42,44] in which the sample is scanned across a coherent divergent illumination and magnified images of the sample are recorded on the detector at each scanning position. Ptychographic phase retrieval algorithms are employed to reconstruct the complex transmission function of the specimen, with both absorption and phase, at each angular projection. We then repeat measurements of many projections at different incident angles of the X-rays onto the sample and combine them using standard tomographic reconstruction methods to obtain 3D maps of the electron density and the absorption coefficient of the specimen. In near-field ptychography, if a sufficient number of projections are recorded, the spatial resolution is limited by the magnified pixel size, which is determined by the pixel size of the detector, the distance between the sample and the detector, the divergence of the illumination and the position of the specimen from the point source of the beam, i.e. the focus. We performed our measurements using a high-stability instrument designed for high-resolution PXCT working in air[71,72] and at the hutch temperature of 25 °C, using a photon energy of

8.93 keV. The thickness of the capillary in the imaged region was 160 μm. Therefore, it was scanned with a FOV of 186 μm in order to have more than 10 μm of air outside the capillary, which is required for quantitative phase imaging. The total time to record a full tomogram was between 3 and 4 h, including dead time during the motion of stages in between acquisitions. The voxel size was 186.64 nm. Further experimental details are given in the SI.

Tomographic data analysis

A supervised Machine-Learning (ML) image analysis approach was used to segment the different components of imaged samples, using the IPSDK Explorer software (version 3.2.0.0 for Windows™, Reactiv'IP, Grenoble, France). The plot profiles along the scans electron density/grey value slices and the 3D rendering visualization were done by using Dragonfly software (version 2022.1 for Windows™, Object Research Systems (ORS) Inc., Montreal, Canada). More information about data analysis can be found in the SI.

Data availability

The twelve reconstructed tomograms 'raw' data in tiff format, and the laboratory characterisation data, have been deposited and they can be freely accessed on Zenodo at https://doi.org/10.5281/zenodo.7030107, and used under the Creative Commons Attribution license.

References

1. Habert, G. et al. Environmental impacts and decarbonization strategies in the cement and concrete industries. *Nat. Rev. Earth Environ.* **1**, 559–573 (2020).
2. Monteiro, P. J. M., Miller, S. A. & Horvath, A. Towards sustainable concrete. *Nat. Mater.* **16**, 698–699 (2017).
3. Scrivener, K. L., Ouzia, A., Juilland, P. & Kunhi Mohamed, A. Advances in understanding cement hydration mechanisms. *Cem. Concr. Res.* **124**, 105823 (2019).
4. Ioannidou, K. et al. The crucial effect of early-stage gelation on the mechanical properties of cement hydrates. *Nat. Commun.* **7**, 12106 (2016).
5. Juilland, P., Gallucci, E., Flatt, R. & Scrivener, K. L. Dissolution theory applied to the induction period in alite hydration. *Cem. Concr. Res.* **40**, 831–844 (2010).
6. Ouzia, A. & Scrivener, K. L. The needle model: A new model for the main hydration peak of alite. *Cem. Concr. Res.* **115**, 339–360 (2019).
7. Neubauer, J. et al. Evolution of the particle size distribution of tricalcium silicate during hydration by synchrotron X-ray nanotomography. *Cem. Concr. Res.* **156**, 106769 (2022).
8. Masoero, E., Thomas, J. J. & Jennings, H. M. A reaction zone hypothesis for the effects of particle size and water-to-cement ratio on the early hydration kinetics of C3S. *J. Am. Ceram. Soc.* **97**, 967–975 (2014).
9. Shen, D., Wang, X. & Wu, S. Determining hydration mechanisms for initial fall and main hydration peak in tricalcium silicate hydration using a two-scale hydration simulation model. *Cem. Concr. Res.* **156**, 106763 (2022).
10. Pustovgar, E. et al. Understanding silicate hydration from quantitative analyses of hydrating tricalcium silicates. *Nat. Commun.* **7**, 10952 (2016).
11. Cuesta, A. et al. Multiscale understanding of tricalcium silicate hydration reactions. *Sci. Rep.* **8**, 8544 (2018).
12. Allen, A. J., Thomas, J. J. & Jennings, H. M. Composition and density of nanoscale calcium–silicate–hydrate in cement. *Nat. Mater.* **6**, 311–316 (2007).
13. Juilland, P., Nicoleau, L., Arvidson, R. S. & Gallucci, E. Advances in dissolution understanding and their implications for cement hydration. *RILEM Tech. Lett.* **2**, 90–98 (2017).
14. Kjellsen, K. O. & Lagerblad, B. Microstructure of tricalcium silicate and Portland cement systems at middle periods of hydration-development of Hadley grains. *Cem. Concr. Res.* **37**, 13–20 (2007).
15. Gallucci, E., Mathur, P. & Scrivener, K. Microstructural development of early age hydration shells around cement grains. *Cem. Concr. Res.* **40**, 4–13 (2010).
16. de Matos, P. R. et al. In-situ laboratory X-ray diffraction applied to assess cement hydration. *Cem. Concr. Res.* 106988 https://doi.org/10.1016/j.cemconres.2022.106988 (2022).
17. Aranda, M. A. G. Recent studies of cements and concretes by synchrotron radiation crystallographic and cognate methods. *Crystallogr. Rev.* **22**, 150–196 (2016).
18. Lewis, J. A. et al. Linking void and interphase evolution to electrochemistry in solid-state batteries using operando X-ray tomography. *Nat. Mater.* **20**, 503–510 (2021).
19. Zhang, X. et al. In situ imaging of amorphous intermediates during brucite carbonation in supercritical CO2. *Nat. Mater.* **21**, 345–CO351 (2022).
20. Bullard, J. W. et al. Measurement and modeling needs for microstructure and reactivity of next-generation concrete binders. *Cem. Concr. Compos.* **101**, 24–31 (2019).
21. Monteiro, P. J. M. et al. Advances in characterizing and understanding the microstructure of cementitious materials. *Cem. Concr. Res.* **124**, 105806 (2019).
22. Withers, P. J. et al. X-ray computed tomography. *Nat. Rev. Methods Prim. 2021 11* **1**, 1–21 (2021).
23. Brisard, S., Serdar, M. & Monteiro, P. J. M. Multiscale X-ray tomography of cementitious materials: A review. *Cem. Concr. Res.* **128**, 105824 (2020).
24. Gallucci, E., Scrivener, K. L., Groso, A., Stampanoni, M. & Margaritondo, G. 3D experimental investigation of the microstructure of cement pastes using synchrotron X-ray microtomography (μCT). *Cem. Concr. Res.* **37**, 360–368 (2007).
25. Gastaldi, D. et al. In situ tomographic investigation on the early hydration behaviors of cementing systems. *Constr. Build. Mater.* **29**, 284–290 (2012).
26. Parisatto, M. et al. Examining microstructural evolution of Portland cements by in-situ synchrotron micro-tomography. *J. Mater. Sci.* **50**, 1805–1817 (2015).
27. Hu, Q. et al. Direct measurements of 3d structure, chemistry and mass density during the induction period of C3s hydration. *Cem. Concr. Res.* **89**, 14–26 (2016).
28. Hu, Q. et al. Direct three-dimensional observation of the microstructure and chemistry of C3S hydration. *Cem. Concr. Res.* **88**, 157–169 (2016).
29. Bae, S. et al. In situ soft X-ray spectromicroscopy of early tricalcium silicate hydration. *Mater. (Basel).* **9**, 1–16 (2016).
30. Prade, F. et al. Time resolved X-ray Dark-Field Tomography Revealing Water Transport in a Fresh Cement Sample. *Sci. Rep.* **6**, 29108 (2016).
31. Moradian, M. et al. Direct observation of void evolution during cement hydration. *Mater. Des.* **136**, 137–149 (2017).
32. Geng, G. et al. Synchrotron X-ray nanotomographic and spectromicroscopic study of the tricalcium aluminate hydration in the presence of gypsum. *Cem. Concr. Res.* **111**, 130–137 (2018).
33. Moradian, M. et al. Multi-scale observations of structure and chemical composition changes of portland cement systems during hydration. *Constr. Build. Mater.* **212**, 486–499 (2019).
34. Vigor, J. E., Bernal, S. A., Xiao, X. & Provis, J. L. Automated correction for the movement of suspended particulate in microtomographic data. *Chem. Eng. Sci.* **223**, 115736 (2020).
35. Vigor, J. E., Bernal, S. A., Xiao, X. & Provis, J. L. Time-resolved 3D characterisation of early-age microstructural development of Portland cement. *J. Mater. Sci.* **57**, 4952–4969 (2022).

36. Seiller, J. et al. 4D in situ monitoring of the setting of α plaster using synchrotron X-ray tomography with high spatial and temporal resolution. *Constr. Build. Mater.* **304**, 124632 (2021).
37. Cheikh Sleiman, H., Tengattini, A., Briffaut, M. & Huet, B. & Dal Pont, S. Simultaneous x-ray and neutron 4D tomographic study of drying-driven hydro-mechanical behavior of cement-based materials at moderate temperatures. *Cem. Concr. Res.* **147**, 106503 (2021).
38. Li, X. et al. Direct observation of C3S particle dissolution using fast nano X-ray computed tomography. *Cem. Concr. Res.* **166**, 107097 (2023).
39. Li, X., Hu, Q., Robertson, B., Tyler Ley, M. & Xiao, X. Direct observation of C3S particles greater than 10 μm during early hydration. *Constr. Build. Mater.* **369**, 130548 (2023).
40. Poirier, M. et al. Synchrotron X-ray micro-tomography investigation of the early hydration of blended cements: A case study on CaCl2-accelerated slag-based blended cements. *Constr. Build. Mater.* **321**, 126412 (2022).
41. Dierolf, M. et al. Ptychographic X-ray computed tomography at the nanoscale. *Nature* **467**, 436–439 (2010).
42. Pfeiffer, F. X-ray ptychography. *Nat. Photonics* **12**, 9–17 (2018).
43. Miao, J., Ishikawa, T., Robinson, I. K. & Murnane, M. M. Beyond crystallography: diffractive imaging using coherent x-ray light sources. *Science* **348**, 530–535 (2015).
44. Guizar-Sicairos, M. & Thibault, P. Ptychography: A solution to the phase problem. *Phys. Today* **74**, 42 (2021).
45. Cuesta, A. et al. Chemistry and Mass Density of Aluminum Hydroxide Gel in Eco-Cements by Ptychographic X-ray Computed Tomography. *J. Phys. Chem. C.* **121**, 3044–3054 (2017).
46. Cuesta, A. et al. Quantitative disentanglement of nanocrystalline phases in cement pastes by synchrotron ptychographic X-ray tomography. *IUCrJ* **6**, 473–491 (2019).
47. Stockmar, M. et al. Near-field ptychography: phase retrieval for inline holography using a structured illumination. *Sci. Rep.* **3**, 1927 (2013).
48. Linderoth, O., Wadsö, L. & Jansen, D. Long-term cement hydration studies with isothermal calorimetry. *Cem. Concr. Res.* **141**, 106344 (2021).
49. Taylor, H. F. W. *Cement chemistry*. (Thomas Telford Pub, 1997).
50. Scrivener, K. L., Juilland, P. & Monteiro, P. J. M. Advances in understanding hydration of Portland cement. *Cem. Concr. Res.* **78**, 38–56 (2015).
51. Paganin, D., Mayo, S. C., Gureyev, T. E., Miller, P. R. & Wilkins, S. W. Simultaneous phase and amplitude extraction from a single defocused image of a homogeneous object. *J. Microsc.* **206**, 33–40 (2002).
52. Donnelly, C. et al. Time-resolved imaging of three-dimensional nanoscale magnetization dynamics. *Nat. Nanotechnol.* **15**, 356–360 (2020).
53. van Heel, M. & Schatz, M. Fourier shell correlation threshold criteria. *J. Struct. Biol.* **151**, 250–262 (2005).
54. Diaz, A. et al. Quantitative x-ray phase nanotomography. *Phys. Rev. B* **85**, 020104 (2012).
55. Tang, S. et al. Structure, fractality, mechanics and durability of calcium silicate hydrates. *Fractal Fract.* **5**, 47 (2021).
56. Cuesta, A. et al. Local structure and Ca/Si ratio in C-S-H gels from hydration of blends of tricalcium silicate and silica fume. *Cem. Concr. Res.* **143**, 106405 (2021).
57. Zhu, X. & Richardson, I. G. Morphology-structural change of C-A-S-H gel in blended cements. *Cem. Concr. Res.* **168**, 107156 (2023).
58. Duque-Redondo, E., Bonnaud, P. A. & Manzano, H. A comprehensive review of C-S-H empirical and computational models, their applications, and practical aspects. *Cem. Concr. Res.* **156**, 106784 (2022).
59. Bellmann, F., Sowoidnich, T., Ludwig, H. & Damidot, D. Cement and Concrete Research Dissolution rates during the early hydration of tricalcium silicate. *Cem. Concr. Res.* **72**, 108–116 (2015).
60. Scherer, G. W., Zhang, J. & Thomas, J. J. Nucleation and growth models for hydration of cement. *Cem. Concr. Res.* **42**, 982–993 (2012).
61. Diamond, S. The microstructure of cement paste and concrete–a visual primer. *Cem. Concr. Compos.* **26**, 919–933 (2004).
62. Kjellsen, K. O. & Justnes, H. Revisiting the microstructure of hydrated tricalcium silicate—A comparison to Portland cement. *Cem. Concr. Compos.* **26**, 947–956 (2004).
63. Li, X. & Scrivener, K. L. Cement and Concrete Research Impact of ZnO on C 3 S hydration and C-S-H morphology at early ages. *Cem. Concr. Res.* **154**, 106734 (2022).
64. Xu, Z. et al. Research on cement hydration and hardening with different alkanolamines. *Constr. Build. Mater.* **141**, 296–306 (2017).
65. Lavrov, A., Panduro, E. A. C. & Torsæter, M. Synchrotron Study of Cement Hydration: Towards Computed Tomography Analysis of Interfacial Transition Zone. *Energy Procedia* **114**, 5109–5117 (2017).
66. Da Silva, J. C. et al. Mass Density and Water Content of Saturated Never-Dried Calcium Silicate Hydrates. *Langmuir* **31**, 3779–3783 (2015).
67. Gao, Z. et al. Sparse ab initio x-ray transmission spectrotomography for nanoscopic compositional analysis of functional materials. *Sci. Adv.* **7**, eabf6971 (2021).
68. Hendriksen, A. A. et al. Deep denoising for multi-dimensional synchrotron X-ray tomography without high-quality reference data. *Sci. Rep.* **11**, 11895 (2021).
69. Bouniol, P. & Aspart, A. Disappearance of oxygen in concrete under irradiation: the role of peroxides in radiolysis. *Cem. Concr. Res.* **28**, 1669–1681 (1998).
70. Morales-Cantero, A. et al. C-S-H seeding activation of Portland and Belite Cements: an enlightening in situ synchrotron powder diffraction study. *Cem. Concr. Res.* **161**, 106946 (2022).
71. Holler, M. et al. An instrument for 3D x-ray nano-imaging. *Rev. Sci. Instrum.* **83**, 073703 (2012).
72. Holler, M. et al. X-ray ptychographic computed tomography at 16 nm isotropic 3D resolution. *Sci. Rep.* **4**, 3857 (2014).

Acknowledgements

Financial support from PID2019-104378RJ-I00 research grant, which is co-funded by FEDER, is gratefully acknowledged. SLS is thanked for granting beamtime at cSAXS under proposal 20210147. ESRF is thanked for beamtime at ID19. ToScA (United Kingdom) is gratefully acknowledged for awarding Jim Elliott Award to Shiva Shirani, which supported her stay at ESRF. Dr. Manuel Guizar-Sicairos is thanked for his assistance with the ptychography data processing. I.R.S. is thankful for funding from PTA2019-017513–I.

Author contributions

M.A.G.A. conceived, designed and supervised this study. S.S. and I.S. did initial rheological and laboratory-tomographic studies to fill the 200-micron capillaries. S.S. and A.M.-C. carried out the laboratory characterization. M.A.G.A., S.S., A.C., A.D, P.T., M.H. applied for beamtime at the SLS and designed the PXCT experiment. S.S., A.D., P.T. and M.H. carried out the synchrotron ptychographic experiment. S.S., B.L. and A.R. conducted the synchrotron microtomographic experiment. I.R.S. did the laboratory diffraction and microtomographic experiments. S.S. did all the X-ray imaging data analysis with assistance of M.A.G.A., A.D. and A.C. The machine learning segmentation was carried out by S.S. under E.B.'s supervision. M.A.G.A. wrote the first draft. S.S. prepared all the figures, with help of A.C. for bivariate and Rietveld plots. All authors discussed the results and commented on the manuscript.

Article https://doi.org/10.1038/s41467-023-38380-1

Competing interests
The authors declare no competing interests.

Additional information
Supplementary information The online version contains supplementary material available at https://doi.org/10.1038/s41467-023-38380-1.

Correspondence and requests for materials should be addressed to Miguel A. G. Aranda.

Peer review information *Nature Communications* thanks the anonymous reviewer(s) for their contribution to the peer review of this work. A peer review file is available.

3.5 Article 5 (A#5): Mix and Measure - combining X-ray microtomography and powder diffraction for accurate *in situ* hydrating cement studies

Submitted to *Cement and Concrete Research*

Mix and measure - combining *in situ* X-ray powder diffraction and microtomography for accurate hydrating cement studies

S. Shirani,[1] A. Cuesta,[1] A.G. De la Torre,[1] I. Santacruz,[1] A. Morales-Cantero,[1] I. Koufany,[1] C. Redondo-Soto,[1] I.R. Salcedo,[2] L. León-Reina,[2] M.A.G. Aranda[1,*]

[1]*Departamento de Química Inorgánica, Cristalografía y Mineralogía, Universidad de Málaga, Málaga, 29071, Spain*

[2]*Servicios Centrales de Apoyo a la Investigación, Universidad de Málaga, 29071 Málaga, Spain*

** email: g_aranda@uma.es*

Abstract:

It is reported an innovative methodology based on *in situ* MoKα_1 laboratory X-ray powder diffraction (LXRPD) and microtomography (μCT) avoiding any sample conditioning. The pastes are injected in 2.0 mm capillaries and the extremes are just sealed. The measurements take place in the same region of the hydrating paste. Thick capillaries are key to avoiding self-desiccation. This approach has been tested with a PC 42.5 R paste having w/c=0.50. μCT data were collected at 12 hours and 1, 3, 7 and 79 days. LXRPD data were acquired at 1, 3, 7 and 77 days. In this proof-of-principle research, the same paste was also cured *ex situ*. Portlandite contents obtained by thermal analysis, *ex situ* powder diffraction, *in situ* mass balance calculation and *in situ* powder diffraction were 13.8, 13.1, 13.1 and 12.5 wt%, respectively. From the μCT study, the grey value histogram evolution with time showed a crossing point which allowed us to distinguish (appearing) hydrated products from (dissolving) unhydrated cement particles. Segmentations were carried out by global thresholding and supervised Machine Learning. The comparison of the segmented results for the unhydrated cement fraction and the Rietveld quantitative phase analysis outputs gave an agreement of 2%. The potential of this methodology to deal with more complex binders is also presented.

Keywords: Portland cement hydration; Rietveld analysis; microCT; 4D X-ray imaging

1. Introduction

Understanding of the hydration of Portland cements (PC), at the different length scales, is puzzling because of the interaction of many intervening parameters [1,2]. PC are multiphase materials with variable (i) elemental compositions, (ii) phase contents, (iii) textural properties (particle size distributions and specific surface areas of the different components), and an increasing trend of using inorganic additions and organic admixtures. Moreover, the hydration processes occur under variable conditions, including but not restricted to, (i) water-to-cement mass ratio (w/c), (ii) temperature, (iii) pressure and (iv) alkalinity. Therefore, a range of analytical techniques, as accurate as possible, are needed to understand the hydration reactions/processes. There are many techniques used for studying cement hydration and the most common ones were thoroughly treated in a book published in 2016 [3] which is the standard in the field.

Cement notation is used hereby. On the one hand, PCs have more than five crystalline components before water mixing: $C\underline{S}H_2$ (and/or other calcium sulfates), C_3S, C_3A, C_4AF, C_2S, ordered by their hydration kinetics in commercial PCs. On the other hand, and after partial dissolution, transport of mass and supersaturation, interacting precipitation reactions take place over existing surfaces, i.e. heterogeneous nucleation, and within the capillary porosity, i.e. homogeneous nucleation. In this hydrating environment, more than four hydration products are formed: crystalline ettringite (AFt), nanocrystalline calcium silicate hydrate (C-S-H gel), crystalline portlandite (CH) and amorphous iron-siliceous hydrogarnet. Other hydrates can crystallize like AFm-type (sulfate, hemicarbonate, monocarbonate) depending upon the sulfate balance, etc. In PC blends containing supplementary cementitious materials (SCMs), there are even more hydrates but this is not the focus of the present investigation.

With due precaution, it can be stated that the faithful quantification of the time-dependent components for neat PC hydration is well-established [3]. This is still not the case for PC-SCMs blends where the degree of hydration of the SCMs is still not routinely obtained accurately by easy-to-automatize techniques. Moreover, the accurate analysis of the unaltered microstructures, at the different length scales, is still not well-established neither in PCs nor in PC-SCMs binders. This investigation focuses on the *in situ* analysis of PC hydration by combining two laboratory X-ray techniques, X-ray powder diffraction and X-ray microtomography (μCT), to contribute to help fill this scientific gap. It is noted that μCT was not covered in [3].

On the one hand and after decades of research, the quantitative phase analysis of crystalline components in hydrating PCs by laboratory X-ray powder diffraction (LXRPD) is well-established [4–8]. Moreover, the overall amorphous content may be obtained by using external [9] or internal [10] standard methodologies. These approaches have advantages and disadvantages, but this analysis is out of the scope of the present work. On the other hand and after about fifteen years of research, the quantitative analysis of the hydrating components and microstructures by μCT [11] is still challenging. The uses of μCT in cements have been reviewed [12–17]. The readers are referred to these works to find out the features that can be followed and, in some cases, quantified.

This work is part of a long-term endeavour devoted to better understanding the development of the components and microstructures in cementitious materials by using techniques that do not require sample conditioning and where the data analysis can be automatized. To that end and in an initial work, laboratory X-ray powder diffraction and X-ray imaging were employed to analyse the same PC paste-filled capillary [18]. However, this initial work did not carry out any *in situ* hydration study. The PC hydration at early ages has been very recently *in situ* investigated by ptychographic synchrotron nanotomography [19]. The spatial dissolution rate of alite was reported and the etch-pit growth rate was also estimated. However, the access to this technique is not straightforward and the capillaries must currently have a maximum diameter of 200 μm to access nanoimaging spatial resolution. Here, we report the combined use of LXRPD and μCT for *in situ* studying the hydration of a PC 42.5 R paste. A small fraction of this work has been accepted as a proceeding of the 16th International Congress on the Chemistry of Cement, 2023 [20]. Additional samples have been (*ex situ*) prepared here by well-established methodologies to assay the accuracy of the obtained results. These additional samples are investigated by thermal analysis, LXRPD and calorimetry. It is demonstrated that the proposed *in situ* methodology is accurate. This is a first, necessary, step before extending this methodology to more challenging hydrating binders like PC-SCMs blends. The final aim is to be able to determine the SCMs degree of reaction from this combination of techniques.

2. Materials and Methods

2.1. The Portland cement and its initial characterization.

A commercial Portland Cement type CEM I 42.5 R, conforming to EN 197–1, has been used. Its elemental analysis by X-ray fluorescence was: 61.6(4), 19.9(3), 4.56(9), 3.3(1), 3.9(1), 1.5(1), 1.14(9), 0.24(5) and 0.4 wt% for CaO, SiO_2, Al_2O_3, Fe_2O_3, SO_3, MgO, K_2O, Na_2O and all other minor elements, respectively. The mineralogical analysis determined by Rietveld quantitative phase analysis and thermal analysis was: 58.3, 12.9, 6.7, 10.3, 3.1, 2.2, 5.3 and 1.2 wt% for C_3S, C_2S, C_3A, C_4AF, $C\underline{S}H_{0.5}$, $C\underline{S}H_2$, $C\underline{C}$ and all other minors, respectively. The textural properties were also measured. The air permeability, i.e. Blaine, value was 3750 cm^2/g. The specific surface area, measured by nitrogen isotherm, and the density determined by He pycnometry, were 1.9 m^2g^{-1} and 3.09 gcm^{-3}. Fig. 1 displays its particle size distribution as measured by laser diffraction in a Mastersizer 3000 device (Malvern Panalytical) by employing the Aero S dry chamber. $D_{v,10}$, $D_{v,50}$ and $D_{v,90}$ values were 2.0, 17.6 and 59.1 μm, respectively.

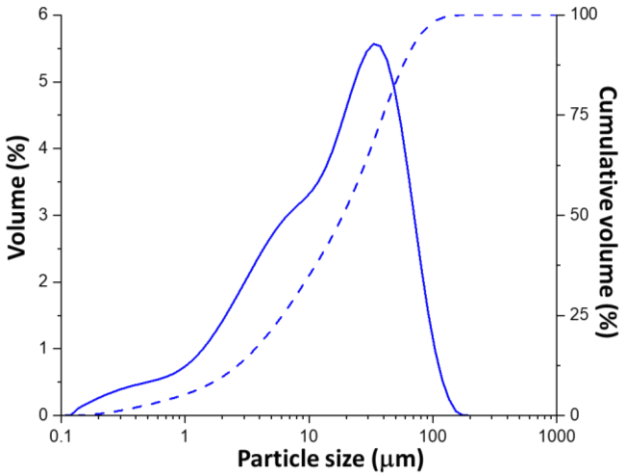

Figure 1. Particle size distribution (left – relative volume percentages, right – cumulative volume) determined by laser diffraction for the anhydrous PC.

2.2. Paste preparation.

The pastes, for all the employed techniques, were prepared in exactly the same way. 50 g of PC and 25 g of twice boiled distilled water were mixed, w/c=0.50, by mechanical stirring at 800 rpm for 90 s. After a resting period of 30 s, the same stirring step was repeated. The resulting homogeneous paste was used for filling three type of holders. A) For the *in situ* LXRPD and μCT studies, the paste was injected into a glass tube with a nominal diameter of 2.0 mm using a syringe. Then, both ends were sealed with ultraviolet (UV) curing adhesive to avoid any water loss and carbonation. B) For the *ex situ* diffraction and thermal studies, the paste was poured into polytetrafluoroethylene (PTFE) cylindrical moulds (length: 35 mm, diameter: 10 mm) sealed and rotated at 16 rpm for 24 hours at 25°C as previously reported [21,22]. After 1 day, the cylinders were demoulded and stored at 25°C for 6 additional days within (1) a plastic bottle filled with $Ca(OH)_2$-saturated water, and (2) a sealed plastic bag. The bottle was tightly closed to prevent carbonation and the volume of water was kept to a minimum to minimise any leaching. The samples were prepared just by gentle grinding in an agate mortar and the powder diffraction and thermal analyses were performed in those powders. C) For the calorimetric study, the paste was poured into the glass ampoule of the calorimeter. Table 1 lists the techniques and the samples used in this study.

2.3. Isothermal calorimetry.

This study was carried out by employing an eight-channel Thermal Activity Monitor (TAM) equipment. The data were acquired at 25°C for a week. The first 45 minutes were not collected as this time was needed for the thermal stabilisation of the equipment. The selected temperature was dictated by the temperature of the X-ray laboratory room where the *in situ* studies were carried out.

2.4. Thermal analysis.

Thermogravimetric (TGA) traces for the two *ex situ* prepared samples, see Table 1, were recorded in an SDT-Q600 analyser from TA instruments (New Castle, DE, USA). The temperature was increased from RT to 1000°C, with a 10 $^oCmin^{-1}$ rate. The powders were loaded in open platinum crucibles and the experiment was carried out under synthetic air flow.

Table 1

Analytical techniques and paste preparation, always w/c=0.50, and holders employed in this study. The abbreviations for fabricated pastes are also detailed.

technique	paste	*procedure*	*age*
μCT	within 2 mm glass capillary	*in situ*	12h, 1d, 3d, 7d, 79d
Mo-LXRPD	within 2 mm glass capillary abbreviation: **insitu-paste**	*in situ*	1d (27.5h), 3d, 7d, 77d
Calorimetry	within glass ampoule	*in situ*	continuous for 1 week
Mo-LXRPD, TA	Cylindrical paste cured in a sealed bag; abbreviation: **s.b.-paste**	*ex situ*	7d
Mo-LXRPD, TA	Cylindrical paste cured within CH-saturated water; abbreviation: **CH-paste**	*ex situ*	7d

2.5. Laboratory X-ray powder diffraction (LXRPD).

The X-ray powder diffraction study of the pastes was carried out by using strictly monochromatic Mo-Kα_1 radiation (λ=0.7093 Å) on a D8 ADVANCE (Bruker AXS) diffractometer at SCAI, University of Malaga (UMA), Spain. The tube worked at 50 kV and 50 mA. The optical setup in both studies (*in situ* and *ex situ*) consisted of a primary monochromator, a focusing mirror, 2 mm anti-scattering slit and 2.5 Soller slits for the incident and transmitted beams. The X-ray detector was an EIGER from DECTRIS, Baden, Switzerland, optimised for Mo radiation, and operated with an aperture of 7×21 degrees. All powder patterns have been taken in transmission configuration, which minimises preferred orientation, with rotating samples (10 rpm), which maximises the random arrangement of the particles within the beam.

For the *ex situ* studies, the pastes were loaded between two Kapton foils, without pressing. The patterns were collected between 3 to 40° (2θ) counting for 101 min. The detector worked in VDO mode. For the *in situ* study, the paste within the glass capillary was mounted in a goniometer head, see Fig. 2, for alignment. The patterns were collected between 1 to 38° (2θ) counting for 188 min. The detector worked in NOUT mode. The *in situ* powder diffraction patterns were collected just after the μCT data acquisition. Moreover, because in this study it is crucial to easily exchange between LXRPD and μCT, an additional piece has been designed which allowed using of a similar setup for the μCT to be able to scan the same volume of the capillary with time. This brass holder, which allows precise vertical positioning of the glass tube in the μCT, is displayed in Fig. 3. The powder patterns were taken at the ages indicated in Table 1.

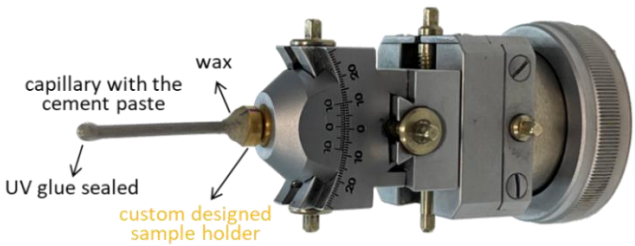

Figure 2. LXRPD setup for the *in situ* paste data collection.

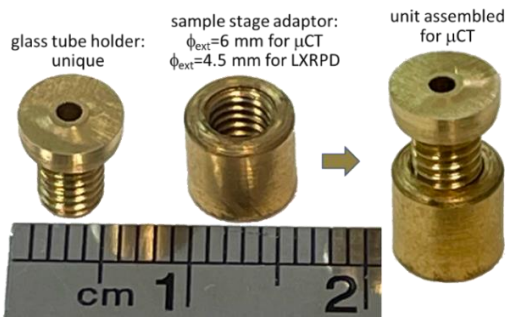

Figure 3. Custom designed sample holder for the *in situ* capillary alignment to scan the same volume with time.

The LXRPD data analysis was carried out by the Rietveld method. This was done by using the GSAS software [23] with an asymmetry-corrected pseudo-Voigt peak shape function [24,25]. The optimised overall parameters were: background coefficients, zero-shift error, phase scale factors, unit cell parameters, peak shape

parameters, and preferred orientation coefficient if needed. The crystal structures used are described elsewhere [26,27].

2.6. Laboratory X-ray computed microtomography (µCT).

The µCT datasets were acquired on a SKYSCAN 2214 scanner from Bruker at SCAI in the University of Malaga. Scans were obtained with an X-ray tube using a LaB_6 source (operated at 55 kV and 130 mA) and employing a 0.25 mm Al foil to reduce beam hardening. After careful sample positioning and alignment, the capillary was rotated 360° during data acquisition. Images were taken every 0.2º, i.e. 1801 projections, with an exposure time of 1.9 s resulting in an overall recording time of 225 min per scan. The geometrical settings were a sample-to-source distance of 9.953 mm and a sample-to-detector distance of 305.496 mm, see Fig.4. The CCD detector has a (physical) pixel size of 17.4 µm (binning 2×2). This pixel size and binning, together with the geometric setting, resulted in a voxel size of 1.1 µm. In these conditions, the field of view was 2.2 mm horizontal and 1.5 mm vertical.

The images were reconstructed using a cylindrical VOI (volume of interest) of 2.0×1.1 mm (H×V) using the software NRecon (version 2.1.0.1, Bruker, Billerica, Massachusetts, United States). The reconstruction details were: (a) beam hardening correction (%)=30; (b) smoothing=1 with smoothing kernel=2 (Gaussian), (c) minimum for CS (cross section) to image conversion=-0.04 and (d) maximum for CS to image conversion=0.7. Each reconstructed dataset has a 7 GB size (as 16-bit data).

Data analysis was carried out in two ways. Firstly, Dragonfly software (version 2022.1 for Windows™, Object Research Systems (ORS) Inc., Montreal, Canada) was employed to segment the data based on global thresholding. The intervals were determined as described in the results section. Secondly, IPSDK Explorer program (version 3.2.0.0 for Windows™, Reactiv'IP, Grenoble, France), was used for a supervised machine learning (ML) image analysis [19]. 4D rendered volumes, showing the results of both approaches, were visualised with Dragonfly.

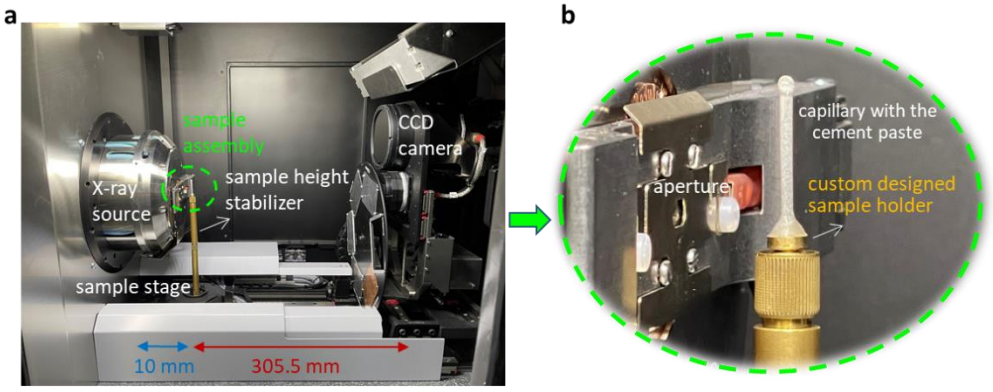

Figure 4. Laboratory µCT setup for the *in situ* paste data collection. (a) General view. (b) Capillary detailed view.

3. Results and discussion.

The main objective of this work is to evaluate the PC paste hydration without sample conditioning and to evaluate the accuracy of the resulting analyses. In order to do so, in addition to the central *in situ* study, well-established *ex situ* studies have been also carried out to have reference values. With this approach, additional values can be obtained, like the key portlandite content.

3.1. *Ex situ* thermal analysis study. Fig. 5 displays the thermal traces for the two pastes hydrated in a portlandite saturated solution and in a sealed bag. The employed PC has 5.3 wt% of calcite that corresponds to 3.53 wt% in the resulting pastes. Because calcite losses 43.9% mass on heating due to the CO_2 release, the expected mass loss due to the initial calcite content is 1.55%. The mass losses in the calcite temperature decomposition interval were 1.87% and 1.57% for the s.b.-paste and CH-paste, respectively. Therefore, carbonation of the pastes is not significant. Moreover, the total expected weight loss is derived from the added water 33.33% and from the initial anhydrous cement components (mainly calcite and gypsum). The calculated, i.e. expected, overall weight loss is 35.32 wt%. The measured weight losses are 35.1 and 35.2% for s.b.-paste and CH-paste, respectively. This indicates: (a) very minor water loss during the gentle grinding prior to the thermal analysis, and (b) a very robust and accurate experimental procedure.

If carbonation is negligible and the experimental procedure is robust and accurate, it is possible to trust in the direct portlandite contents derived from the weight losses in the portlandite decomposition temperature interval, see Fig. 5. The measured weight losses are 3.5 and 3.2% for s.b.-paste and CH-paste, respectively. Thus, the portlandite contents are 14.5 and 13.1 wt% for s.b.-paste and CH-paste, respectively, referred to 100 g of cement paste. The average value, 13.8 wt% of CH at 7 days of hydration, will be the reference for the *ex situ* and *in situ* quantitative phase analyses derived from the powder diffraction data.

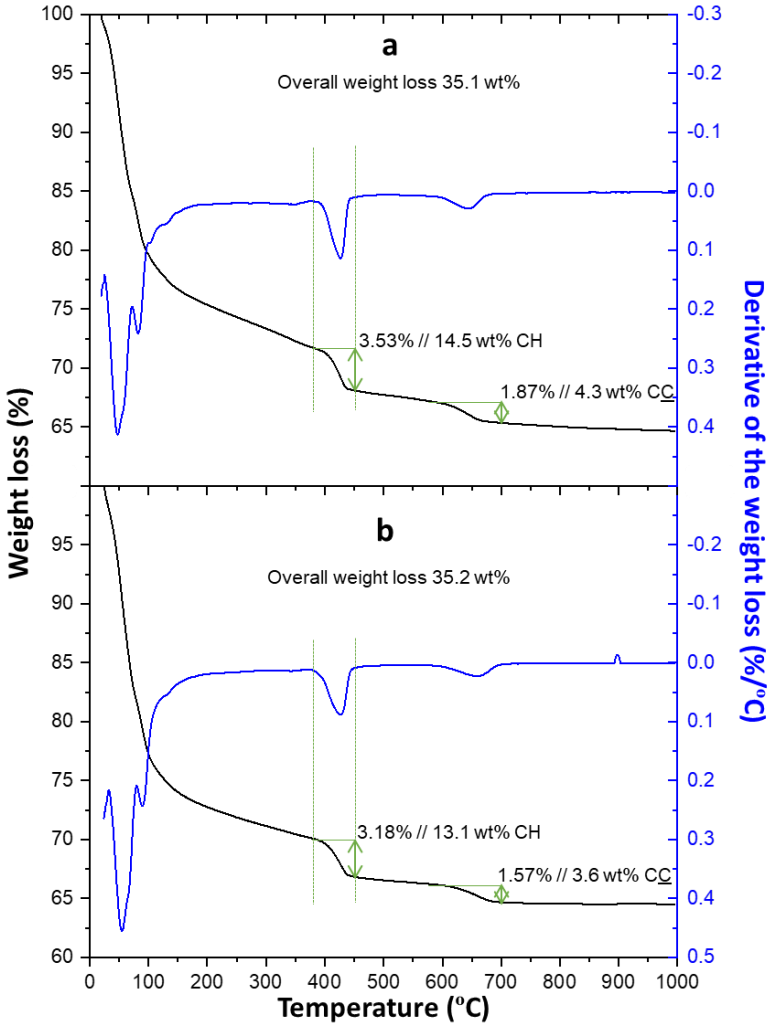

Figure 5. Thermal analysis traces for the studied pastes. **(a)** PC-paste hydrated for 1 day within the PTFE mould and then 6 additional days within the sealed bag (s.b.-paste). **(b)** PC-paste hydrated for 1 day within the PTFE mould and then 6 additional days within a CH-saturated solution (CH-paste).

3.2. *Ex situ* laboratory X-ray powder diffraction study.

The MoKα_1 powder patterns were analysed by the Rietveld method as detailed above. The Rietveld quantitative phase analysis (RQPA) outputs, direct results, are referred to 100% of crystalline phases and they are given in Table 2 and the fits are displayed in Fig. 6. These numbers are quite similar, for the two sample hydration conditions, showing the robustness of the overall employed methodology (i.e. experimental and data analysis). Moreover, and as expected, the reactivities are slightly larger when cured under CH-saturated water. However, the reported numbers do not consider the free water or any amorphous content including the C-S-H amount. In order to make comparisons, these values should be referred to a constant basis. The most used bases in cement studies are 100 g of anhydrous cement or 100 g of cement paste. Our research group always refers the results to 100 g of cement paste for direct comparison to any other cement paste measurement including the thermal analysis outputs. Of course, when referred to a constant basis, the calculation of the degree of hydration of every phase is straightforward. Here, mass balance calculations have been carried out to refer the results to 100 g of cement paste where some assumptions are carried out in order to estimate the amount of amorphous phases: (a) amorphous C-S-H gel is formed according to the hydration of C_3S following reaction (1) [28]; (b) belite hydration is negligible in the first week, and hence it does not produce further C-S-H gel;

(c) ferrite in the presence of alite is assumed to hydrate to give amorphous iron-siliceous hydrogarnet (Fe-Si-Hg) according to reaction (2) [29–31]**,** where all aluminium is incorporated in the Fe-Si-Hg amorphous component; (d) the formation of any amorphous AFm type phase is not considered; and (e) the amount of free water is computed by removing the water content of the hydrated phases (crystalline and amorphous) from the initial water content, 33.33 g in 100 g of cement paste.

$$Ca_3SiO_5 + 5.2H_2O \rightarrow 1.2Ca(OH)_2 + (CaO)_{1.8}SiO_2(H_2O)_{4.0} \quad (1)$$

$$Ca_4Al_2Fe_2O_{10} + 1.68Ca_3SiO_5 + 11.68H_2O \rightarrow 2Ca_3FeAl(SiO_4)_{0.84}(OH)_{8.64} + 3.04Ca(OH)_2 \quad (2)$$

Table 2

Direct *ex situ* RQPA results (referred to 100% of crystalline phases) for the two studied PC pastes, w/c=0.50, expressed in wt%. Hc stands for hemicarboaluminate AFm phase.

Phases	CH-paste	s.b.-paste
C_3S	9.6	12.0
C_2S	15.6	16.5
C_3A	0.8	0.7
C_4AF	10.1	10.0
$C\underline{C}$	9.3	8.9
others	0.9	1.0
AFt	24.8	22.9
CH	28.2	27.2
Hc	0.8	0.9

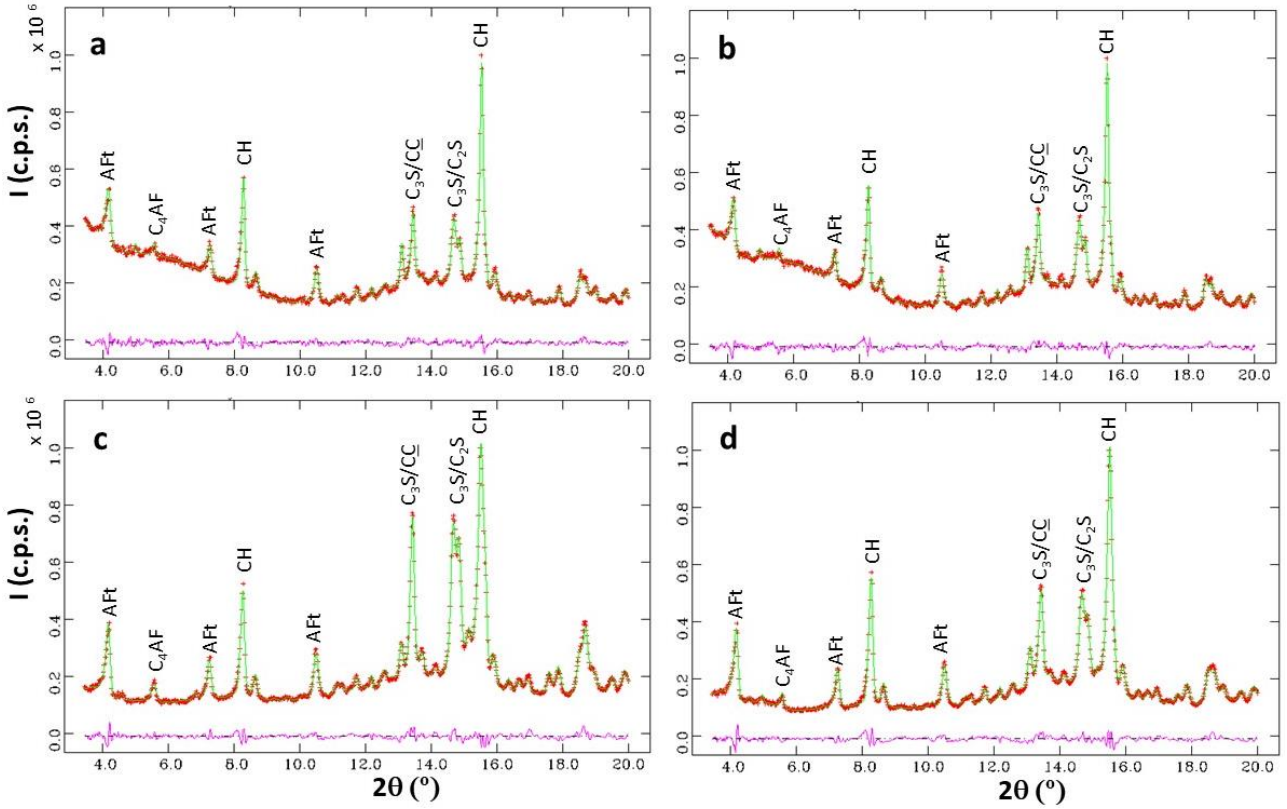

Figure 6. Mo-Kα_1 (λ=0.71 Å) Rietveld plots for **(a)** CH-paste hydrated for 7 days; **(b)** s.b.-paste hydrated for 7 days, **(c)** insitu-paste hydrated for 1 days; and **(d)** insitu-paste hydrated for 7 days.

Table 3 displays the RQPA results referred to 100 g of cement paste. The data at mixing correspond to the analysis of the anhydrous cement, reported in the experimental section, expressed in 100 g of cement paste containing 33.33 wt% of water, i.e. w/c=0.50. For the CH-paste and s.b.-paste, the amorphous phases are calculated according to the reactions given above. The assumptions seem to be close to correct as the resulting portlandite contents at 7 days of hydration are 13.2 and 12.9 wt% for CH-paste and s.b.-paste, respectively. These values agree relatively well with the values obtained from the thermal analysis study: 13.1 and 14.5

wt%, respectively. Moreover, the portlandite contents can be calculated from the reactivities of C_3S and C_4AF given in equations (1) and (2). The calculated CH amounts are 13.72 and 13.26 wt% for CH-paste and s.b.-paste, respectively. The good agreement between the portlandite content from these three approaches, (i) thermal analysis, (ii) measured RQPA, and (iii) calculated amount based on the clinker phase reactivities, shows the accuracy in this study and provides a reference value of the portlandite content at 7 days for the *in situ* study detailed below. The derived degree of hydration (DoH) is totally in line with the known phase reactivities [1,2]. It is noted that neither the internal standard nor the external standard approaches have been used here to determine the overall amorphous phase content. Here, mass balance calculations are employed to estimate the contents of the main amorphous phases based on hydration reactions.

Table 3

Ex situ and *in situ* RQPA results for PC 42.5 R pastes, w/c=0.50, expressed in wt% and referred to 100 g of cement paste. The calculated contents (for the amorphous phases) are given in italics. The values of the factor needed to refer the crystalline contents (referred to 100% of crystalline material) to 100 g of cement paste are also given in bold and italics. The degree of hydration (DoH) of selected phases are also listed. Mc stands for monocarboaluminate (AFm type phase).

	insitu-paste					**CH-paste**	**s.b.-paste**
Phases[#]	**t_0**	**1d**	**3d**	**7d**	**77d**	**7d**	**7d**
C_3S	38.9	15.3	7.5	6.2	4.1	4.5	5.7
C_2S	8.6	8.2	8.5	8.1	7.4	7.3	7.9
C_3A	4.5	2.1	1.0	0.5	0.3	0.4	0.3
C_4AF	6.9	6.2	4.6	4.4	3.7	4.7	4.8
C$\underline{C}$	3.5	4.7	5.1	4.8	5.0	4.3	4.2
others	4.3	0.5	0.3	0.4	0.4	0.4	0.5
H_2O	33.3	*19.1*	*15.0*	*13.9*	*12.5*	*12.4*	*14.1*
AFt	-	9.0	10.2	10.7	11.0	11.6	10.9
CH	-	9.0	11.7	12.5	13.3	13.2	12.9
C-S-H	-	*24.7*	*32.1*	*34.0*	*36.1*	*37.0*	*34.5*
Fe-Si-Hg		*1.2*	*4.1*	*4.3*	*5.6*	*3.8*	*3.9*
Hc	-	-	0.2	0.2	0.1	0.4	0.4
Mc	-	-	-	-	0.6	-	-
Factor	***0.667***	***0.549***	***0.489***	***0.478***	***0.458***	***0.468***	***0.476***
C_3S-DoH	-	61	81	84	89	88	85
C_3A-DoH	-	52	78	89	94	92	93
C_4AF-DoH	-	10	34	36	47	31	31

3.3. *In situ* laboratory X-ray powder diffraction study.

It is noted that the same PC paste has been analysed by *in situ* LXRPD and μCT. This reduces the variability in the studies as PCs are heterogeneous materials. The LXRPD data were analysed by the Rietveld method and the fits at 1 and 7 days, as examples, are also displayed in Fig. 6. The RQPA direct results, referred to 100 wt% of crystalline content, are given in Table 4. The data shown in Table 4 indicate that C_3S keeps reacting for up to 77 days. This is expected but previous results from our research group evidenced that PC hydration stops, for some pastes, as early as one week in capillaries of 1 mm or thinner [32]. This observation was variable because the water availability depends upon the initial w/c ratio but also upon the C_3S content and the amount of AFt formed at early ages. This behaviour was very likely due to self-drying but a thorough investigation to fully understand that feature has not been attempted. This research focuses on developing a robust and easy experimental method yielding accurate results. Hence, thick capillaries, 2 mm of diameter, have been employed in spite that this yields (slightly) poorer resolution in the LXRPD and μCT data. In any case, Table 4 also shows the *in situ* results for the same PC paste but within a capillary of 1.5 mm of nominal diameter. It is clear that the hydration reactions have (slightly) slowed down already at 7 days. The C_3S content is larger and chiefly, the CH content is lower.

The *in situ* RQPA direct results, listed in Table 4, have been referred to 100 g of cement paste and the values were reported in Table 3, together with the results from the *ex situ* LXRPD study for easy comparison. The

previously reported reactions have been again considered to estimate the contents for the non-crystalline phases: C-S-H gel and Fe-Si-Hg. Moreover, and as indicated above, the free water content is estimated by the subtraction of the water contained in all (measured and calculated) hydrates from the added nominal amount of water. Several observations/conclusions can be drawn from the *in situ* RQPA data reported in Table 3: (I) The experimental method is robust, and the data analysis seems to be accurate as the determined portlandite content at 7 days, i.e. 12.5 wt%, agrees very well with the data reported above for the same paste cured in different conditions. Moreover, mass balance calculations based on the reacted amounts of C_4AF and C_3S yield 13.1 wt%. (II) The ettringite content keeps growing up to 77 days without any signature of decrease at later ages, which is in line with the high SO_3 content of the employed PC, i.e. 3.9 wt% (2.6 wt% referred to 100 g of cement paste). It is noted that in many cases inaccurate AFt contents are reported due to the employed hydration arresting procedure(s) [33–36]. The maximum amount of AFt, if all sulfates are incorporated within ettringite, would be 13.6 wt%. This value compares well with the measured one at 7 days, i.e. 10.7 wt%, as a fraction of the sulfates is incorporated/adsorbed in other phases, mainly amorphous ones like C-S-H gel and Fe-Si-Hg. (III) As expected, the obtained contents for the different components at 7 days in the *in situ* study are slightly more similar to the 'sealed bag' results than to the 'CH cured' ones. See for instance the C_3S and free water contents in Table 3. (IV) A minor carbonation is measured in the first analysis and subsequently, no further carbonation is observed. (V) The renormalization factor to refer the contents to 100 g of cement paste, see Table 3, always decreases as the amount of amorphous phases invariably increases. This is the case in the hydration on neat PCs but this is not the case in the hydration of calcium sulfoaluminate cements but the extension of this methodology to those cements will be the subject of a forthcoming publication. Moreover, the evolution of total amorphous phases in PC-SCMs is at the core of a current investigation. (VI) Finally, it is not ruled out that the *in situ* kinetics reported here are slightly slowed down at late ages due to partial self-desiccation. However, increasing the size of the capillary beyond 2 mm is currently judged to be unsatisfactory as the poorer spatial resolution in μCT and the larger peak overlapping in LXRPD which would yield less accurate results.

Table 4

Direct *in situ* RQPA results (referred to 100% of crystalline phases) for the PC paste, w/c=0.50 within a 2 mm capillary, expressed in wt%. Data at 7 days for the same PC paste but filled within a capillary of 1.5 mm of diameter are also given in italics.

Phases	**1d**	**3d**	**7d**	***7d (ϕ=1.5 mm)***	**77d**
C_3S	27.8	15.3	13.0	*14.1*	9.0
C_2S	14.9	17.3	17.0	*15.7*	16.1
C_3A	3.9	2.0	1.0	*1.4*	0.6
C_4AF	11.2	9.3	9.2	*9.6*	8.0
C$\underline{C}$	8.6	10.4	10.0	*11.0*	10.9
others	0.9	0.6	0.8	*0.8*	0.8
AFt	16.3	20.9	22.3	*22.9*	24.0
CH	16.3	23.9	26.2	*23.8*	29.0
Hc	-	0.3	0.5	*0.5*	0.3
Mc	-	-	-	-	1.2

It is remarked here that avoiding carbonation and attaining robust results for AFt and CH are very useful outputs themselves, not to mention the combination with μCT results, see just below. Moreover, the addition of an internal standard is not needed for the reported methodology. The addition of a standard, with a small particle size to have random particle orientation, could affect the kinetics of the PC hydration reactions.

3.4. *In situ* laboratory X-ray computed microtomographic study.

μCT directly shows the dissolution of anhydrous phases, if there is enough contrast and spatial resolution. This is independent of the amorphous or crystalline nature of the imaged particles. Therefore, it is very complementary to LXRPD which is blind to the amorphous phase(s). Moreover, for *in situ* studies there is a strong constraint in the μCT data analysis as the particles/volumes of the anhydrous phases can only decrease. However, μCT is blind to the particles smaller than the true spatial resolution of the measurements. In other words, if the spatial resolution of the measurements is 2.5 μm, the hydration of the particles with smaller spatial resolution cannot be directly followed. For decreasing the variability in the obtained results, the reported

methodology proposes that the same region in the acquired µCT scans (i.e. data from exactly the same volume) is used for data analysis, including segmentation. To illustrate this, the same horizontal view of the cylindrical capillary paste studied at 12 hours and 1, 3, 7, and 79 days of hydration is shown in Fig. 7. The top row displays the full orthoslice and a magnified view of the same region is displayed in the bottom row. The preferential dissolution of the smallest cement grains at early ages (brightest particles) is readily visible as well as the paste densification. This second feature is evident from the evolution of the grey regions with time.

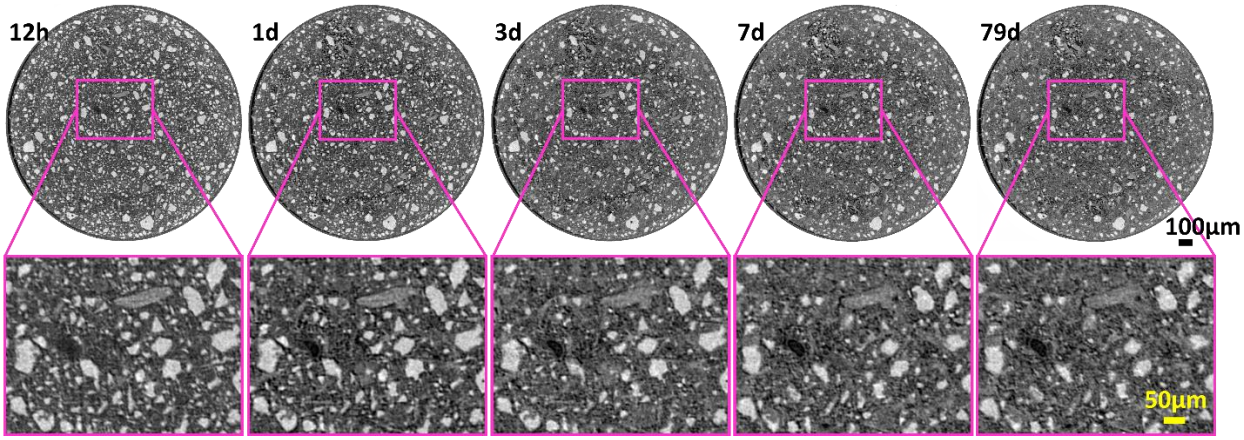

Figure 7. µCT orthoslices at the studied hydration ages. (Top row) full data evidencing the enhanced reactivity of small particles. (Bottom row) Same enlarged view to follow up the paste changes with hydration time.

Four types of regions can be observed in this type of laboratory study, which have different enough linear attenuation coefficients (LAC), and they are highlighted in Fig. 8. Firstly, the darkest regions are porosity, i.e. water and air. This X-ray imaging modality cannot distinguish air from water. Secondly, the darkest-grey volumes are labelled as low-density hydrated products (ld-HP) and these are the regions with lower grey-values. ld-HP should correspond mainly to C-S-H gel and AFt. Thirdly, the whitish-grey regions have higher LAC values and they are labelled as high-density hydrated products (hd-HP). These volumes should mainly correspond to CH, with a contribution of high-density C-S-H. Fourthly, unhydrated cement particles (UCP) are the white particles and they correspond to C_2S, C_3S, C_4AF and any remaining C_3A.

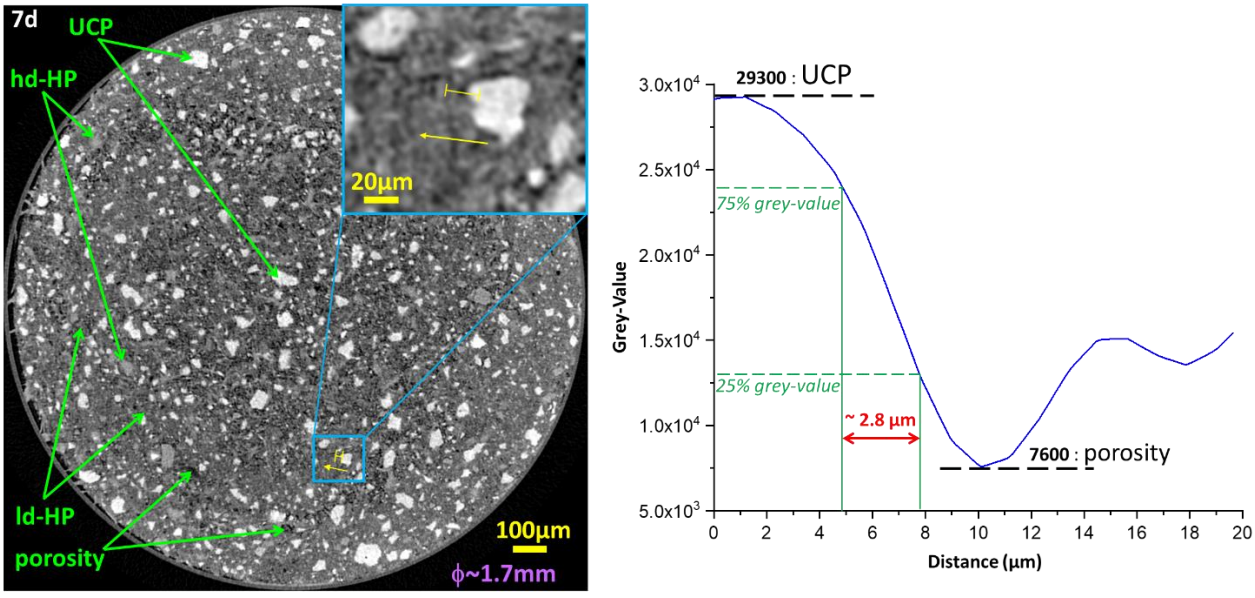

Figure 8. µCT orthoslice where the different components that can be visualized are highlighted: porosity, low-density hydrated products (ld-HP), high-density hydrated products (hd-HP) and unhydrated cement particles (UCP). The spatial resolution can be estimated from the line plot shown in the left panel (yellow line) and the corresponding grey-value profile shown in the right panel, see the text for details.

Pixel size is related, but it does not equal, to the spatial resolution in the µCTs. There is not a universal approach to measure the resolution in a given tomogram. Here, the edge sharpness across selected interfaces has been

used to characterise the spatial resolution. ISO/TS 24597 defines the Gaussian radius of the point spread function of the images as the resolution, which is the change between 25%–75% grey value across the interfaces [19,37,38]. This approach, applied to the interface of the capillary outer wall [19], gave 2.3(6) µm from 10 measurements. This type of plot, for a pore of the paste, is shown in the right panel of Fig. 8. The derived spatial resolution is similar, ~2.8 µm. This value for the resolution is in line with previous investigations where it was reported that spatial resolution is generally 2-3 times poorer than the voxel size.

A first semiquantitative study can be carried out by inspecting the time evolution of the grey-value histograms for exactly the same hydrating volume, see Fig. 9. Several features were observed which deserve discussion: (I) The employed experimental conditions allow the separation of the unhydrated cement particles (UCP) from the hydrated products (HP). However, this does not preclude the existence of partial volume effects. This is unavoidable in cement binders where the size of many particles is smaller than the spatial resolution of the measurements [39]. (II) As expected, the amount of UCP decreases with time and the amount of HP increases, see red arrows. Moreover, it is worth noting that the number of voxels at ~22000 grey-value (i.e. right-tail of the HP peak) decreases with time which is a firm evidence that this is mainly due to UCP. (III) There is a constant crossing point at ~20500 grey-value, see black arrow in Fig. 9. From the time evolution, it is clear that particles with grey values above this number are mainly UCP and particles with grey values below this number are mainly HP. (IV) Densification of HP is evident as the maximum of the HP not only growth, but it is smoothly moved towards larger grey values (see red arrow at the top). (V) High-density and low-density HP cannot be distinguished in the histograms very likely due to the fine intermixing of the particles in the paste. (VI) The signature of air porosity development, i.e. shrinkage, is evident in the left-tails of the HP, see Fig. 9. In spite of water consumption and binder densification (movement of the HP towards larger grey-values), the number of voxels in the left-tails at ~6000-8000 grey-value, increases with time because the development of air, i.e. liquid-water empty, porosity.

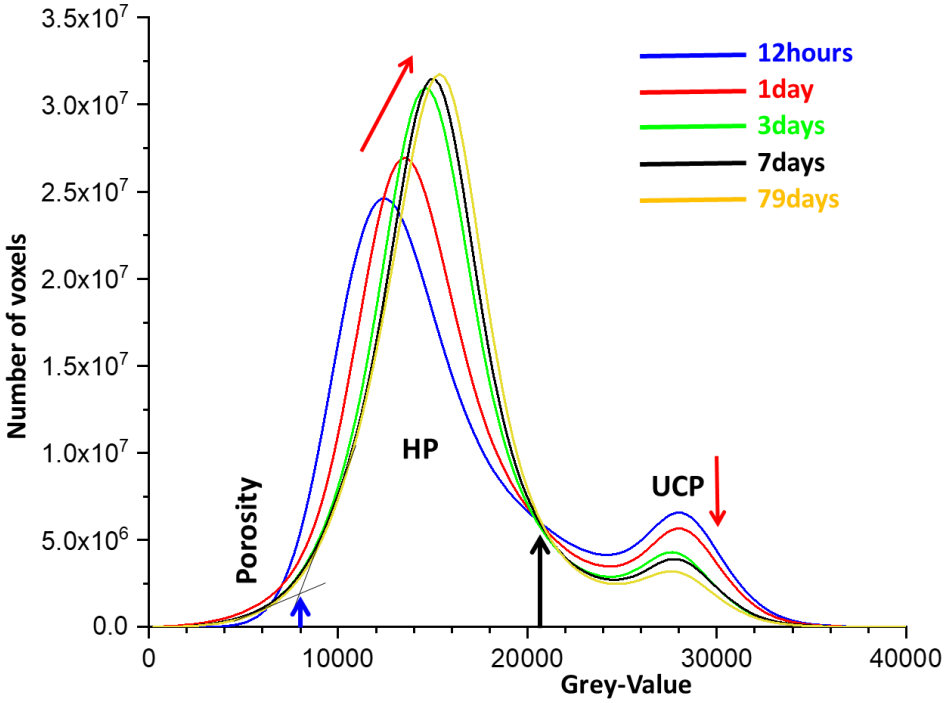

Figure 9. Time evolution of the grey-value histograms showing the evolution of the different components. For the description of the labels, see the text.

Quantitative analysis of the tomograms can be derived from their segmentations, in other words, the quantitative classification of the different components that can be disentangled. The analysed VOI, ~1.4 mm^3, was a cylinder with a height of ~0.6 mm, and a diameter of ~1.7 mm, see Fig.10. This ensures a sufficiently large volume which should not produce any bias because of insufficient averaging. This VOI is the superimposed region inside the capillary that was imaged at each of the 5 hydration ages and it is significantly smaller than the reconstructed VOI for each acquisition, ~4 mm^3. Here, the segmentations have been carried out by two approaches: global thresholding (GT) and Machine Learning (ML). Next, we focus on the GT which only uses the information available in the grey-value histograms. Dragonfly was employed for this and only three components were segmented: UCP, HP and porosity. The grey-value for the UCP/HP boundary is

constant with time, being 20500 grey-value for the employed experimental conditions and reconstruction parameters. Conversely, the HP/porosity boundary is not constant with time and it was estimated for every dataset by the tangent-slope approach [31]. The values ranged 6000-8500 grey-value and the estimation for the 7 days tomogram is depicted in Fig. 9, as an example. The volume percentages of the three components for the *in situ* µCT study are given in Table 5. The time evolution follows the expected trend, a decrease in the UCP contents and an increase in the HP amounts. However, the accuracy of the obtained results required a comparison with expected values which will be carried out below.

ML segmentation was carried out with IPSDK. The ML model training for PC pastes, including the initial pixel labelling and tweaking the model was described elsewhere [19]. It is noted that for this type of analysis, four components were assigned: porosity, ld-HP, hd-HP and UCP. ML profits not only from the grey-values but also from the local features of the (initially) manually labelled particles. The results from this study are given in Table 6. It should be noted that the porosity is always much smaller than the expected one. For instance, the free water content at 1 day from diffraction should be close to 36 vol% (19.1 wt%, see Table 3). Most of the water porosity is smaller than the attained spatial resolution, ~3 µm, and it is concluded that (a) the porosity values shown in Tables 5 and 6 are mainly air porosities, and (b) the free water is manly considered within the HP contribution. A 4D visualization of the ML segmentations is shown in Fig. 10.

Table 5

µCT global-thresholding segmentation results, in volume percentage (vol%).

time	**porosity**	**HP**	**UCP**
12 h	0.8%	76.6%	22.6%
1 d	2.6%	77.8%	19.6%
3 d	4.1%	80.6%	15.3%
7 d	2.4%	82.8%	14.8%
79 d	2.6%	84.3%	13.1%

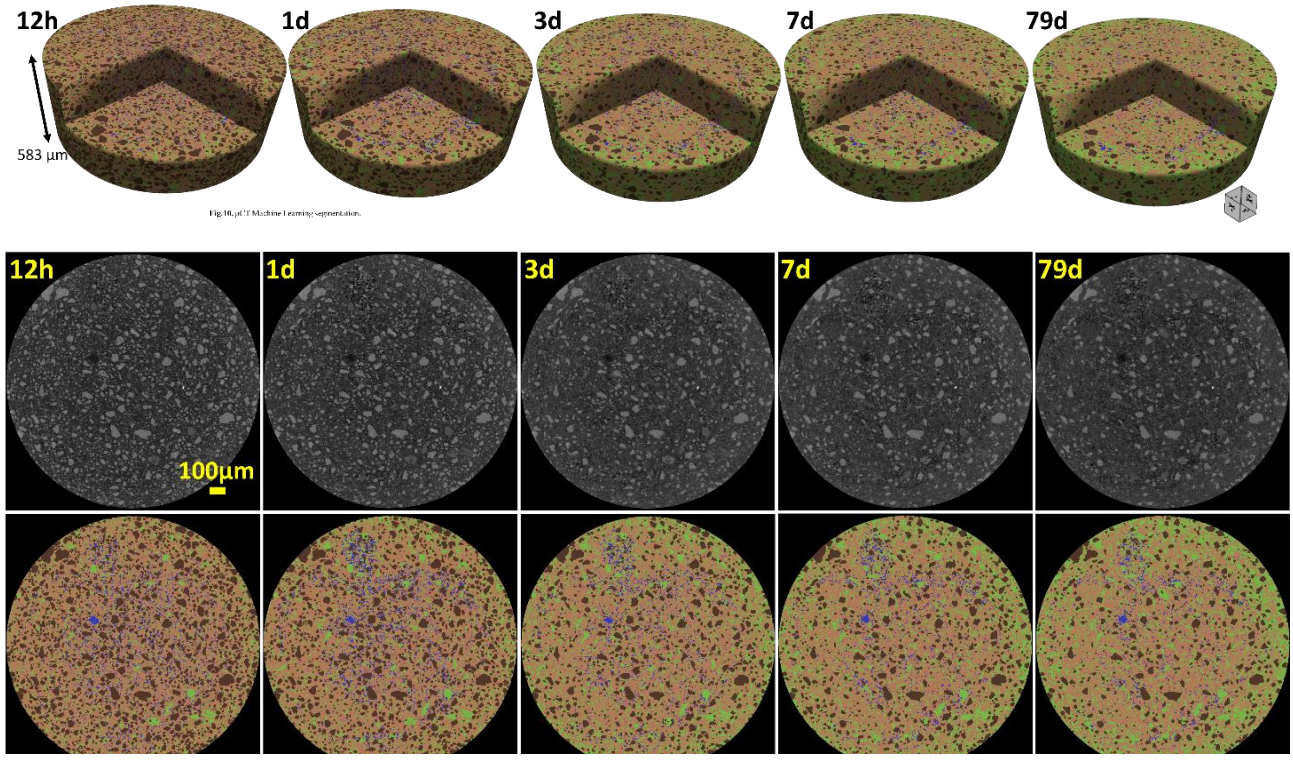

Figure 10. µCT Machine Learning segmentation output. (Top row) 4D renderings. Colour code: porosity (blue), low-density HP (light brown), high-density HP (green), unhydrated cement particles (dark brown). (Bottom row) 2D comparison of the reconstructed orthoslices and the ML segmented output.

Table 6.

µCT machine learning segmentation result, in volume percentage (vol%).

time	porosity	ld-HP	hd-HP	UCP
12 h	4.1%	55.8%	12.6%	27.5%
1 d	4.4%	56.6%	16.2%	22.8%
3 d	3.3%	57.9%	22.6%	16.2%
7 d	3.1%	56.3%	25.3%	15.3%
79 d	2.9%	55.5%	29.1%	12.5%

3.5. *In situ* isothermal calorimetric study.

The hydration kinetic of the employed PC has also been investigated by isothermal calorimetry, see Fig. 11. The maximum in the heat flow trace took place at 8 h. From the cumulative heat trace is deduced that the released heat at 27.5 hours, 3 and 7 days of hydration are 209.6, 295.7 and 325.1 J/g of anhydrous cement, respectively. From the RQPA results, it is possible to calculate the expected heat released considering the reaction degree of the different phases and their heats of hydration. For a detailed explanation, see [40]. Here, it is used 517, 1672 and 418 J/g for the heat of hydration of C_3S, C_3A (to yield AFt) and C_4AF, respectively. For this comparison, the basis is 1 g of anhydrous cement. Therefore, the reacted amount of these phases has to be referred to 1 g of anhydrous PC and then the heats of hydration are used. The calculated heats of hydration, from the RQPA-determined reacted fractions, are 247.5, 345.5 and 369.4 J/g at 27.5 h, 3 and 7 days, respectively. It can be noticed that the calculated heats are invariably higher than those directly measured by calorimetry. There are two main sources of error for this type of comparison: (i) Firstly, lower heats are measured by calorimetry because the data during the first 45 minutes were not collected, due to the needed thermal stabilization of equipment. (ii) Secondly, not all C_3A hydrates yield AFt because of the lack of sulfates. In fact, the reacted amount of C_3A at 7 days, i.e. 4.0 g, should yield 18.6 g of AFt. In fact, only 56% of the reacted C_3A gives AFt. Crystalline sulfate-containing AFm has not been detected in any diffraction study, the heat of hydration for this reaction would be 1144 J/g. Additionally, the heats of hydration of C_3A to yield aluminates adsorbed in the amorphous components and amorphous AFm are not known to the authors. 44% of C_3A, not yielding AFt, rests 19.6 J, and this is judged as the largest source of error for this comparison.

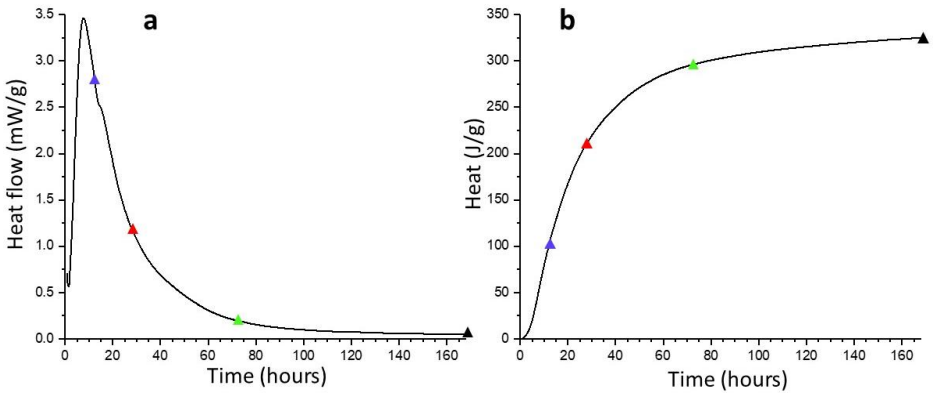

Figure 11. Isothermal calorimetry traces for the PC paste, w/c=0.50, at 25ºC up to 7 days. (a) Heat flow. (b) Cumulative heat. The triangles highlight the times for µCT or LXRPD data acquisitions. Blue: µCT recorded at 12 h. Red: LXRPD recorded at 27.5 h. Green and black: data acquired at 3 and 7 days, respectively.

4. General discussion.

The core of this investigation is to develop a methodology that allows obtaining accurate results from *in situ* powder diffraction and microtomography. It has been shown above that the RQPA results arising from the *in situ* MoKα_1 LXRPD study are relatively accurate, as the comparison with *ex situ* LXRPD data and thermal data were very satisfactory. Hence, sample preparation and *in situ* LXRPD data acquisition and data analysis were validated. Next, we focus on the comparison of the *in situ* RQPA results with the *in situ* µCT results.

In order to carry out this comparison, firstly the contents given in Table 3, in wt%, determined/calculated from LXRPD are transformed to vol% taking into account the known densities for all the components. Thus, Table 7 displays the contents both in cm^3 refereed to 100 g of cement paste and in vol%. It is noted that 100 cm^3 of a paste is not a constant basis in cement hydration because of the difference in volumes between reactants and products. Once the paste sets, this decrease in volume is shared between the bulk volume shrinkage and internal

gas (air/water) porosity development. It is noted that C-S-H gel would be around 35 vol% of the paste when expressed as $(CaO)_{1.8}SiO_2(H_2O)_{4.0}$, i.e. containing the gel pore water but not containing the free-water/capillary-water. Because of the fine intermixing of C-S-H and capillary water, if these two components are considered together, this would be around 60 vol% of the paste. Moreover, this means that any diffraction study of cement pastes is blind to more than 60 % of the volume of the probed sample. However, features like portlandite content increase and alite amount decrease can be accurately determined by LXRPD if the employed experimental approach is robust enough.

For the comparison between the LXRPD and μCT results, the anhydrous cement components have been gathered, i.e. C_3S, C_2S, C_3A, C_4AF and C$\underline{C}$. From the LAC point of view, it is not currently clear if C$\underline{C}$ is below or above the crossing point at 20500 grey value. This is the subject of an ongoing investigation which has also the goal to expand this approach to Portland-Limestone cements. In any case, the amount of calcite is minor in the investigated PC, and therefore this choice should not severely bias the results. For the ML results, the hd-HP and ld-HP are summed for easier comparison. The results are shown in Table 8. Here, the implications of the small differences in the evolving overall volume up to 7 days are not considered, as they are likely within the errors of the segmentations.

Table 7

In situ RQPA results for the PC 42.5 R pastes, w/c=0.50, expressed in cm^3 (referred to 100 g of cement paste). The mass densities used for the transformation are also reported. The corresponding values in vol% are given in italics, but 100 cm^3 of paste is not a constant basis in a hydrating cement.

phases	**ρ / gcm^{-3}**	**t_0/ cm^3**	***t_0/vol%***	**1d/ cm^3**	***1d/vol%***	**3d/ cm^3**	***3d/vol%***	**7d/ cm^3**	***7d/vol%***	**77d/ cm^3**	***77d/vol%***
C_3S	3.15	12.18	*22.4*	4.79	*9.1*	2.34	*4.5*	1.95	*3.8*	1.29	*2.5*
C_2S	3.30	2.59	*4.8*	2.47	*4.7*	2.55	*4.9*	2.45	*4.7*	2.22	*4.3*
C_3A	3.05	1.46	*2.7*	0.70	*1.3*	0.32	*0.6*	0.16	*0.3*	0.09	*0.2*
C_4AF	3.73	1.82	*3.4*	1.63	*3.1*	1.21	*2.3*	1.17	*2.3*	0.97	*1.9*
C$\underline{C}$	2.71	1.29	*2.4*	1.73	*3.3*	1.86	*3.6*	1.75	*3.4*	1.83	*3.5*
minors	-	1.67	*3.0*	0.20	*0.4*	0.11	*0.2*	0.14	*0.3*	0.14	*0.3*
H_2O	1.00	33.33	*61.3*	19.13	*36.4*	14.99	*28.8*	13.87	*26.7*	12.48	*24.1*
AFt	1.78		-	5.03	*9.6*	5.74	*11.0*	5.99	*11.5*	6.18	*11.9*
CH	2.23		-	4.02	*7.6*	5.24	*10.1*	5.62	*10.8*	5.96	*11.5*
C-S-H	2.11		-	12.37	*23.5*	16.04	*30.8*	17.00	*32.7*	18.07	*34.9*
Fe-Si-Hg	2.52			0.49	*0.9*	1.61	*3.1*	1.70	*3.3*	2.22	*4.3*
Hc	1.90		-	-	-	0.08	*0.2*	0.13	*0.2*	0.07	*0.1*
Mc	2.22		-	-	-	-	-	-	-	0.25	*0.5*
TOTAL		54.36	*100.0*	52.55	*100.0*	52.08	*100.0*	51.94	*100.0*	51.78	*100.0*

Table 8 allows to initially discuss the ML and GT results. At 1 day and later, the results are quite similar. At 12 h this is not the case as the UCP contents are 28.7 and 22.8 vol% for ML and GT, respectively. There are no available results from LXRPD at this age, but the overall PC degree of hydration can be calculated considering the UCP content at the time of mixing, i.e. 35.6 vol%. The PC DoHs are 36 and 19% for GT and ML results, respectively. The DoH at 12 h from GT is too high and this result seems to be inaccurate.

The comparison between the UCP contents from *in situ* LXRPD and *in situ* μCT has to be exercised with care as the data are not taken simultaneously but sequentially. This means that there is always a delay between both sets of measurements. With our employed experimental conditions, *in situ* LXRPD were taken 3 hours later than the corresponding μCT measurements. This is important at 1 day, when the reactions are fast, and likely negligible at 7 days or later when the hydration kinetics are very slow. With this caveat, the agreement between UCP contents from LXRPD and μCT are within 2.3 wt% at 1 day and within 1.5% at later hydration ages. This disagreement/error is considered acceptable and means that the UCP results from μCT data analysed both by GT and ML are relatively accurate. Global thresholding is easier to do from the methodological point of view. However, the final aim of this investigation is to be able to use μCT for helping to determine the reaction degree of SCMs. In this case, the LAC of most SCMs is located within the HP peaks and global thresholding is not useful. Conversely, ML profits from the LAC/grey-values and the local features such as particle shapes

and homogeneity within the reconstructed volume. Therefore, for the long-term development of this approach to obtain relevant scientific results, ML segmentation is judged to be much superior.

Table 8

Comparison of RQPA and μCT results in vol%. The outputs for the μCT study have been renormalized to leave out the (air) porosities, i.e. the results are shown respect to the HP and UCP contents.

Hydration age	Components	LXRPD	GT	ML*
t_0	HP	64.4	-	-
	UCP	35.6	-	-
12h	HP	-	77.2	71.3
	UCP	-	22.8	28.7
1d	HP	78.5	79.9	76.2
	UCP	21.5	20.1	23.8
3d	HP	84.1	84.0	83.2
	UCP	15.9	16.0	16.8
7d	HP	85.5	84.8	84.2
	UCP	14.5	15.2	15.8
79d	HP	87.6	86.6	87.1
	UCP	12.4	13.4	12.9

*ld-HP and hd-HP derived from ML have been summed as a single hydrate phase (HP) for comparison to global-thresholding and LXRPD results.

5. Conclusions.

This investigation reports an accurate experimental protocol for *in situ* cement hydration studies avoiding any alteration after mixing due to sample conditioning. The pastes are just injected within thick glass capillaries/tubes, nominal diameter of 2.0 mm, and both ends are sealed. The thick capillaries are vital to have very good powder averaging and to avoid self-desiccation. The sealing avoids any water loss and portlandite carbonation. The paste rotation within a capillary minimises portlandite prefer orientation. The pastes are sequentially analysed by X-ray microtomography and MoKα_1 X-ray powder diffraction.

Results for a w/c=0.50 paste, made out of a commercial PC 42.5 R, are reported. To determine the accuracy of the proposed *in situ* methodology, the same sample was cured *ex situ* and also quantitatively studied by thermal analysis and powder diffraction. Portlandite contents were 13.8, 13.1 and 12.5 wt% by thermal analysis, *ex situ* powder diffraction and *in situ* powder diffraction, respectively. Moreover, a mass balance calculation from the reacted fractions of C_3S and C_4AF yielded 13.1 wt% of CH. AFt keeps growing with time up to 77 days without any sign of partial transformation to AFm, despite the lack of sulfates at later hydration ages. The second stream of this study was to collect microtomographic data in exactly the same region of the hydrating paste. This minimises the variability in the obtained results and shows a crossing, invariant, point in the grey-value histogram evolution with time. Segmentations have been carried out by global thresholding and supervised Machine Learning. The comparison of the segmented results for the unhydrated cement particles and the Rietveld quantitative phase analysis outputs indicate an agreement within 2 %.

In a nutshell, here it is proposed an innovative and accurate methodology, based on *in situ* X-ray powder diffraction and microtomography, with potential to determine binder reaction degrees with smaller errors and the possibility for automatize data analysis. This approach is developed to analyse more challenging binders, PC-SCMs, which will be the subject of forthcoming publications.

Acknowledgement. This research was partly supported by the research grant PID2020-114650RB-I00 which is co-funded by ERDF.

Author Contributions:
SS: investigation, μCT data analysis, writing–original draft, review & editing. **AC**: investigation, *in situ* LXRPD data analysis, writing–original draft, review & editing. **AGDT**: investigation, review & editing. **IS**: investigation, review & editing. **AM-C**: investigation, *ex situ* LXRPD data analysis, review & editing. **IK**: investigation, review & editing. **CR-S**: investigation, *ex situ* LXRPD data analysis, calorimetry, review & editing. **IRS:** investigation, LXRPD and μCT data collection, review & editing. **LL-R:** investigation, LXRPD and μCT data collection, review & editing. **MAGA**: conceptualization, supervision, mass balance calculations, writing–original draft, review & editing.

Funding: PID2020-114650RB-I00
Data Availability Statement: All raw data used in this paper (X-ray μCT scans, LXRPD, TA and calorimetry files) are openly accessible on Zenodo at https://doi.org/10.5281/zenodo.8084221
Conflicts of Interest: The authors declare no conflict of interest.

References

[1] H.F.W. Taylor, Cement chemistry. 2nd ed., Acad. Press. 20 (1997) 335. https://doi.org/10.1016/S0958-9465(98)00023-7.

[2] P.C. Hewlett, M. Liska, Lea's Chemistry of Cement and Concrete, 5th ed., Elsevier, 2017.

[3] K.L. Scrivener, R. Snellings, B. Lothenbach, A Practical Guide to Microstructural Analysis of Cementitious Materials, CRC Press, Boca Raton, FL, 2016.

[4] A.G. De la Torre, A. Cabeza, A. Calvente, S. Bruque, M.A.G. Aranda, Full phase analysis of portland clinker by penetrating synchrotron powder diffraction, Anal. Chem. 73 (2001) 151–156. https://doi.org/10.1021/ac0006674.

[5] M.A.G. Aranda, A.G. De la Torre, L. Leon-Reina, Rietveld Quantitative Phase Analysis of OPC Clinkers, Cements and Hydration Products, Rev. Mineral. Geochemistry. 74 (2012) 169–209. https://doi.org/10.2138/rmg.2012.74.5.

[6] D. Jansen, C. Stabler, F. Goetz-Neunhoeffer, S. Dittrich, J. Neubauer, Does Ordinary Portland Cement contain amorphous phase? A quantitative study using an external standard method, Powder Diffr. 26 (2011) 31–38. https://doi.org/10.1154/1.3549186.

[7] L. León-Reina, A.G. De la Torre, J.M. Porras-Vázquez, M. Cruz, L.M. Ordonez, X. Alcobé, F. Gispert-Guirado, A. Larrãaga-Varga, M. Paul, T. Fuellmann, R. Schmidt, M.A.G. Aranda, Round robin on Rietveld quantitative phase analysis of Portland cements, J. Appl. Crystallogr. 42 (2009) 906–916. https://doi.org/10.1107/S0021889809028374.

[8] G. Le Saoût, V. Kocaba, K. Scrivener, Application of the Rietveld method to the analysis of anhydrous cement, Cem. Concr. Res. 41 (2011) 133–148. https://doi.org/10.1016/j.cemconres.2010.10.003.

[9] D. Jansen, F. Goetz-Neunhoeffer, C. Stabler, J. Neubauer, A remastered external standard method applied to the quantification of early OPC hydration, Cem. Concr. Res. 41 (2011) 602–608. https://doi.org/10.1016/j.cemconres.2011.03.004.

[10] A.G. De la Torre, S. Bruque, M.A.G. Aranda, Rietveld quantitative amorphous content analysis, J. Appl. Crystallogr. 34 (2001) 196–202. https://doi.org/10.1107/S0021889801002485.

[11] P.J. Withers, C. Bouman, S. Carmignato, V. Cnudde, D. Grimaldi, C.K. Hagen, E. Maire, M. Manley, A. Du Plessis, S.R. Stock, X-ray computed tomography, Nat. Rev. Methods Prim. 2021 11. 1 (2021) 1–21. https://doi.org/10.1038/s43586-021-00015-4.

[12] Í.B. da Silva, X-ray Computed Microtomography technique applied for cementitious materials: A review, Micron. 107 (2018) 1–8. https://doi.org/10.1016/j.micron.2018.01.006.

[13] A. du Plessis, W.P. Boshoff, A review of X-ray computed tomography of concrete and asphalt construction materials, Constr. Build. Mater. 199 (2019) 637–651.

https://doi.org/10.1016/j.conbuildmat.2018.12.049.

[14] S. Brisard, M. Serdar, P.J.M. Monteiro, Multiscale X-ray tomography of cementitious materials: A review, Cem. Concr. Res. 128 (2020) 105824. https://doi.org/10.1016/j.cemconres.2019.105824.

[15] W. Kong, Y. Wei, S. Wang, J. Chen, Y. Wang, Research progress on cement-based materials by X-ray computed tomography, Int. J. Pavement Res. Technol. 13 (2020) 366–375. https://doi.org/10.1007/s42947-020-0119-8.

[16] T. Sugiyama, M.A.B. Promentilla, Advancing concrete durability research through X-ray computed tomography, J. Adv. Concr. Technol. 19 (2021) 730–755. https://doi.org/10.3151/jact.19.730.

[17] S.Y. Chung, J.S. Kim, D. Stephan, T.S. Han, Overview of the use of micro-computed tomography (micro-CT) to investigate the relation between the material characteristics and properties of cement-based materials, Constr. Build. Mater. 229 (2019) 116843. https://doi.org/10.1016/j.conbuildmat.2019.116843.

[18] I.R. Salcedo, A. Cuesta, S. Shirani, L. León-Reina, M.A.G. Aranda, Accuracy in Cement Hydration Investigations: Combined X-ray Microtomography and Powder Diffraction Analyses, Mater. 2021, Vol. 14, Page 6953. 14 (2021) 6953. https://doi.org/10.3390/MA14226953.

[19] S. Shirani, A. Cuesta, A. Morales-Cantero, I. Santacruz, A. Diaz, P. Trtik, M. Holler, A. Rack, B. Lukic, E. Brun, I.R. Salcedo, M.A.G. Aranda, 4D nanoimaging of early age cement hydration, Nat. Commun. 14 (2023) 2652. https://doi.org/10.1038/s41467-023-38380-1.

[20] A. Cuesta, S. Shirani, A.G. De la Torre, I. Santacruz, A. Morales-Cantero, I. Koufany, C. Redondo-Soto, I.R. Salcedo, L. Leon-Reina, M.A.G. Aranda, Combined use of laboratory X-ray diffraction and microtomography in early age cement hydration, in: Proc. 16th Int. Congr. Chem. Cem., Bangkok, 2023: p. accepted (to be published in September).

[21] M. García-Maté, A.G. De la Torre, L. León-Reina, E.R. Losilla, M.A.G. Aranda, I. Santacruz, Effect of calcium sulfate source on the hydration of calcium sulfoaluminate eco-cement, Cem. Concr. Compos. 55 (2015) 53–61. https://doi.org/10.1016/j.cemconcomp.2014.08.003.

[22] J.D. Zea-Garcia, I. Santacruz, M.A.G. Aranda, A.G. De la Torre, Alite-belite-ye'elimite cements: Effect of dopants on the clinker phase composition and properties, Cem. Concr. Res. 115 (2019) 192–202. https://doi.org/https://doi.org/10.1016/j.cemconres.2018.10.019.

[23] A.C. Larson, R.B. Von Dreele, General structure analysis system (GSAS), Los Alamos Natl. Lab. Rep. LAUR. 748 (2004) 86–748.

[24] P. Thompson, D.E. Cox, J.B. Hastings, Rietveld Refinement of Debye-Scherrer Synchrotron X-ray Data from A1203, J. Appl. Crystallogr. 20 (1987) 79–83. https://doi.org/10.1107/S0021889887087090.

[25] L.W. Finger, D.E. Cox, A.P. Jephcoat, Correction for powder diffraction peak asymmetry due to axial divergence, J. Appl. Crystallogr. 27 (1994) 892–900. https://doi.org/10.1107/S0021889894004218.

[26] A.G. De la Torre, I. Santacruz, A. Cuesta, L. León-Reina, M.A.G. Aranda, Diffraction and crystallography applied to anhydrous cements, in: H. Pöllmann (Ed.), Cem. Mater., De Gruyter, 2017: pp. 3–29.

[27] M.A.G. Aranda, A. Cuesta, A.G. De la Torre, I. Santacruz, L. León-Reina, Diffraction and crystallography applied to hydrating cements, in: H. Pöllmann (Ed.), Cem. Mater. Compos. Prop. Appl., De Gruyter, Berlin, Boston, Germany, 2017: pp. 31–60. https://doi.org/10.1515/9783110473728-003.

[28] A. Cuesta, J.D. Zea-Garcia, D. Londono-Zuluaga, A.G. De la Torre, I. Santacruz, O. Vallcorba, M. Dapiaggi, S.G. Sanfélix, M.A.G. Aranda, Multiscale understanding of tricalcium silicate hydration reactions, Sci. Rep. 8 (2018) 8544. https://doi.org/10.1038/s41598-018-26943-y.

[29] F. Avet, X. Li, K.L. Scrivener, Determination of the amount of reacted metakaolin in calcined clay blends, Cem. Concr. Res. 106 (2018) 40–48. https://doi.org/10.1016/J.CEMCONRES.2018.01.009.

[30] F. Zunino, Y. Dhandapani, M. Ben Haha, J. Skibsted, S. Joseph, S. Krishnan, A. Parashar, M.C.G.

Juenger, T. Hanein, S.A. Bernal, K.L. Scrivener, F. Avet, Hydration and mixture design of calcined clay blended cements: review by the RILEM TC 282-CCL, Mater. Struct. Constr. 55 (2022) 234. https://doi.org/10.1617/s11527-022-02060-1.

[31] S. Shirani, A. Cuesta, A. Morales-Cantero, A.G. De la Torre, M.P. Olbinado, M.A.G. Aranda, Influence of curing temperature on belite cement hydration: A comparative study with Portland cement, Cem. Concr. Res. 147 (2021) 106499. https://doi.org/10.1016/j.cemconres.2021.106499.

[32] S. Shirani, C. Redondo-soto, I.M.R. Bernal, A. Cuesta, I. Santacruz, A.G. De La Torre, I.R. Salcedo, M.P. Olbinado, M.A.G. Aranda, X-ray Microtomographic Studies of LC3 and Related Binders, in: Proc. Int. Conf. Calcined Clays Sustain. Concr. 2022, 2022: p. accepted.

[33] J. Zhang, G.W. Scherer, Comparison of methods for arresting hydration of cement, Cem. Concr. Res. 41 (2011) 1024–1036. https://doi.org/10.1016/j.cemconres.2011.06.003.

[34] I. Galan, H. Beltagui, M. García-Maté, F.P. Glasser, M.S. Imbabi, Impact of drying on pore structures in ettringite-rich cements, Cem. Concr. Res. 84 (2016) 85–94. https://doi.org/10.1016/j.cemconres.2016.03.003.

[35] R. Snellings, J. Chwast, Ö. Cizer, N. De Belie, Y. Dhandapani, P. Durdzinski, J. Elsen, J. Haufe, D. Hooton, C. Patapy, M. Santhanam, K. Scrivener, D. Snoeck, L. Steger, S. Tongbo, A. Vollpracht, F. Winnefeld, B. Lothenbach, Report of TC 238-SCM: hydration stoppage methods for phase assemblage studies of blended cements—results of a round robin test, Mater. Struct. Constr. 51 (2018). https://doi.org/10.1617/s11527-018-1237-5.

[36] A. Mezhov, D. Kulisch, A. Goncharov, S. Zhutovsky, A Comparative Study of Factors Influencing Hydration Stoppage of Hardened Cement Paste, Sustain. 15 (2023) 1080. https://doi.org/10.3390/su15021080.

[37] C. Donnelly, S. Finizio, S. Gliga, M. Holler, A. Hrabec, M. Odstrčil, S. Mayr, V. Scagnoli, L.J. Heyderman, M. Guizar-Sicairos, J. Raabe, Time-resolved imaging of three-dimensional nanoscale magnetization dynamics, Nat. Nanotechnol. 15 (2020) 356–360. https://doi.org/10.1038/s41565-020-0649-x.

[38] X. Li, Q. Hu, B. Robertson, M.T. Ley, V.J. De Andrade, G. Sokhansefat, Direct observation of C3S particle dissolution using fast nano X-ray computed tomography, Cem. Concr. Res. 166 (2023) 107097. https://doi.org/10.1016/j.cemconres.2023.107097.

[39] M.A.G. Aranda, Recent studies of cements and concretes by synchrotron radiation crystallographic and cognate methods, Crystallogr. Rev. 22 (2016) 150–196. https://doi.org/10.1080/0889311X.2015.1070260.

[40] O. Linderoth, L. Wadsö, D. Jansen, Long-term cement hydration studies with isothermal calorimetry, Cem. Concr. Res. 141 (2021) 106344. https://doi.org/10.1016/j.cemconres.2020.106344.

General results and discussion 4

In this chapter, we will attempt to explore the findings and implications of the extensive research conducted in the previous "Articles section" chapter 3. We will critically examine the evidence gathered in the light of the study objectives and provide a thorough interpretation of the data. We will consider the relevance of our findings in the context of the field as a whole, as well as their possible contributions and limitations, and revise our previous studies if necessary to improve the results.

4.1 Resolution

In general, resolution can be divided into three main groups. These are described below.

4.1.1 Temporal resolution

The ability to capture and display changes over time is called temporal/-time resolution. The exposure time or frame rate at which X-ray images are taken affects the temporal resolution of X-ray imaging. Dynamic processes can be visualised at a higher frame rate, so higher frame rates give better temporal resolution.

4.1.2 Spatial resolution

Spatial resolution is often confused with the voxel size. While the pixel size relates the measurements in pixel (the smallest identifiable unit in an image) to physical units, resolution refers to the quality and the amount of detail in the reconstructed images. More specifically, spatial resolution describes the ability of an imaging system to discriminate between nearby components. The choice of the pixel size is fundamental when designing an imaging detector. It is necessary to find balance between a small pixel size, which brings a better spatial resolution, and a big pixel size, which results in better Signal-to-Noise Ratio and higher dynamic range. In order to understand the key elements in such trade-off, we need to define metrics and methods helping us choose the optimal pixel size:

- **Dynamic Range (DR)**. Dynamic range is a metric measuring the capacity of the imaging system to detect highlights (high pixel intensity values) and shadows (low pixel intensity values).
- **Signal-to-Noise Ratio (SNR)**: SNR is a metric defined by the ratio of the power of the input signal (containing meaningful information) and the power of the background noise contained in the signal.
- **Modulation Transfer Function (MTF)**. The MTF is a measurement describing how well the imaging system reproduces the incoming signal that is below the Shannon-Nyquist frequency. The latter corresponds to half the inverse of pixel size.

> In most cases, we can simplify the MTF as the product of the optical, geometric and diffusion MTF, accumulating the degradation of each subpart of the imaging system. Decreasing pixel size then means that we increase the Nyquist frenquency, thus increasing the MTF.

As explained before, a smaller pixel size is desirable given the fact that it increases spatial resolution and MTF. But bigger pixel size improves SNR and DR. Every experimental setup design then needs to find balance between the two, which is not always clear and most of the time depend on the needs of the expected results. A broadly used criterion helping measuring the spatial resolution is the Fourier Shell Correlation (FSC). However, such criterion is sometimes criticized as it mostly depends on a *FSC threshold* level defining a reproducible resolution.

The FSC was first described by Harauz and Van Heel in 1986 , measuring the normalized cross-correlation value between two 3 dimensional volumes over corresponding "shells" in the Fourier space (Harauz and Heel 1986).

This FSC is a 3D generalisation of the 2D Fourier Ring Correlation (FRC) introduced by Van Heel et al in 1982 (Frank and van Heel 1982). Many authors then started using a fixed threshold in combination with the FSC curve, more specifically, Bottcher et al., 1997 used a threshold = 0.5 value (Böttcher, Wynne, and Crowther 1997), until Rosenthal proposed a 0.143 threshold value in 2003, better fitting the needs for imaging (Rosenthal and Henderson 2003). A "2σ" threshold criterion was also introduced by Saxton and Baumeister, better adapting the threshold value based on the expected noise behaviour (Saxton and Baumeister 1982). Nevertheless, the FSC curve still arguably remains richer as a representation of Spatial Resolution compared to a single value obtained using a fixed threshold. And in this thesis for some of the articles we used the FSC plots (Van Heel and Schatz 2005) for having sense of spatial resolution.

In addition to the FSC, which we followed for most of the experiments in this thesis, another way to determine the spatial resolution is by observing the grey value/electron density variations in the plot profiles and the interface edge sharpness. In Article 2 (A#2) we calculated this for a tiny pore and for Article 4 (A#4) and Article 5 (A#5) we followed this approach by the capillary edge sharpness. For this reason we have revisited the spatial resolution for all derived data in this thesis and the previous imaging paper of our research group. The results are summarised in Table 4.1. The values given in the table are the average of 3 to 10 measurements and also 25 measurements for Article 4 (A#4), an example is shown in Figure 4.2. It should be noted that this approach to measuring the sharpness of the interface between the glass capillary and the surrounding air is general and can be applied to most imaging cement studies. The spatial resolution of the images is determined by a Point Spread Function (PSF), as ISO/TS 24597 specifies the Gaussian radius of the PSF as the resolution, which corresponds to a 25%-75% change in grey value/electron density along the studied interfaces, as is shown in Figure 4.2.

Table 4.1: Overview of the spatial resolution of the different imaging modalities, including the parameters used for acquisition.

Imaging modality and Sample	Energy or Voltage	Acquired projections	Crowther limit	Scan duration (h/min)	ϕ (μm)	FOV (μm)	Voxel size (nm)	Spatial resolution (nm)	
								edge	FSC
Absorption:									
PC+0.5w/c 7d-(Article 5)	55kV	1801	3140	3.75h	1700	2200	1100	2300	-
67%PC+30%MK +3%Gyp+0.5w/b 3d-(Article 1)	55kV	1637	1884	3.5h	1000	1200	1000	1900	-
PC+0.5w/c 93h-(Article 4)	55kV	1637	1884	3.5h	1000	1200	1000	2200	1800
Phase-Contrast:								**(Pag.)**	
(ID19)								***(Abs.)***	
PC+0.5w/c 93h-(Article 4)	19keV	6000	3908	5min	716	1618	650	750	650
52%PC+30%MK +15%CC+3%Gyp +0.5w/b-4d (Future article)	19keV	6000	3908	5min	836	1618	650	650 *540*	-
(TOMCAT)									
PC+0.5w/c-20°C 28d-(Article 2)	15keV	1501	4019	5min	487	832	325	700 *600*	-
BC+0.5w/c-20°C 28d-(Article 2)	15keV	1501	4019	5min	505	832	325	750 *540*	-
Near-field Ptychography:		***(=step size [μm])***							
PC+0.5w/c 93h-(Article 4)	8.93keV	420 *(=7)*	1565	3h	160	186	186.64	270	500
PC+0.5w/c 19h-(Article 4)	8.93keV	420 *(=6)*	1565	4h	160	186	186.64	250	430
52%PC+30%MK +15%CC+3%Gyp+ 0.5w/b (Future article)	8.93keV	1540 *(=7)*	1926	20h	209	229	186.64	240	187
Far-field Ptychography:					(cone shape*)				
CAC 4°C-(Article 3)	6.2keV	800 *(=2.6)*	2097	14h	43	52	38.94	71	62
CAC 20°C-(Article 3)	6.2keV	1300 *(=3)*	2338	17h	54	58	38.94	67	58
neat PC	6.2keV	800 *(=2.5)*	2419	15.5h	53	60	38.94	93	80
PC-CC (Cuesta et al. 2019)	6.2keV	1300 *(=3)*	2621	22h	58	65	38.94	75	56

*See Figure 4.1 for capillary shapes.

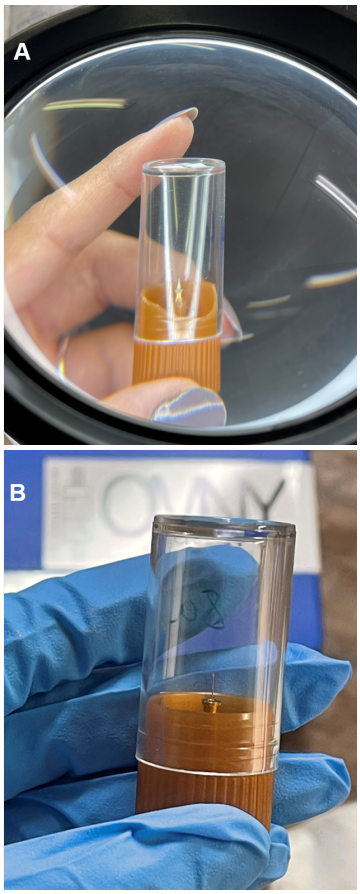

Figure 4.1: A) Cone shape capillary of the "Far-field Ptychography", **B)** Tube capillary of the "Near-field Ptychography" experiment mounted on brass sample holder of OMNY.

In Article 4 (A#4) in section 3.4, we studied the "edge sharpness out of the capillary" (from surrounded air to the capillary outer wall).
The electron density of the air is close to zero, and the electron density of the glass capillary is around 0.62 $eÅ^{-3}$ and by calculating the changes we would get 250nm for this particular sample (see Figure 4.2).

Based on the knowledge gained in Article 4 (A#4), a common interface present in the imaging modalities used in this thesis for the plot profiles is the glass capillary wall - air (i.e. the outside of the capillaries). We evaluated the interfaces in each tomogram to determine the average spatial resolution.

According to the table 4.1, the spatial resolution of the laboratory "Absorption" modality is the poorest. The ID19 setup, which is the "Phase-contrast" modality with a voxel size of 0.65 μm, has a better spatial resolution than the laboratory. And also the TOMCAT experiment with 0.325 μm has a slightly better spatial resolution than ID19. It is noted that the spatial resolution for TOMCAT data is not double than that of ID19 spite of that the voxel size was half. This is likely due to the number of projections, see Table 4.1. The best spatial resolution belongs to the ptychography modalities. "Near-field Ptychography" has a small voxel size of 186.94 nm with a good spatial resolution in the order of 250 nm, it should be noted that many more projections do not significantly improve the spatial resolution. "Far-field Ptychography" has the smallest voxel size and therefore the best spatial resolution of all these experiments.

The scan duration of the "Ptychography" modality is the longest among the other modalities. It should be noted that in order to get the best possible contrast from ptychography, we need to have a smaller "step size", which increases the duration of the scan (if other parameters such as the number of projections remain constant). The reason we switched to "Near-field Ptychography" for the Nature Communications (Article 4 (A#4)) is that we wanted to scan a larger capillary. For the study of hydration in early age Portland cement, we needed a shorter scan time with an adequate and good enough contrast to distinguish the hydrate components. This led us to a 3h-4h scan, which has a larger step size and a minimum enough number of projections. In other words, we decided to scan less vertical FOV to take advantage of the faster scan and to be able to follow the early hydration of the cement.

In "Near-field Ptychography" setup (shown in section 1.2.6.2 in Figure 1.28) the focus is not exactly on the capillary and it is close to the capillary and the spot size is larger (compared to the "Far-field Ptychography"). So if we have larger sample, the time of the scan is longer; therefore using "Near-field Ptychography" (with larger spot size) shortens the overall scan duration.

A possible disadvantage of edge sharpness studies for spatial resolution is that in this method we measure the spatial resolution far from the centre of the sample and it may be slightly better in the core of the sample and inside the capillary. The obtained edge sharpness spatial resolution value for "Near-field Ptychography" was close to 250 nm in *in*

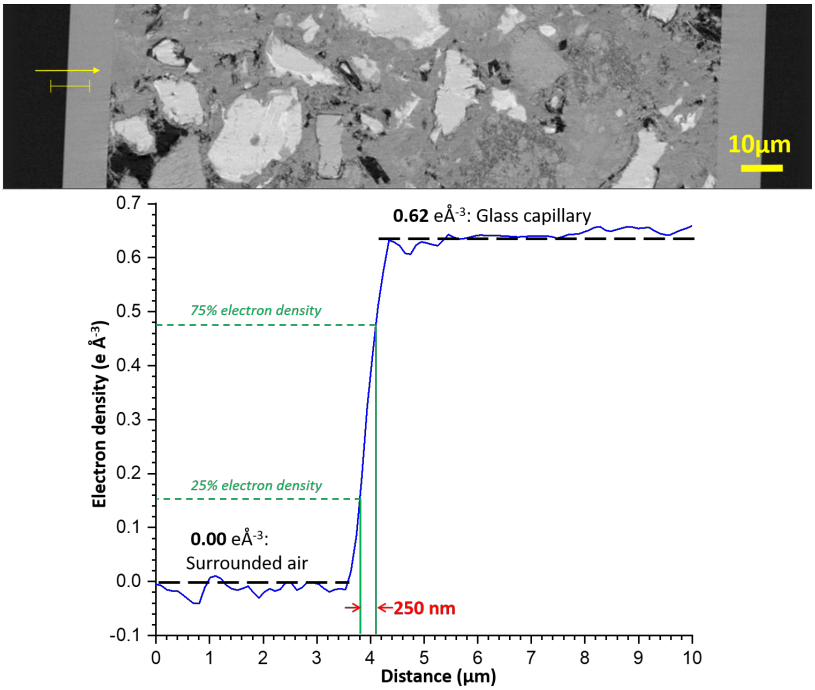

Figure 4.2: Capillary surrounded air edge sharpness spatial resolution in Near-field Ptychography modality.

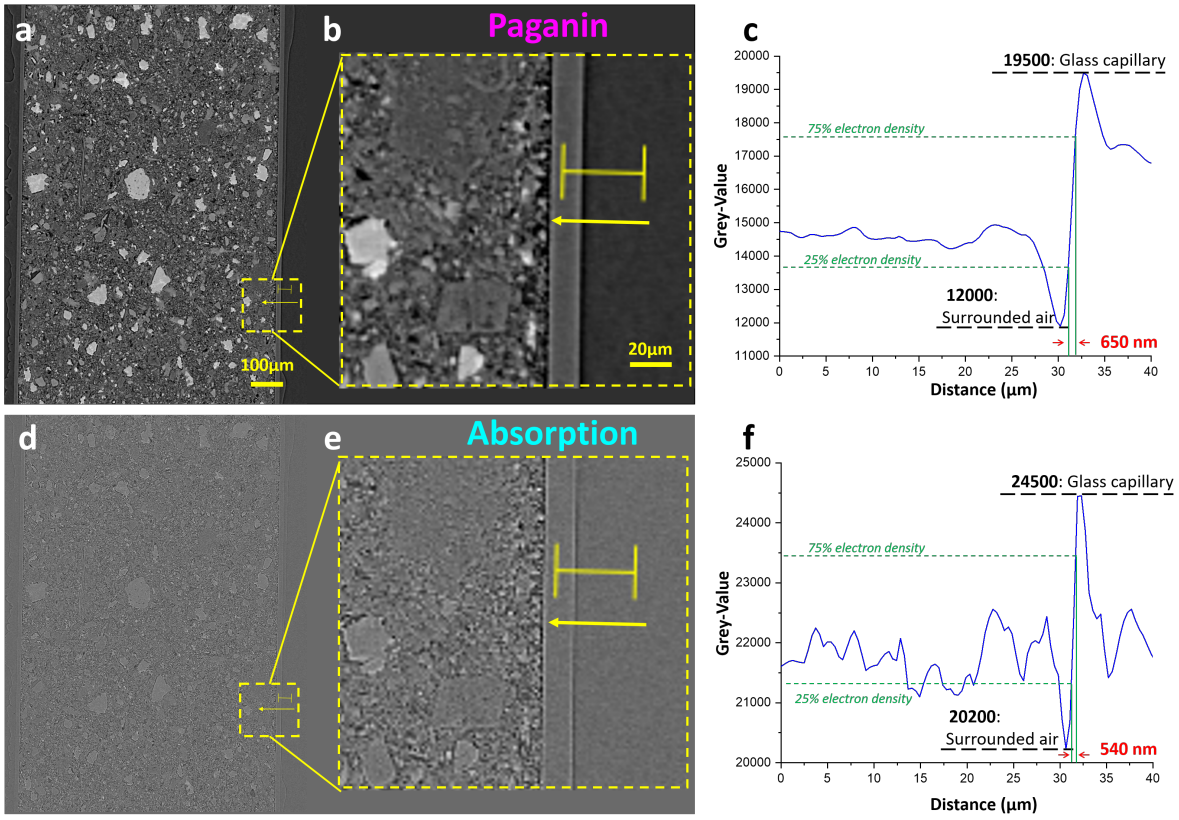

Figure 4.3: Capillary surrounded air edge sharpness spatial resolution in Phase-Contrast modality. **a)** Vertical section of the tomogram of the capillary in the Paganin reconstruction. **b)** Enlargement of a line that is shown in the "c" panel. **c)** The plot profile of the line shown in "b". **d)** Vertical section of the same tomogram of the capillary in the Absorption reconstruction. **e)** Enlargement of a line that is shown in the "d" panel. **f)** The plot profile of the line shown in "e" (i.e. Paganin filter not corrected).

situ experiment of Article 4 (A#4)).

Edge enhancement is a method used in "Phase-Contrast" imaging to improve the visibility of edges and boundaries of the components in the image. And this would make the plot profile for the capillary edge spatial resolution somewhat difficult to plot because the plot would have a sudden rise and fall at the boundaries (see Figure 4.3). Also for the comparison of the "Paganin" and "Absorption" datasets, we show exactly the same line profile of the same sample. Figure 4.3 displays the in-line Phase-Contrast data as recorded and processed in two ways. The top row of panels show the images correcdted with the "Paganin" filter. The bottom row of images show "Absorption" reconstructed data (i.e. "Paganin" filter was not applied). In the "Absorption" dataset the curve is less smooth and more noisy, see Figure 4.3. Furthermore, the jump/difference in the "Paganin" dataset is 7500 meanwhile the change in the "Absorption" dataset is 4300, indicating less visibility or less contrast or information in the "Absorption".

Although the "Absorption" dataset of both ID19 and TOMCAT "Phase-Contrast" experiments shows slightly better spatial resolution at the capillary edge compared to the "Paganin" dataset, this may be due to the large edge enhancement/artifact that can bias the method within the absorption dataset, which is evident along the plot profile in Figure 4.3.

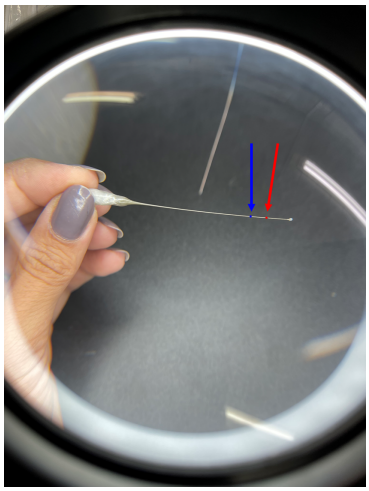

Figure 4.4: Nominal and real diameter of capillary tube. The area between the two arrows is the 200 μm diameter. The upper blue arrow (to the left) is greater than this value and the lower red arrow (to the right) is less than this value.

The FOV of the scans is another important factor. For the "Far-field Ptychography" experiment the capillary had a cone shape and the value given in Table 4.1 is the largest section of the cone that was scanned. However, for the rest of the experiments in this thesis, the "Marked Tube Capillary" (as described in chapter 1) was used. These types of capillaries have a nominal diameter, but the diameter is not constant along the length of the capillary, for this reason finding the "real diameter" is essential for imaging modalities that have a limited FOV, such as "Ptychography". In Figure 4.4, a sealed and filled cement capillary with a nominal diameter of 0.2mm is shown under a magnifier and the region with this exact diameter is between the two arrows. The area above the blue arrow (to the left) is greater than 0.2mm and the area below the red arrow (to the right) is less than 0.2mm. This is the reason why we scanned the 160μm capillary for the PC+0.5w/c in the *in situ* experiment of Article (A#4) and we scanned 209μm capillary for the 52%PC+30%MK+15%C$\underline{\text{C}}$+3%Gyp+0.5w/b (Future article) sample (see Table 4.1).

It can be pointed out that if the capillary diameter is larger, the FOV must be larger and therefore to have similar spatial resolutions we need more projects.

An important point to consider is how many projections are required to obtain an acceptable image. The angular displacement between projections should not exceed the voxel size at the outer diameter of the object. Consequently, the number of points required along the circle to satisfy the sampling requirement is qπ (Withers et al. 2021). The **"Crowther**

limit" can be calculated as follows, and it is an estimate for finding a reasonable number of projections:

$$q = \frac{\text{FOV}_x}{\text{voxel size}} \tag{4.1}$$

$$\text{Crowther limit} = \frac{q\pi}{2} \tag{4.2}$$

Based on this "Crowther limit" calculated for each scan in Table 4.1, the number of acquired projections from the TOMCAT experiment may not be sufficient. On the other hand, the number of projections acquired for the ID19 experiment was more than the limit.

4.1.3 Contrast resolution

For several decades now, X-ray imaging has been exploiting, in addition to the notion of absorption, the refraction information generated by a sample. This refraction is generally referred to as the δ magnitude, and enables better characterization of the materials making up a sample. Better characterization of these materials enables better differentiation, and therefore better contrast. This technique has been dubbed phase contrast, and the difficulty lies in enabling a detector to measure this delta quantity. In the introductory chapter, we talked about the different ways of recovering this phase information. Each modality ("Ptychrography", etc.) is capable of recovering this information by relying on the high spatial coherence of synchrotron radiation. Contrast enhancement is generally achieved by placing the detector further away from the sample and by using dedicated algorithms such as the Paganin algorithm (Paganin et al. 2002), see Figure 4.6.

Thus, the results obtained on the different beamlines of the various synchrotron facilities (TOMCAT, cSAXS, ID19...), each give results enabling more or less phases of the cement samples studied to be distinguished. For example, in images acquired on TOMCAT (voxel size= 0.325 μm), it is possible to distinguish 3 main components by Global Thresholding (GT) and 4 components by Machine-Learning (ML) segmentation, while on images acquired on cSAXS, it is possible to distinguish 7 components by Machine-learning segmentation (voxel size= 186.64 nm). On ID19 beamline (voxel size= 0.65 μm), it was possible to distinguish 4 components same as TOMCAT. This difference can be explained by the different parameters used for each acquisition, such as the energy of the radiation used. Indeed, the lower the energy of the X-rays, the greater the chances of absorption of these rays by the sample (remember that attenuation of materials is non-linear as a function of energy).

We also note that the acquisition times for each modality are different: between 4 hours to 22 hours for cSAXS, 5 minutes for TOMCAT and ID19. These time constraints can sometimes be limiting, depending on the nature of the experiment. In our case, it was possible to achieve better contrast with the Ptychography acquisition, in addition to better spatial resolution. Another constraint of these different types of imaging is the thickness of the sample to be imaged. Indeed, as presented previously, the capillaries we imaged have a different thickness depending on the modality used, in order to obtain the best possible reproducibility

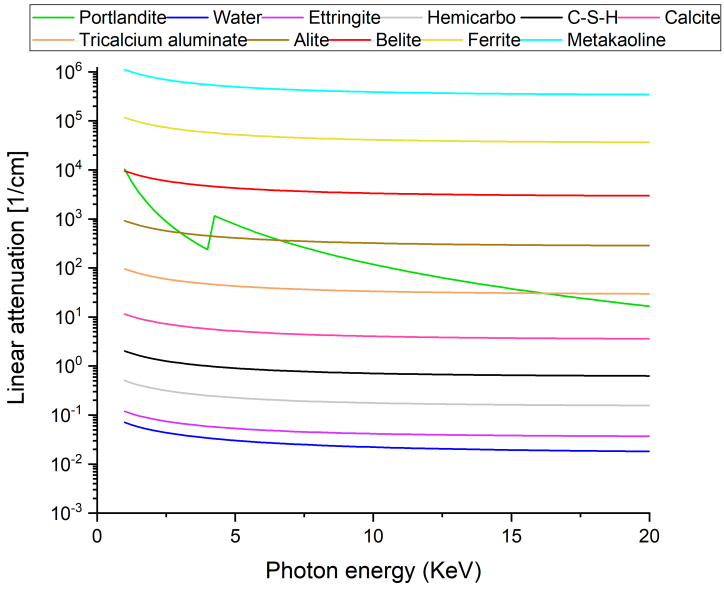

Figure 4.5: The attenuation coefficient of the different cementitious components.

in sample preparation. Thus, the limitation of each of these methods concerns the size of the sample to be analysed, a sample that is too thick being difficult to analyse on certain beamlines but controlling the water-to-cement ratio in thicker capillaries is more feasible.

Besides scanning the samples in the appropriate and distinguishable contrast, the quantitative analysis of complex materials such as cement, which contains phases with close grey values/intensities, deriving the accurate *in situ* histogram is a great help for further analysis and segmentation. Synchrotron CT provides higher spatial resolution but has a limited beamtime, whereas laboratory CT allows longer-term observations with lower spatial resolution (This can be seen clearly in the Table 4.1).

The grey values/intensities represent the local microstructure as they are related to the local chemical composition. Contrast or rather the lack of it, becomes a problem when segmentation of pores and tiny features is required.

In general, the contrast between the different hydration products is so low that we may need to consider them as a single component. This results in the typical three-component segmentation for cementitious materials: Porosity, Hydrate Product (HP) and Unreacted Cement Particles (UCP), the same as the results of Article 2 (A#2). One of the approaches is the Paganin filter in the Phase-Contrast modality. Paganin would enhance the anhydrous components (initial whitish grains) and make them brighter, which is a help for the segmentation. But we still pay a price for the quantitative phase analysis because in this phase contrast modality Paganin filter can not fully eliminate the edge enhancement (i.e. artifacts), see Figure 4.6. By applying the Paganin filter the whole histogram would have a stretch from both sides (low grey-value becomes the blackest and high grey-value becomes the brightest) and this causes the appearing/sharpening in small shoulders such as calcite (CC) in Figure 4.6.

Phase-retrieval helps to improve contrast in an image by reducing the

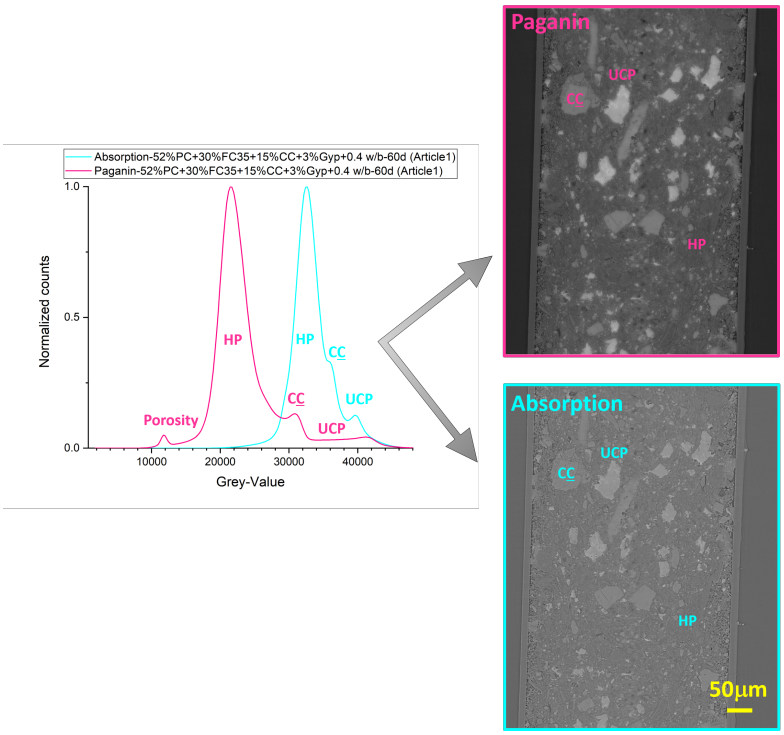

Figure 4.6: Paganin and absorption datasets for the 52%PC +30%FC35 +15%CC +3%Gyp + 0.4 w/b -60days sample from Article 1 (A#1). The main components are shown on both histograms and vertical slices of both the "Absorption" and "Paganin" reconstructions of this sample.

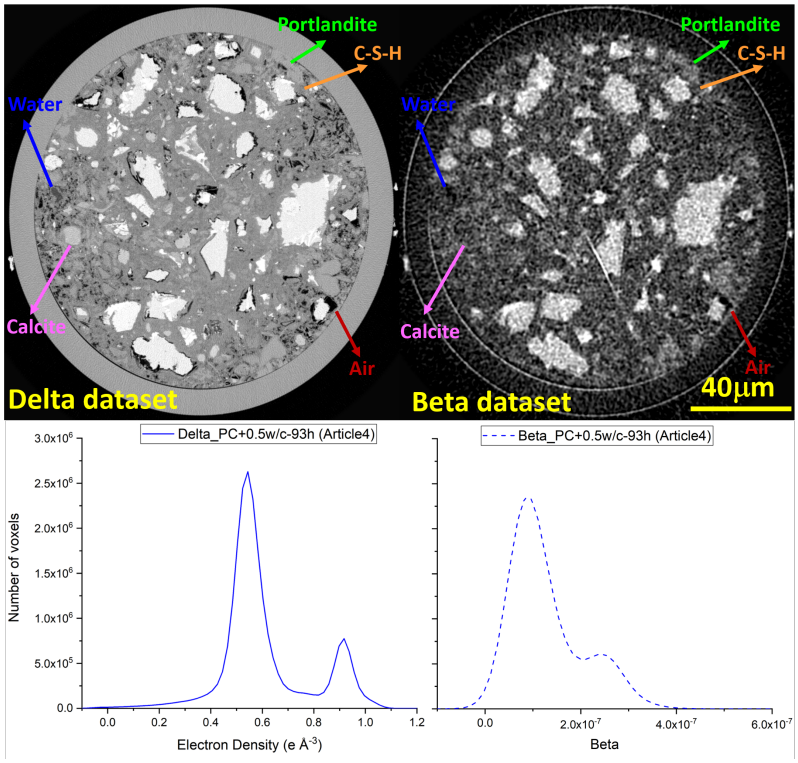

Figure 4.7: Delta and Beta datasets for the Pc+0.5w/c-93hours sample from Article 4 (A#4). Some components are shown on both orthoslices for comparison of these electron density and absorption data sets.

standard deviation within the same phase, and to better mark the interface between two phases. Some techniques measure a phase mainly caused by refraction, such as the propagation-based phase-contrast technique performed on ID19, while others measure diffraction phenomena on the detector (Small Angle Scattering or Ptychography techniques). These techniques are only possible because the synchrotron radiation generated by undulators and bending magnets results in excellent spatial coherence, meaning that the patterns measured on imaging are almost entirely caused by the passage of X-rays through the sample. Phase contrast is becoming more and more widespread, and is gradually making the transition to laboratory sources.

In "Ptychography" analysis, the "Beta" dataset is additional complementary information that helps to study the components that have similar electron density (derived from the "Delta" dataset). For example, in Figure 4.7 the "Portlandite" and "C-S-H" are shown in an area close to each other and the "Portlandite" is also slightly visible in the "Beta" dataset but the "C-S-H" gel is not obvious. This also happens for "calcite" that it is not shown in the "Beta" dataset. Also "Water" and "Air" are both seen completely black in the "Beta" dataset, although we can distinguish "Water" in the "Delta" dataset.
In Figure 4.8, we have collected all the histograms of "Absorption" and "Phase-Contrast" reported in Table 4.1, and the three main visible components in these modalities are labelled on the histogram peaks. In addition, the Full Width Half Maximum (FWHM) of the Hydrate Product (HP) is calculated.

In Figure 4.9, we have collected all the histograms of **a)** "Near-field ptychography", **b)** "Far-field ptychography" from the previous work of our research group and **c)** "Far-field ptychography" from Article 3 (A#3), all of which are reported in Table 4.1. The components are also shown on the electron density histograms. A vertical line at 0.82 $eÅ^{-3}$ electron density is shown to compare the "calcite peak" of "Near-field Ptychography" with "Far-field Ptychography". The "Far-field Ptychography" histogram has narrower peaks than "Near-field Ptychography" histogram. It should be noted that the sharper the peak, the less overlap we would have between the components. This would result in more obvious information in the images, making it easier to distinguish the components.

We then show the orthoslices that belong to these datasets, which are listed in Table 4.1, see Figure 4.10. This allows us to compare the components shown in each orthoslice. **a)** PC+0.5w/c-19h from Article 4 (A#4), **b)** 52%PC+30%MK+15%C$\underline{\text{C}}$+3%Gyp+0.5w/b (Future article, this data will be published elsewhere after the thesis and they are not discussed in this thesis), **c)** neat PC and **d)** PC-C$\underline{\text{C}}$ from previous paper of our research group, **e)** CAC-20 °C and **f)** CAC-4 °C both from Article 3 (A#3). In orthoslice **"a"** we see more water content as it is after 19 hours of hydration in an *in situ* experiment. In **"b"** we see the reacted MK content and there is more air content as the sample is after months of hydration. In **"d"** we can see the additional calcite components compared to **"c"** which is the neat PC. In sample **"f"**, that is CAC-4 °C, the anhydrous grains are larger and there are more hydrate components in comparison to **"e"**, this means that by raising the temperature to 20 °C, more reaction has taken place and the anhydrous grains will have the smaller particle size as hydration progresses.

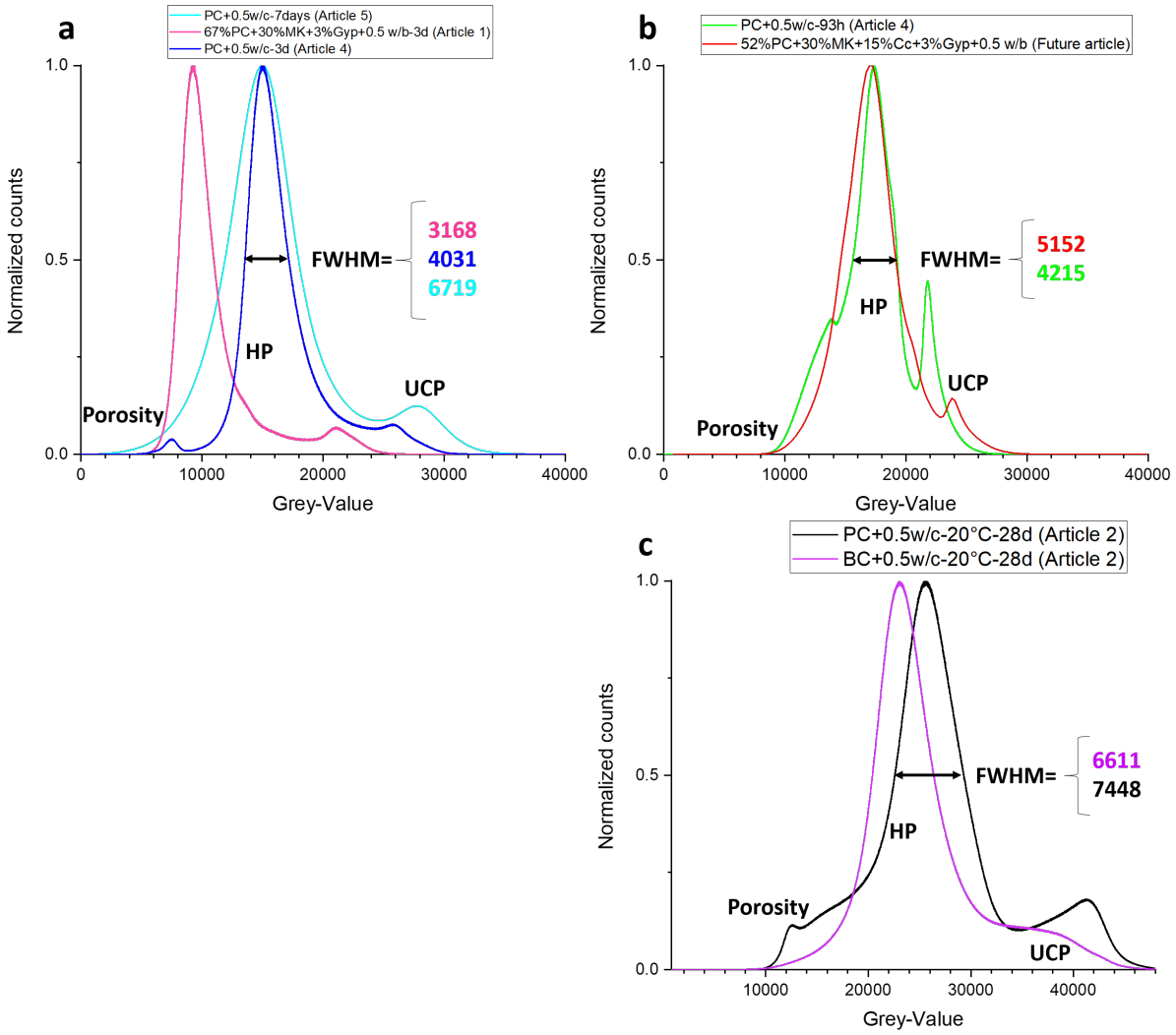

Figure 4.8: "Absorption" and "Phase-Contrast" modality histograms for the samples in Table 4.1. The three-component peaks are shown and the FWHM for the HP is calculated.
a) "Absorption" modality; sample PC+0.5 w/c-7days from Article 5 in pale-blue color, sample 67%PC+30%MK+3%Gyp+0.5 w/b-3days from Article 1 in pink-color, and sample PC+0.5 w/c-3days from Article 4 in dark-blue color.
b) ID19 "Phase-Contrast" modality; for the sample PC+0.5w/c-93hours from Article 4 in green-color, and sample 52%PC +30%MK +15%CC +3%Gyp+ 0.5 w/b from the Future article in red-color.
c) TOMCAT "Phase-Contrast" modality; for the sample PC+0.5w/c-20 °C-28days in black-color, and sample BC+0.5 w/c-20 °C-28days in purple-color both from the Article 2.

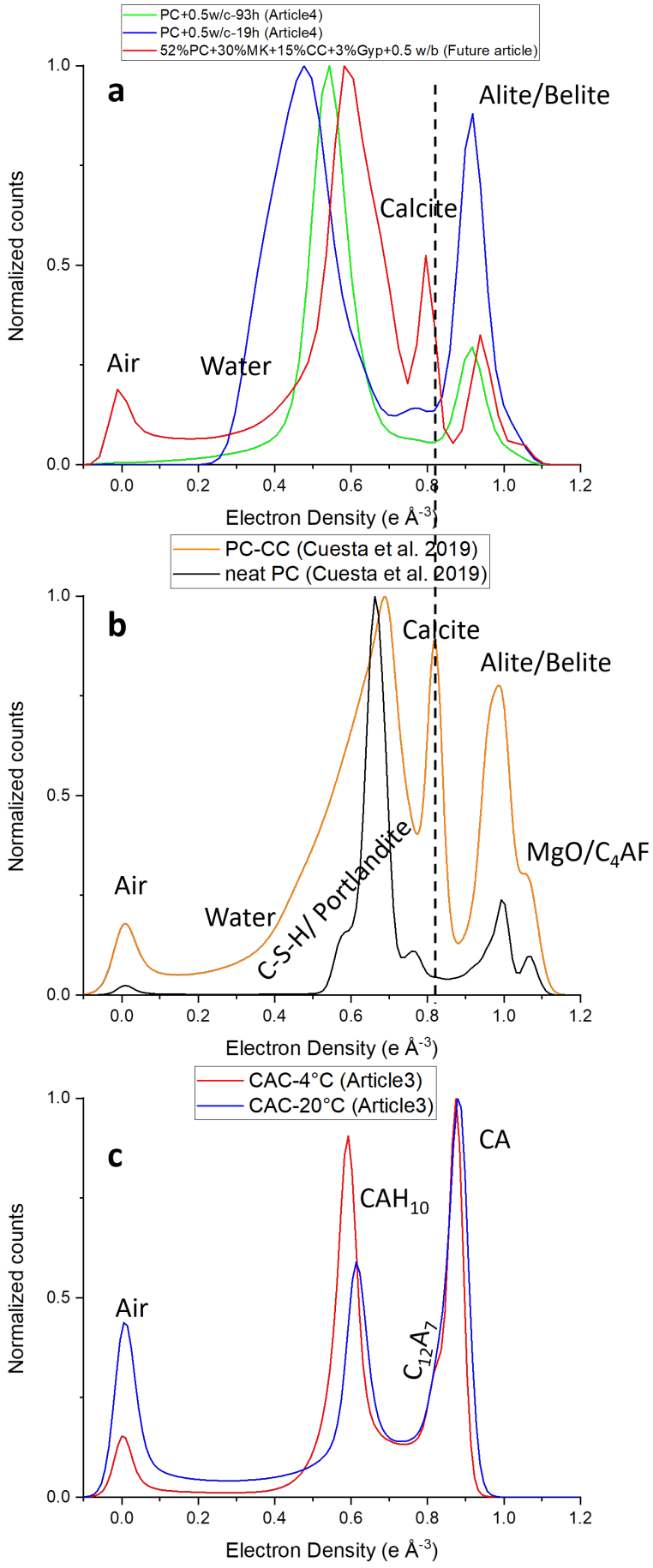

Figure 4.9: Synchrotron "Ptychography" modality histograms for the samples in Table 4.1. The components are labelled on the corresponding peaks. **a)** "Near-field Ptychography" modality for the sample PC+0.5w/c-19hours in blue-color and PC+0.5w/c-93hours in green-color both from Article 4. The sample 52%PC+30%MK+15%CC+3%Gyp+0.5w/b in red-color.**b)** "Far-field Ptychography" for the sample PC-CC in orange-color and the sample neat PC from previous work of our research group. **c)** "Far-field Ptychography" for the sample CAC-4 °C in red-color and sample CAC-20 °C in blue-color both from the Article 3.

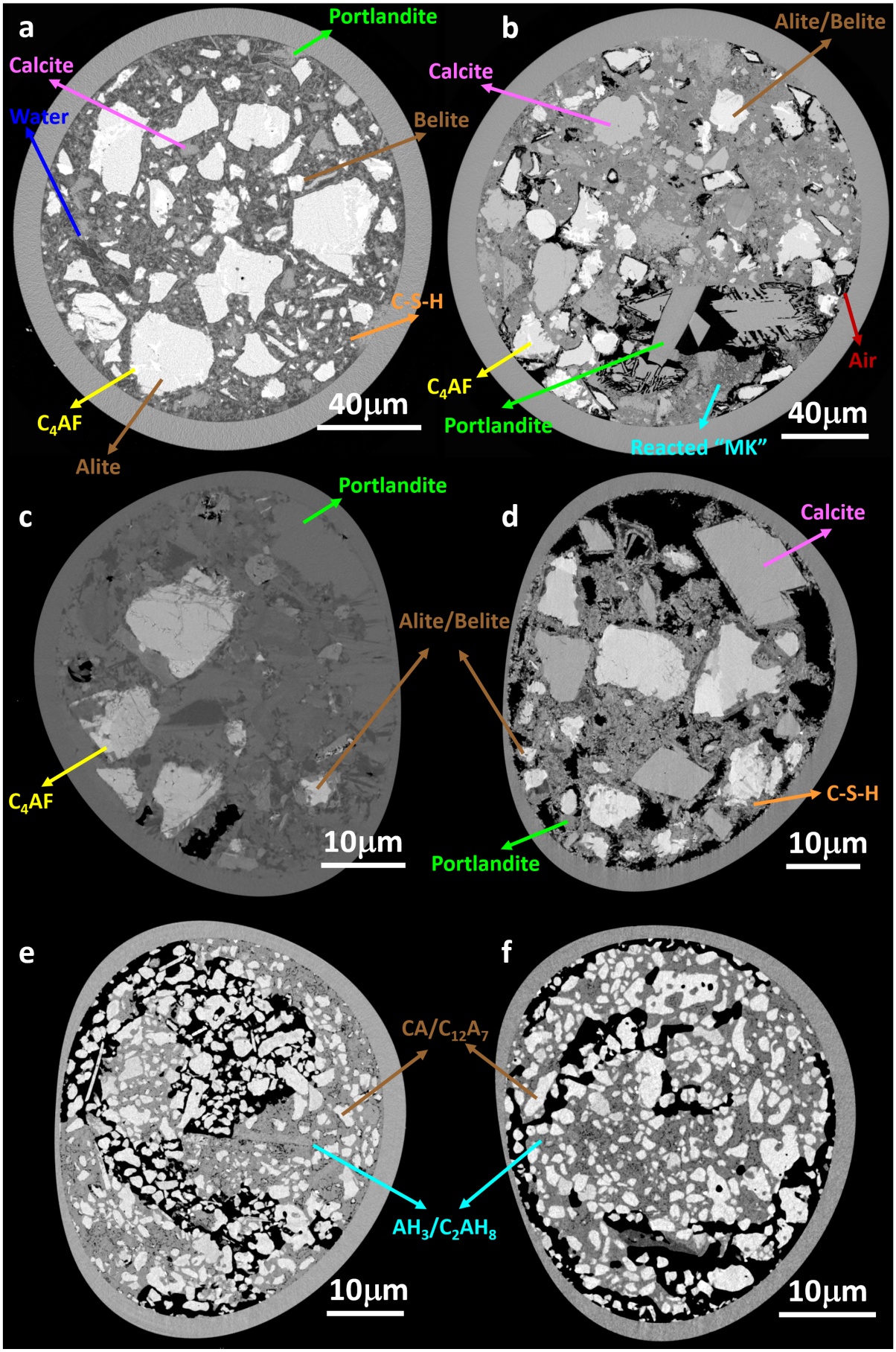

Figure 4.10: "Ptychography" modality components for the samples in Table 4.1 and Figure 4.9. The components are shown on the selected orthoslices. **a)** "Near-field Ptychography" modality for the sample PC+0.5w/c-19hours from Article 4.**b)** "Near-field Ptychography" modality for the sample 52%PC+30%MK+15%C$\underline{\text{C}}$+3%Gyp+0.5w/b. **c)** "Far-field Ptychography" for the sample neat PC **d)** "Far-field Ptychography" for the sample PC-C$\underline{\text{C}}$ from previous work of our research group. **e)** "Far-field Ptychography" for the sample CAC-20 °C and **f)** "Far-field Ptychography" for the sample CAC-4 °C both from the Article 3.

4.2 Segmentation

The technique of dividing an image into different Regions of Interest or segments to facilitate further image analysis is known as segmentation. There are different types of segmentation, and in this thesis we outline the types that are used.

4.2.1 Thresholding

This strategy involves setting a threshold and assigning pixels above or below that threshold to separate main phases/components. It works effectively for images with a strong contrast between the components. Global Thresholding (GT) is a method used in image analysis to distinguish Region of Interest (ROI) or sample components from the background/-surroundings. In this approach, based on the intensity levels of the pixels in the scanned image, it attempts to determine an appropriate intensity value (known as an "interval" in image processing software packages) that classifies different phases/components. This threshold is usually calculated by visually examining the statistical histogram of the image. The histogram shows the distribution of pixel intensities across the image or in the selected Volume of Interest (VOI). This means that for complex materials containing phases/components with close intensities/grey values, this interval would be difficult to select. The "Otsu's method" is the simplest and most generally used automatic global threshold selection algorithms, which assumes the image comprises only two types of pixels: object and background. "Binarization" is the term used to describe the process of segmenting an image into two classes, producing a black and white binary image from a grey level input.

Global Thresholding (GT) has limitations, and in some circumstances, images with complicated intensity (such as cementitious materials) distributions may lead to incorrect segmentation. In such cases, more complex thresholding techniques or adaptive thresholding approaches that take into account local image features may be required. The tangent-slope technique of the Grayscale Histogram (GSH) is another approach for selecting the greyscale threshold and in the absence of obvious valleys

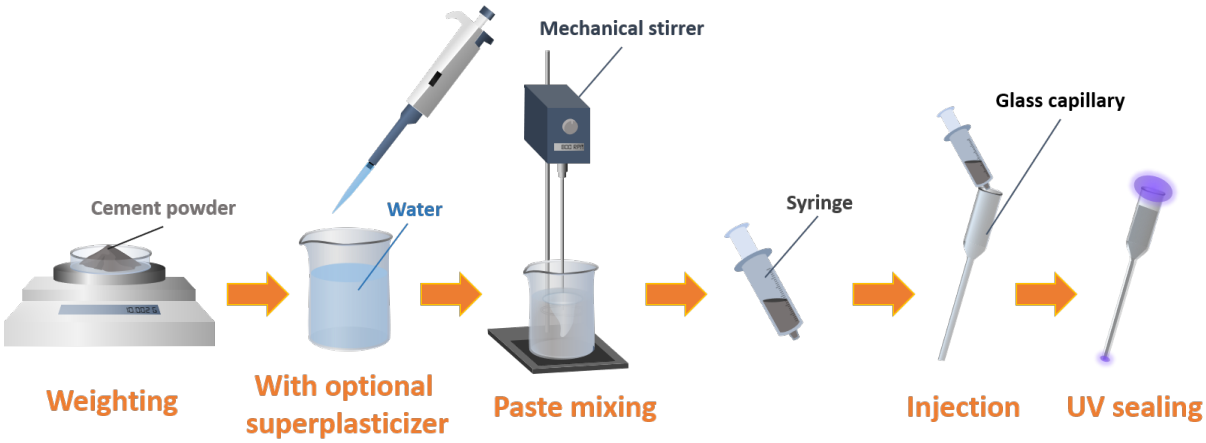

Figure 4.11: Capillary sample preparation steps.

between the contributions. For example, for the *ex situ* samples of Article 2 (A#2) in section 3.2, the greyscale threshold distinguishing the porosity from the hydrate phase was determined as the point at which the tangent-slope changed for both contributions, and for the unhydrate phase the histogram valley grey value was chosen.

After all this, and with the knowledge we have today, in the last paper we submitted: we brought the precise *in situ* imaging from the synchrotron (Article 4 (A#4) in section 3.4) to our laboratory imaging and combined it with complementary tests, see Article 5 (A#5).

In this experiment, we followed the optimized sample preparation for Article 4 (A#4) in section 3.4 as is shown in Figure 4.11 but for a larger FOV so the nominal capillary diameter is 2mm. The images were acquired on a SKYSCAN 2214 scanner from Bruker Corporation (see the 1.2.5.1 descriptrion). In this work, we adapted another sample holder (as is shown in Figure 4.13) for having the dual alignment for both LXRPD and Laboratory X-ray Computed Microtomography (μCT) tool for more accurate comparison. Scans were obtained with an X-ray tube using a LaB_6 source (operated at 55 kV and 130 mA) and employing a 0.25 mm Al foil to reduce beam hardening. The capillary was rotated 360° during data acquisition. Images were taken every 0.2, i.e., 1801 projections, with an exposure time of 2.0 s resulting in an overall recording time of 3h:45m per scan. The geometrical settings were a source-to-object distance of 9.953 mm and an object-to-detector distance of 305.496 mm. The detector system was the CCD3 which has a physical pixel size of 17.4 μm (binning 2 × 2), which together with the geometric settings resulted in a voxel size of 1.1 μm.

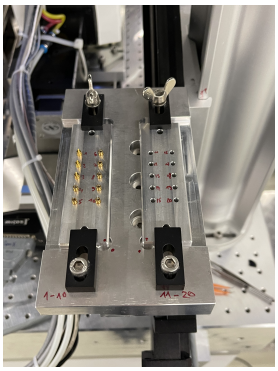

Figure 4.12: flOMNY sample stage tray.

For post-processing, the same region and section of all five overlayed CT scans (i.e. the scan is from exactly the same section of the capillary) were used for segmentation and further data analysis.

As indicated in chapter 3 for Article 4 (A#4) in section 3.4 (see Article 4 (A#4) in section 7.3 Supplementary Information in chapter 7), data re-alignment was first thoroughly investigated. The capillary position was particularly accurate for the PXCT because the capillary/holder system was installed by the flOMNY gripper (robot) from the tray storage (see Figure 1) to the sample stage. As a result, the angular orientation of the

Figure 4.13: Custom designed sample holder.

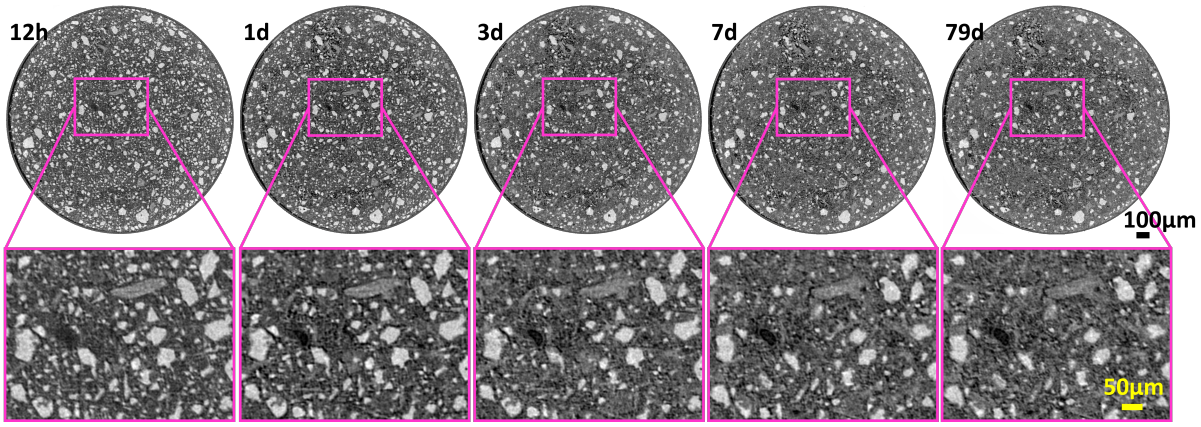

Figure 4.14: *in situ* Laboratory orthoslices over time. Microtomographic orthoslices in 12 hours, 1, 3, 7 and 79 days studied hydration ages (top); the same close-up view to follow-up the paste changes during ages (below).

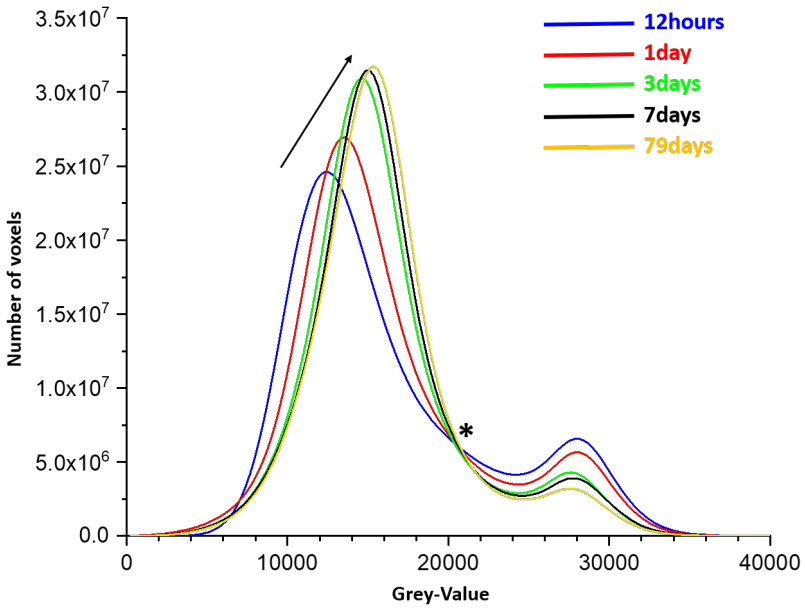

Figure 4.15: *in situ* Laboratory grayscale histogram.

sample was maintained. For Article 5 (A#5), to reduce the variability of the initial incidence angular position, a mark was placed on the specimen holder (the custom designed holder shown in Figure 4.13) and specimen height stabiliser for the incident beam. Automatic registration was used to align the multiple scans in this Lab-μCT. We modelled the capillary as a cylinder and centred the cylinders in the reconstructed volume. As we marked the scan zone, automatic registration was implemented for rotations around axes for the same single capillary. By superimposing identifiable landmarks in the comparison images, the identical scanned slices were visually located. The exact same slice of the single specimen in this study over time (in 12 hours, 1 day, 3, 7, and 79 days after hydration) is shown in Figure 4.14 in the top row and a magnified view of the exact region in the bottom row to show the evolution of hydration and visible features in the acquired μCT setup. The dissolution of the anhydrous particles and the appearance of hydrates can be seen at each time step.

Due to the setup voxel size (1.1 μm) to some extent a conversion of water to air porosity can be seen mostly by the blurriness in the 12h scan which means more water content in an early age cement sample and after densification for example at 7 or 79days, the air porosity is shown in more blackish colour as the water consumption results in a higher contrast between the components, which is in agreement with the result that we reported in Article 4 (A#4) in section 3.4.

Table 4.2: Comparison of the crossing point and global threshold results

Sample	Valley Threshold Grey-Value **(Volume%)**	Crossing Point Grey-Value **(Volume%)**	LXRPD	Error † of "Vally"	of "Crossing"
PC-79d [Article 5]	24,800 ***(6.9%)***	20,500 ***(13.4%)***	***(12.4%)***	+5.5%	-1.0%

The "Error" is the threshold methods difference from the LXRPD result.

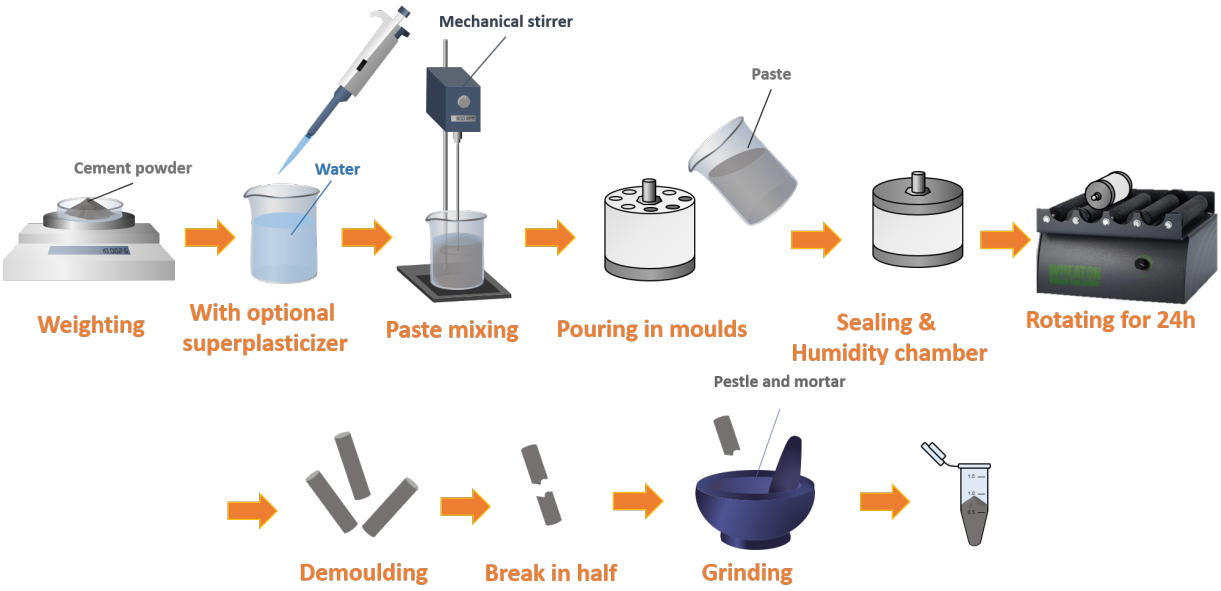

Figure 4.16: Cylinder preparation and demoulding steps.

Previously in Article 2 (A#2) in section 3.2, the evolution of cement at different ages was carried out in different samples (*ex situ*), which didn't allow the selection of certain threshold intervals for segmentation and also made the visualization of the evolution of porosity with time difficult, as described above. However, by being able to select the exact same region in the *in situ* scans, we see the appearance of a **"crossing point"** (located just before the valley of the unhydrated phase). This **"asterisk point (*)"** in Figure 4.15 is the threshold that can be used for all the scans, making the volume percentage of the unhydrated phase more precise and comparable at each hydration age.

In order to verify our published result and to have a sense of the magnitude of the error that can occur in conventional global threshold and tangent-slope methods, we revised one of the samples from Article 5 (A#5) in section 3.5 and obtained these values in Table 4.2

Partial Volume Effect It should be mentioned that the partial volume effect and the application of the enhancement filter would affect this intersection and the valley, which directly affect the chosen threshold. Therefore, for this comparison we studied the reconstructed "Absorption" dataset and not the "Paganin" dataset used for the segmentation in Article (A#2) in section 3.2.

In the same study we prepared the paste cylinder for other complementary tests as shown in Figure 4.16 and for the LXRPD studies we obtained the curves in Figure 4.17.Rietveld plots for the pastes in **(a)** capillary for 1 d; **(b)** capillary for 7 d; **(c)** sealed bag for 7 d; and **(d)** CH-saturated solution for 7 d.

4.2.2 Machine Learning

Machine learning (ML) has shown great promise in a variety of fields, and we are seeing its use increase in the field of X-ray imaging and data analysis. However, it is important to understand the limitations of this

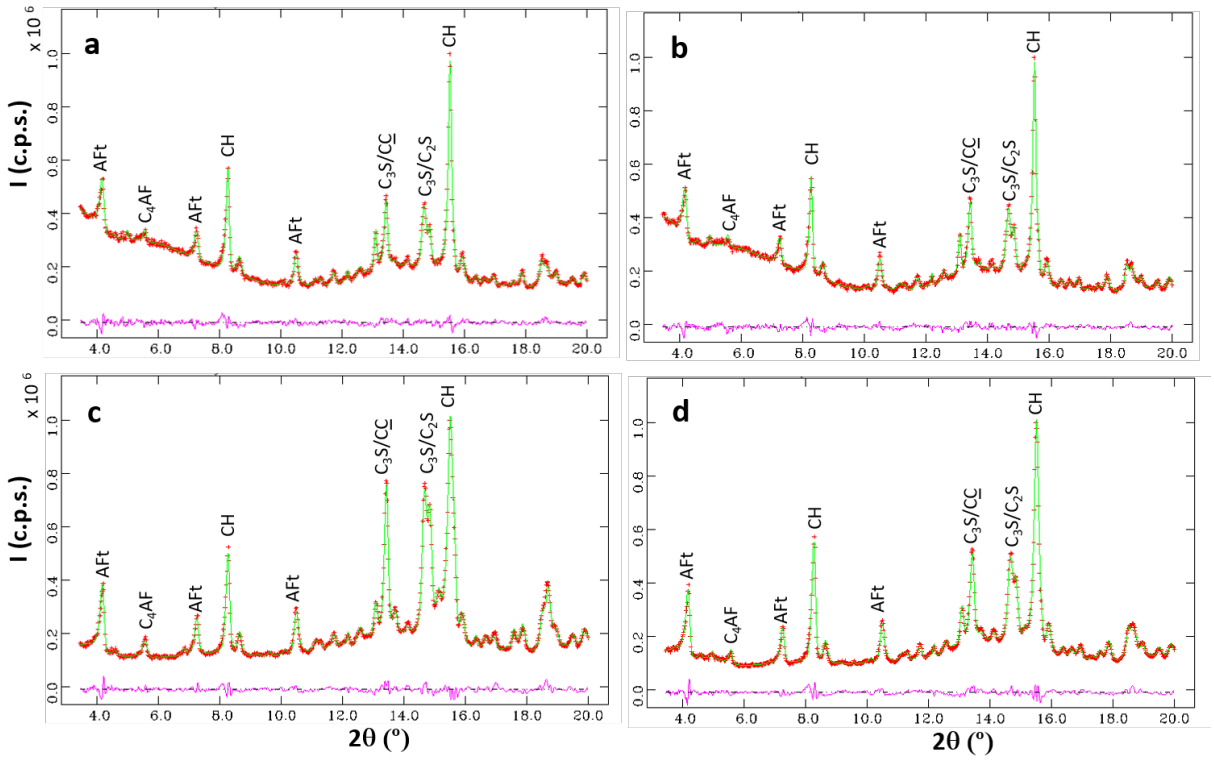

Figure 4.17: *in situ* LXRPD Rietveld plots.Mo-Kα_1 (λ=0.71 Å) Rietveld plots for **a)** CH-paste hydrated for 7 days; **b)** sealed bag-paste hydrated for 7 days, **c)** *in situ*-paste hydrated for 1 days; and **d)** *in situ*-paste hydrated for 7 days.

technique for our specific studies of cementitious materials. Machine learning algorithms differ from conventional algorithms in that the tasks they have to perform are not explicitly programmed. In fact, these algorithms rely on learning methods to best match a function giving an expected output as a function of a given input. There are three main categories of machine learning:

1. **unsupervised learning**, i.e. the algorithm has no ground truth enabling it to learn the task in hand; it learns directly from the input data.
2. **supervised learning**, i.e. the model learns from ground truth data, in the form of a pair (theoretical input, theoretical output), thus requiring external assistance, since it is necessary for a user to provide this theoretical data.
3. **semi-supervised learning**, which combines supervised and unsupervised methods, since this time the data on which the model will learn is only partially labeled, i.e. it only corresponds to an approximate ground truth, which can often be the case when data labeling is laborious.

Among these broad categories, the one we're interested in concerns supervised learning models. Indeed, even if image labelling can sometimes be laborious, it's preferable to use this type of model when labelling is possible, since it may give better results. An example of Ground Truth labelling is shown in Figure 4.18. The first learning algorithms are decision trees, which classify data according to different criteria. As shown in Figure 4.19, at each node, the algorithm seeks to classify a criterion, which then determines which node it will go to. If the criterion matches,

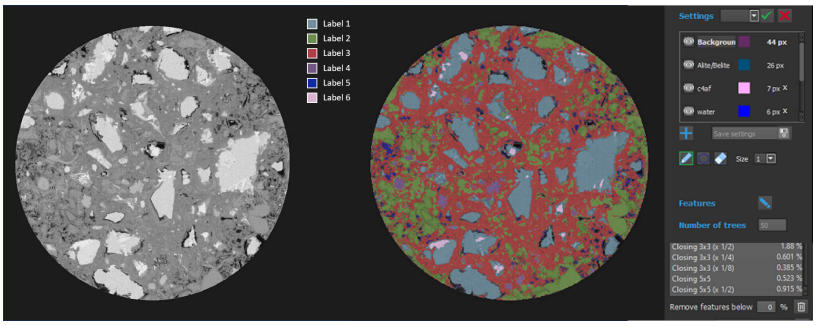

Figure 4.18: Labelling process on IPSDK software explorer.

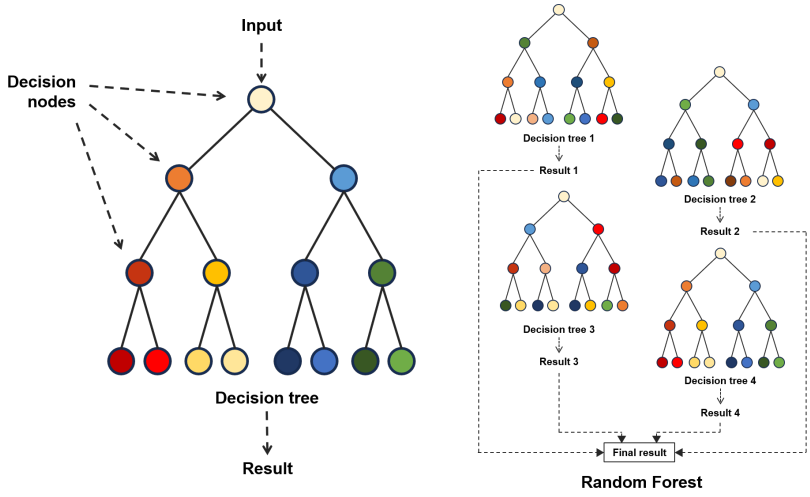

Figure 4.19: ML decision tree

it follows a first branch, otherwise it follows an alternative branch. These algorithms seek to determine the best criteria for classifying input data into one category or another, as in the Classification and Regression Tree (CART) algorithm, for example.

In 1996, Breiman proposed a method known as bagging (Breiman 1996), in which multiple methods are trained on several subgroups of data, starting from an initial group of data. These subgroups are not totally independent and share some of their data. This method then combines these models to produce solutions that are more accurate than conventional decision trees.

In 2001, Breiman proposed a new method that is now widely used: the **Random Forest** method (Breiman 2001). This method is an extension of the bagging method, with the addition of **"feature randomness"**. In a normal decision tree, each node looks for the feature that best discriminates the input data. In the case of **"feature randomness"**, the node will draw from a random sub-group of features to perform its discrimination, resulting in more diverse and less correlated decision trees. This is the method used by IPSDK to classify the pixels in the images it has trained on.

The data on which Machine Learning algorithms are trained is extremely important. If the training data does not sufficiently represent the full range of changes and circumstances observed across our entire VOI, the algorithm may not successfully generalise to the remaining untrained/unseen data. This can lead to poor performance and inaccurate predictions.

Moreover, the quality and variety of the input data can have a significant

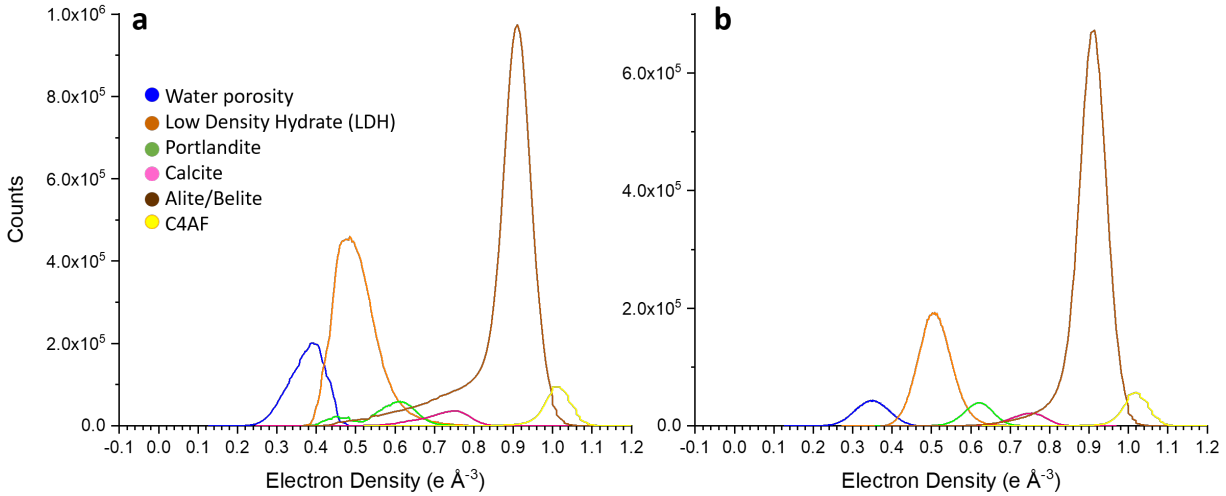

Figure 4.20: Partial volume effect in quantitative analysis in Near-field Ptychography. **a)** The components mean electron density values without reducing the partial volume effect on the border of the components. **b)** The components mean electron density values after reducing the partial volume effect.

impact on its performance. Data that is low resolution, noisy or poorly labelled can introduce errors and inaccuracies into the training process. Furthermore, differences in imaging techniques and acquisition can make it difficult to obtain robust and trustworthy results.

This is the reason that for each of our *in situ* imaging modalities (with the same acquisition circumstances) in Article (A#4) in section 3.4, we were able to use almost the same ML model, with only slight changes in the 19h scan, due to the existence of more water content at this hydration age. This means that one of our components needs to be labelled more in the training step. The data handling flowcharts for this article are described in the Supplementary Information of Article 4 (A#4) in the chapter 7 in the section 7.3.

Some machine learning algorithms, especially deep learning in our cement sample case, faced problems. This is because deep learning requires a lot of RAM as well as a good GPU. This may not seem like a big issue when working on large facilities such as synchrotrons, but having hundreds of data waiting to be analysed and lack of computing power can be problematic, especially when access to a cluster or supercomputer is not possible. Because cement is a complicated substance, the deep learning technique needs a large amount of annotated training data to learn well. However, obtaining this type of annotated data on a GPU can be difficult and time-consuming, and doing so on a workstation was problematic. It took a long time to detect insufficient or incorrect predictions from the annotated data, which meant that more and more trained slices had to be added to the models.

That's why we moved to ML approaches that use the Random Forest algorithm, and the training and tuning only requires suitable RAM depending on the dataset size (16bit, etc.) and a good CPU for calculating the quantitative analysis that we are aiming at (no need for a super good GPU).

As we mentioned that the partial volume effect would affect the threshold segmentation, it would also affect the quantitative analysis. In Figure 4.20,

histogram of the PC 19h of the cSAXS *in situ* experiment (Article 4 (A#4) in section 3.4) is shown and by providing the overlapped components by the machine learning segmentation, we show that if we eliminate a few pixels belonging to the partial volume effect, the measured mean electron density of the Gaussian peak of each phase would be more accurate and close to the expected theoretical values. This is somehow another proof that we need ML to treat these effects of our quantitive analysis.

Table 4.3: Comparison of LXRPD and µCT results from the Global Thresholding and Machine Learning approaches.

Sample [*in situ*-Article 5]	Components	LXRPD	Global Threshold (GT) [vol%]	Machine Learning (ML) [vol%]
12h	HP	-	77.2%	71.3%
	UCP	-	22.8%	28.7%
1d	HP	78.5	79.9%	76.2%
	UCP	21.5	20.1%	23.8%
3d	HP	84.1	84.0%	83.2%
	UCP	15.9	16.0%	16.8%
7d	HP	85.5	84.8%	84.2%
	UCP	14.5	15.2%	15.8%
79d	HP	87.6	86.6%	87.1%
	UCP	12.4	13.4%	12.9%

In Article 5 (A#5) in section 3.5, we compared the result of Laboratory X-ray Powder Diffraction (LXRPD) with Global Threshold (GT) and Machine Learning (ML) for the *in situ* Laboratory. In Table 4.3, low-density Hydrate Phase and high-density Hydrate Phase derived from Machine Learning (ML) have been summed as a single Hydrate Phase (HP) for comparison to Global Thresholding (GT). These reported data have been renormalised to remove the (air) porosities, i.e. the results are shown with respect to the HP and UCP contents. Firstly, at 12 hours there is a significant disagreement and GT of 12 hours is not correct, which is known from the reactivity of cement in the books and also from calorimetry. Secondly, at 7 days both GT and ML give us accurate measurements. Overall, it is true that GT may be an easier approach to apply in some cases, but we prefer to use ML because we would like to study complicated samples in the future investigation.

Conclusion 5

The main goal of this thesis is to contribute to the establishment of methodologies and optimisation of sample preparation for quantitative analysis of cementitious materials using X-ray imaging for cement hydration monitoring.

In Article 1 (A#1), we conclude that in synchrotron microtomography experiments, a sample-to-detector propagation distance increases the contrast in the Paganin-reconstructed datasets. This experimental setup and data processing approach produces tomograms in which calcite can be clearly distinguished from the other components. We also used a similar propagation distance in Article 4 (A#4) to take advantage of this component enhancement and we demonstrated this contrast enhancement in chapter 4.
Although tiny capillaries with a nominal diameter of 0.5 mm provide a limited Field of View and thus superior spatial resolution, conventional filling of narrow capillaries with cement pastes resulted in poor repeatability of the w/b ratios of the scanned samples. We have therefore used larger capillaries, 2.0 mm of nominal diameter, for scanning in other articles such as Article 5 (A#5), but for some of the imaging modalities such as "Ptychography", where we have a limited FOV, we still have to stick to the smallest possible diameter narrower than 250 microns.
In Article 1 (A#1), tomography scans and laboratory X-ray powder diffraction data were collected over time in the same hydration capillary. This showed us the potential to improve the understanding of hydration and reactions, which we followed in 4D nanoimaging of Article 4 (A#4) to study hydration in the exact same sample.

In Article 2 (A#2), propagation-based phase contrast imaging was used to show that the mechanical strength of BC cements improved with curing temperature in the tested range of 20 to 60 °C. This is in contrast to the normal behaviour of PCs, where mechanical strength deteriorates with increasing curing temperature. Two results explain why BC has higher mechanical properties at higher curing temperatures. The difference in the activation energies of C_2S and C_3S is the most important contributing element. Quantitative Rietveld phase analysis showed that changing the curing temperature from 20 to 40 °C increased the degree of belite hydration from 54% to 78% at 28 days for the BC studied.
The curing of the Belite cement at mild temperatures did not result in a significant coarsening of the porosity. When cured at 60 °C, the hydration degrees of alite and belite were almost comparable (87 and 88% respectively) after 28 days of hydration of the Belite cement.

In Article 3 (A#3), the described $CaAl_2O_4$ hydration processes have been validated by mass density analysis of the products, and the hydration products of $CaAl_2O_4$ have been studied as a function of hydrating temperature using X-ray synchrotron ptychographic nanotomography. The first innovative aspect of this study is the determination of the mass densities of the resulting $Al(OH)_3$ gels. The resulting mass densities

for samples hydrated at 4, 20 and 50 °C are 1.94, 1.98 and 2.23 g/cm^3 respectively, assuming that the gels have an $Al(OH)_3$ composition. These results are lower than the standard value of 2.42 gcm^3 for $Al(OH)_3$ with a gibbsite crystal structure. Secondly, the study of a sample hydrated at 4 °C for 2 months and then held at 50 °C for 3 months to induce the conversion of the CAC hydrated reactions was critical to the results. The secondary water porosity created by the hydrate conversion was quantified using ptychographic nanotomography. This secondary porosity appears to form at the mesoscale with an average pore diameter of 140 nm.

In Article 4 (A#4), PC-52.5 was used for the *in situ* X-ray Computed Tomography (XCT) study to capture more hydrated particles, while PC-42.5 was used for the synchrotron CT imaging study. During hydration, PC-52.5 emitted more heat than PC-42.5, indicating greater reactivity, as expected. The degree of hydration (DOH) was assessed at 19, 47 and 93 hours of hydration and used as a reference for the imaging experiments. The PXCT scan showed superior resolution and contrast but limited field of view compared to the synchrotron and laboratory CT studies. The results of the laboratory CT and PXCT studies were very similar, demonstrating the significance of the nanoimaging findings.
Both explained edge sharpness and Fourier Shell Correlation methods were used to determine the spatial resolution of the imaging data. As expected, the spatial resolution of the different imaging modalities varied, with PXCT having the highest resolution. The obtained value for "Near-field Ptychography" was close to 250 nm in this *in situ* experiment. Generally, the PXCT imaging approach provided extensive information on the cement hydration process, including visualisation of the C-S-H gel shell and porosity gaps. The results highlighted the need to use appropriate imaging techniques to effectively capture the relevant features and understand the cement hydration mechanisms.
The PC paste imaged by PXCT has a water/cement ratio (w/c) of 0.41, which is consistent with the reported hydration levels. Radiation damage was investigated but found to be minor. It was possible to identify seven sets of components: air, water, AFt/C-S-H gel/other, CH, C$\underline{\text{C}}$, $C_3A/C_3S/C_2S$ and C_4AF in the tomograms. The measured and predicted electron densities differed due to partial volume effects mainly caused by residual water porosity below the measurement resolution.
The key findings of the study highlight sub-micron aspects of cement hydration. PXCT successfully distinguishes between air and water porosity based on electron densities. The evolution of the cement paste over time shows the consumption of capillary water, the densification of the C-S-H gel and the appearance of air-containing regions which is a feature of the chemical shrinkage. The study of etch-pits shows a reduction in certain areas during the deceleration phase. The spatial dissolution rate of alite was measured to be faster, with smaller alite particles dissolving faster than larger ones. Alite particles smaller than 3 μm are completely hydrated within 19 hours, resulting in a spatial dissolution rate of 100 nm/h in the acceleration period. The largest size of Hadley grains found here agrees well with previous studies (at 24 hours), which show a maximum size of 5 μm with shells of 500 nm. From the data analysis in the deceleration period, 19h to 47h, the measured alite dissolution rate was 25nm/h. As a result, there appears to be a 3-4 fold difference in the spatial dissolution rate of small alite grains during acceleration versus

large alite grains during deceleration. The hydration of alite particles, the formation of C-S-H gel shells surrounding the alite grains and the passage of water through these shells were observed. Water-filled areas within calcite particles were also seen, as was C-S-H gel dissolving to form dry capillary pores. The growth rate of the alite etch-pit is estimated to be 40 nm/h between 19 and 47 hours and 7 nm/h between 47 and 93 hours. In addition, the visible coalescence of many branches, known as etch-pit coalescence, was recorded.
By quantitative analysis of different imaging techniques, the study used data to evaluate the hydration process of Portland cement (PC) at high spatial resolution. The results show that tiny particles (less than 3 μm) dominate PC hydration in the early stages (1 day), but larger alite particles (about 10 μm) dominate hydration after 3 days. The study also showed the formation of C-S-H gel shells around alite grains and the decreasing dissolution rates of alite particles with time.
The measured electron densities for "Portlandite" at 19 h and 93 h were 0.62 eÅ^{-3} and 0.651 eÅ^{-3}, which is lower than the 0.69 eÅ^{-3} theoretical value. Also, the measured "C-S-H shell" at 19 h was 0.47 eÅ^{-3}, which is lower than the value of 0.64 eÅ^{-3} obtained value for "C-S-H gel" in our research group's previous investigation for a mature paste (Cuesta et al. 2019). These lower values may be due to a partial volume effect, as there is more water in the early stages of hydration that can be occluded within the segmented volumes. This water can not be distinguished due to the attained spatial resolution, close to 250 nm.

In Article 5 (A#5), the thick capillaries are essential for excellent powder averaging and avoidance of self-drying. Article 5 (A#5) presents a precise experimental technique for *in situ* cement hydration studies in thick glass capillaries, which avoids any post-mixing changes caused by sample conditioning. Capillary sealing prevents water loss and carbonation of the portlandite. X-ray microtomography and Mo-Kα_1 X-ray powder diffraction are combined to study the pastes.
To test the accuracy of the proposed in situ process for PC w/c=0.50, the identical material was cured ex situ and quantitatively analysed by thermal analysis and powder diffraction. Thermal analysis, *ex situ* powder diffraction and *in situ* powder diffraction all indicated Portlandite concentrations of 13.8, 13.1 and 12.5 wt% respectively. In addition, a mass balance estimate based on the reacted fractions of C_3S and C_4AF yielded 13.1 wt% CH. Despite the lack of sulphates at later hydration ages, AFt grows with time up to 77 days without showing signs of partial transition to AFm.
Finally, it is shown that the segmentation results from the laboratory μCT data provide accurate information when this methodology is applied. The ML and GT results of this paste at 79 days were 87.1/12.9 and 86.6/13.4 vol% (for HP/UCP) respectively. Rietveld quantitative phase analysis of the powder diffraction data at this age gave an HP/UCP ratio of 87.6/12.4. The agreement is noteworthy.

To end, the future development is discussed with due precaution. On the one hand, X-ray tomography in their different modalities (phase contrast, absorption, etc.) is being employed for the study and quantification of the pore network topological evolution of pastes and mortars. This application is envisaged only as a first approximation and with a severe

problem. The spatial resolution that it can be obtained is about 1 mm, if a larger field of view is to be mapped out. This is much larger that relevant porosity features, which have dimensions in the range 10-100 nm. In order to improve the spatial resolution to about 200nm (still large) a field of view must be strongly reduced which may yield poor statistics / reproducibility.

Moreover, to go beyond 100 nm may imply large scanning times resulting in radiation damage. On the other hand, ptychographic X-ray imaging can yield a spatial resolution ranging 200-300 nm and excellent electron density contrast (between components) and very good contrast to noise ratio. Our proof-of-concept investigation has showed its potential (Shiva Shirani et al. 2023). The obtained results could be extended to the acceleration stage, and the roles of the commercially-employed admixtures (e.g. superplasticisers, accelerators) can established; or at least some specific features during early age cement hydration. Moreover, the reactivity (hydration) of amorphous component(s), within the SCMs, could also be followed which is a clear advantage over powder diffraction. The reported investigations, using advanced X-ray imaging techniques, have only scratched the surface.

Conclusiones (Spanish conclusion)* 6

El objetivo principal de esta tesis es contribuir a establecer metodologías y a la optimización de la preparación de muestras para el análisis cuantitativo de materiales del cemento utilizando técnicas que usan imágenes de rayos X para la monitorización de la hidratación del cemento.

En el artículo 1 (A#1), concluimos que en experimentos de microtomografía sincrotrón, la distancia de propagación muestra-detector aumenta el contraste en los conjuntos de datos reconstruidos por Paganin. Esta configuración experimental y este enfoque de procesamiento de datos produce tomogramas en los que la calcita puede distinguirse claramente de los otros componentes. También utilizamos una distancia de propagación similar en el artículo 4 (A#4) para aprovechar esta mejora de los componentes y demostramos esta mejora del contraste en el capítulo 4.

Aunque los capilares con un diámetro nominal de 0.5 mm proporcionan un campo de visión limitado y, por tanto, una resolución espacial superior, el llenado convencional de capilares muy pequeños con pastas de cemento dio lugar a una escasa repetibilidad de las relaciones w/b de las muestras escaneadas. Por lo tanto, hemos utilizado capilares más grandes, de 2.0 mm de diámetro nominal, para llevar a cabo las medidas en otros artículos como el artículo 5 (A#5), pero para algunas de las modalidades de imagen como la "pticotomografía", en la que tenemos un FOV limitado, todavía tenemos que usar un diámetro muy pequeño, en torno a 250 micras.
En el artículo 1 (A#1), se recogieron tomografías y datos de difracción de polvo de rayos X de laboratorio a lo largo del tiempo en el mismo capilar de hidratación. Esto nos mostró el potencial que tiene la metodología para mejorar la comprensión de la hidratación y las reacciones. Como ejemplo, en el artículo 4 se estudia la hidratación exactamente en la misma muestra, a través de la metodología de nanoimagen en 4D.

En el artículo 2 (A#2), se utilizaron imágenes de contraste de fases basadas en la propagación para demostrar que la resistencia mecánica de los cementos belíticos mejoraba con la temperatura de curado en el intervalo ensayado de 20 a 60 °C. Esto contrasta con el comportamiento normal de los cementos de Portland, en los que la resistencia mecánica se deteriora con el aumento de la temperatura de curado. Dos resultados explican por qué el cemento belítico tiene mayores propiedades mecánicas a temperaturas de curado más altas. La diferencia en las energías de activación de C_2S y C_3S es el elemento contribuyente más importante. El análisis cuantitativo de fases de Rietveld mostró que el cambio de la temperatura de curado de 20 a 40 °C aumentaba el grado de hidratación de la belita del 54% al 78% a los 28 días para el cemento belítico estudiado. El curado del cemento belítico a temperaturas intermedias no produjo un

* Note: The abbreviations used in the Spanish summary and Spanish conclusion are the same as those used in the English, which are listed in the "Spatial Terms" section.

engrosamiento significativo de la porosidad. Cuando la muestra se curó a 60 °C, los grados de hidratación de alita y belita fueron casi comparables (87 y 88% respectivamente) después de 28 días de hidratación del cemento belítico.}

En el artículo 3 (A#3), los procesos de hidratación del $CaAl_2O_4$ descritos se han validado mediante el análisis de la densidad de masa de los productos, y se han estudiado los productos de hidratación del $CaAl_2O_4$ en función de la temperatura de hidratación utilizando pticotomografía de campo lejano. El primer aspecto innovador de este estudio es la determinación de las densidades de masa de los geles de $Al(OH)_3$ resultantes. Las densidades de masa resultantes para las muestras hidratadas a 4, 20 y 50 °C son de 1.94, 1.98 y 2.23 g/cm^3 respectivamente, suponiendo que los geles tienen una composición química $Al(OH)_3$. Estos resultados son inferiores al valor estándar de 2.42 gcm^3 para $Al(OH)_3$ con una estructura cristalina de gibbsita. En segundo lugar, el estudio de una muestra hidratada a 4 °C durante 2 meses y luego mantenida a 50 °C durante 3 meses para inducir la conversión de las reacciones que se dan en un CAC fue fundamental para los resultados. La porosidad secundaria del agua creada por la conversión del hidrato se cuantificó mediante pticotomografía. Esta porosidad secundaria parece formarse en la mesoescala con un diámetro medio de poro de 140 nm.

En el artículo 4 (A#4), el PC-52.5 se utilizó para el estudio *in situ* de tomografía computarizada por rayos X (XCT) para captar más partículas hidratadas, mientras que el PC-42.5 se utilizó para el estudio de imágenes CT de sincrotrón. Durante la hidratación, el PC-52.5 emitió más calor que el PC-42.5, lo que indica una mayor reactividad, como era de esperar. El grado de hidratación (DOH) se evaluó a las 19, 47 y 93 horas de hidratación y se utilizó como referencia para los experimentos de obtención de imágenes. El escáner PXCT mostró una resolución y un contraste superiores, pero un campo de visión limitado, en comparación con los estudios CT de sincrotrón y de laboratorio. Los resultados de los estudios CT de laboratorio y PXCT fueron muy similares, lo que demuestra la importancia de los hallazgos de nanoimagen. Para determinar la resolución espacial de los datos de imagen se utilizaron tanto los métodos de nitidez de bordes explicados como el de Fourier Shell Correlation. Como era de esperar, la resolución espacial de las distintas modalidades de imagen varió, siendo la más alta la de los estudios de nanoimagen. El valor obtenido para "pticotomgrafía de campo cercano" fue cercano a 250 nm en este experimento *in situ*.
En general, el método de obtención de imágenes PXCT proporcionó una amplia información sobre el proceso de hidratación del cemento, incluida la visualización de la cubierta de gel C-S-H y los huecos de porosidad. Los resultados pusieron de manifiesto la necesidad de utilizar técnicas de imagen adecuadas para captar eficazmente las características relevantes y comprender los mecanismos de hidratación del cemento. La pasta de cemento Portland obtenida mediante PXCT tiene una relación agua/cemento de 0.41, que coincide con los niveles de hidratación registrados. Se investigaron los daños por radiación, pero se comprobó que no era relevante. Fue posible identificar siete conjuntos de componentes: aire, agua, AFt/C-S-H gel/otros, CH, C$\underline{C}$, $C_3A/C_3S/C_2S$ y C_4AF en los tomogramas. Las densidades de electrones medidas y predichas diferían

debido a a efectos de volúmenes parciales causados principalmente por la porosidad residual del agua que esta por debajo de la resolución de la medición.
Las principales conclusiones del estudio destacan aspectos submicrónicos de la hidratación del cemento. PXCT distingue con éxito entre la porosidad del aire y la del agua basándose en las densidades electrónicas. La evolución de la pasta de cemento a lo largo del tiempo muestra el consumo de agua capilar, la densificación del gel y la aparición de regiones que contienen aire, característica de la contracción química. El estudio de etch-pits muestra una reducción en determinadas zonas de las partículas durante la fase de desaceleración. Se midió que la velocidad de disolución espacial de la alita era más rápida, y que las partículas de alita más pequeñas se disolvían más rápidamente que las más grandes. Las partículas de alita menores de 3 μm se hidratan completamente en 19 horas, lo que da lugar a una velocidad de disolución espacial de 100 nm/h en el periodo de aceleración. El mayor tamaño de los granos de Hadley encontrado aquí concuerda bien con estudios anteriores (a las 24 horas), que muestran un tamaño máximo de 5 μm con envolturas de 500 nm. A partir del análisis de los datos en el período de desaceleración, de 19h a 47h, la velocidad de disolución de la alita fue de 25 nm/h. Como resultado, parece haber una diferencia de 3-4 veces en la velocidad de disolución espacial de los granos pequeños de alita durante la aceleración frente a los granos grandes de alita durante la deceleración. Se observó la hidratación de las partículas de alita, la formación de las envolturas de gel alrededor de los granos de alita y el paso de agua a través de estas las envolturas. También se observaron zonas llenas de agua dentro de las partículas de calcita, así como gel disuelto para formar poros capilares secos. Se estima que la velocidad de crecimiento de los etch-pit en la alita es de 40 nm/h entre las 19 y las 47 horas y de 7 nm/h entre las 47 y las 93 horas. Además, se registró la coalescencia visible de muchas ramificaciones, lo que se conoce como coalescencia de etch-pit.

Mediante el análisis cuantitativo de diferentes técnicas de imagen, en este estudio se utilizaron datos para evaluar el proceso de hidratación del cemento Portland a alta resolución espacial. Los resultados muestran que las partículas diminutas (menos de 3 μm) dominan la hidratación del cemento Portland en las primeras etapas (1 día), pero las partículas de alita más grandes (unos 10 μm) dominan la hidratación después de 3 días. El estudio también mostró la formación de capas de gel alrededor de los granos de alita y la disminución de la velocidad de disolución de las partículas de alita con el tiempo.

Las densidades de electrones medidas para los distintos componentes se han comparado con los valores teóricos. Por ejemplo, la densidad de electrones medida para la "Portlandita" a las 19 h y 93 h fue de 0.62 e$Å^{-3}$ y 0.651 e$Å^{-3}$, que es inferior al valor teórico de 0.69 e$Å^{-3}$. Este valor inferior puede deberse a un efecto de volumen parcial, ya que hay más agua en las primeras edades de hidratación que puede quedar ocluida dentro de los volumenes segmentados. Esta agua no se puede distinguir debido a la resolución espacial que es cercana a 250 nm.

En el artículo 5 (A#5), los capilares de mayor tamaño son esenciales para

obtener un infinitas partículas al azar en el polvo y evitar el autosecado. En el artículo 5 (A#5) se presenta una técnica experimental precisa para estudios de hidratación del cemento *in situ* en capilares de vidrio de 2.0 mm, evitando así cualquier cambio posterior en la mezcla provocado por el acondicionamiento de la muestra. El sellado de los capilares evita la pérdida de agua y la carbonatación de la portlandita. Para el estudio de las pastas se combinan la microtomografía de rayos X y la difracción de rayos X en polvo Mo-Kα_1.
Para comprobar la precisión del proceso *in situ* propuesto para PC auga/cemento=0.50, el mismo material se curó ex situ y se analizó cuantitativamente mediante análisis térmico y difracción en polvo. El análisis térmico, la difracción de polvo *ex situ* y la difracción de polvo *in situ* indicaron concentraciones de Portlandita del 13.8, 13.1 y 12.5 % respectivamente. Además, una estimación del balance de masas basada en las fracciones de C_3S y C_4AF que habían reaccionado dió lugar a un 13.1% en peso de CH. A pesar de la falta de sulfatos en las edades de hidratación más tardías, AFt crece con el tiempo hasta 77 días sin mostrar signos de transición parcial a AFm.
Por último, se demuestra que los resultados de segmentación a partir de los datos de μCT de laboratorio proporcionan información precisa cuando se aplica esta metodología. Los resultados ML y GT de esta pasta a los 79 días fueron 87.1/12.9 y 86.6/13.4 vol% (para HP/UCP) respectivamente. El análisis cuantitativo de fase Rietveld de los datos de difracción de polvo a esta edad dio una relación HP/UCP de 87.6/12.4. La concordancia es notable.

Para finalizar, se discute aquí, con debida precaución, el desarrollo futuro. Por un lado, se está empleando la tomografía de rayos X en sus diferentes modalidades (contraste de fase, absorción, etc.) para el estudio y cuantificación de la evolución topológica de la red de poros en pastas y morteros. Esta aplicación se plantea sólo como una primera aproximación, pero tiene un grave problema. La resolución espacial que se puede obtener es de aproximadamente 1 mm, si se quiere escanear un campo de visión mayor. Esto es mucho mayor que el tamaño de las porosidad relevantes, que tienen dimensiones del orden de 10-100 nm. Para mejorar la resolución espacial a unos 200 nm (que sigue siendo grande) hay que reducir mucho el campo de visión, lo que puede dar lugar a estadísticas/reproducibilidades deficientes.
Además, ir más allá de los 100 nm puede implicar grandes tiempos de exploración, lo que provoca daños por radiación. Por otro lado, con las imagenes de rayos X por ticotomografía se obtiene una resolución espacial que oscila entre 200 y 300 nm y un excelente contraste de densidad electrónica (entre componentes) y una muy buena relación contraste/ruido. Nuestra investigación basada en la prueba de concepto ha demostrado su potencial (Shiva Shirani et al. 2023). Los resultados obtenidos podrían extenderse a la etapa de aceleración, y a los roles de los aditivos empleados comercialmente (por ejemplo, superplastificantes, aceleradores); o al menos a algunas de las características específicas durante la hidratación del cemento a edades tempranas. Además, la reactividad (hidratación) de los componentes amorfos, dentro de los SCMs, también puede ser seguida, lo cual es una clara ventaja sobre la difracción de polvo. Las investigaciones que se encuentran en bibliografía realizadas con técnicas avanzadas de obtención de imágenes de rayos X muestras estudios iniciales aún muy básicos.

Articles Supplementary Information

7

In addition to the publications in Chapter 3, this chapter provides supplementary information. It aims to provide additional information, supporting data and in-depth analysis that complements and enhances the conclusions presented in the original papers. This chapter provides a thorough overview of the research conducted and improves the validity and transparency of our work by delving into specific topics such as methodology, experimental results and supporting figures.

7.1 SI of Article 2 (A#2): Influence of curing temperature on belite cement hydration: A comparative study with Portland cement

7.2 SI of Article 3 (A#3): Calcium aluminate cement conversion analysed by ptychographic nanotomography

7.3 SI of Article 4 (A#4): 4D nanoimaging of early age cement hydration

Supplementary Information

4D nanoimaging of early age cement hydration

Shiva Shirani[1], Ana Cuesta[1], Alejandro Morales-Cantero[1], Isabel Santacruz[1], Ana Diaz[2], Pavel Trtik[3], Mirko Holler[2], Alexander Rack[4], Bratislav Lukic[4], Emmanuel Brun[5], Inés R. Salcedo[6] and Miguel A. G. Aranda[1]*

[1]Departamento de Química Inorgánica, Cristalografía y Mineralogía, Universidad de Málaga, 29071 Málaga, Spain.
[2]Laboratory for Macromolecules and Bioimaging, Paul Scherrer Institut, 5232 Villigen PSI, Switzerland.
[3]Laboratory for Neutron Scattering and Imaging, Paul Scherrer Institut, 5232 Villigen PSI, Switzerland.
[4]ESRF-The European Synchrotron, 71 Rue des Martyrs, 38000 Grenoble, France.
[5]Université Grenoble Alpes, Inserm UA7 STROBE, 38000 Grenoble, France.
[6]Servicios Centrales de Apoyo a la Investigación, Universidad de Málaga, 29071 Málaga, Spain.

*Corresponding author: g_aranda@uma.es

In the format provided by the authors and unedited

Table of contents:

- **Supplementary Methods**

Synchrotron X-ray computed microtomography experiment (Syn-μCT).

Microtomographic scans were acquired at the 150 m-long beamline ID19 of the European Synchrotron (ESRF) in Grenoble, France. A so-called single-harmonic undulator (type: u17.6, gap 16.5 mm) was chosen as a source due to its excellent photon flux density at a narrow bandwidth around approximately 19 keV photon energy. The u17.6 allows beamline ID19 to be operated only with the two mandatory windows (0.8 mm diamond in the front-end and 0.5 mm Beryllium in the experimental hutch) and an 0.7 mm-thick Aluminium attenuator and hence, guaranties a homogeneous wave front: which is suited for high-sensitivity measurements by means of inline propagation-based phase contrast. The propagation distance between sample and detector was set to 15 mm. The indirect high-resolution detector consisted of a so-called revolver-microscope by the French company OptiquePeter (Lentilly, France)[1], the system lens-couples an 8.7 μm-thin LSO:Tb (Tb-doped Lu_2SiO_5) single-crystal scintillator with a 10× Olympus microscope (0.3NA) to a sCMOS-based camera (type: pco.edge, PCO AG, Germany)[2]. The effective pixel size of the detector assembly is approximately 0.6 μm. 6000 projection angles were acquired over a 360 degree tomographic scan with an exposure time of 0.05 s, i.e. 5 minutes scan, at ~21.5 °C. During this experiment, the ESRF operated in so-called 4bunch timing mode with a reduced ring current of maximum 20 mA. The estimated flux density at the sample position was 4.2×10^{11} photons·s^{-1}·mm^{-2}. Phase retrieval of the projections was performed using the Paganin algorithm[3], considering the ratio of the refractive and absorption index δ/β equal to 70. In order to retrieve the microstructural content introduced by the inherent smoothing characteristics of the phase retrieval method, a Gaussian unsharp mask was applied. The voxel size with the employed configuration, to fully image a capillary of 0.7 mm of diameter, was 0.65 μm.

The tomographic reconstructions were performed using the open-source tomography software available at the ESRF, relying on the sub-packages NXtomoMill and NABU[4]. Given its straightforward Graphics Processing Unit (GPU)-based implementation, the full volume reconstructions were performed on the Power9 cluster using the gold-standard filtered back projection (FBP) algorithm. The projections are first corrected for beam profile illumination (flat field), dark current noise of the detector (dark field) and filtered for any potential pixel outliers arising from stray photons. The reconstructed volume, consisting of 2490×2490×1950 pixels, is cast to 16 bit format considering the 10-90% of the volume histogram and cropped to the region of interest. In the case of the reconstructions used for the Fourier Shell Correlation (FSC) analysis,[5] the original reconstruction is split into two sub-sampled reconstructions considering the number of the reconstructed either even or odd projections.

Near-field ptychographic X-ray computed tomography (PXCT).

The measurements were carried out with a high-stability instrument designed for high-resolution PXCT working in air and at room temperature[6,7], using a photon energy of 8.93 keV. The coherent illumination was defined with a Fresnel zone plate (FZP) of 120 μm diameter and 60 nm outer-most-zone width, which at this energy had a focal distance of 51.9 mm. The FZP had locally displaced zones, specifically designed to produce an optimal illumination for ptychograph[8]. The flux of the X-ray beam was 1.7×10^{8} photons·s^{-1} at the sample position. The sample was placed at 13 mm downstream the focus, where the illumination had a size of about 30 μm. Ptychographic scans were recorded following the positions of a Fermat spiral[9] with an average step size of 6 or 7 μm and a field of view of 186 μm × 30 μm (horizontal × vertical). The field of view must be larger than the size of the capillary to include an air region at both sides of the sample, which is needed for successful tomographic reconstructions and for quantitative contrast. At each scanning position, magnified images of the sample were recorded with an in-vacuum Eiger 1.5M detector[10] with a pixel size of 75 μm placed at 5.237 m downstream the sample, with an acquisition time of 0.1 s. A scan speed of ~5 Hz was achieved thanks to a combined motion of the FZP and the sample, while achieving an effective static illumination on the sample during acquisition[11]. Near-field ptychographic scans were repeated at 420 rotation angles of the sample in equal intervals from 0 to 180 deg. We recorded a total of 3 tomograms at different times from the start of the cement hydration at ~25 °C, the temperature of the

experimental hutch. The first tomogram was recorded with an average scanning step size of 6 μm, it started at 17 h and finished at 20h and 55 minutes, after water mixing, i.e. 3h 55 min of total acquisition time. This scan is hereafter labelled 19 h dataset. The other two tomograms were recorded with a step size of 7 μm lasting 3h 6 min. The scans labelled 47 and 93 h started at 46 and 92 h (after water mixing), respectively. The scan times include the dead time during motion of stages in between acquisitions. The dose absorbed by the specimen during data acquisition was estimated to be 0.7 and 0.5 MGy for the tomograms with 6 and 7 μm of step size, respectively.

Near-field ptychographic reconstructions were performed for each projection using the Ptycho Shelves package[12] developed by the Coherent X-ray Scattering group at PSI, using 5000 iterations of a difference map algorithm[13] adapted for near-field geometry. The pixel size of the images, determined by geometric magnification, is 186.64 nm and we estimate by Fourier ring correlation[5] that the 2D resolution of each reconstructed image is about 200 nm. For each tomographic dataset, projections were aligned with sub-pixel accuracy and processed for phase tomographic reconstruction from phase projections as previously reported[14,15]. The 3D spatial resolution was estimated by FSC[5]. The resolution obtained, see subsection dedicated to the spatial resolution, was limited by the number of projections, which was chosen to have reasonable scan times.

PXCT provides 3D maps of the electron density of the specimen with quantitative contrast, the sensitivity being about 0.02 $e^{-}Å^{-3}$.[16] For attaining quantitative electron densities, the entire specimen must be included in the field of view, containing some empty space around it, which was the case in our measurements. Therefore, it is possible to easily distinguish air and water regions in the specimen, which have electron densities of 0.00 and 0.33 $e^{-}Å^{-3}$, respectively. Obviously, neutron imaging is the standard technique to disentangle water from air porosities.[17] A key advantage of neutron imaging is its ability to can scan large volumes. However, it must also be noted that at inferior spatial resolution compared to PXCT.

Tomographic data analysis.

Initially, the re-alignment of the data, when needed must be detailed.

For the PXCT, the capillary position was very accurate, as the capillary/holder system was mounted from the tray storage to the sample stage by the flOMNY gripper (robot). Hence, the angular orientation of the sample was maintained. The field of view of the sample was aligned carefully based on features visible in the 2D projections. The scanned regions with time were consistent within a few voxels and therefore no alignment between different acquisitions was required.

For the Syn-μCT, a mark was drawn on the sample holder and sample stage for the incident beam to minimise the initial incidence angular position variability. Before each scan, a projection was acquired as a reference for the next one in order to scan the same region. A minor manual registration was required, mostly rotations around x- and y-axes.

For the Lab-μCT, manual registration was required to align the different acquisitions. The process is described next. The capillary was considered as a cylinder and we manually made the cylinders vertical and centred in the reconstructed volume. The remaining rotation around the z-axis was visually done by superimposing distinguishable landmarks in the corresponding images.

The segmentation was done on a Volume of Interest (VOI) corresponding to the inner part of the capillaries for each imaged sample. The total volume of these VOIs varies depending on the sample sizes, amounting to $\sim 1\times10^{5}$ μm^3 for each PXCT dataset and $\sim 1\times10^{8}$ μm^3 for Syn-μCT and Lab-μCT samples. A supervised Machine-Learning (ML) image analysis approach was used to segment the different components of the scanned samples, using the IPSDK Explorer software (version 3.2.0.0 for Windows™, Reactiv'IP, Grenoble, France). This software allows us to manually label voxels on a selected training dataset (approximately 31 voxels for each component on average for PXCT, 20 voxels on average for Syn-μCT and Lab-μCT) and to rapidly obtain test results to determine if the labelling is sufficient or if it requires more information/re-training. The initial classification was based on the electron densities with a variation of ~5% of the measured values, from selected volumes, which are given in Table S7. These test results are obtained after

a first learning step using a random forest method. It is also possible for the user to keep or remove features used in the random forest decision trees based on their relevance. This method permitted to segment the components with comparable grey values and/or electron densities, overlaid ML models on raw datasets are shown in Fig. 7.

On the one hand, the good contrast and the high spatial resolution in PXCT allowed to classify the components into seven categories. They are given next from higher to lower electron densities: i) C_4AF (yellow) with highest values; ii) $C_3S/C_2S/C_3A$ (dark brown) which are the clinker particles; iii) calcite (pink); iv) portlandite (green); v) the rest of the hydrated phases with lower electron densities were labelled as 'Low-Density Hydrates' (light brown), i.e. C-S-H gel, iron-silicon-hydrogarnet, hemicarbonate and ettringite; vi) water porosity (blue); and vii) air porosity (black). On the other hand, due to the contrast and spatial resolution limitations in the two other modalities, Syn-μCT and Lab-μCT, the components were classified into four categories. The classification from higher to lower grey-values was: i) clinker particles (dark brown), i.e. $C_4AF/C_3S/C_2S/C_3A$; ii) a component labelled 'High-Density Hydrates' (green), being mainly portlandite and calcite; iii) another component labelled 'Low-Density Hydrates' (light brown), being mainly C-S-H gel, iron-silicon-hydrogarnet, hemicarbonate and ettringite; and iv) porosity (black) which contain both water and air. It is noted that Syn-μCT and Lab-μCT microtomographies do not allow to distinguish water from air porosities due to the similarities in their X-ray attenuation values.

This ML approach also permits to mitigate the influence of partial volume effects in-between labelled components for accurate quantitative analysis of PXCT, i.e. mean electron density. Selected results after the PXCT segmentation procedure are summarised SI. Movie 1. In addition, after grains were segmented using the ML approach described above, the C-S-H gel shell thickness was computed on PXCT imaged sample at 19 h, see Fig. 6 and SI. Movie 2. The wall thickness script computes the object thickness. For a given pixel, the thickness is the radius of the largest circle centred on this pixel entirely included in the object. The steps of the data analysis process are shown in flowcharts, see Fig. S20 and S21. A further post-segmentation data analysis calculation was carried out in order to show the particle size distribution evolution with hydration time. The anhydrous cement particles, at the three hydration times, were classified by computing their mean Feret diameters. Fig. 8b displays the volume percentage of the segmented grains (and their cumulative volumes) as function of the particle sizes that can be compared with the initial characterization by laser diffraction, see Fig. 1a. 3D rendering visualization was done using Dragonfly software (version 2022.1 for Windows™, Object Research Systems (ORS) Inc., Montreal, Canada).

Spatial resolution analysis.

The spatial resolution was characterised by two approaches as recently reported[18]. On the one hand, it can be determined from the grey-value changes in line profiles through the edge sharpness of the interfaces. A point spread function (PSF) used to determine the spatial resolution of the images as ISO/TS 24597 defines the Gaussian radius of the PSF as the resolution, which equals to a change between 25 %–75 % grey value along the studied interfaces.[19] Here, a common interface present in the three imaging modalities has been selected for the line profiles: the glass capillary wall – air (i.e. exterior of the capillaries). We have measured 25 interfaces in every tomogram, which allowed us to determine the average spatial resolution and its associated standard deviation. Moreover, as examples, Figures S2-S4 display line profiles of sharp interfaces between high (i.e. alite) and low density (i.e. porosity) components within the capillaries. The spatial resolutions, as determined by this approach, were 250(25) nm, 264(25) nm, 272(34) nm, 748(19) nm and 2.21(17) μm, for PXCT-19h, PXCT-47h, PXCT-93h, Syn-μCT and Lab-μCT datasets, respectively.

On the other hand, FSC plots[5] have been also computed. The traces are displayed in Figures S5-S7 giving spatial resolution values of 430 nm, 470 nm, 500 nm, 650 nm and 1.9 μm, for PXCT-19h, PXCT-47h, PXCT-93h, Syn-μCT and Lab-μCT datasets, respectively. Moreover, the FSC trace for PXCT-19h shows a smooth decrease in the 0.0-0.2 spatial frequency range, which is likely due to the hydration of cement during the 4-hour measurement. As expected, this behaviour is not shown at later ages.

It should be noted that the agreement between the spatial resolution results between the edge sharpness approach and FSC method is satisfactory for Syn-μCT (750 vs. 650 nm) and Lab-μCT (2.2 vs.1.9 μm) datasets.

However, the agreement between these two approaches is not good for PXCT (for instance, 250 vs 430 nm at 19 h). The poorer resolution estimated by FSC can be explained because the angular sampling is very tight, i.e. 420 projections, so the two employed subtomograms in the FSC, each of 210 projections, were significantly undersampled compared to the number of voxels across the diameter of the sample. This means that the correlation between two such undersampled tomograms can give a low estimation of the spatial resolution. This feature is not observed for Syn-μCT and Lab-μCT as the total number of projections were 6000 and 1637, respectively. In other words, the subtomograms with half the number of projections were not undersampled for these two imaging modalities.

Etch-pit growth rate evaluation.

The estimation of the etch-pit growth rate was based on the analysis of 27 etch-pits from 5 different large alite grains. It is noted that the etch-pits have irregular 3D shapes and therefore, for its spatial dissolution rate estimation, some simplifications were undertaken. Moreover, the spatial resolution of this PXCT work, ~250 nm, is limited for accurate analyses. Therefore, we consider this approach as an estimation. Firstly, etch-pits were visually selected from grains with sizes larger than 10 μm. Secondly, their overall shapes were compared in two hydrating steps. Then, two envelopes from pixels with at least 90% of the electron density of alite were developed. The estimated/calculated distance (in pixels) was computed between these edges for the deepest perpendicular length. These values were converted to dissolution rate by taking the ratio respect to the time between measurements. The result for the analysis between 19 and 47 h datasets gave 6.1 pixels of average distance which is equivalent to 41(29) nm/h. There was large variability in the rates, the fastest being 110 nm/h and the slowest being 10 nm/h. From this investigation, it is not possible to know if this large variability comes from the heterogeneity in the defects within these regions, or if other variables like the spatial resolution of this work and the local water-to-cement ratio variations are also playing important roles. More imaging studies are necessary to establish this. The very same 27 etch-pits were also analysed between 47 and 93 h datasets. In this case, the etch-pit growth rate was slower 7 nm/h, showing that the water diffusion is already limiting hydration at four days.

Water/cement ratio estimation of the scanned sample by PXCT

The w/c ratios of the scanned capillaries in a selected region can be calculated at the different ages according to the procedure previously reported[20]. The final β-mean values obtained by PXCT were used after converting to μ values, see Table S6. Then, using the mineralogical compositions of the anhydrous cement (given in the Supporting information, Table S2) the μ value is estimated, taking into account the μ value of free water, 22.2 cm^{-1}. For instance, for the 19 h sample, it can be estimated that the paste was composed of 69.9 wt% PC and 30.1 wt% water to account for the overall μ of the paste. This calculation yielded a w/c ratio of 0.39, see Table S6.

Chemical reactions

I. The chemical reactions used for the FW calculation, see Table S5, are: (1) the consumption of water by the hydration of C_4AF, with C_3S which is the source of silicates, to give amorphous iron siliceous hydrogarnet (Fe-Si-Hg) and crystalline portlandite; (2) the hydration of C_3S to yield amorphous C-S-H gel and crystalline portlandite; (3) the hydration of C_3A, consuming a calcium sulfate source, to yield ettringite if there are enough sulfates available (which is the case here); and (4) the possible carbonation of portlandite gives crystalline (and amorphous) calcium carbonate(s) and it releases free (capillary) water.

II. In the absence of belite hydration, the chemical reaction contributing to C-S-H gel formation, see Table S5, is just (2). It is underlined that a small fraction of the consumed alite did not result in C-S-H gel but in the formation of iron siliceous hydrogarnet from the ferrite hydration (reaction 1).

It is noted here that for the calculations presented in Table S5, the amount of C_3S which is needed for the silicate groups in iron-silicon-hydrogarnet, is calculated first from the degree of hydration of C_4AF (applying reaction #1). Then, the portlandite and C-S-H gel contents are determined from the reaction of C_3S after subtracting the number obtained in the process described just above.

$Ca_4Al_2Fe_2O_{10} + 1.68Ca_3SiO_5 + 11.68H_2O \rightarrow 2Ca_3AlFe(SiO_4)_{0.84}(OH)_{8.64}$ (amorph.) $+ 3.04Ca(OH)_2$ (1)

$Ca_3SiO_5 + 5.2H_2O \rightarrow 1.2Ca(OH)_2 + (CaO)_{1.8}SiO_2(H_2O)_{4.0}$ (2)

$Ca_3Al_2O_6 + 3CaSO_4{\cdot}2H_2O + 26H_2O \rightarrow Ca_6Al_2(SO_4)_3(OH)_{12}{\cdot}26H_2O$ (3)

$Ca(OH)_2 + CO_2 \rightarrow CaCO_3 + H_2O$ (4)

Open access raw data availability and description

The following raw data has been openly deposited on Zenodo and can be acceded at: https://doi.org/10.5281/zenodo.7030107

1. Tomographic reconstructed raw data of all the X-ray imaging modalities (twelve tomograms) in 16 bit and .tif format. The size of the files is also given in the following table.

Folder Name	Sub-folders Label	File Size*	Additional Information
Phase-PXCT	1_PXCT-19h 2_PXCT-47h 3_PXCT-93h	736.9MB	4D Synchrotron Ptychographic X-ray Computed Tomography Cement Hydration (Delta Dataset)
Syn-microCT	4_Syn-microCT-19h 5_Syn-microCT-47h 6_Syn-microCT-93h	52.8GB	4D Synchrotron Phase-contrast Microtomography Cement Hydration
Lab-microCT	7_Lab-microCT-19h 8_Lab-microCT-47h 9_Lab-microCT-93h	7.5GB	4D Laboratory Attenuation-contrast Microtomography Cement Hydration
Absorption-PXCT	10_abs-PXCT-19h 11_abs-PXCT-47h 12_abs-PXCT-93h	722.9MB	Absorption Dataset for 4D Synchrotron Ptychographic X-ray Computed Tomography Cement Hydration (Beta Dataset)

Net total size of all datasets: **82.8GB**

**These are zipped files. The original file size for every single 16 bit Syn-microCT dataset is 22.8GB, for each Lab-microCT dataset is 3.0GB and for each PXCT dataset is 500MB.*

2. Laboratory raw data

2.1. Particle size distribution (PSD)

"PSD" labelled folder contains two files in .mmes format.

2.2. Isothermal calorimetry

"Calorimetry" labelled folder contains six files in .xlsx excel format.

2.3) Laboratory X-ray powder diffraction (LXRPD)

"LXRPD" labelled folder contains five files in .ASC text format.

• Supplementary Tables

Table S1. Chemical (elemental) analysis (by X-ray fluorescence) of the two employed Portland cements in this investigation. All data expressed in weight percentages of the corresponding oxides.

	CaO	SiO_2	SO_3	Al_2O_3	Fe_2O_3	MgO	K_2O	Na_2O	Others	LoI
PC-52.5	62.2	20.4	3.6	4.9	3.2	1.5	1.1	0.3	0.5	2.3
PC-42.5	62.9	19.7	3.4	5.0	3.4	1.5	1.1	0.3	0.3	2.7

Table S2. Rietveld quantitative phase analysis of the employed anhydrous Portland cements, in wt%.

	C_3S	β-C_2S	C_4AF	o-C_3A	$C\bar{S}H_2$	$C\bar{S}H_{0.5}$	Cc	Q	$K\bar{S}$	CaO
PC-52.5	61.0	11.8	11.5	8.2	1.9	2.0	2.8	0.8	-	-
PC-42.5	61.6	11.1	10.8	7.8	0.9	2.1	3.7	0.6	1.1	0.4

Table S3. Textural details of the two cements.

	Density (gcm^{-3})	BET (m^2g^{-1})	Blaine (m^2Kg^{-1})	$D_{v,10}$ (µm)	$D_{v,50}$ (µm)	$D_{v,90}$ (µm)
PC-52.5	3.108(1)	2.27(1)	409(8)	1.8	11.5	32.7
PC-42.5	3.126(1)	1.25(1)	368(1)	2.1	18.0	50.0

Table S4. Selected cumulative heat release data (from the isothermal calorimetry study) for the two employed cements. All values in J per gram of Portland cement.

	19 h		47 h		93 h		7 d		Maximum peak		
	Heat/J	DoH$^{\$}$/%	Heat/J	DoH$^{\$}$/%	Heat/J	DoH$^{\$}$/%	Heat/J	DoH$^{\$}$/%	Time/h	Heat/J	DoH$^{\$}$/%
PC-52.5, w/c=0.40	180.8	33.7	279.8	52.4	300.7	56.3	313.5	58.7	14.2	102.9	19.3
PC-52.5, w/c=0.50	157.2	29.4	306.6	57.4	346.9	64.9	365.2	68.4	15.6	102.7	19.2
PC-42.5, w/c=0.40	116.5	22.1	220.5	41.9	270.8	51.5	291.5	55.4	10.4	50.4	9.6
PC-42.5, w/c=0.50	114.4	21.7	223.3	42.4	279.8	53.1	310.0	58.9	11.0	53.4	10.2

$^{\$}$Total heat of hydration of PC52.5 as calculated in ref.[21] option-1: **534 J.**

$^{\$}$Total heat of hydration of PC42.5 as calculated in ref.[21] option-1: **526 J.**

Table S5. Rietveld quantitative phase analysis (of MoKα_1 radiation powder diffraction data) results (wt%) for the studied PC-52.5 pastes, w/c=0.40. Laboratory X-ray diffraction data were taken on the same capillary used for the laboratory, attenuation-contrast, microtomographic study. The data are referenced to 100 grams of paste.

phases	t_0*	t=22h	t=50h	t=96h
C_3S	43.57	18.9	17.0	16.3
β-C_2S	8.43	8.3	8.7	9.1
C_3A	5.86	2.9	1.9	1.5
C_4AF	8.21	7.7	5.8	5.4
Cc#	2.00	3.1	3.2	3.6
CH	-	10.6	13.5	13.8
AFt	-	12.2	12.4	12.4
AFm-Hc	-		0.4	0.4
C-S-H&	-	20.3	20.6	20.9
Fe-Si-Hg&	-	0.5	2.8	3.1
FW&	28.57	14.4	12.9	12.7
DoH C_3S (%)	-	56	61	63
DoH C_2S (%)	-	0	0	0
DoH C_3A (%)	-	50	67	74
DoH C_4AF (%)	-	5	29	34

* This cement also has at t_0: 1.4 wt% of gypsum, 1.4 wt% of bassanite and 0.6 wt% of quartz.
& C-S-H, Fe-Si-Hg and FW (free water) contents calculated from the assumed chemical reactions as described in supplementary methods.
# The calcite content increased from 2.0 wt% at t=0 to 3.6 wt% at 96 h, highlighting a significant carbonation of the paste within this large capillary, i.e. 1 mm of diameter. The thinner capillary used in the PXCT study, i.e. 0.2 mm of diameter, did not show a measurable conversion of CH to Cc, see below. Carbonation of a cement paste has been previously measured by PXCT, when its extension was significant.[22]

Table S6. Experimental mean β values converted to μ values obtained from a VoI in the PXCT study. The calculation of the w/c ratio of this region at the different hydration ages is also included. More details about this calculation is given in the Supplementary Methods.

Scan	Experimental β*	Experimental μ/cm^{-1}	Weight /g		Weight /wt%		w/c ratio
			water	cement	water	cement	
PXCT-19h	1.316×10^{-7}	119.1	55.0	139.4	28.3	71.7	0.39
PXCT-47h	1.265×10^{-7}	114.5	57.2	132.8	30.1	69.9	0.43
PXCT-93h	1.274×10^{-7}	115.3	56.8	133.9	29.8	70.2	0.42

*The β values have been calculated using the same volume used for the calculation of delta but excluding the regions where the electron density is smaller than 0.24 $e^-Å^3$, as they have been considered air porosity. It is noted that air is not included in this calculation.

Table S7. Expected (from the crystallographic data,[23,24]) mass and electron densities. The attenuation length values are calculated[$] for the employed wavelength, E=8.93 keV. The measured electron densities for selected components from the PXCT data, where relatively large volumes could be chosen, are also given.

Cement Phases	Abbrev.	Formula	Mass density /gcm^{-3}	Electron density /e$^-$Å^{-3}	Measured electron density /e$^-$Å^{-3} (within selected particles)[#] 19 h	47 h	93 h	Attenuation length /μm	μ /cm^{-1}	β
#0, air	-	-	~0.00	~0.00			0.00(4)			
#1, water	-	H_2O	1.00	0.33	0.31(1)			1388.6	7.2	7.96 10^{-09}
#2, ettringite	AFt	$Ca_6Al_2(SO_4)_3(OH)_{12}\cdot 26H_2O$	1.78	0.56				154.6	64.7	7.15 10^{-08}
Hemicarbo-aluminate[=]	Hc	$Ca_4Al_2(OH)_{13}(CO_3)_{0.5}\cdot 5.5H_2O$	1.90	0.59				118.6	84.3	9.32 10^{-08}
Monosulfate[=]	AFm-SO_4	$Ca_4Al_2(OH)_{12}(SO_4)\cdot 6H_2O$	2.02	0.63				112.4	89.0	9.83 10^{-08}
#3, calcium silicate hydrate	C-S-H	$(CaO)_{1.8}(SiO_2)(H_2O)_4$	*2.11*[%]	*0.66*[%]				*95.9*	*104.3*	*1.15 10^{-07}*
#4, portlandite	CH	$Ca(OH)_2$	2.23	0.69	0.62(2)	0.649(6)	0.651(5)	61.5	162.6	1.80 10^{-07}
#5, calcium carbonate	Cc	$CaCO_3$	2.71	0.82	0.782(3)	0.776(3)	0.776(3)	66.3	150.8	1.67 10^{-07}
#6, tricalcium aluminate	C_3A	$Ca_3Al_2O_6$	3.05	0.91				49.0	204.0	2.25 10^{-07}
#7, alite	C_3S	Ca_3SiO_5	3.15	0.95	0.936(2)	0.931(2)	0.932(1)	41.8	239.1	2.64 10^{-07}
#8, belite	C_2S	Ca_2SiO_4	3.30	0.99	0.98(2)	0.98(1)	0.98(1)	43.3	231.1	2.55 10^{-07}
#9, ferrite	C_4AF	Ca_2AlFeO_5[&]	3.73	1.10				26.4	379.4	4.19 10^{-07}

[#] Electron densities, from particle picking, were obtained by the average of 10 cubes for the capillary; 5, 4, 5 and 6 grains for portlandite, calcium carbonate, alite and belite, respectively. Moreover, 5 cubes at 19 h gave the reported measured electron density for capillary water. Similarly, 5 cubes at 93 h were computed to obtain the value for air. Finally, the electron density of LDH (low density hydrates) was measured at 93 h in 5 cubes yielding 0.56(1) e$^-$Å^{-3} that it corresponds to ettringite and/or C-S-H as they cannot be distinguished.

[=] The expected values for these phases, i.e. hemicarbo-aluminate and monosulfate, are given for the sake of completeness but they are not numbered as they were not identified in the bivariate plots, see Figures S9.

[%] There are not expected values for an amorphous material. The quoted values (italics) were determined for five months cured C-S-H gel by PXCT[20].

[&] The reported values are for stoichiometric Ca_2AlFeO_5, i.e. an Al/Fe molar ratio of 1.0, which is an approximation as this ratio could be different from 1.0.

[$] The *attenuation length* values have been calculated from[25], https://henke.lbl.gov/optical_constants/atten2.html

The μ values were calculated from: $\mu\ [cm^{-1}] = \frac{1}{Attenuation\ Length\ [\mu m] \times 10^{-4}}$

Finally, β was calculated as $\beta = \frac{\mu\lambda}{4\pi}$

Table S8. Component segmentation (vol%) and average electron densities obtained by PXCT at the different hydration ages; expected electron densities (from crystallographic data when it is possible) are also given for reference.

Component	Expected electron density /e⁻Å⁻³	19 h			47 h			93 h		
		Vol /%	Electron density* /e⁻Å⁻³	Electron density& /e⁻Å⁻³	Vol /%	Electron density* /e⁻Å⁻³	Electron density& /e⁻Å⁻³	Vol /%	Electron density* /e⁻Å⁻³	Electron density& /e⁻Å⁻³
Capillary	-	-	-	0.63(1)	-	-	0.63(1)	-	-	0.63(1)
Air porosity	0.00	0.2	0.01(5)	-	4.1	0.10(1)	-	6.7	0.10(1)	-
Water porosity	0.33	15.1	0.33(6)	-	2.2	0.33(5)	-	2.8	0.32(6)	-
LD-Hydrates	*0.38-0.53*	45.5	0.50(4)	-	56.5	0.52(4)	-	51.8	0.53(4)	-
Portlandite	0.69	4.6	0.63(1)	0.62(2)	13.1	0.62(4)	0.65(1)	15.7	0.62(4)	0.65(1)
Calcite	0.82	2.5	0.74(2)	0.78(1)	2.2	0.74(4)	0.78(1)	2.3	0.74(5)	0.78(1)
Belite/Alite/C_3A	0.99/0.95/0.91	30.4	0.90(1)	0.94(1)/0.98(2)	20.3	0.90(4)	0.93(1)/0.98(1)	19.3	0.90(5)	0.93(1)/0.98(1)
Ferrite	1.10	2.1	1.02(2)	-	1.5	1.01(4)	-	1.4	1.02(4)	-

*Electron densities, from full volume, were obtained by segmentation excluding the external voxels to avoid partial volume effect

&Electron densities, from particle picking, were obtained by the average of 10 cubes for the capillary; 5, 4, 5 and 6 grains for portlandite, calcium carbonate, alite and belite, respectively.

Table S9. Volume percentages for the cement pastes at the different ages of hydration determined by the techniques used in this paper. Degrees of hydration are also included.

Technique	Hydration age /h	Porosity /vol%: air & water	LD-hydrates /vol%	Portlandite & calcite /vol %	Anhydrous components /vol %: $C_3S/C_2S/C_3A/C_4AF$	DoH /%
Calorimetry PC-52.5, w/c=0.40	19	-	-	-	-	34
	22	-	-	-	-	39
	47-50	-	-	-	-	53
	93-96	-	-	-	-	56
Calorimetry PC-42.5, w/c=0.50	19	-	-	-	-	22
	47	-	-	-	-	42
	93	-	-	-	-	53
LXRPD PC-52.5, w/c=0.40	0	56.1[$]	-	-	39.9[$]	-
	22	26.4	39.6	11.6	22.0	45
	50	22.3	44.8	13.7	20.6	48
	96	21.9	45.5	14.2	19.9	50
Lab-µCT PC-52.5, w/c=0.40	0	56.1[$]			39.9[$]	-
	19	5.6	35.7	35.7	23.5	41
	47	2.1	21.7	60.8	15.4	61
	93	2.1	20.2	62.8	15.0	62
Syn-µCT PC-42.5, w/c=0.50	0	61.5[#]	-	-	35.0[#]	-
	19	1.9	43.8	27.3	27.0	23
	47	14.5	32.9	31.7	20.8	41
	93	13.7	34.3	35.2	16.9	52
PXCT PC-52.5, w/c=0.40	0	56.1[$]			39.9[$]	-
	19	15.3	45.5	7.1	32.1	20
	47	6.3	56.5	15.3	21.8	45
	93	9.5	51.8	18.0	20.7	48

[$] The amount of water and clinker phases is 96.0 vol%. The remaining 4.0 vol% is due to the minor components: gypsum, bassanite, calcite and quartz
[#] The amount of water and clinker phases is 96.4 vol%. The remaining 3.6 vol% is due to the minor components: gypsum, bassanite, calcite and quartz

• Supplementary Figures

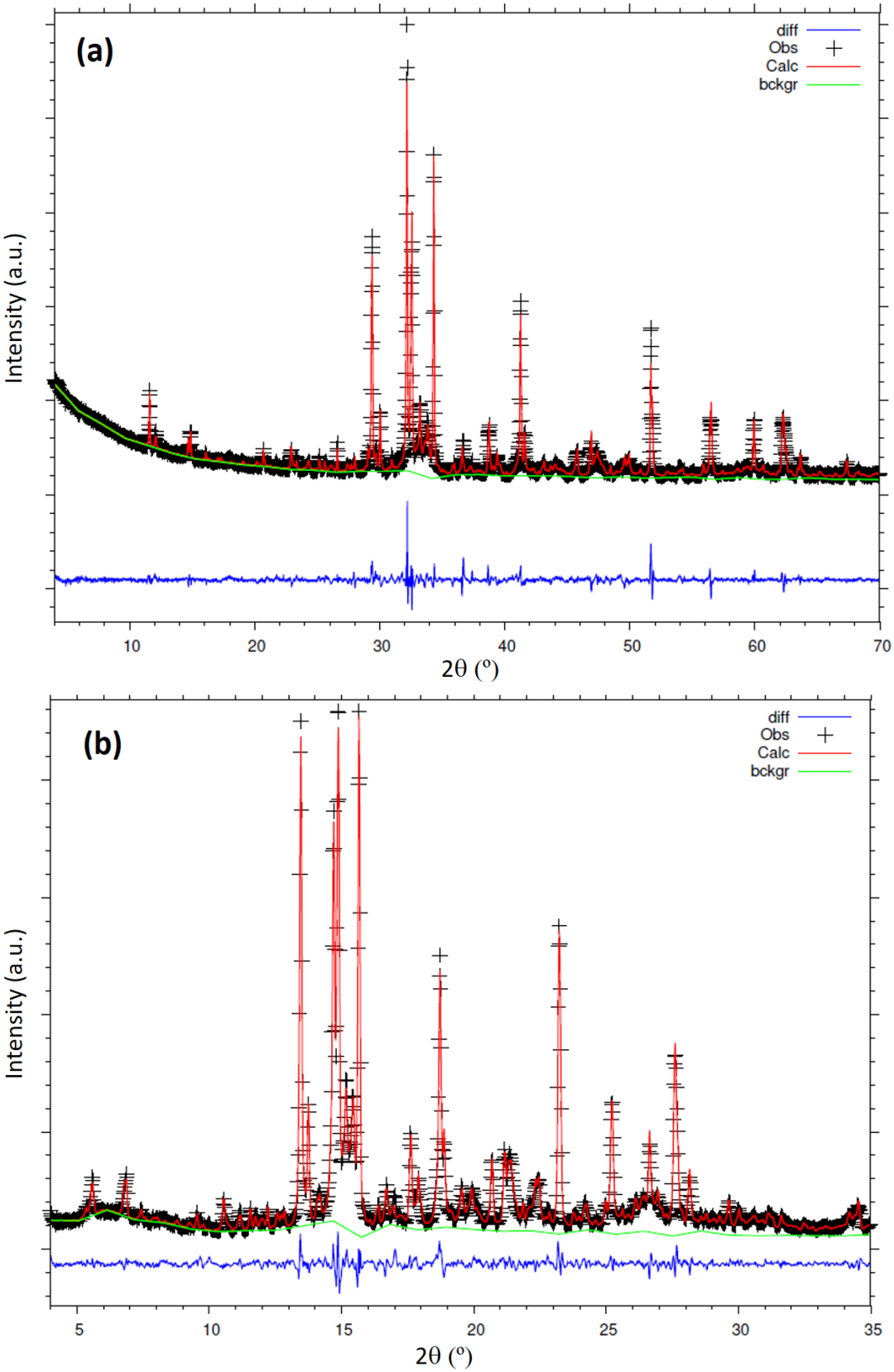

Figure S1. Laboratory Rietveld plots for the anhydrous cements. (a) PC-52.5 (CuKα_1 radiation, λ=1.5416 Å). (b) PC-42.5 (MoKα_1 radiation, λ=0.7093 Å).

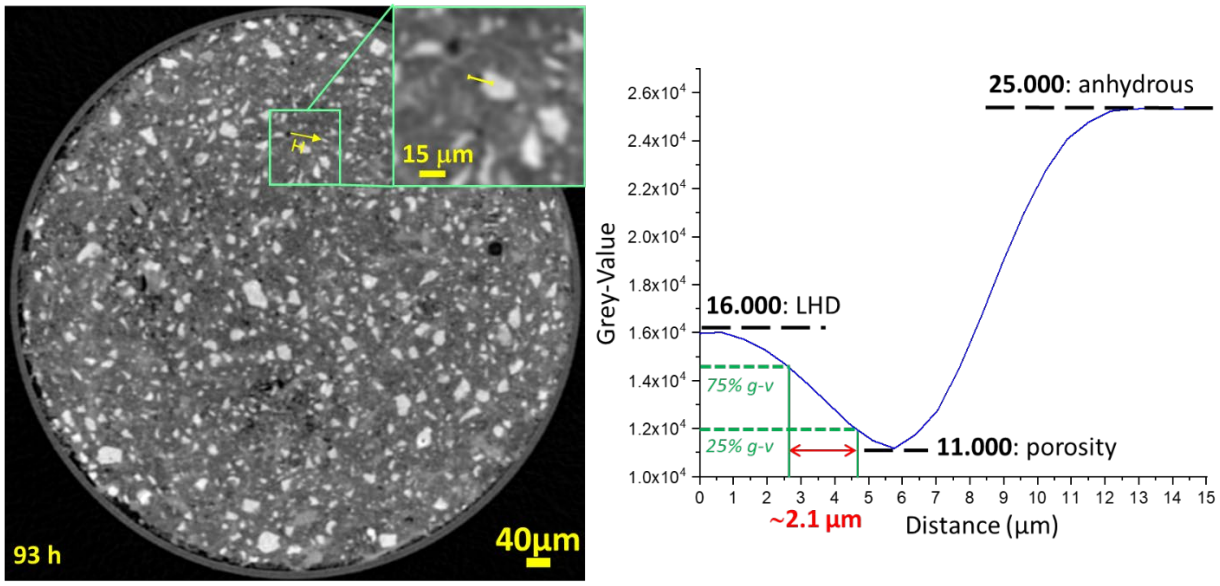

Figure S2. (Left) Selected orthoslice and (Right) grey-value profile of the yellow line (shown in the right panel) including a sharp interface for the laboratory, attenuation-contrast, microtomographic study (PC-52.5 paste with w/c=0.40, dataset at 4 days of hydration). The estimated spatial resolution, from this approach, is ~1.9 µm.

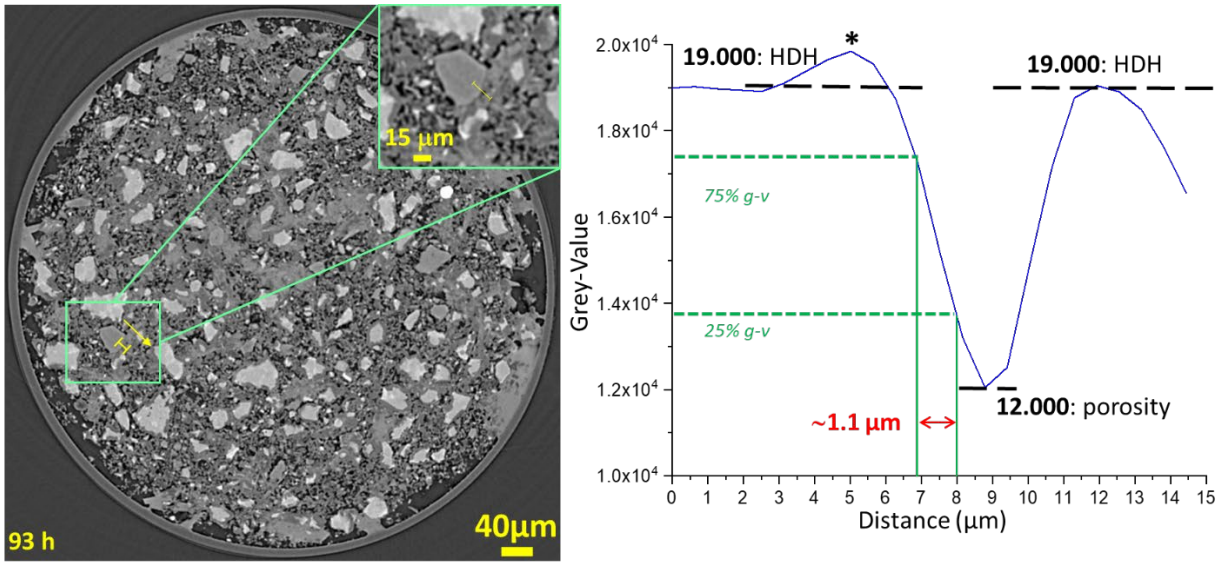

Figure S3. (Left) Selected orthoslice and (Right) grey-value line profile of a sharp interface for the synchrotron, phase propagation based-contrast, microtomographic study (PC-42.5 paste with w/c=0.50, dataset at 4 days of hydration). The estimated spatial resolution, from this approach, is ~ 0.75 µm. The star symbol highlights the small artefact (edge enhancement not fully corrected by the Paganin algorithm) which is commonly observed in in-line propagation-based phase-contrast synchrotron tomography.

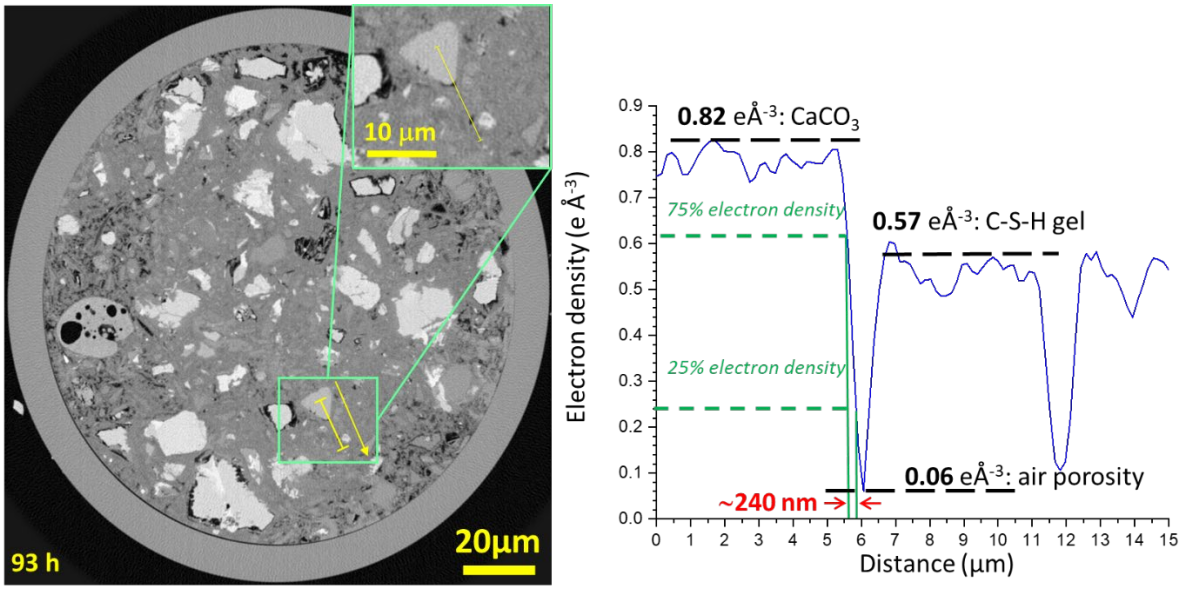

Figure S4. (Left) Selected orthoslice and (Right) line profile of a sharp interface for the near-field ptychographic X-ray computed tomographic study (PC-52.5 paste with w/c=0.40, dataset at 4 days of hydration). The estimated spatial resolution, from this approach, is ~250 nm.

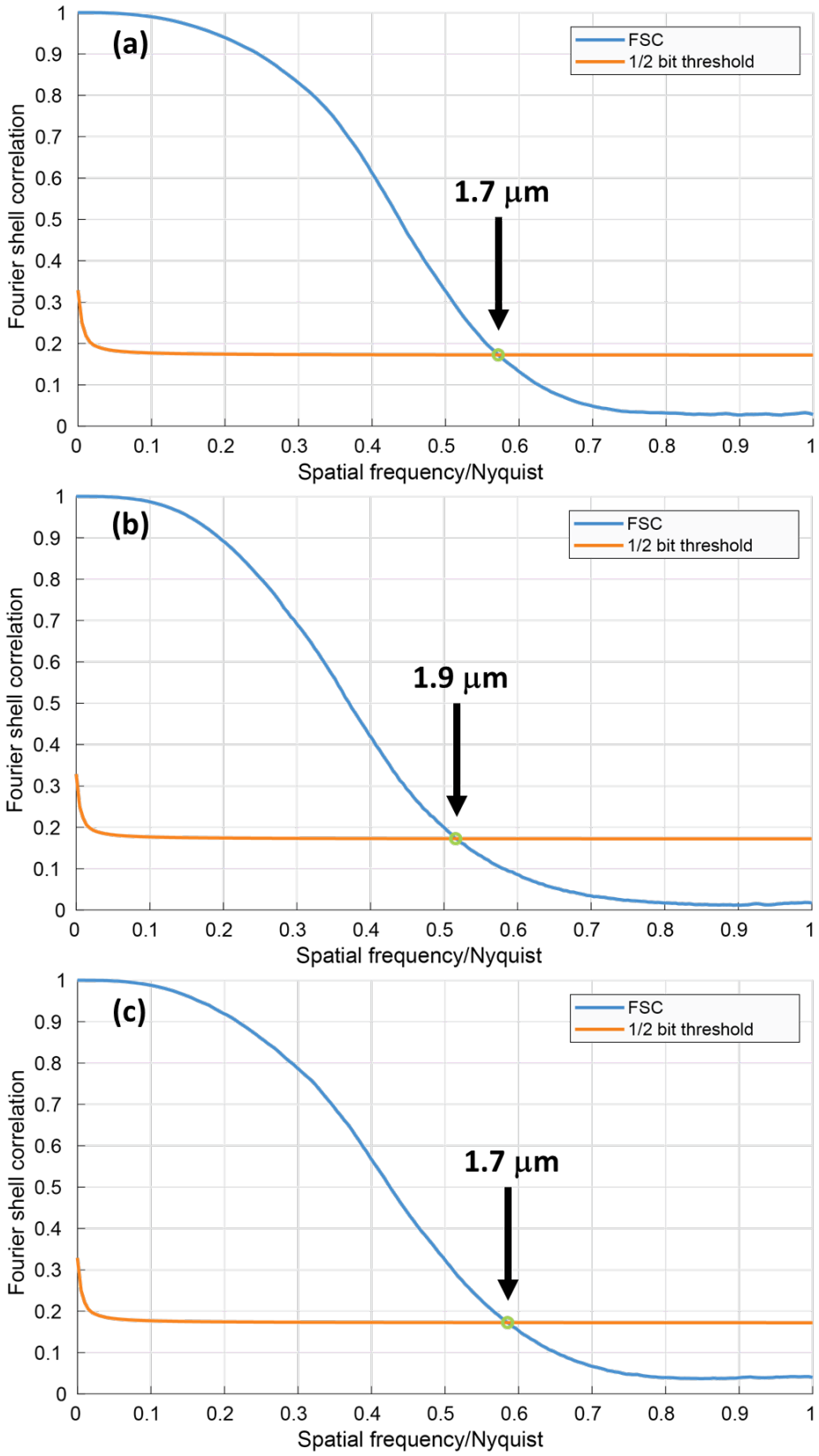

Figure S5. Fourier Shell Correlation plots for the laboratory, attenuation-contrast, microtomographic study, PC-52.5 paste (w/c=0.40) at (a) 19 h, (b) 47 h and (c) 93 h of hydration. The cuts between the FSC traces and the threshold lines give an indication of the spatial resolution of each tomogram.

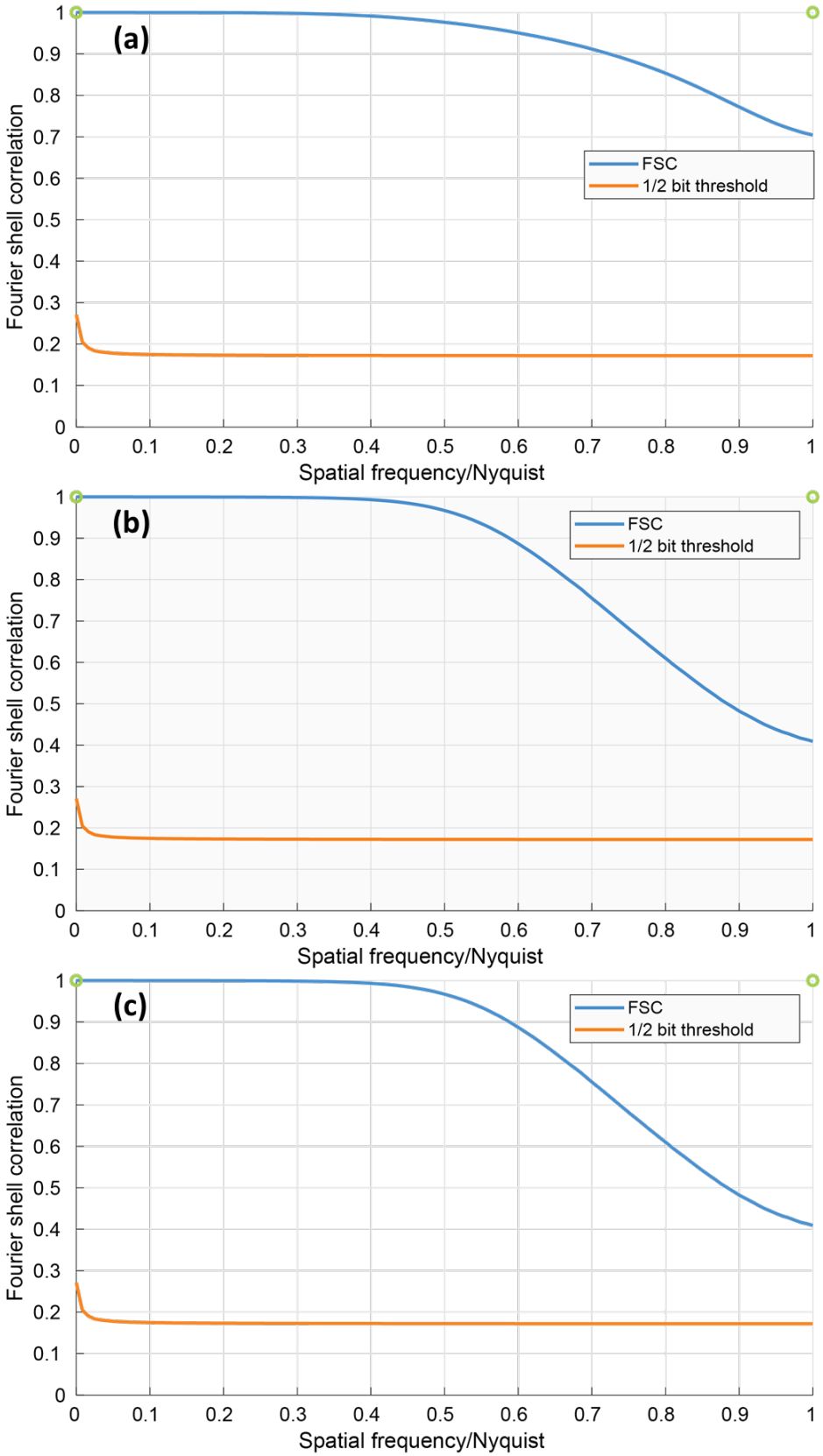

Figure S6. Fourier Shell Correlation plots for the propagation-based synchrotron phase-contrast X-ray computed microtomographic study, PC-42.5 paste (w/c=0.50) at (a) 19 h, (b) 47 h and (c) 93 h of hydration. The FSC traces do not cut the threshold indicating that, from this approach, the overall spatial resolution is limited by the sampling (pixel size).

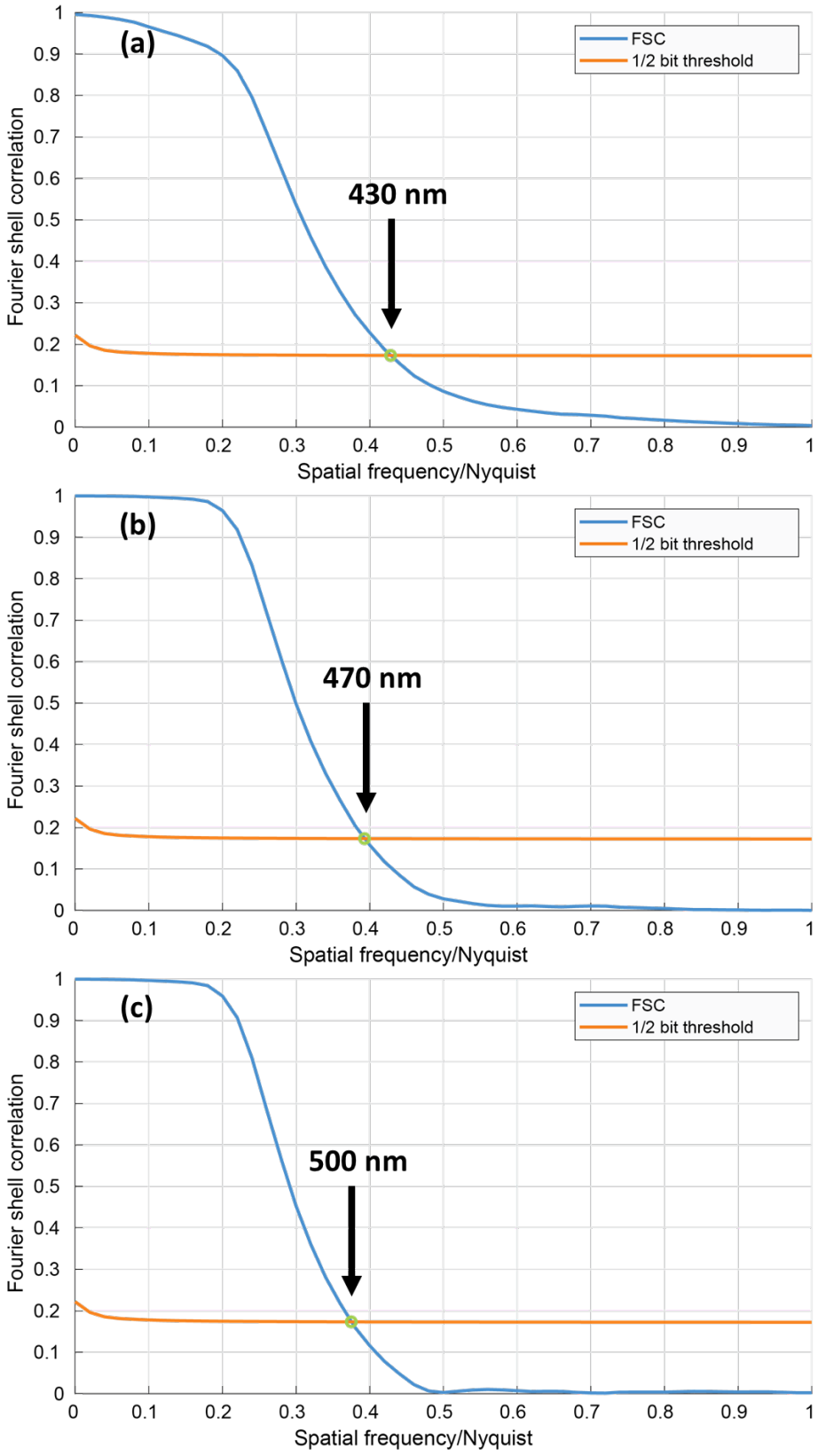

Figure S7. Fourier Shell Correlation plots from the near-field ptychographic X-ray computed tomographic study for the PC-52.5 paste (w/c=0.40) at (a) 19 h, (b) 47 h and (c) 93 h of hydration. The cuts between the FSC traces and the threshold lines give an indication of the spatial resolution of each tomogram. The slightly better spatial resolution measured for the 19 h tomogram is very likely due to the smaller scanning step size, i.e. 6 µm, and the corresponding larger acquisition time, i.e. 3h 55 min. The scanning step size for the other two tomograms was 7 µm, yielding 3h 6 min of acquisition time.

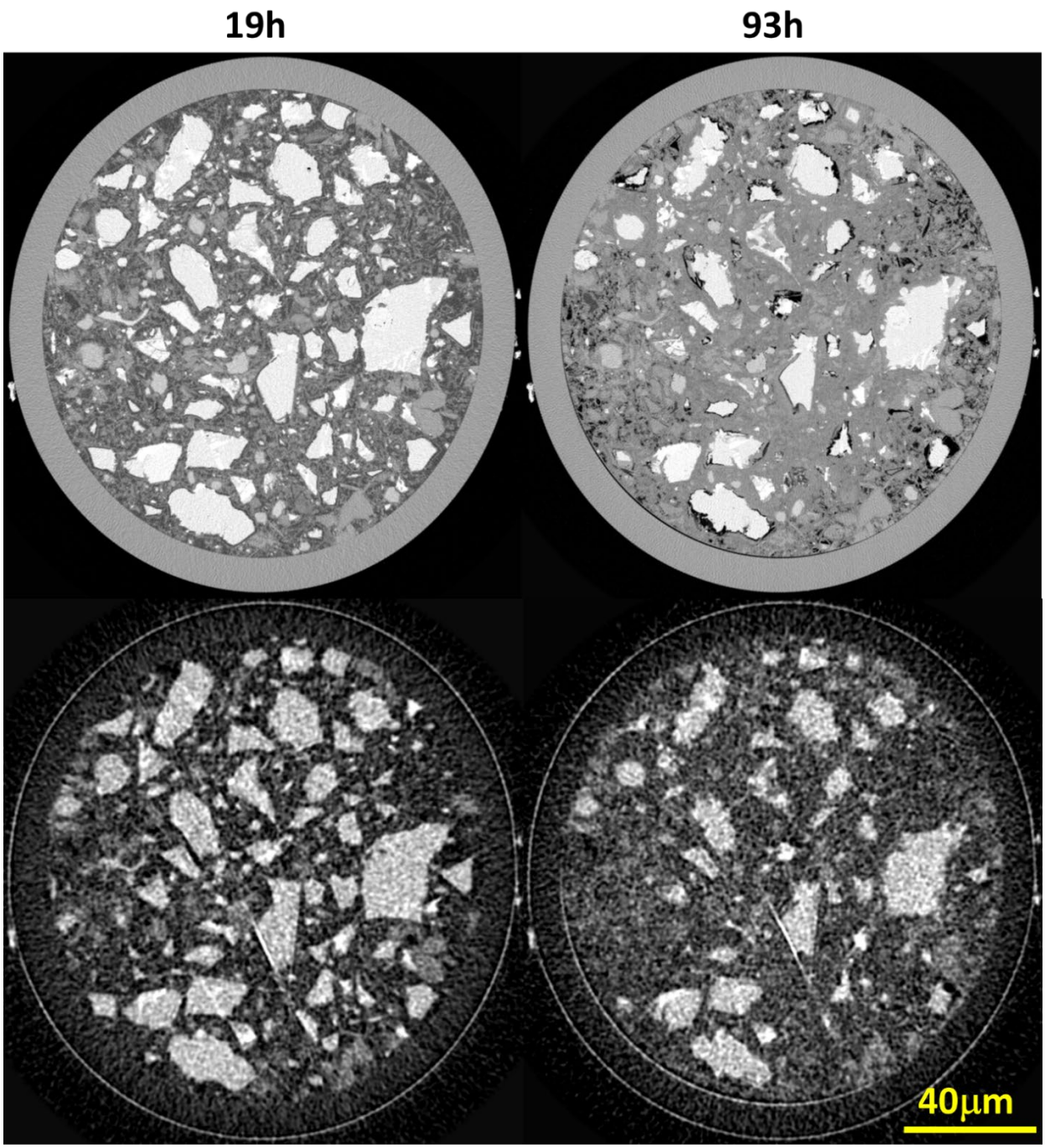

Figure S8. Selected PXCT orthoslices at 19 and 93 h of hydration. (Top) Electron density datasets. (Bottom) Absorption datasets.

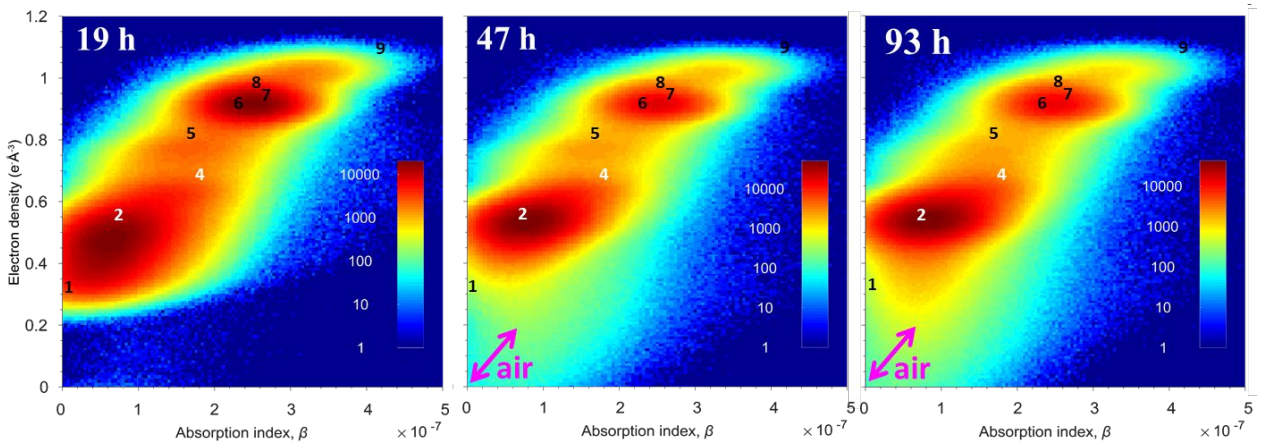

Figure S9. Bivariate histograms of electron densities and absorption indexes (β) for the PXCT study of the PC-52.5 paste (w/c=0.40) at the three studies hydration ages. The positions of the different components, as expected from the crystallographic data, are given. C-S-H gel position (component #3) is not given, as it is a non-stoichiometric solid, but it should be close to ettringite (#2). The electron density and absorption of air is zero but the partial volume effect slightly displaces the values, see pink arrows. For the numbers/components, the reader is referred to Table S7.

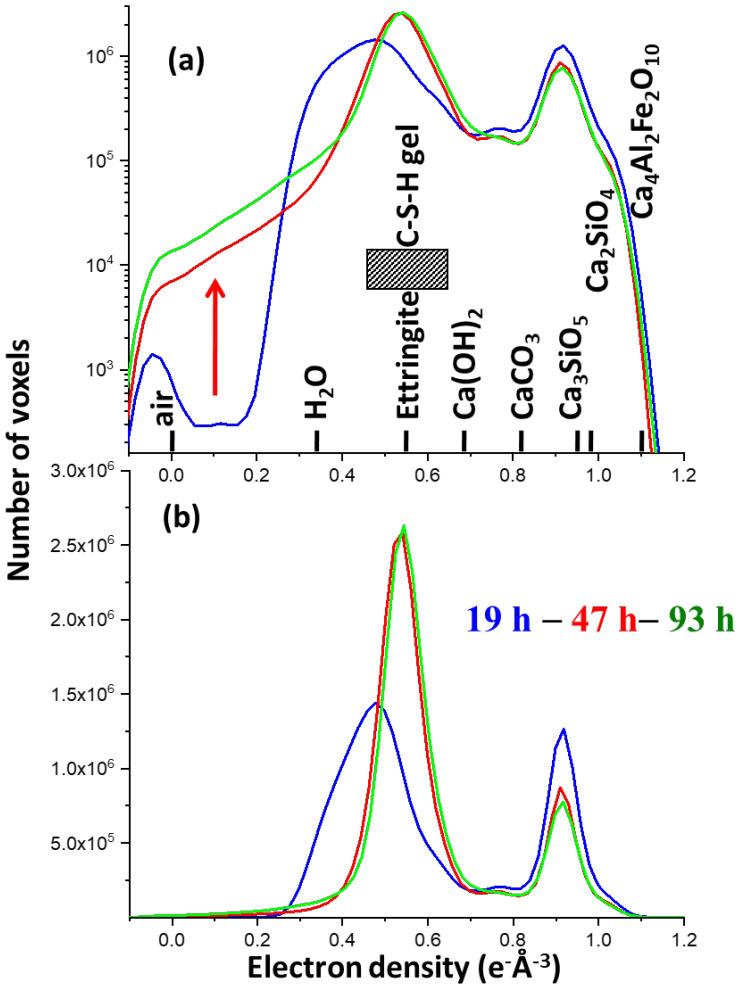

Figure S10. Volume-of-interest histogram of the electron densities for the PXCT study of the PC-52.5 paste (w/c=0.40) at (blue) 19 h, (green) 47 h and (red) 93 h of hydration. (a) Logarithmic scale, (b) Linear scale. The expected (from the crystal structures) electron densities for the different components are labelled in (a). C-S-H gel is an amorphous solid with variable water content and Ca/Si molar ratio and therefore, the expected electron densities are a range.

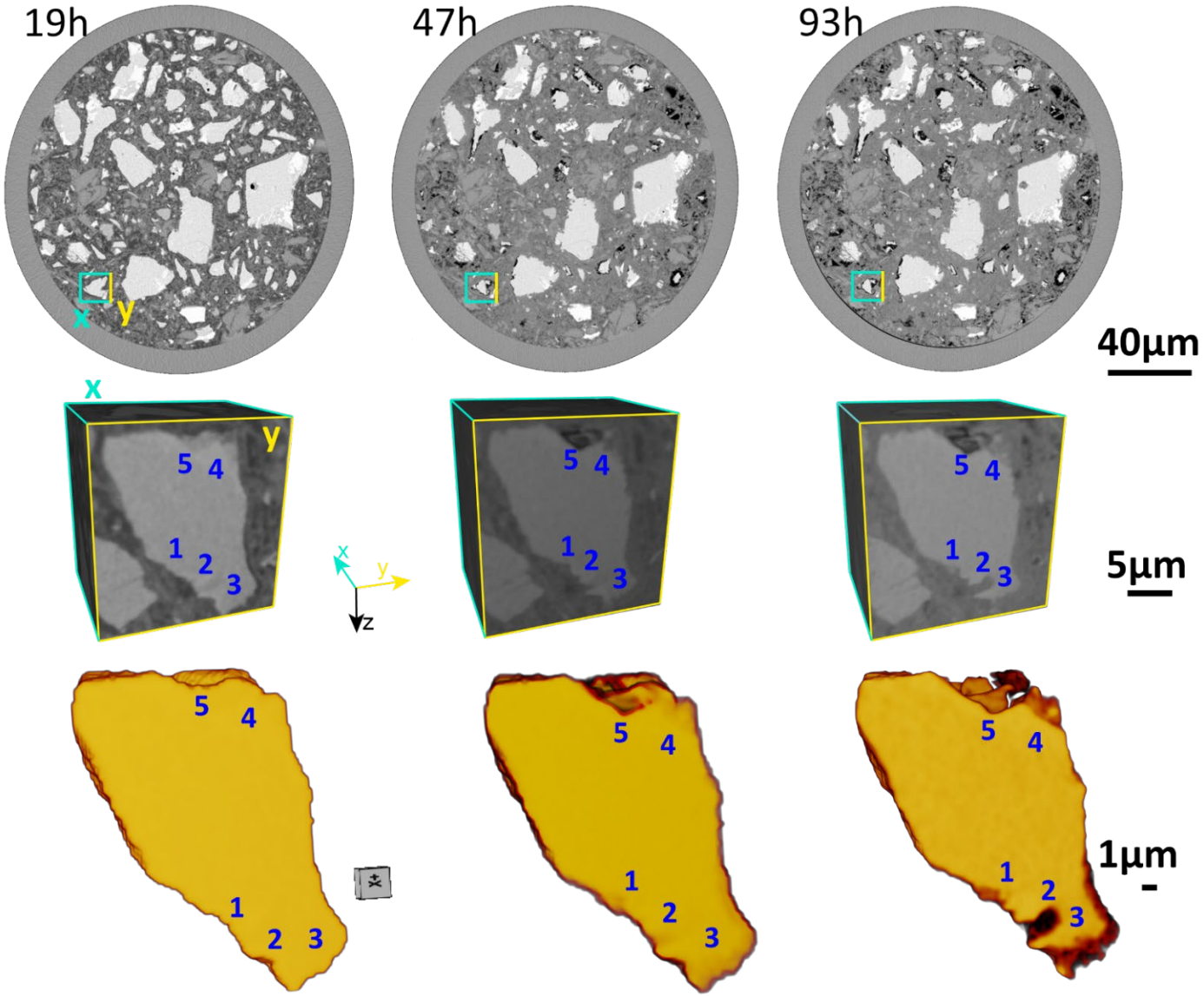

Figure S11. Second etch-pit evolution picture. (Top row) PXCT orthoslices at the three studied ages. (Intermediate) 3D rendering of a volume including a fraction of the alite particle highlighted in the top panels. (Bottom) 3D representation of the segmented particle to highlight the evolution of the etch-pits. These 3D rendered views do not show exactly the electron densities as they are affected by visualization features like the lighting source.

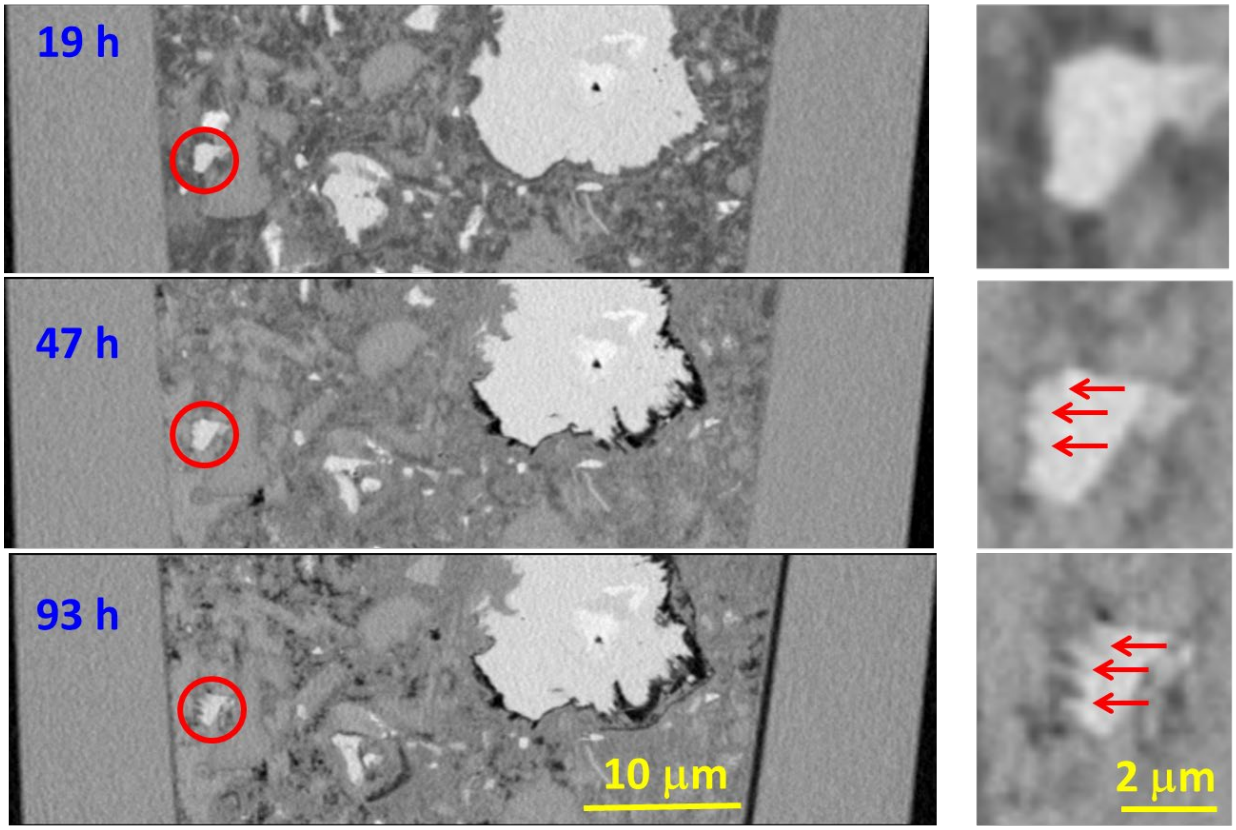

Figure S12. Selected PXCT vertical views at the studied ages showing the evolution of the PC-52.5 paste. This series is intended to show the evolution of water porosity (dark-grey) towards air porosity (black) with time. Moreover, the enlarged views (right images) show the evolution of a small alite particle, initial size about 3 µm, which develops etch-pits of sizes of ~700 nm, highlighted with red arrows.

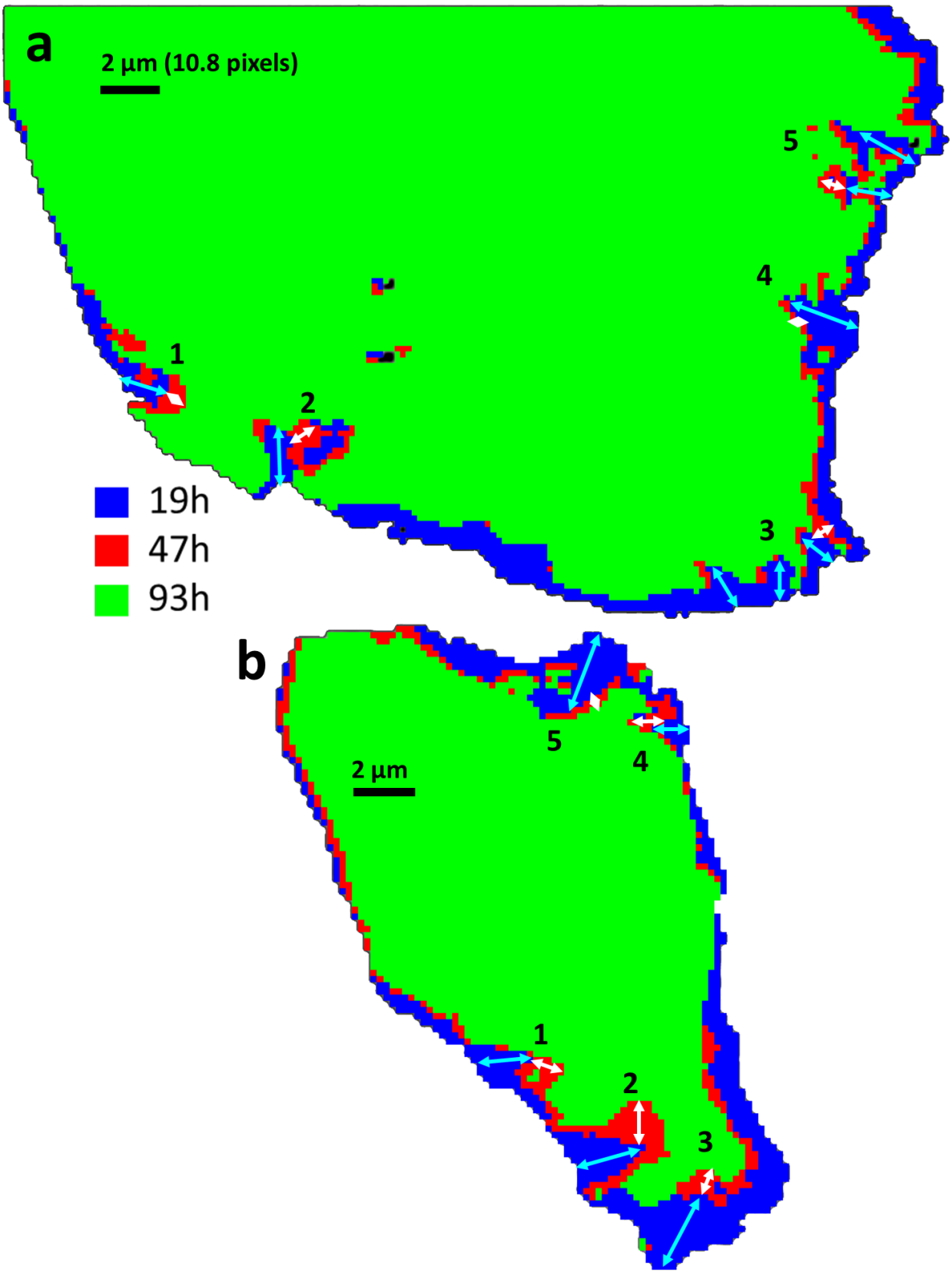

Figure S13. Overlay of the (2D-projected) alite segmented pixels during the hydration process to show the large variability in the growth rates of the etch-pits. a, five etch-pits corresponding to the Figure 4 of the manuscript. b, five etch-pits corresponding to the Figure S11 of this SI. Pale-blue arrows show size changes from 19h to 47h, meanwhile white arrows display to the changes from 47h to 93h.

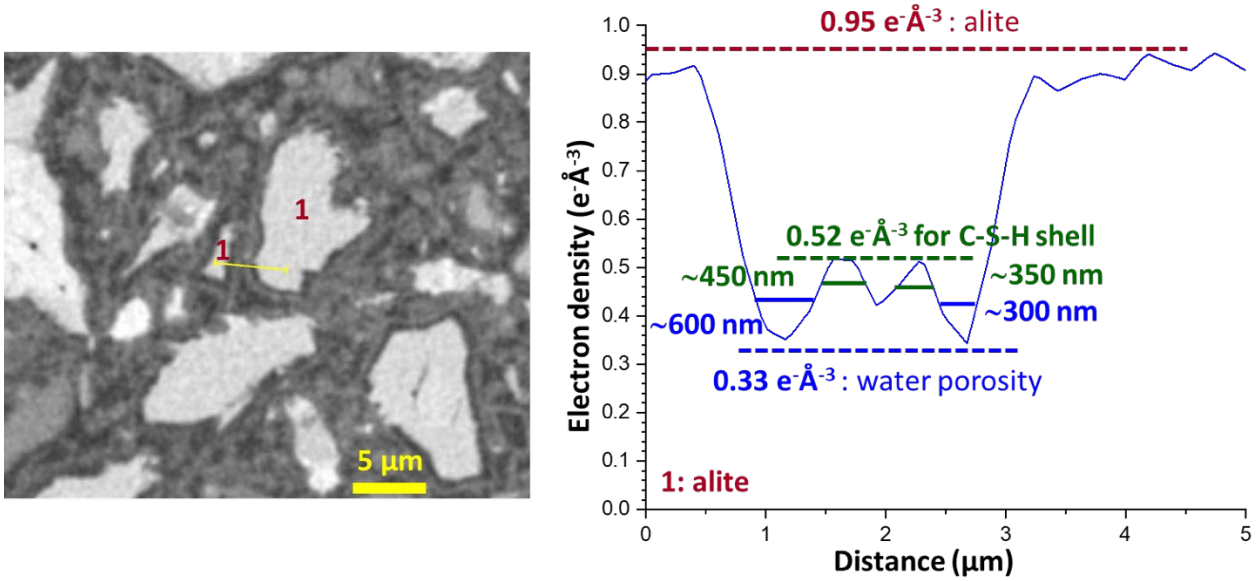

Figure S14. (Left panel) Selected 2D view of the PXCT data at 19 h. (Right) Electron density profile corresponding to the yellow straight line. The line profile signals the water porosity region (blue) surrounding the two alite particles, with the sizes of the C-S-H gel shells and their electron densities given in green.

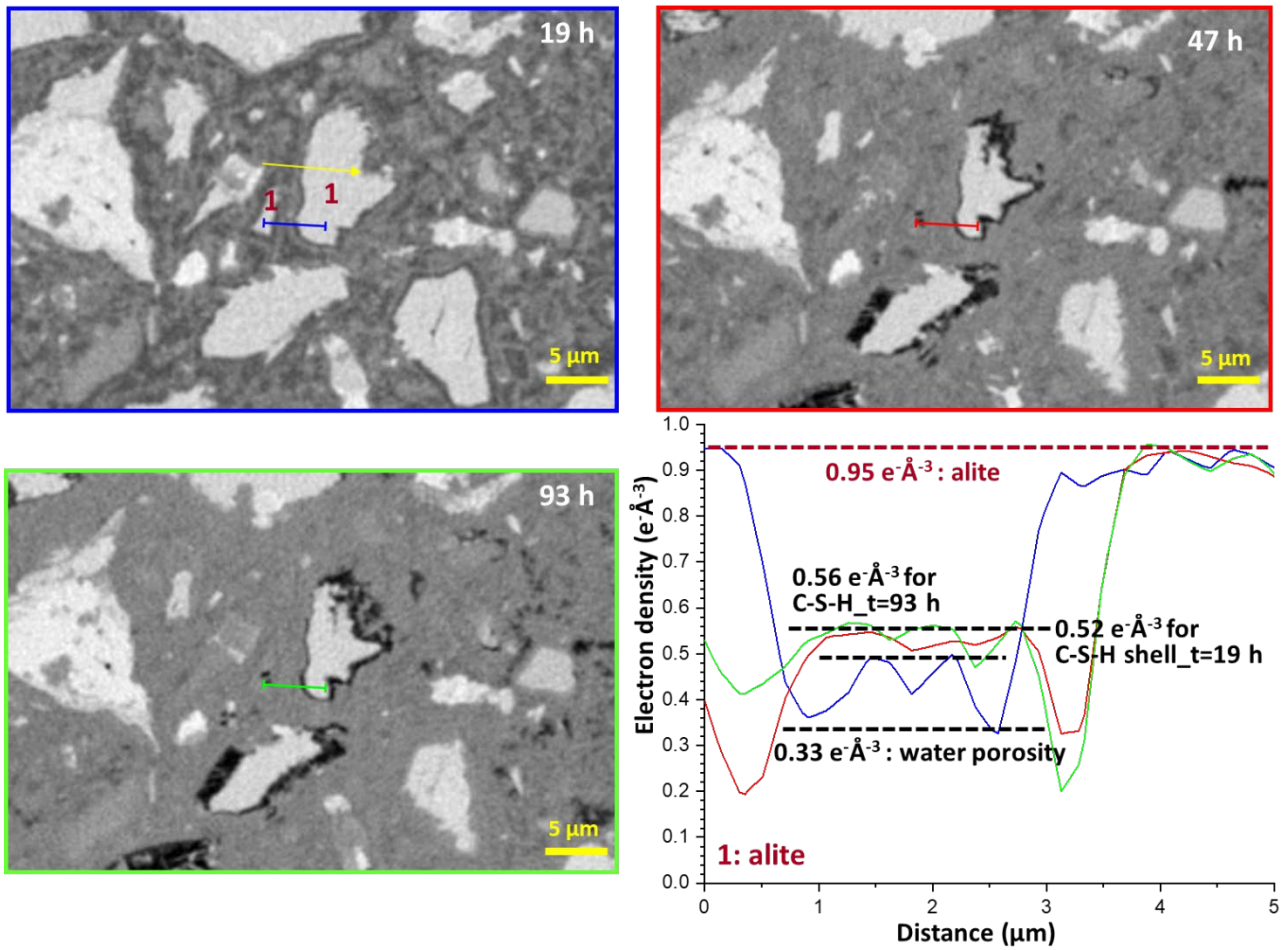

Figure S15. Study of the alite dissolution and C-S-H gel (shell) densification with hydration time. Same region than that shown in Fig. S13.

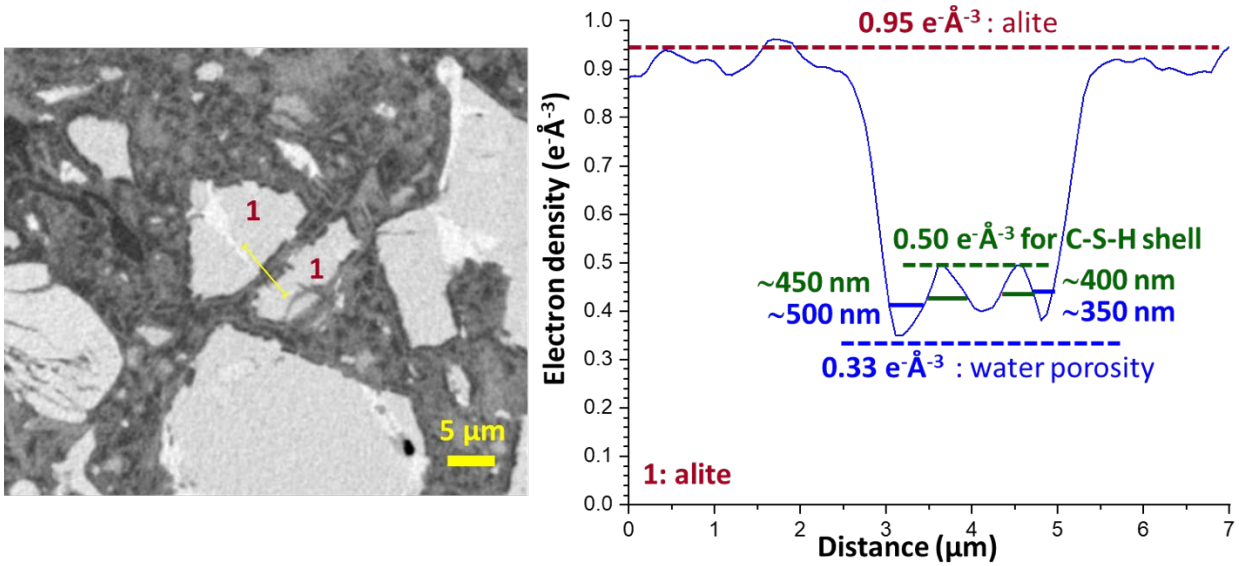

Figure S16. (Left panel) Selected 2D view of the PXCT data at 19 h. (Right) Electron density profile corresponding to the yellow straight line. The line profile signals the water porosity region (blue) surrounding the two alite particles, with the sizes of the C-S-H gel shells and their electron densities given in green.

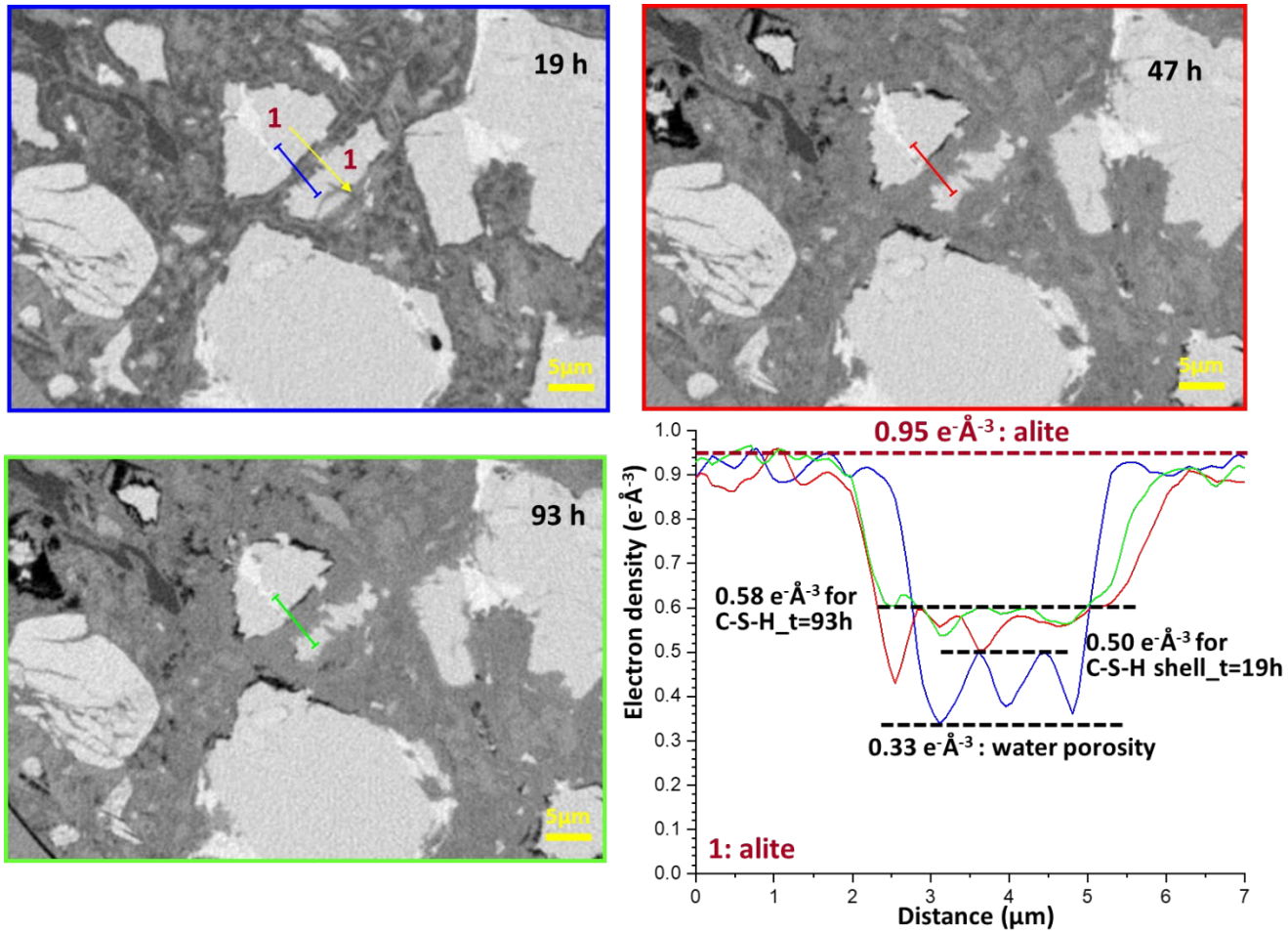

Figure S17. Study of the alite dissolution and C-S-H gel (shell) densification with hydration time. Same region than that shown in Fig. S15. Capillary pore water is still visible at 93 h in the top left region of the image.

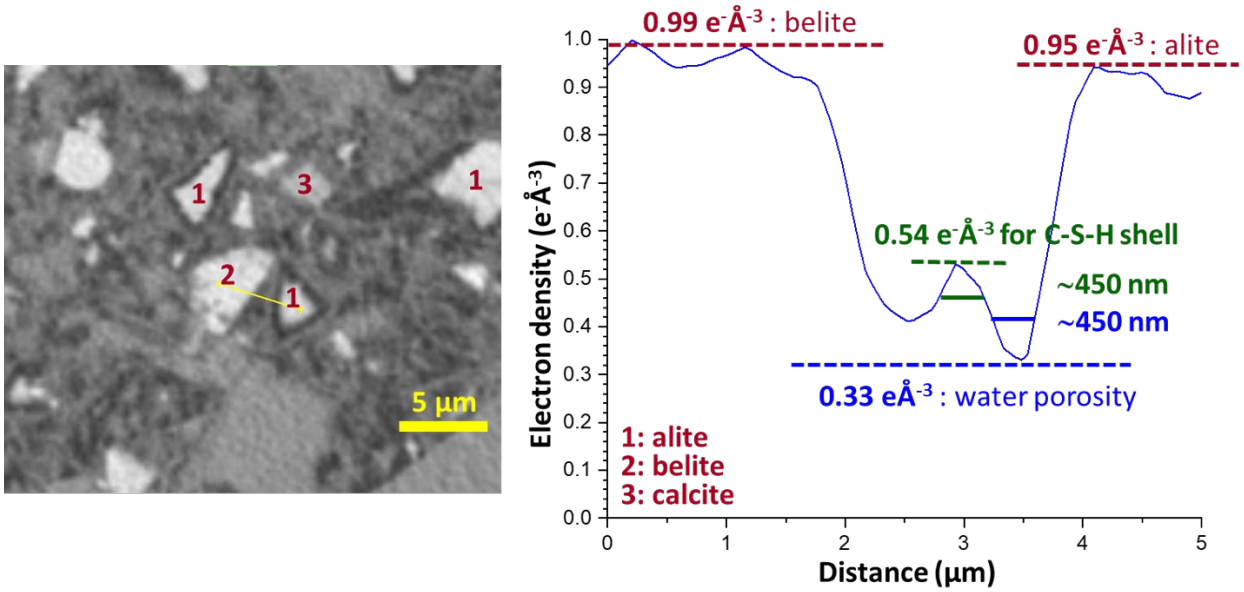

Figure S18. (Left panel) Selected 2D view of the PXCT data at 19 h. (Right) Electron density profile corresponding to the yellow straight line in the right image. The C-S-H porous shell covers every alite particle but it does not surround belite neither calcite. The line profile signals the water porosity region (blue) surrounding alite, with the size of the C-S-H gel shell and its electron density given in green.

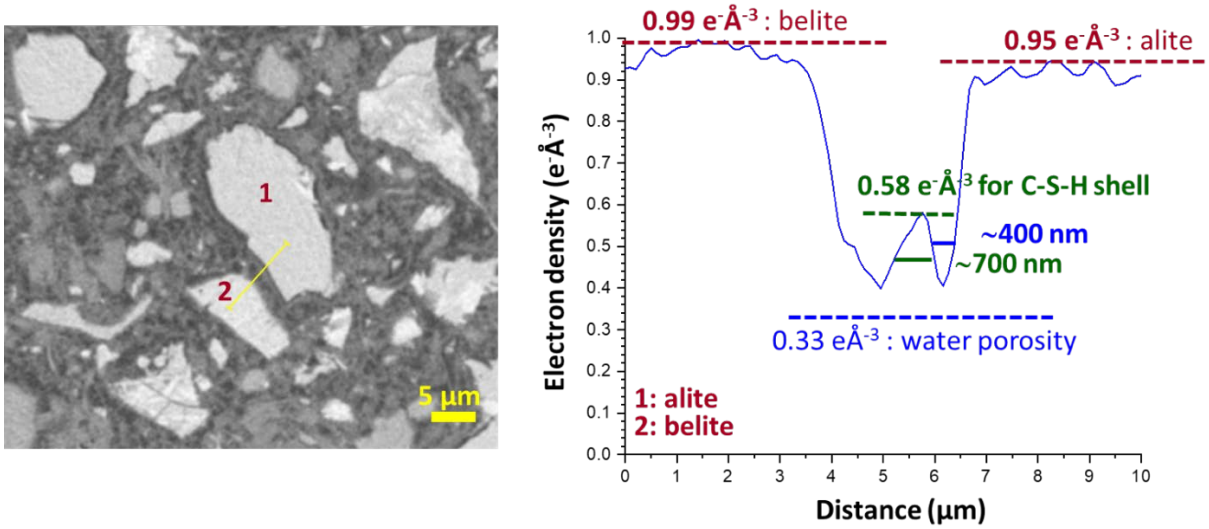

Figure S19. (Left panel) Selected 2D view of the PXCT data at 19 h. (Right) Electron density profile corresponding to the yellow straight line. The C-S-H porous shell covers every alite particle but it does not surround belite grains. The line profile signals the water porosity region (blue) surrounding alite, with the size of the C-S-H gel shell and its electron density given in green.

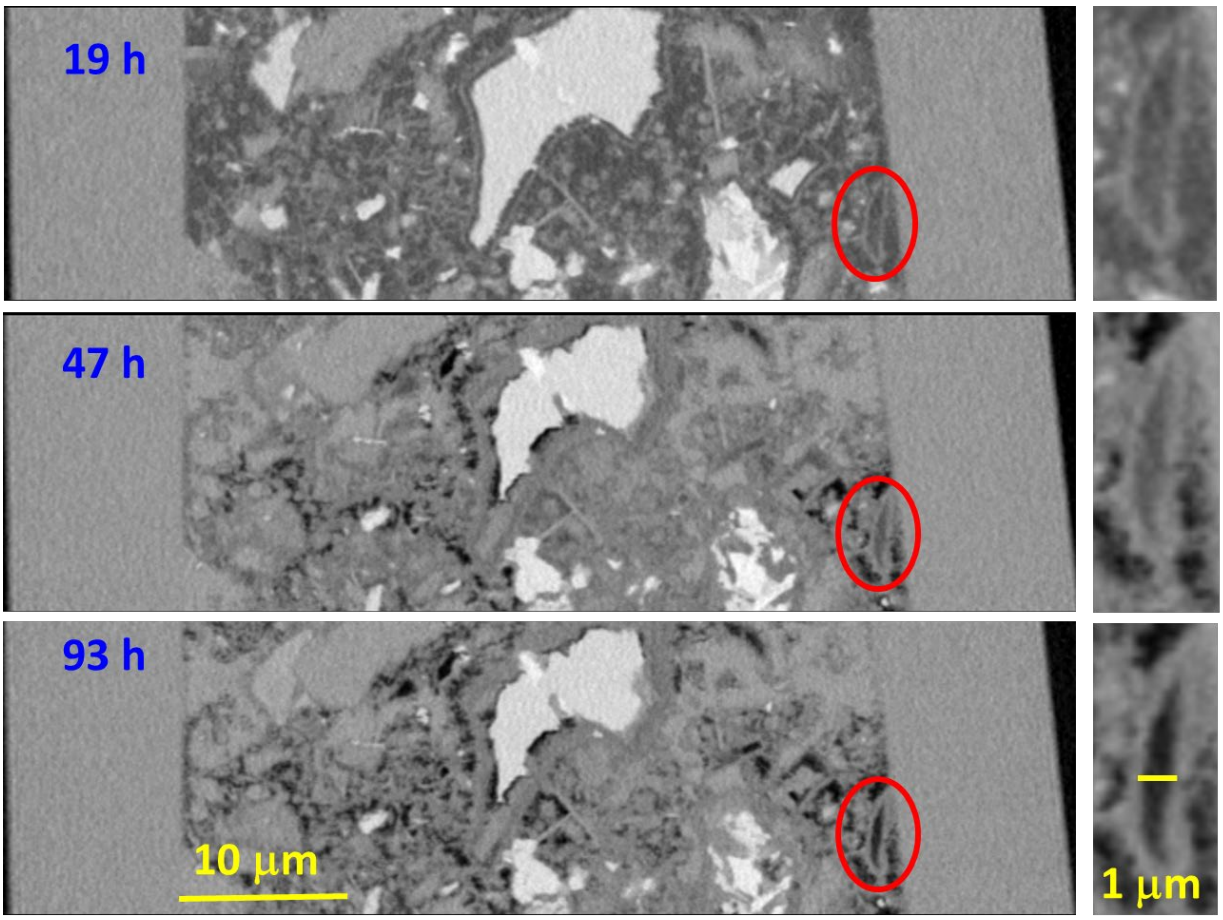

Figure S20. Selected PXCT vertical views at the studied ages showing the evolution of the PC-52.5 paste. This series is intended to show the evolution of water porosity (dark grey) towards air porosity (black) with time. The enlarged views (right images) show the change of a hollow-shell volume, also known as Hadley grain, with hydration time. The hollow-shells, Hadley grains, are fully hydrated small alite particles that contain a void within the original boundary of the anhydrous grain. The hollow regions of the Hadley grains are filled with water at 19 and 47 h but dried at 93 h, see enlarged pictures to the right. This illustrates that most of the capillary pores with sizes larger than ~1 µm are already water emptied at 93 h of hydration, see bottom right. Moreover, it also illustrated that the C-S-H shells are porous as they allow the water diffusion from the inner regions towards the exterior.

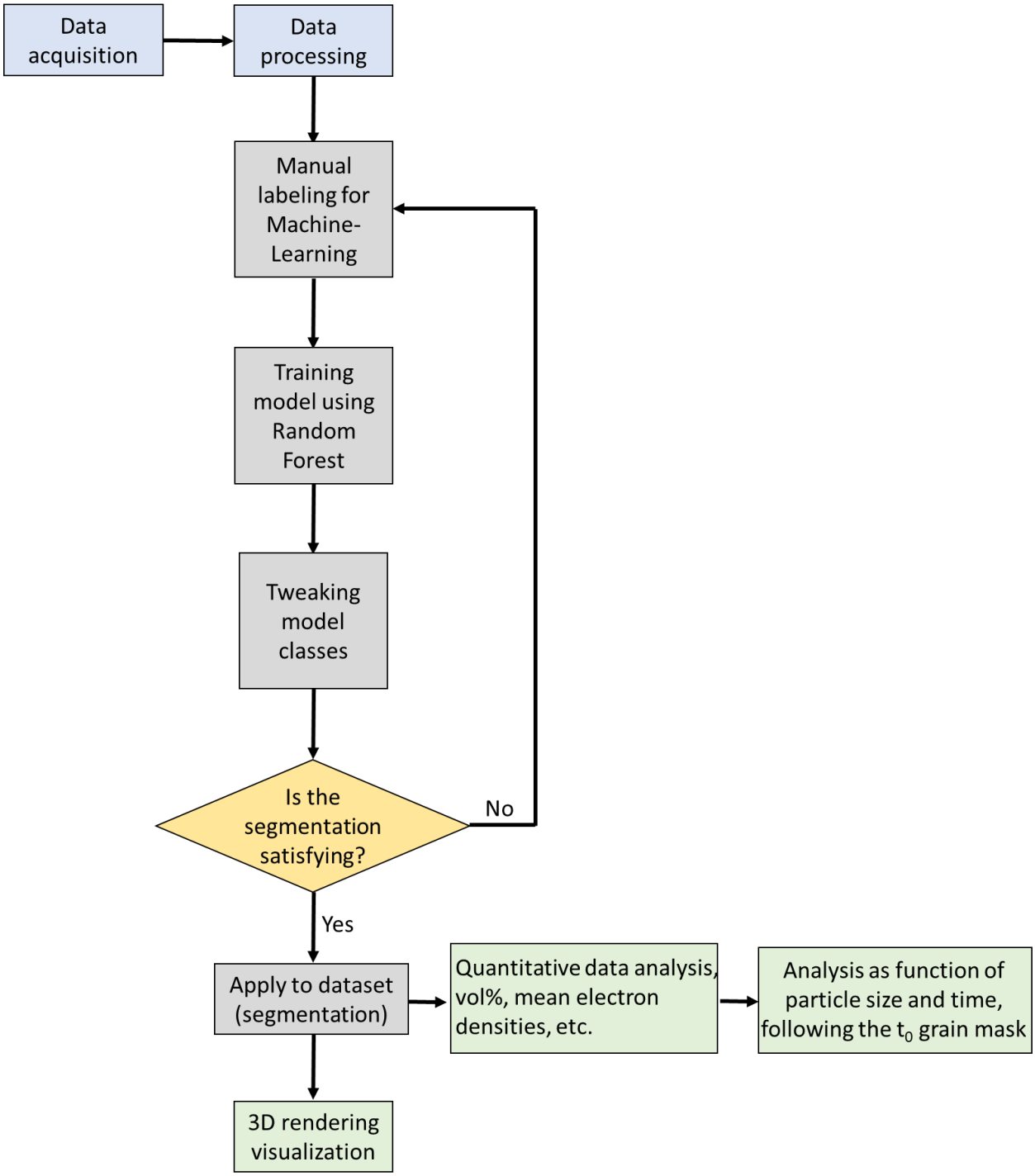

Figure S21. Flow chart describing the data treatment in this work and detailing the machine learning training steps (boxes in grey).

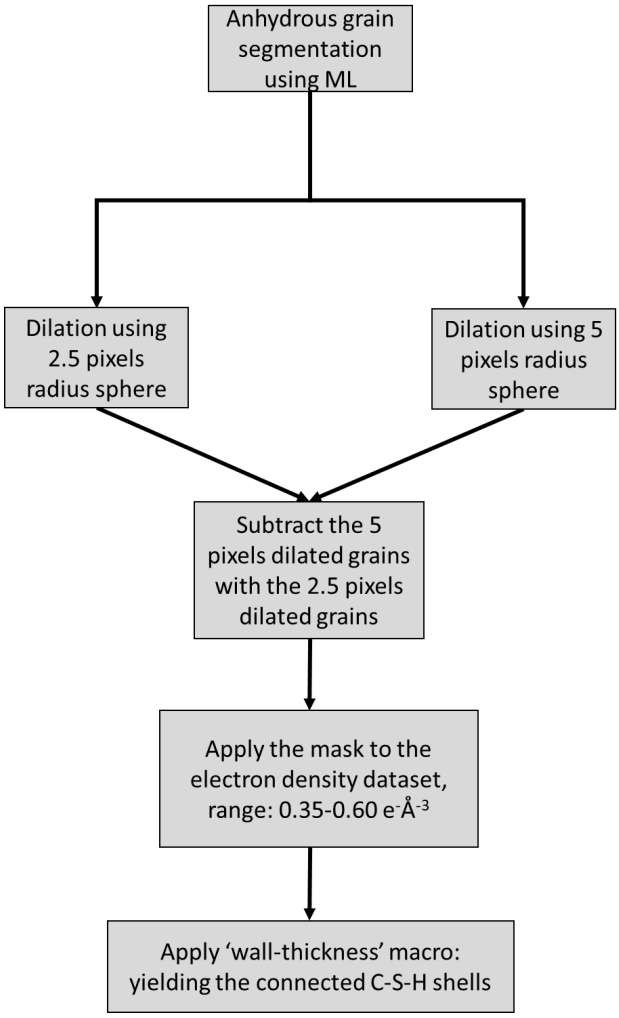

Figure S22. Flow chart detailing the steps for the C-S-H shell segmentation in the 19 h PXCT dataset.

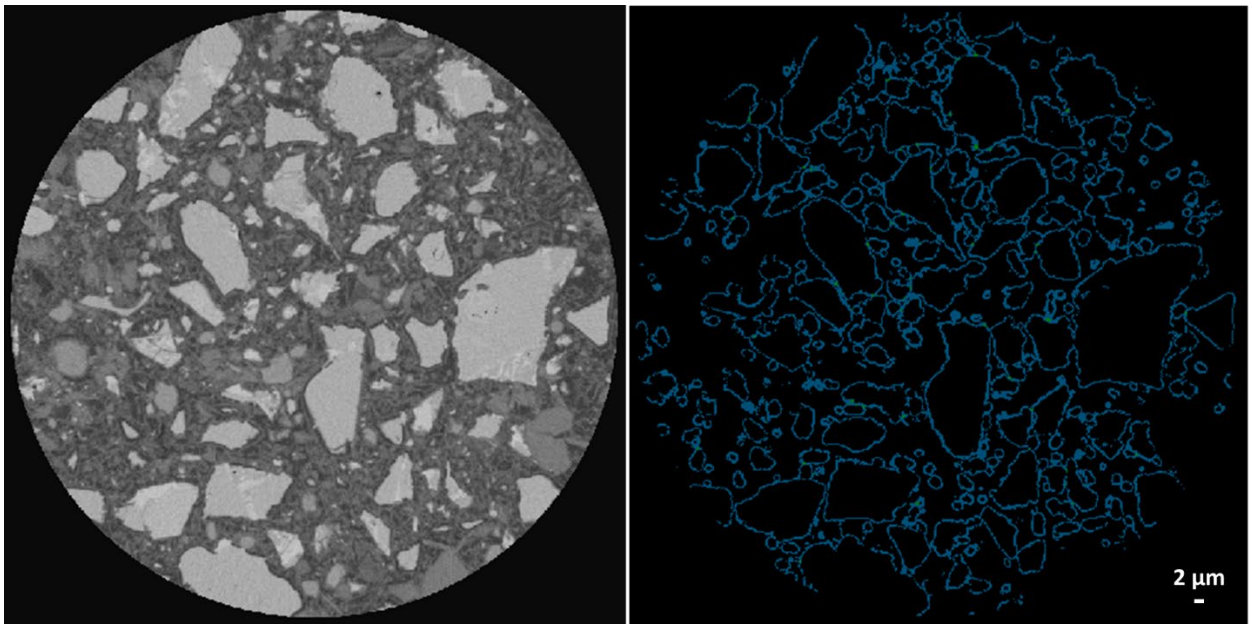

Figure S23. Views, at the same scale, comparing the C-S-H shell as observed in the PXCT raw dataset at 19 h of hydration (left) and the C-S-H shell segmentation output applying the procedure detailed in Fig. S21.

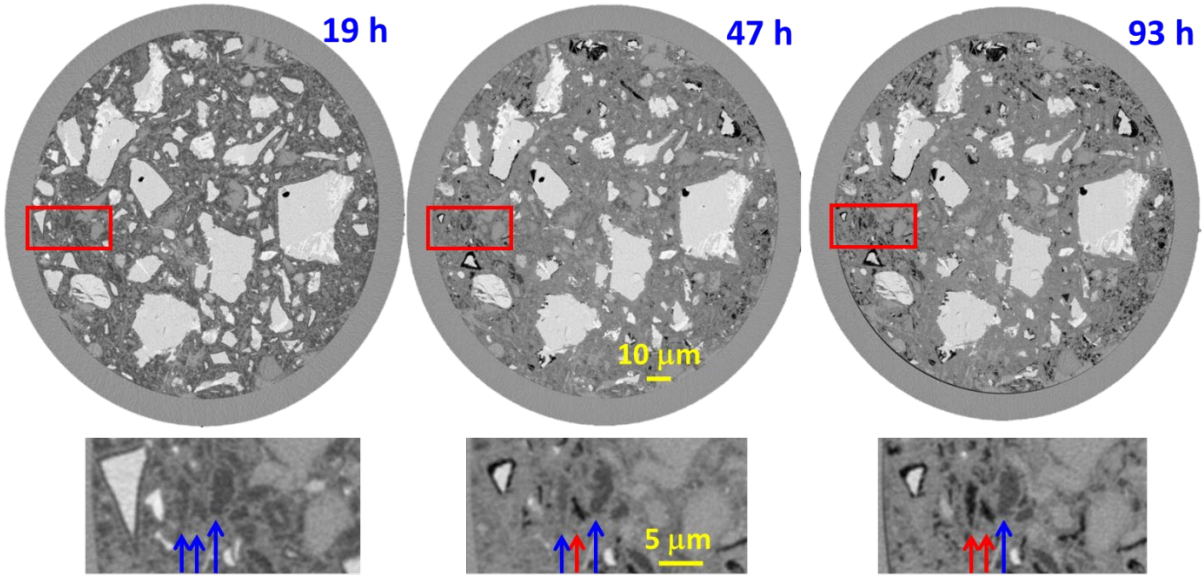

Figure S24. Selected PXCT orthoslices at the studied ages showing the evolution of the PC-52.5 paste. The enlarged views (bottom) show the evolution of porosity within the paste, where several pores of sizes smaller than ~2 µm are dried (red arrows) at 93 h but other larger, pores keep filled with water (blue arrows).

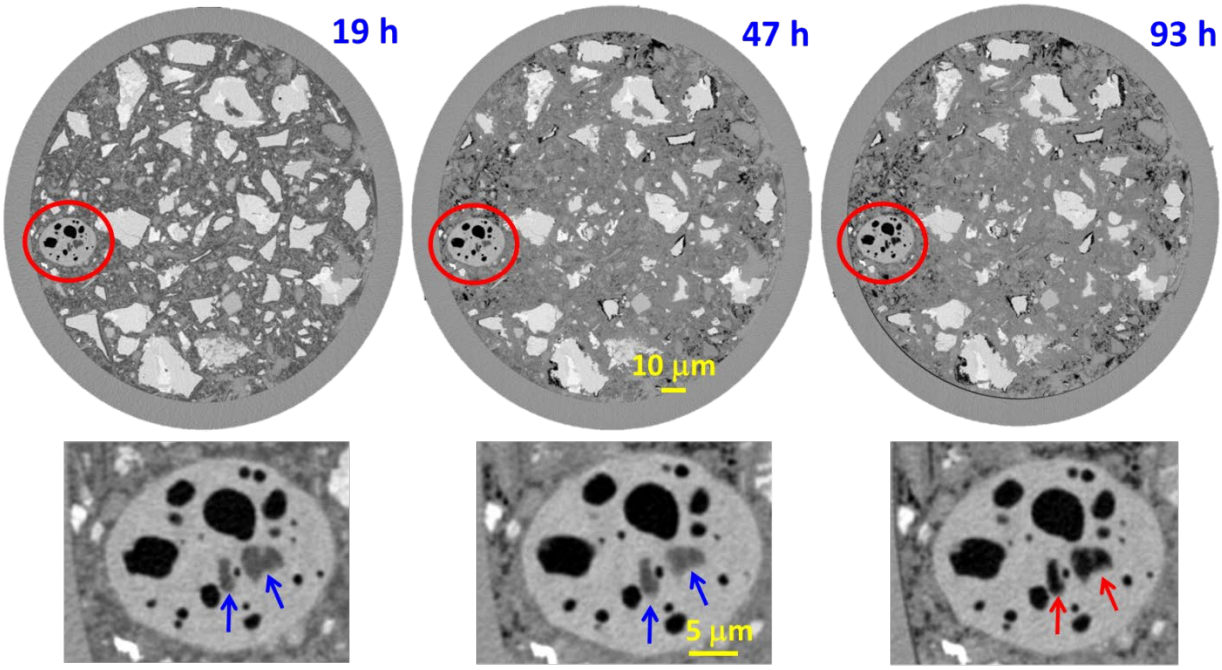

Figure S25. Selected PXCT orthoslices at the three studied ages showing the evolution of the PC-52.5 paste. The enlarged views (bottom) show the evolution of a large calcite particle with internal pores. At 19 and 47 h of hydration some pores are filled with water (highlighted with blue arrows) which are connected to the surface. At 93 h, these pores are empty (red arrows) releasing water for further hydration.

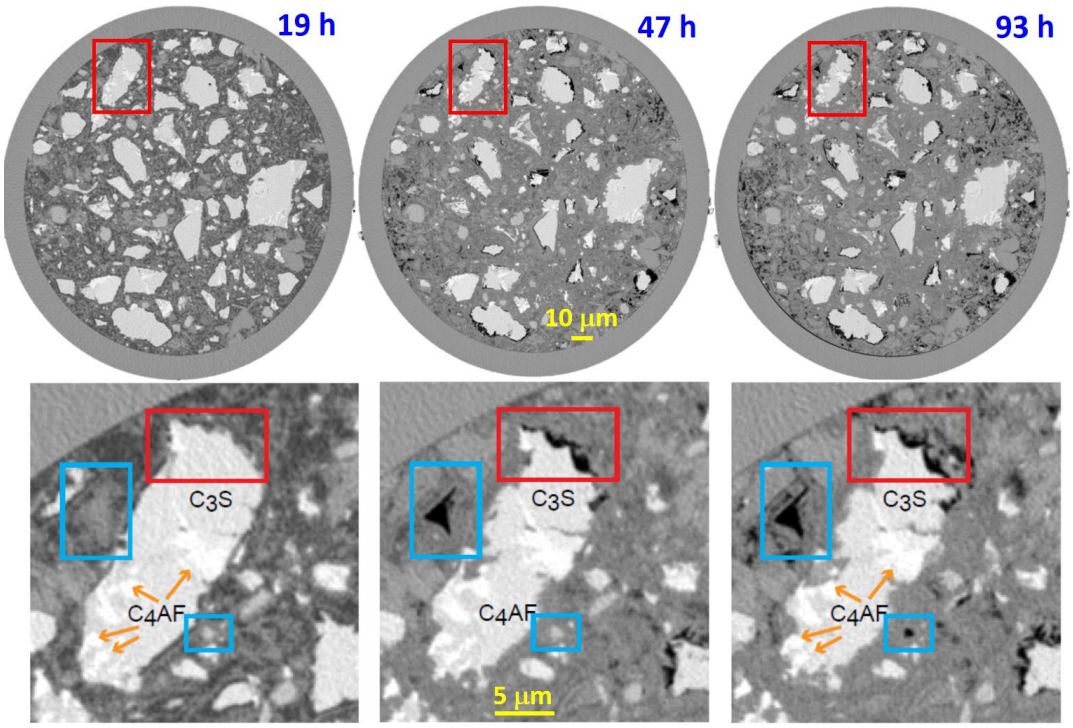

Figure S26. Selected PXCT orthoslices at the studied ages. The chemical shrinkage is evident at 93 h because the appearance of empty (black) regions. The enlarged views (bottom) show: (1) the hydration of a large alite particle with aluminoferrite, C_4AF, intergrown, i.e. the whitest regions, see brown arrows. In addition to the etch-pit evolution, it can be seen that hydration stops at the regions where C_4AF is exposed to the hydration medium; (2) the blue rectangles highlight the dissolution of C-S-H gel particles to give dry (air-filled) pores. Moreover, alite hydration also stops as soon as air porosity (pore drying) develops on the surfaces of the anhydrous grains, see red rectangles in the bottom panels.

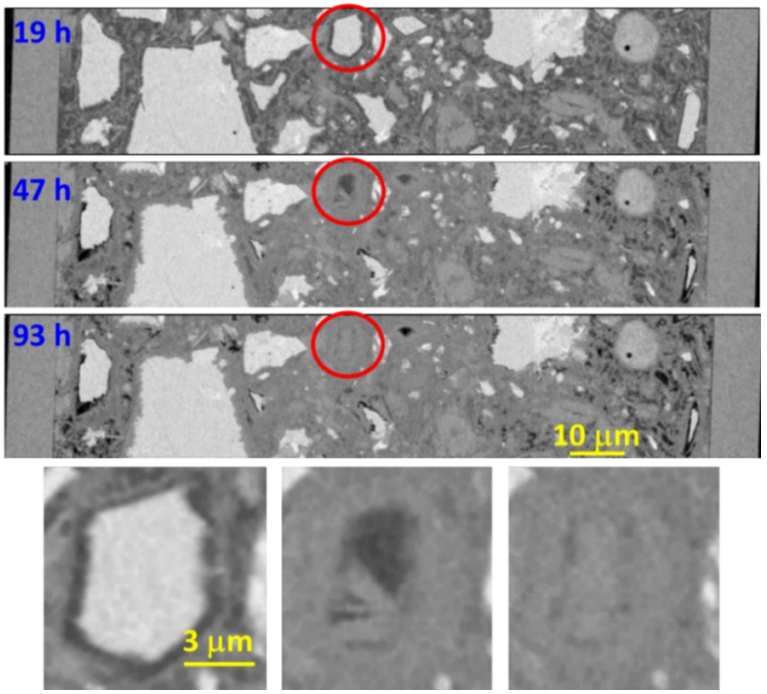

Figure S27. Selected PXCT vertical pictures with enlarged views (bottom) displaying the hydration pathway of a very fast dissolving particle, i.e. a 4 µm particle fully dissolved between 19 and 47 h. The electron density of this small volume, 0.91 $e^{-}Å^{-3}$, is compatible with C_3S or C_3A. It already shows a gap at 19 h indicating a highly soluble component. At 47 h, two hydrate rods of diameter smaller than 1 µm, morphologically suggesting ettringite, grow in the pristine region which is filled with capillary water. At 93 h, the volume is fully occupied by hydrate(s). The dissolution rate between 19 and 43 h is faster than 75 nm/h suggesting C_3A. However, the chemical nature of this tine particle could not be firmly established.

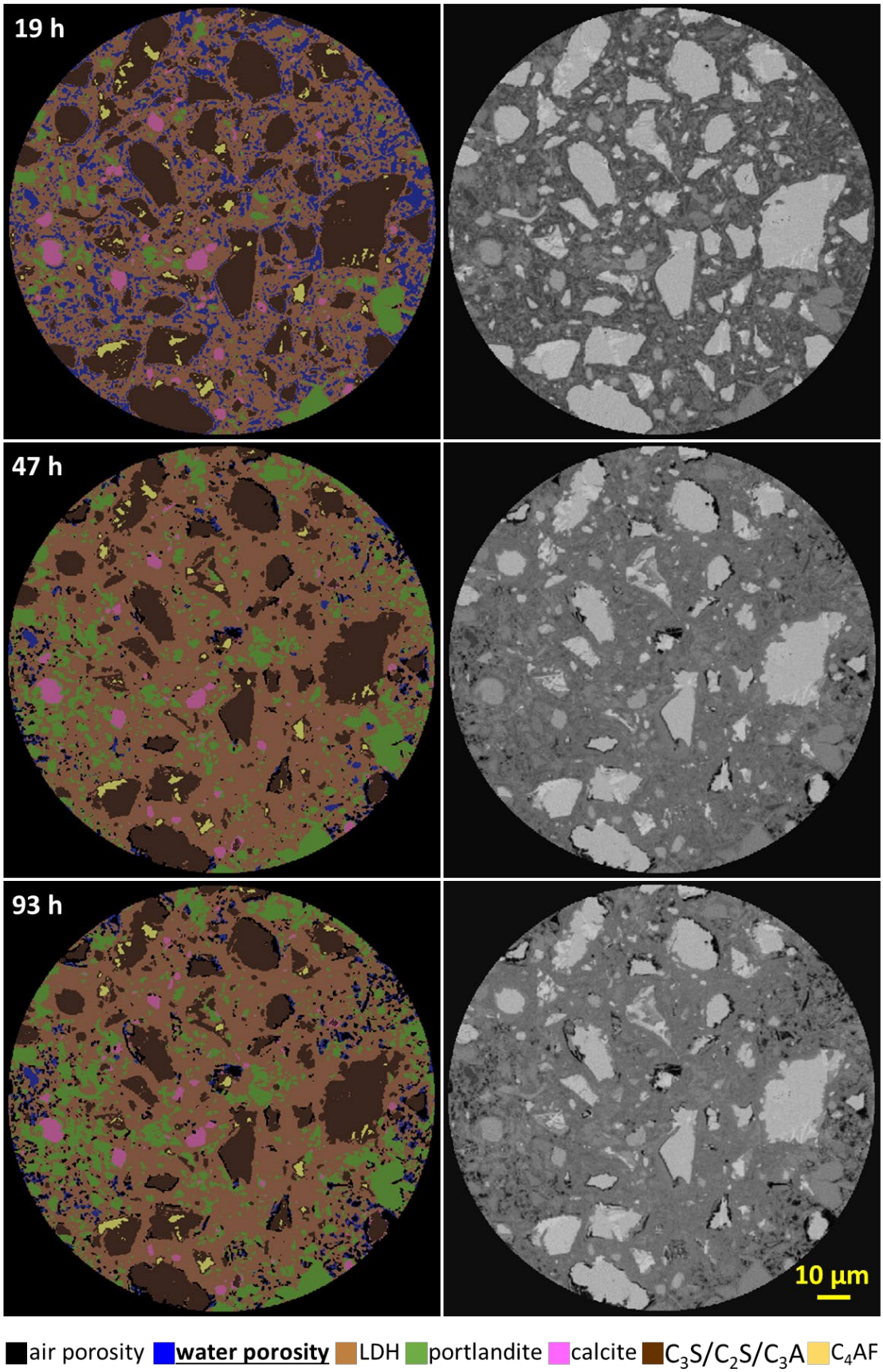

Figure S28. Capillary water porosity evolution, with the obtained spatial resolution (i.e. approximately two voxels). Field of view ~160 µm. (Left) ML segmentation output. (Right) 2D orthoslices of the raw PXCT datasets.

• Supplementary movies

- **Movie-1:** "Summary of 4D nanoimaging of cement hydration" 43 seconds.

  A summarized display of the cement paste hydration evolution as seen by this nanoimaging study. The progress of the different components is displayed after segmentation by Machine-Learning. Moreover, key changes like water porosity evolution or shrinkage development are highlighted on the video by embedded written text.

- **Movie-2:** " C-S-H shell characterization at 19 hours " 17 seconds.

  A video revealing the arrangement of the 3D segmented C-S-H shells through the 19 h nanoimaging dataset.

The size of each short video is standard 640×480 pixels in mp4 format as suggested by Nature journal. Therefore, users can download them quickly.

Article cover image:

Title: "X-ray nanoimaging of a hydrating cement paste at early ages"

Description: The precipitating calcium silicate hydrate shells (blue) surround the dissolving alite particles (yellow) with regions of calcium aluminoferrite highlighted in orange. For better visualisation: only the C-S-H shells in the left part, the three components in the middle region, just the anhydrous cement particles in the right part. The gaps, approximately 500 nm, between the C-S-H shells and the dissolving alite particles are readily visible in the central part of the image.

The cover image is a high resolution 5000×4005 pixels size in .tif format.

Cover image credit: Shiva Shirani, Cover design: Maziar Moussavi

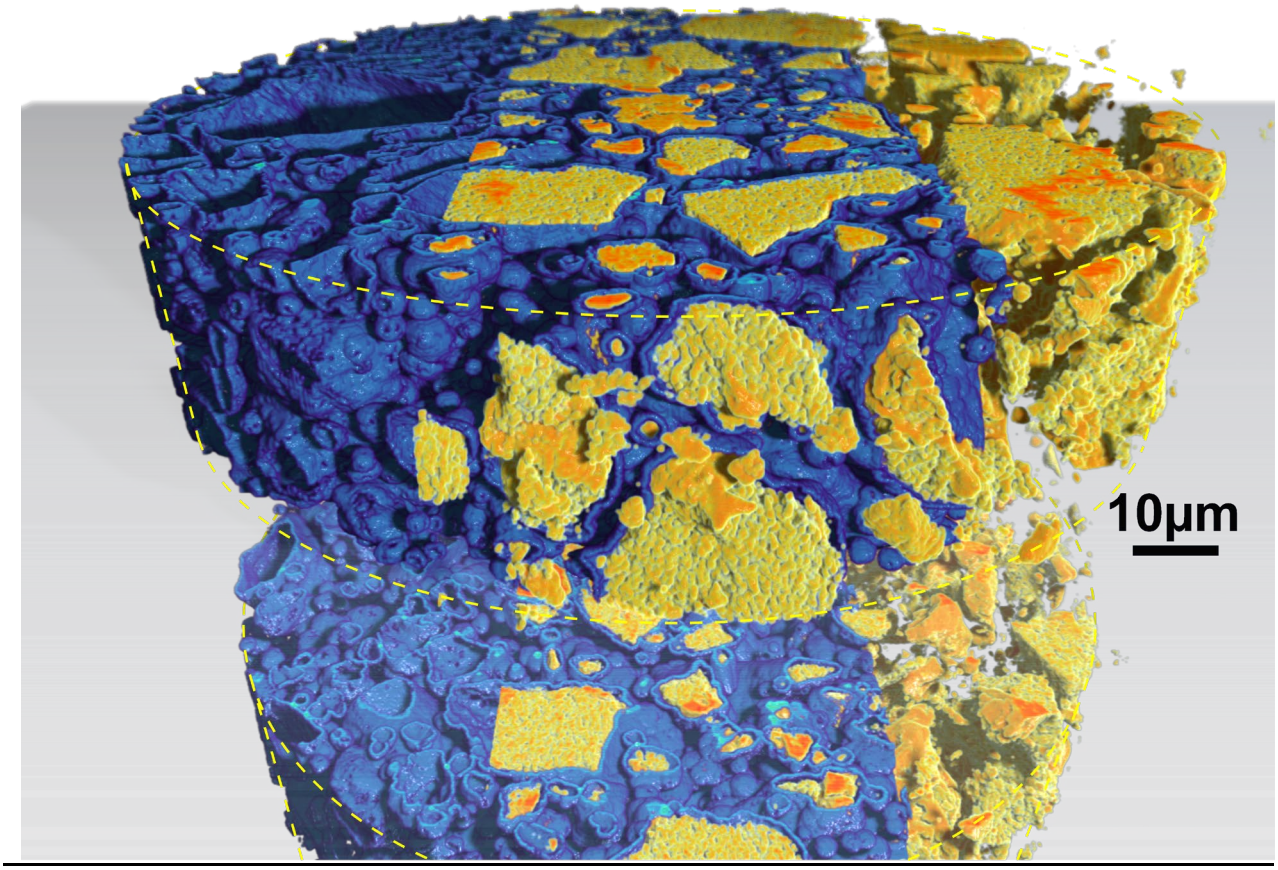

• **Supplementary References**

1. Douissard, P. A. *et al.* A versatile indirect detector design for hard X-ray microimaging. *J. Instrum.* **7**, P09016 (2012).
2. Martin, T. *et al.* LSO-based single crystal film scintillator for synchrotron-based hard X-ray micro-imaging. *IEEE Trans. Nucl. Sci.* **56**, 1412–1418 (2009).
3. Paganin, D., Mayo, S. C., Gureyev, T. E., Miller, P. R. & Wilkins, S. W. Simultaneous phase and amplitude extraction from a single defocused image of a homogeneous object. *J. Microsc.* **206**, 33–40 (2002).
4. Vigano, N., Cloetens, P., di Michiel, M., Rack, A. & Tafforeau, P. Redefining the ESRF tomography software. in *Digital Holography and Three-Dimensional Imaging 2021* paper DF2G.4 (OSA Technical Digest, Optica Publishing Group, 2021). doi:10.1364/DH.2021.DF2G.4.
5. van Heel, M. & Schatz, M. Fourier shell correlation threshold criteria. *J. Struct. Biol.* **151**, 250–262 (2005).
6. Holler, M. *et al.* An instrument for 3D x-ray nano-imaging. *Rev. Sci. Instrum.* **83**, 073703 (2012).
7. Holler, M. *et al.* X-ray ptychographic computed tomography at 16 nm isotropic 3D resolution. *Sci. Rep.* **4**, 3857 (2014).
8. Odstrčil, M., Lebugle, M., Guizar-Sicairos, M., David, C. & Holler, M. Towards optimized illumination for high-resolution ptychography. *Opt. Express* **27**, 14981 (2019).
9. Huang, X. *et al.* Optimization of overlap uniformness for ptychography. *Opt. Express* **22**, 12634 (2014).
10. Dinapoli, R. *et al.* EIGER: Next generation single photon counting detector for X-ray applications. *Nucl. Instruments Methods Phys. Res. Sect. A Accel. Spectrometers, Detect. Assoc. Equip.* **650**, 79–83 (2011).
11. Odstrcil, M., Lebugle, M., Lachat, T., Raabe, J. & Holler, M. Fast positioning for X-ray scanning microscopy by a combined motion of sample and beam-defining optics. *J. Synchrotron Radiat.* **26**, 504–509 (2019).
12. Wakonig, K. *et al.* PtychoShelves, a versatile high-level framework for high-performance analysis of ptychographic data. *J. Appl. Cryst* **53**, 574–586 (2020).
13. Thibault, P., Dierolf, M., Bunk, O., Menzel, A. & Pfeiffer, F. Probe retrieval in ptychographic coherent diffractive imaging. *Ultramicroscopy* **109**, 338–343 (2009).
14. Guizar-Sicairos, M. *et al.* Phase tomography from x-ray coherent diffractive imaging projections. *Opt. Express* **19**, 21345 (2011).
15. Odstrčil, M., Holler, M., Raabe, J. & Guizar-Sicairos, M. Alignment methods for nanotomography with deep subpixel accuracy. *Opt. Express* **27**, 36637–36652 (2019).
16. Diaz, A. *et al.* Quantitative x-ray phase nanotomography. *Phys. Rev. B* **85**, 020104 (2012).
17. Kaestner, A. P. *et al.* Recent developments in neutron imaging with applications for porous media research. *Solid Earth* **7**, 1281–1292 (2016).
18. Donnelly, C. *et al.* Time-resolved imaging of three-dimensional nanoscale magnetization dynamics. *Nat. Nanotechnol.* **15**, 356–360 (2020).
19. Li, X. *et al.* Direct observation of C3S particle dissolution using fast nano X-ray computed tomography. *Cem. Concr. Res.* **166**, 107097 (2023).
20. Cuesta, A. *et al.* Quantitative disentanglement of nanocrystalline phases in cement pastes by synchrotron ptychographic X-ray tomography. *IUCrJ* **6**, 473–491 (2019).
21. Linderoth, O., Wadsö, L. & Jansen, D. Long-term cement hydration studies with isothermal calorimetry. *Cem. Concr. Res.* **141**, 106344 (2021).
22. Trtik, P., Diaz, A., Guizar-Sicairos, M., Menzel, A. & Bunk, O. Density mapping of hardened cement paste using ptychographic X-ray computed tomography. *Cem. Concr. Compos.* **36**, 71–77 (2013).
23. Aranda, M. A. G., Cuesta, A., De la Torre, A. G., Santacruz, I. & León-Reina, L. Diffraction and

crystallography applied to hydrating cements. in *Cementitious Materials: Composition, Properties, Application* (ed. Pöllmann, H.) 31–60 (De Gruyter, 2017). doi:10.1515/9783110473728-003.

24. De la Torre, A. G., Santacruz, I., Cuesta, A., León-Reina, L. & Aranda, M. A. G. Diffraction and crystallography applied to anhydrous cements. in *Cementitious Materials* (ed. Pöllmann, H.) 3–29 (De Gruyter, 2017).
25. Henke, B. L., Gullikson, E. M. & Davis, J. C. X-Ray Interactions: Photoabsorption, Scattering, Transmission, and Reflection at E=50−30,000 eV, Z= 1−92. *At. Data Nucl. Data Tables* **54**, 181–342 (1993).

nature portfolio

Peer Review File

4D nanoimaging of early age cement hydration

REVIEWER COMMENTS

Reviewer #1 (Remarks to the Author):

The strength of this study, in my opinion, is in the exploration of a new nanoimaging technique, PXCT, to study the early hydration of Portland cement. With the unprecedented spatial resolution and contrast of PXCT, in situ identification of the evolution of various mineral phases, the C-S-H gel shells, etch pits, water pores and air pores, etc. became possible, hence the corresponding cement dissolution and precipitation processes at early ages associated with them was studied, and qualitative and quantitative results were obtained. The results are of potential interest to researchers working in X-ray computerized tomography and could illustrate a new characterization direction for the cement-based materials community.

The approach, data analysis and interpretation are valid, comprehensive and correct, and the evidence presented justify the conclusions. The literature is adequately cited. The clarity and accessibility of the text is good, and the results have been provided with sufficient context and consideration of previous work.

There are several issues however that I think should be clarified to help improve the work.

1.In the manuscript, it is said "In situ near-field data were taken as detailed in methods……. radiation damage cannot be discarded but it is small, if any. (Page 5) " "Time resolutions of ~1 h will open the way to accurately study the processes in the acceleration period. However, in these cases, radiation damage could be an issue if the total dose is not kept low. (Page 12)"
Will radiation damage affect the visualization results of the evolution of water porosity towards air porosity with time? In addition, migration of C-S-H gel was observed. Is it possible that this was also affected by radiation damage? How will the effect of radiation damage be considered in the future research with higher time resolution?

2.The evolution of water porosity towards air porosity with time was observed around some Alite grains. How will this affect further hydration of Alite and etch pits growth when there is no water around?

3.In the manuscript, it is said "The hollow regions of the Hadley grains are filled with water at 19 and 47 h but dried at 93 h, see enlarged pictures to the right. This illustrates that most of the capillary pores with sizes larger than ~1 μm are already water emptied at 93 h of hydration, see bottom right. (Figure S19)", "The enlarged views (bottom) show the evolution of porosity within the paste, where several pores of sizes smaller than ~2 μm are dried (red arrows) at 93 h but other larger, pores keep filled with water (blue arrows). (Figure S23)"
Is there a contradiction between those two conclusions, for the pores to be empty at 93 h, the former is >1μm and the latter is <2μm? Does the water migrate randomly?

4.The water to cement ratio is relatively higher near the capillary wall than that in the center. In Figure S27, wall effect in the 19h capillary tube sample could be observed. Will the degree of hydration of cement particles of the same size be affected by wall effect at different locations? It should be addressed in the manuscript.

Reviewer #2 (Remarks to the Author):

In this manuscript, the authors report the study of the early stage of cement hydration using mainly near-field ptychographic X-ray computed tomography. They provide a unique combination of spatial & temporal resolution + field of view. It allows the determination of quantitative values for dissolution rates and etch-pit growth rates. A comparison with data obtained by lab and synchrotron X-ray micro-tomography is also proposed. The paper shows an extended collection of data using state of the art technique and an interesting 3D data analysis based on machine learning process. Nevertheless, the manuscript shows some incoherencies and approximations, the results are not sufficiently described and discussed, especially the ones reported in the abstract.

Thus, I cannot support this work for publication in Nature communications in its present form.
Some specific comments and remarks linked to my previous general comment:
For the PXCT study, the size of the capillary used is different between the different sections and figures 160 µm vs 200 µm. This information is important. Indeed, it is highlighted (in the supplementary methods) that the sample should be smaller than the FOV (186 µm) in order to have quantitative results (" The field of view must be larger than the size of the capillary to include an air region at both sides of the sample, which is needed for successful tomographic reconstructions and for quantitative contrast.").
It is mentioned in the first paragraph of the "result and discussion" section that the particles size of the sample PC-52.5 for PXCT study are finer than the sample described in the table S3 and used for the lab measurements (XRD, tomography…). How is it done? What is the impact on the comparison of the results between the different measurements?
The w/c ratio value for the sample used for PXCT measurements differs from 0.4 to 0.5 when described in the SI file, in situ multicontrast X-ray tomographic studies of cement hydration and method sections.
What are the units in Table2 ?

In figure 2:
- In b, it can be seen that the images of the Lab-uCT scan are more blurred at 93h than at 19h. Why ? Why does the analysis performed in Figure S5 not show the same tendency?
- On the contrary, Figure S7 clearly shows a degradation on the spatial resolution that is not observed by eye on the images.
- It is concluded that the resolution is estimated at two pixels (How?). It means that the resolution of the PXCT study is 374 nm. Then, how representative and trustable are the values given in figure S13 –Figure S15 ?
- Looking at the figure c: Can you link the difference of the grey-value in the diagram of lab-uCT and syn-uCT to the different behaviour of the two different cements ?
- There is a comparison between the lab-uCT diagram and the PXCT one. What is the abscissa axis label for the lab-uCT ? I understood that it was grey-value. If yes, what is the link to compare grey-values of absorption tomography to electron density obtain by PXCT ?
- Is the diagram of figure 2c the same than Figure S10? Are they representative of the same sub-volume ? Is "the largest possible volumes without including the glass capillary walls" is equivalent to the ~1×10 5 µm3 VOI mentioned in the "tomographic data analysis section" of SI for the PXCT study?

Looking at the spatial resolution analysis:
How many interfaces have been studied as in figures S2-3-4 to determine the resolution estimations? What is the standard deviation? Can the calculation linked to the figure s5-s6-s7 be detailed? How the resolution values are deduced from the curves?

Are the volumes used to determine the data of Table S7 and Figure S10 equal to the VOI?
It can be seen that there is a difference between the theoretical electron density of the components and the measured one. How do you explain the difference? Why did you choose to use the theoretical value to indicate the different components in figure S10 ? Why is there no measured values for air, water and LDH ? Which electron densities have been used to train the machine learning for those phases?

Why the grey values of the 3D rendering in figure 4 are different from one-step to another?

How has been the etch pit growth rate evaluated?

At the beginning of page 6 it is mentioned the spatial dissolution rate of alite. Since alite, C3A and belite has been classified in the very same category for the segmentation, how is it possible to make the difference between them when looking at C-S-H gel shells. I guess that the belite particles are not surrounded by gel shells because the DoH is equal to zero in table S5 but what about the differentiation between C3S and C3A?
Do we have an idea of how many particles of alite <3um were present in the sample at the beginning of the experiment?

Is the figure 5b representative of the 19h step?

At the end of the page 9 and in figure 8, it is mentioned, "PXCT yields underestimated values for the DoH likely due to the limited scanned volume" and "These data are scattered for PXCT because the limited height of the studied cylinder yields a poor representative elementary volume for this feature". It is in contradiction with the conclusion given in page 4 "giving confidence to the relevancy of the nanoimaging results in spite of the limited amount of volume scanned to have submicrometer resolution". Can you give more info and comment on the representativeness of the volume scanned by PXCT?

What is the UCP volume mentioned in page 10?

How is it possible to link the results obtained from 2D figures 5 and S13 to S18 to the ones obtained with the 3D segmentation? Are the results giving the same spatial dissolution rate?

Can you specify what you mean by quantification in this sentence: "Etch-pit growth rate, ~40 nm/h, and coalescence have also been measured but better spatial resolution is required for etch-pit quantification"?
At the end of the " implications and outlook" paragraph it is written that " The current spatial resolution of in situ near-field PXCT, ~370 nm, can be improved by increasing the number of projections, without larger acquisition times" which, from my knowledge, is false. While in the supplementary info section it is reported and especially pointed out that "The resolution obtained, see subsection dedicated to the spatial resolution, was limited by the number of projections, which was chosen to have reasonable scan times".

Is the sample perfectly stable from one measurement to another? Is there a need to "realign" the volume from one-step to another? Is there a need for volume registration? If yes, how has it be done ?

Reviewer #3 (Remarks to the Author):

Major revision is needed.
This paper presents a method to observe the hydration process of cement using 4D nanoimaging. The idea is novel, but there are some problems:
[1]The literature should be updated, more literature should be in recent three years.
[2]In the Introduction, the disadvantages of the references should be summarized clearly to emphasize the importance of this work. The difficulties of 4D nanoimaging also need to be summarized.
[3]In Fig.7, the time selection is very strange."19h","47h","93h". what is the reason. The title of this paper focuses on the early hydration. why not select some early hydration points? for example, Non-contact multiple-frequencies AC impedance instrument for cement hydration based on a high-frequency weak current sensor.
[4]This paper is interesting, cement pastes are multi-phase materials. Some phases are overlapped with others in some localized regions. Some nano-scale C-S-H and CH may be mixed together. It is said that the intrinsic size of C-S-H is about 5 nm(doi.org/10.3390/fractalfract5020047). Therefore, in Fig.4 nanoimaging, C-S-H may not be identified in the scale bar 5 μm. Therefore, at least, the typical size of each phase during the cement hydration should be listed out from literature, so that reader can compare comprehensively.
[5]As we know, some commercial PCs have some mineral admixtures. What about the XRF results of these two commercial PCs in this work.
[6]Fig. 3. Left figure is terrible. We can not identify which is which. It is only black and while.
[7]From Fig.7, the samples used in PXCT have serious carbonation. However, other samples do not have such carbonation. Besides, in Fig.7, how do authors identify the different kinds of C-S-H gels. Is it from AFM test according to porosity or NMR according to silicate calcium chain(doi.org/10.1016/j.conbuildmat.2020.118807 & doi.org/10.1016/j.measurement.2021.110019)

[8]In Fig.6,authors claim they can monitor the evolution of water porosity (dark-grey) to air porosity (black). Does it mean that water can be distinguished by near field PXCT? As I know, only neutron can examine the presence of water.
[9]In Fig.8,PXCT test results seem that C4AF content does not change much. It is not reasonable. Common sense tells us that the hydration rate is C3A > C3S > C4AF > C2S.

Reviewer #4 (Remarks to the Author):

A superbly presented, detailed study of cement hydration using various X-ray methods. I would recommend a review by someone expert in the cement hydration field, since I cannot comment on the impact of the results from the point of view of the application. What I can say is that the ptychographic imaging is a significant real-world demonstration of the near-field approach and, to my mind, represents the current state-of-the-art.

I have no issue recommending the article for publication, subject only to minor improvement of the English - which although always comprehensible could do with a proof-read.

Malaga, 7th of March, 2023

Response to reviewers document. Reference **NCOMMS-22-47460-T**
Title. "**4D nanoimaging of early age cement hydration**"

To help the readability and understanding of this revision, our answers are highlighted **in green** in the response to reviewer's letter and the changes are highlighted **in blue** in the revised version of the manuscript and in the S.I. file.

Reviewer #1 (Remarks to the Author):

The strength of this study, in my opinion, is in the exploration of a new nanoimaging technique, PXCT, to study the early hydration of Portland cement. With the unprecedented spatial resolution and contrast of PXCT, in situ identification of the evolution of various mineral phases, the C-S-H gel shells, etch pits, water pores and air pores, etc. became possible, hence the corresponding cement dissolution and precipitation processes at early ages associated with them was studied, and qualitative and quantitative results were obtained. The results are of potential interest to researchers working in X-ray computerized tomography and could illustrate a new characterization direction for the cement-based materials community.

The approach, data analysis and interpretation are valid, comprehensive and correct, and the evidence presented justify the conclusions. The literature is adequately cited. The clarity and accessibility of the text is good, and the results have been provided with sufficient context and consideration of previous work.

Author reply: Many thanks for acknowledging the main contributions of this work.

There are several issues however that I think should be clarified to help improve the work.

1.1. In the manuscript, it is said "In situ near-field data were taken as detailed in methods……. radiation damage cannot be discarded but it is small, if any. (Page 5) " "Time resolutions of ~1 h will open the way to accurately study the processes in the acceleration period. However, in these cases, radiation damage could be an issue if the total dose is not kept low. (Page 12)"

Will radiation damage affect the visualization results of the evolution of water porosity towards air porosity with time? In addition, migration of C-S-H gel was observed. Is it possible that this was also affected by radiation damage? How will the effect of radiation damage be considered in the future research with higher time resolution?

1.1. Author general reply: With the data currently available, we can only speculate on these interesting questions. It is known that the radiolysis of water in cement pastes yields, in a first stage, electrons and H_2O_2. After a cascade of reactions, the identified products (under gamma irradiation) are H_2 and calcium peroxide, i.e. $CaO_2{\cdot}8H_2O$ [see for instance, Bouniol and Aspart, Cement and Concrete Research (1998) "Disappearance of oxygen in concrete under irradiation: the role of peroxides in radiolysis"]. There are many papers dealing with gamma-irradiation of mortars and concretes but we are not aware of any investigation dealing with the radiation damage mechanism by 'mild' X-ray irradiation, that it does not necessarily need to be identical.

1.1. Author reply-a: We do not think that possible radiation damage will significantly modify the water porosity towards air porosity evolution. However, at this stage, this is a speculation that we prefer not to include in the revised version of the manuscript.

1.1. Author reply-b: C-S-H migration (dissolution and re-precipitation) has been observed in some small volumes/regions of the sample and we think this is due to local under/over saturation fluctuations rather than radiation damage. Unfortunately, we do not have data to firmly establish this point. More high-resolution imaging studies are required.

1.1. Author reply-c: Higher time resolution does not necessarily imply higher doses (and therefore larger radiation damage). For instance, sparsity techniques can be coupled to PXCT in order to decrease the overall acquisition time for the whole series by 90% [Gao et al., *Sci. Adv.* 7, eabf6971 (2021)]. Another approach could be to use ML for the reconstruction and denoising of datasets collected with (much) less X-ray dose [Hendriksen, et al., *Sci. Rep.* 11, 11895 (2021)].

The two key important points are now addressed in the revised version on page 14: "… Higher time resolution does not necessarily imply higher doses and therefore possibly larger radiation damage. For instance, sparsity techniques could be coupled to PXCT in order to decrease the overall acquisition time for the whole series by as much as 90%, as recently reported[64]. Another approach could be to use machine learning/deep learning for denoising of datasets collected with much less X-ray dose[65]. On the other hand, gamma irradiation of Portland pastes, mortars and concretes is known to produce water radiolysis finally leading to H_2 microbubbles and

calcium peroxide, $CaO_2{\cdot}8H_2O$[66]. Therefore, the signatures of these species should be monitored for studies with high X-ray doses.…" Three new references have been added.

1.2. The evolution of water porosity towards air porosity with time was observed around some Alite grains. How will this affect further hydration of Alite and etch pits growth when there is no water around?

1.2. Author reply: As soon as there is no contact with water, alite hydration stops. This can be seen in Figs. 5 and 6 and also in some figures in the S.I. However, with the data at hand, it is not possible to know if later-age water diffusion could re-wet some alite grain, and hence, hydration could progress. This is the reason we prefer not to speculate too much about this. In any case, this feature is now explicitly stated in the manuscript in the caption of Fig. 6 by adding "... Moreover, alite hydration also stops as soon as air porosity (pore drying) develops on the surfaces of the anhydrous grains, see red rectangles...". Figure 6 has been consequently updated with the corresponding red rectangles.

1.3. In the manuscript, it is said "The hollow regions of the Hadley grains are filled with water at 19 and 47 h but dried at 93 h, see enlarged pictures to the right. This illustrates that most of the capillary pores with sizes larger than ~1 μm are already water emptied at 93 h of hydration, see bottom right. (Figure S19)", "The enlarged views (bottom) show the evolution of porosity within the paste, where several pores of sizes smaller than ~2 μm are dried (red arrows) at 93 h but other larger, pores keep filled with water (blue arrows). (Figure S23)"

Is there a contradiction between those two conclusions, for the pores to be empty at 93 h, the former is >1μm and the latter is <2μm? Does the water migrate randomly?

1.3. Author reply-a: We do not think that there is a contradiction between the highlighted observations. Our interpretation is the importance of heterogeneity, which is key in cement hydration when analysed with enough spatial resolution and contrast. Just in Fig. 6, panel b, it can be directly seen that at 47 h, a pore of about 1 μm size is dried, but being very close to two larger water-filled pores, of sizes larger than 2 μm. At first sight, this seems to contradict Kelvin-Laplace equation that relates the relative humidity (RH) to the size of the dried pores. This implies that the pores are emptied of water from largest to smallest sizes as hydration progresses. This is indeed correct in the absence of impediments for water diffusion (which is not the case as C-S-H gel is a barrier to diffusion) and if the RH is constant within the paste, which is also not held. For instance, in regions where ettringite crystallizes, consuming a lot of water, the RH drops more than in other regions where only C-S-H/portlandite precipitates, which have lower water contents. This has been clarified in the caption of figure 6, b-panel, by adding the following statements. "… It is noted that at 47 h, a tiny pore of about 1 μm size is already dried, but being very close to two larger water-filled pores, of sizes larger than 2 μm. This observation remarks the heterogeneity in cement hydration. It can be deduced that the relative humidity is not constant, at a given time, through the sample. This is due to a set of factors including the barriers to water diffusion and the crystallization/precipitation of different hydrates with quite different water contents, for instance ettringite and portlandite...".

1.3. Author reply-b: We do not have enough data to model/deal with the migration of water. This is indeed a very interesting issue that will be treated when we collect a major number of tomograms at different ages.

1.4. The water to cement ratio is relatively higher near the capillary wall than that in the center. In Figure S27, wall effect in the 19h capillary tube sample could be observed. Will the degree of hydration of cement particles of the same size be affected by wall effect at different locations? It should be addressed in the manuscript.

1.4. Author reply: This is a quite important observation that was not treated in the submitted version. The 'wall effect' –the increased cement paste content near the wall of the container respect to the large aggregate particles in mortars and concretes– is well known (in mortars and concretes) and it has been extensively studied by numerous techniques including electron microscopy and synchrotron microtomography. The 'wall effect' in pastes, where water is partly segregated towards the wall of the capillary, has also been reported but it has been less studied. We have addressed the reviewer's comment by adding the following set of sentences on page 11, and the corresponding two new references. "… It seems that at 19 h, the free water is preferentially located close to the walls of the capillary. This could be related to the 'wall effect' well known in mortars and concretes, where the cement paste content is slightly higher near the wall of the container respect to the larger aggregate particles which are preferentially arranged towards the centre. This feature, and its implications in the interfacial transition zone, has been extensively studied by numerous techniques, including synchrotron microtomography, see for example[62]. For cement pastes, higher porosity near the capillary wall has been observed by synchrotron microtomography.[24] For a water-rich alite paste, wall effect was clearly observed by PXCT where the resulting C-S-H gel had higher water content near the capillary wall.[63] In order to quantitatively study this feature, the scanned capillary was divided into two volumes, a central cylinder with half of the radius and the outer region up to the glass capillary wall. The mean electron densities were computed, but the voxels with electron density smaller than 0.24 $e^{-}Å^{-3}$, air porosity, were not included in order to minimise any bias due to the shrinkage / pore

drying. The results for the centre volume were 0.614, 0.618 and 0.617 $e^{-}Å^{-3}$ for the 19, 47 and 94 h datasets, respectively. The corresponding mean electron density values for the outer region were 0.608, 0.610 and 0.601 $e^{-}Å^{-3}$. The 1 % difference between the two regions at 19 h is quite small but not negligible. Hence, the degree of hydration could slightly be a function of the horizontal position of the particles....”

Two new references have been added:
(62) *Energy Procedia* **114**, 5109–5117 (2017) (63) *Langmuir* **31**, 3779–3783 (2015)

Reviewer #2 (Remarks to the Author):

In this manuscript, the authors report the study of the early stage of cement hydration using mainly near-field ptychographic X-ray computed tomography. They provide a unique combination of spatial & temporal resolution + field of view. It allows the determination of quantitative values for dissolution rates and etch-pit growth rates. A comparison with data obtained by lab and synchrotron X-ray micro-tomography is also proposed. The paper shows an extended collection of data using state of the art technique and an interesting 3D data analysis based on machine learning process. Nevertheless, the manuscript shows some incoherencies and approximations, the results are not sufficiently described and discussed, especially the ones reported in the abstract. Thus, I cannot support this work for publication in Nature communications in its present form.

Author reply: thanks for your general comment which explicitly acknowledges the key contribution of this work “… They provide a unique combination of spatial & temporal resolution + field of view. …”.

Some specific comments and remarks linked to my previous general comment:

2.1. For the PXCT study, the size of the capillary used is different between the different sections and figures 160 µm vs 200 µm. This information is important. Indeed, it is highlighted (in the supplementary methods) that the sample should be smaller than the FOV (186 µm) in order to have quantitative results (“ The field of view must be larger than the size of the capillary to include an air region at both sides of the sample, which is needed for successful tomographic reconstructions and for quantitative contrast.”).

2.1. Author reply: We thank the reviewer for allowing us to clarify this issue, which is very important. The glass capillary has a nominal diameter of 200 µm, however it is not fully uniform in its length. In the imaged vertical region, it has a thickness of 160 µm. Therefore, it was scanned with a FoV of 186 µm in order to have more than 10 µm of air outside the capillary, which is needed as a reference for quantitative phase imaging. This is now explicitly stated in the method section of the main manuscript. On page 15: “... introduced in a glass capillary of 200 µm of nominal diameter...” and “... The thickness of the capillary in the imaged region was 160 µm. Therefore, it was scanned with a FOV of 186 µm in order to have more than 10 µm of air outside the capillary, which is required for quantitative phase imaging...”.

2.2. It is mentioned in the first paragraph of the “result and discussion” section that the particles size of the sample PC-52.5 for PXCT study are finer than the sample described in the table S3 and used for the lab measurements (XRD, tomography…). How is it done? What is the impact on the comparison of the results between the different measurements?

2.2. Author reply: We now are aware that our wording was misleading. We have used two PCs, one PC-52.5 and another PC-42.5. PC-52.5 was used for the PXCT study, and for the laboratory characterization: µ-CT, Rietveld quantitative phase analysis and calorimetry. The PC-52.5 employed in these measurements was identical. Indeed, PC-42.5, employed for the synchrotron µ-CT, has slightly larger particle sizes as measured in Fig. 1a, Table S3 and Fig. 8. This is clarified in the revised version by explicitly stating on page 3: “PC-52.5 was used for the PXCT and laboratory µ-CT imaging studies and the additional laboratory characterization. PC-42.5, with slightly larger average particle size, was used for the synchrotron µ-CT imaging study.”

2.3. The w/c ratio value for the sample used for PXCT measurements differs from 0.4 to 0.5 when described in the SI file, in situ multicontrast X-ray tomographic studies of cement hydration and method sections.

2.3. Author reply: The nominal w/c ratio employed for the paste, that filled the capillary in the PXCT study, was 0.50. However, it is very challenging to control the w/c homogeneity within very thin capillaries. Therefore, the w/c ratio of the scanned volume in the PXCT study was measured and the value was slightly smaller. This is now fully clarified by adding on page 4 “… The nominal w/c mass ratio employed to fill the PXCT narrow capillary, 200 µm of nominal diameter, was 0.50, see methods. However, it is very difficult to accurately control the w/c ratio in very thin capillaries. Therefore, the w/c ratio of the scanned volume for the PXCT measurement was measured as previously published[46] and detailed in a subsection of the S.I. The w/c ratio of the scanned volume in the PXCT study was 0.41.”.

2.4. What are the units in Table 2?

2.4. Author reply: The units are wt%, and this is corrected in the heading of Table S2.

2.5. In figure 2: - In b, it can be seen that the images of the Lab-uCT scan are more blurred at 93h than at 19h. Why? Why does the analysis performed in Figure S5 not show the same tendency?

2.5. Author reply: The FSC for laboratory microtomography, shown in Fig. S5, does not indicate higher degradation of the spatial resolution at 93 h. This is a direct observation. Fig 2b (laboratory data) shows a change which is not blurring but the consequence of hydration. At 19 h, the image has more free water and anhydrous components, hence it has higher contrast. At 93 h, the consumption of water to give hydrated phases results in a poorer contrast between them and the unhydrated phases, which may appear as a blurring effect.

2.6. On the contrary, Figure S7 clearly shows a degradation on the spatial resolution that is not observed by eye on the images.

2.6. Author reply: We thank the reviewer for allowing us to clarify this issue. The spatial resolution, as measured by FSC, for the 47 and 93 h tomograms, i.e. 470-500 nm, is slightly poorer than that of the 19 h, 430 nm. This was very likely due to the employed scanning step size that was 6 µm for the 19 h tomogram (resulting in 3h 55 min of total acquisition time), and 7 µm for the other two tomograms (resulting in 3h 6 min of total acquisition time). This was detailed in the experimental section, but now we understand that this was not enough. Therefore, this is now clarified in Figure S7 caption by adding "The slightly better spatial resolution measured for the 19 h tomogram is very likely due to the smaller scanning step size, i.e. 6 µm, and the corresponding larger acquisition time, i.e. 3h 55 min. The scanning step size for the other two tomograms was 7 µm, yielding 3h 6 min of acquisition time.".

2.7. It is concluded that the resolution is estimated at two pixels (How?). It means that the resolution of the PXCT study is 374 nm. Then, how representative and trustable are the values given in figure S13 –Figure S15?

2.7. Author reply-a: We thank him/her for allowing us to clarify this point about the spatial resolution which is indeed very important. Be aware that this point is intimately linked to the point 2.11, below. We acknowledge that this point was not treated with the required depth in the submitted version. We have carried out further studies to characterise this key feature: Now in the revised version "… The spatial resolution was characterised by two approaches as recently reported[52]. The procedures are thoroughly detailed in Supplementary Information (SI). On the one hand, the spatial resolution can be determined by the edge sharpness across selected interfaces. A point spread function (PSF) used to determine the spatial resolution of the images as ISO/TS 24597 defines the Gaussian radius of the PSF as the resolution, which equals a change between 25 %–75 % grey value along the studied interfaces.[38] The spatial resolutions, determined by this approach, were 250(25) nm, 264(25) nm, 272(34) nm, 748(19) nm and 2.21(17) µm, for PXCT-19h, PXCT-47h, PXCT-93h, Syn-µCT and Lab-µCT datasets, respectively. As examples of this procedure, Figures S2-S4 display line profiles of sharp interfaces between high (i.e. alite) and low density (i.e. porosity) components within the capillaries. On the other hand, Fourier-shell-correlation (FSC)[53] has also been employed to estimate spatial resolution. Figures S5-S7 displays the FSC traces for the three imaging modalities. The agreement between both approaches is satisfactory for Syn-µCT and Lab-µCT, but not for PXCT. The worse spatial resolution estimated by FSC for PXCT is very likely due to the low number of projections, i.e. 420, which make the subtomograms employed in the FSC calculation severely undersampled." Reference 52 has been added: (52) *Nat. Nanotechnol.* **15**, 356–360 (2020).

2.7. Author reply-b: Moreover, we have included a full new subsection in S.I. which reads:

"Spatial resolution analysis.

The spatial resolution was characterised by two approaches as recently reported[17]. On the one hand, it can be determined from the grey-value changes in line profiles through the edge sharpness of the interfaces. A point spread function (PSF) used to determine the spatial resolution of the images as ISO/TS 24597 defines the Gaussian radius of the PSF as the resolution, which equals to a change between 25 %–75 % grey value along the studied interfaces.[18] Here, a common interface present in the three imaging modalities has been selected for the line profiles: the glass capillary wall – air (i.e. exterior of the capillaries). We have measured 25 interfaces in every tomogram, which allowed us to determine the average spatial resolution and its associated standard deviation. Moreover, as examples, Figures S2-S4 display line profiles of sharp interfaces between high (i.e. alite) and low density (i.e. porosity) components within the capillaries. The spatial resolutions, determined by this approach, were 250(25) nm, 264(25) nm, 272(34) nm, 748(19) nm and 2.21(17) µm, for PXCT-19h, PXCT-47h, PXCT-93h, Syn-µCT and Lab-µCT datasets, respectively.

On the other hand, FSC plots[5] have been also computed. The traces are displayed in Figures S5-S7 giving spatial resolution values of 430 nm, 470 nm, 500 nm, 650 nm and 1.9 µm, for PXCT-19h, PXCT-47h, PXCT-93h, Syn-µCT and Lab-µCT datasets, respectively. Moreover, the FSC trace for PXCT-19h shows a smooth decrease in the 0.0-0.2 spatial frequency range, which is likely due to the hydration of cement during the 4-hour measurement. As expected, this behaviour is not shown at later ages.

It should be noted that the agreement between the spatial resolution results between the edge sharpness approach and FSC method is satisfactory for Syn-µCT (750 vs. 650 nm) and Lab-µCT (2.2 vs.1.9 µm) datasets. However, the agreement between these two approaches is not good for PXCT (for instance, 250 vs 430 nm at 19 h). The poorer resolution estimated by FSC can be explained because the angular sampling is very tight, i.e. 420 projections, so the two employed subtomograms in the FSC, each of 210 projections, were significantly undersampled compared to the number of voxels across the diameter of the sample. This means that the correlation between two such undersampled tomograms can give a low estimation of the spatial resolution. This feature is not observed for Syn-µCT and Lab-µCT as the total number of projections were 6000 and 1637, respectively. In other words, the subtomograms with half the number of projections were not undersampled for these two imaging modalities."

2.7. Author reply-c: In our opinion, we can trust the results shown in Figures S13-S15 as these features have dimensions 400-500 nm, significantly larger than the spatial resolution of PXCT study, which is determined as ~250 nm, see just above.

2.8. Looking at the figure 2c: Can you link the difference of the grey-value in the diagram of lab-uCT and syn-uCT to the different behaviour of the two different cements?

2.8. Author reply: It is not straightforward to link the different behaviour of PC-52.5 in Lab-µCT and PC-42.5 in Syn-µCT in Figure 2c because the Paganin phase retrieval is highly sensitive to the initial porosity. However, the expected behaviour: faster reactivity of PC-52.5 at early ages than PC-42.5, because of the finer particle sizes, is beautifully shown in Figure 8 b. As dictated by the particle sizes and as measured by calorimetry, PC-52.5 reacts faster between 19 and 47 h and then very little from 47 to 93 h, see Fig. 1b panel. This is clearly shown in the cumulative volume traces from Lab-µCT, see Figure 8 (top). Conversely, from calorimetry, PC-42.5 reacts slower between 19 and 47 h but it keeps reacting between 47 to 93 h, see Fig. 1b panel. This is evident in the cumulative volume traces obtained from Syn-µCT, see Figure 8 (intermediate). This was discussed in the segmentation subsection of the manuscript.

2.9 There is a comparison between the lab-uCT diagram and the PXCT one. What is the abscissa axis label for the lab-uCT? I understood that it was grey-value. If yes, what is the link to compare grey-values of absorption tomography to electron density obtain by PXCT?

2.9. Author reply-a: Yes, the abscissa axis label for lab-µCT is "grey-value". This is corrected in the revised version of the manuscript.

2.9. Author reply-b: It is not possible to quantitatively link the grey-values in the lab-µCT and the electron density in PXCT. The electron density values in PXCT are related to the imaginary part of the refractive index of every component. This relationship is quantitative but some nuances should be taken into account, such as partial volume effects and that amorphous phases and solid solutions have (slightly) variable compositions and hence, electron density values. Conversely, the grey-values in Lab-µCT are related to the attenuation coefficient of every component (i.e. the real part of the refractive index). Moreover, the relationship between grey-values and the attenuations is not quantitative because the polychromatic nature of the laboratory radiation. This has been clarified in the revised version by adding on pages 4-5"… The grey-values in the Lab-µCT study, see Fig. 2c (top panel), are related to the attenuation coefficients of the components in this PC-52.5 paste, but the relationship is not quantitative due to the polychromatic nature of the employed radiation. Conversely, the electron density values obtained for the same paste by PXCT are quantitative. Therefore, the grey scales in the Lab-CT and the electron densities in the PXCT datasets cannot be directly related as they derived from the imaginary and the real part of the refractive index of every component.".

2.10. Is the diagram of figure 2c the same than Figure S10? Are they representative of the same sub-volume? Is "the largest possible volumes without including the glass capillary walls" is equivalent to the ~1×10 5 µm^3 VOI mentioned in the "tomographic data analysis section" of SI for the PXCT study?

2.10. Author reply: Yes, the VOI were exactly the same and as big as possible without incorporating the glass capillary walls. There was a problem with the colours of the different traces in Fig S10, to be consistent with the main text, and this is now corrected. The revised figure S10 has the 93 h trace in green.

2.11. Looking at the spatial resolution analysis: How many interfaces have been studied as in figures S2-3-4 to determine the resolution estimations? What is the standard deviation? Can the calculation linked to the figure s5-s6-s7 be detailed? How the resolution values are deduced from the curves?

2.11. Author reply: For the reported number, we have studied 25 interfaces for every type of imaging modality. The average values and the associated standard deviations are now given, see point 2.7 above. The calculations are fully detailed now in the S.I.

2.12. Are the volumes used to determine the data of Table S7 and Figure S10 equal to the VOI?

2.12. Author reply: We thank the reviewer for allowing us to clarify this. The VOI used to obtain Figure S10 is the biggest possible volume leaving out the capillary. However, for Tables S7 and S8, the measured electron densities for the different phases/components are carried out for the large available particles. This was explicitly stated at the bottom of Table S8 but not in Table S7, which was misleading. This has been corrected by adding the information at the bottom of Table S7. " # Electron densities, from particle picking, were obtained by the average of 10 cubes for the capillary; 5, 4, 5 and 6 grains for portlandite, calcium carbonate, alite and belite, respectively."

2.13. It can be seen that there is a difference between the theoretical electron density of the components and the measured one. How do you explain the difference? Why did you choose to use the theoretical value to indicate the different components in figure S10 ? Why is there no measured values for air, water and LDH ? Which electron densities have been used to train the machine learning for those phases?

2.13. Author reply-a: We thank the reviewer for allowing us to clarify this point which was not dealt with in the original submission. The differences between the theoretical electron densities and the measured ones are mainly due to partial volume effects. This is now explicitly stated in the revised version on pages 6-7 "… The differences between the theoretical electron densities and the measured ones are mainly due to partial volume effects. For instance, portlandite, i.e. $Ca(OH)_2$, has a theoretical electron density value of 0.69 $e^-Å^{-3}$. The measured values at 19 and 93 h were 0.62(2) and 0.651(5) $e^-Å^{-3}$, see Table S7. These numbers are 6-10% smaller than the theoretical one, with the difference being higher than the errors of the measurements, which are estimated in 2-3%[46,54]. This difference is very likely due to the presence of residual water porosity below the spatial resolution of the measurements, which we refer to partial volume effects." Reference 54 has been added:
(54) *Phys. Rev. B* **85**, 020104 (2012).

2.13. Author reply-b: We prefer to indicate the theoretical values of electron densities in Fig. S10 because they are free of partial volume effects and they can be used in future works with higher spatial resolution and therefore, where the implications of the partial volume effects will be smaller.

2.13. Author reply-c: Concerning the measured values for air, water and LDH. They are now included in Table S7. "… Moreover, 5 cubes at 19 h gave the reported measured electron density for capillary water. Similarly, 5 cubes at 93 h were computed to obtain the value for air. Finally, the electron density of LDH (low density hydrates) was measured at 93 h in 5 cubes yielding 0.56(1) $e^-Å^{-3}$ that it corresponds to ettringite and/or C-S-H as they cannot be distinguished."

2.13. Author reply-d: Concerning the electron density values used to train the machine learning. It should be noted that we did not use a single value of electron density but a range of approximately 5% of the measured electron density value for the initial classification and training of the different components. Afterwards, based on the obtained results, some voxels were relabelled and further training was carried out based on the electron density values and on the morphology of the components. We acknowledge that this information was not given and this is now corrected in the revised version of the S.I. by adding "… The initial classification was based on the electron densities with a variation of ~5% of the measured values, from selected volumes, which are given in Table S7."

2.14. Why the grey values of the 3D rendering in figure 4 are different from one-step to another?

2.14. Author reply: The change in grey values between each step in Fig 4b is caused by the "diffuse light" effect used for 3D rendering. We have to note that the 3D rendered views do not show exactly the grey values (or electron densities) but they are affected by the visualization features. This is now clarified in the figure caption. "… These 3D rendered views do not show exactly the electron densities as they are affected by visualization features like the lighting source."

2.15. How has been the etch pit growth rate evaluated?

2.15. Author reply: We acknowledge that the procedure for etch pit growth rate estimation/evaluation was not detailed and this is now corrected two-fold. We have added a small subsection in the S.I. detailing the procedure and its limitations. Furthermore, the results have been updated in the main text. This point is also very much related to the point 2.22, from this reviewer, see below. It is noted that this is not a full quantitative determination but an estimation, as the spatial resolution of our imaging study, ~250 nm, is not good enough for a thorough study of these tiny features.

Now in the S.I.: **Etch pit growth rate evaluation.**

The estimation of the etch-pit growth rate was based on the analysis of 27 etch-pits from 5 different large alite grains. It is noted that the etch-pits have irregular 3D shapes and therefore, for its spatial dissolution rate estimation, some simplifications were undertaken. Moreover, the spatial resolution of this PXCT work, ~250 nm, is limited for accurate analyses. Therefore, we consider this approach as an estimation. Firstly, etch pits were visually selected from grains with sizes larger than 10 µm. Secondly, their overall shapes were compared in two

hydrating steps. Then, two envelopes from pixels with at least 90% of the electron density of alite were developed. The estimated/calculated distance (in pixels) was computed between these edges for the deepest perpendicular length. These values were converted to dissolution rate by taking the ratio with respect to the time between measurements. The result for the analysis between 19 and 47 h datasets gave 6.1 pixels of average distance which is equivalent to 41(29) nm/h. There was large variability in the rates, the fastest being 110 nm/h and the slowest being 10 nm/h. From this investigation, it is not possible to know if this large variability comes from the heterogeneity in the defects within these regions, or if other variables like the spatial resolution of this work and the local water-to-cement ratio variations are also playing important roles. More imaging studies are necessary to establish this. The very same 27 etch-pits were also analysed between 47 and 93 h datasets. In this case, the etch-pit growth rate was slower 7 nm/h, showing that the water diffusion is already limiting hydration at four days.

Now, in the manuscript on page 7: "… The etch-pit growth rate was estimated, as detailed in S.I., from the analysis of 27 dissolving regions in five alite grains. The resulting rate, between 19 and 47 h, was 41(29) nm/h. The etch-pit growth rate between 47 and 93 h was slower with a large variability, 7(8) nm/h, showing that the water diffusion is already limiting hydration."

2.16. At the beginning of page 6 it is mentioned the spatial dissolution rate of alite. Since alite, C3A and belite has been classified in the very same category for the segmentation, how is it possible to make the difference between them when looking at C-S-H gel shells. I guess that the belite particles are not surrounded by gel shells because the DoH is equal to zero in table S5 but what about the differentiation between C3S and C3A?

2.16. Author reply: This comment is quite related to 2.21 below, both related to the C3S spatial dissolution rate. Here we clarify that, in the original submission, the spatial dissolution rate of alite was not determined from the segmentations but from the analysis of 22 surfaces of particles of different sizes. Firstly, C_2S particles were excluded because they do not have a C-S-H shell at 19 h of hydration. C_3A particles were also discarded as they have a smaller electron density, ~0.90 $e^-Å^{-3}$ instead of the ~0.95 $e^-Å^{-3}$ of alite particles. This is now clarified in the text by "Chiefly, the spatial dissolution rate of alite was determined from the study of the surface evolution of selected particles, see Fig. 5a and Figs. S13-S18, as examples. C_2S particles were identified and excluded from this analysis, because they do not have C-S-H shells at 19 h of hydration. C_3A particles were also recognised and discarded because of their smaller electron density values, i.e. ~0.91 $e^-Å^{-3}$, 5 % lower than that of alite. From 22 measurements along different surfaces, the dissolution rate between 19 and 47 h was 25(14) nm/h...".

2.17. Do we have an idea of how many particles of alite <3um were present in the sample at the beginning of the experiment?

2.17. Author reply: From the particle size distribution measurement by laser diffraction, we can estimate that ~20 vol% of PC has sizes smaller than 3 µm. Because the cement has 61 % of alite, the initial cement had about 12 vol% of alite with these particle sizes. Moreover, the scanned region of the capillary is filled with a paste containing a w/c mass ratio of 0.40. Due to the large difference in densities (water=1 g/cc and cement=3.12 g/cc) the capillary contained at the time of mixing, 56.1 vol% of water and 43.9 vol% of cement particles. Therefore, the alite volume at the beginning of the experiment with particle sizes smaller than 3 µm is estimated as ~5.3 vol%. As the scanned volume of paste was ~5 10^5 $µm^3$ (the total volume was 8.1 10^5 $µm^3$ but this included the glass capillary and the air) and it contained about ~26000 $µm^3$ of alite particles smaller than 3 µm. A back of the envelope calculation indicates that if all particles have 3 µm, and they have cubic shape, it should be around 1000 particles. Conversely, if all particles have 1 µm isotropic size, it should be around 26,000 particles. This coarse calculation agrees reasonably well with the segmented number of alite particles at 19 h of hydration with sizes between 1 and 3 µm, i.e. 1117 particles which come from partly hydrated larger ones, stated in the manuscript (given the number of approximations, and taken into account that all small particles are dissolved at early hydration ages). At this stage, we prefer not to include this calculation in the manuscript as all data to carry out this coarse estimation are in the paper. However, if the reviewer thinks differently, we could include this calculation in the supplementary information file.

2.18. Is the figure 5b representative of the 19h step?

2.18. Author reply: Yes, fully representative. We forgot to include that description in the figure caption. This mistake has been corrected by adding "… for the 19 h tomogram."

2.19. At the end of the page 9 and in figure 8, it is mentioned, "PXCT yields underestimated values for the DoH likely due to the limited scanned volume" and "These data are scattered for PXCT because the limited height of the studied cylinder yields a poor representative elementary volume for this feature". It is in contradiction with the conclusion given in page 4 "giving confidence to the relevancy of the nanoimaging results in spite of the limited amount of volume scanned to have submicrometer resolution". Can you give more info and comment on the representativeness of the volume scanned by PXCT?

2.19. Author reply: We do not think that there is a contradiction between these statements. In fact, it is highlighted from the very beginning "… in spite of the limited amount of volume scanned to have submicrometer resolution" We have also carried out Syn-µCT and Lab-µCT, because the scanned volume in PXCT is limited. It is explicitly stated in the experimental section, and visually in Figure 7, that PXCT only scans 30 µm in the vertical direction of the capillaries (meanwhile Syn-µCT and Lab-µCT scan 1000 µm). With large alite grains of about 20 µm, scanning 30 µm in the vertical direction is limited (although 160 µm was imaged in the transversal section of the capillary which allowed to scan many particles. Indeed, to image a larger volume, vertical dimension of about 60-100 µm would require about 7-9 hours per scan which may not allow to accurately study the hydration as important changes can occur during the acquisition time.

We have clarified this by adding the following set of sentences to the revised version on page 12: "… Finally, it should be noted that the scanned length in the vertical direction, 30 µm, for PXCT is limited taking into account that some alite grains with sizes of 20 µm, or slightly larger, are present in PC cements. This was mitigated by imaging 160 µm in the transversal direction. This type of experiment will benefit from imaging cylindrical volumes with 60-100 µm of height. However, with the current experimental procedure, this would lead to acquisition times larger than 7-9 hours and therefore changes due to hydration could take place during an acquisition. Procedures for faster data collection are being explored and some are discussed in the next section."

2.20. What is the UCP volume mentioned in page 10?

2.20. Author reply: This is the total volume of the anhydrous cement particles at 19 h as determined from PXCT. We now realize the sentence was not fully clear and we have replaced on page 12 "… The groups contained 1117, 204, 61 and 20 particles, respectively, and the corresponding percentages with respect to the UCP volume were 5.4, 12.9, 21.5 and 60.2%." by "… The groups contained 1117, 204, 61 and 20 particles, respectively. The corresponding volume percentages with respect to the overall anhydrous cement particle volume at this hydration age, were 5.4, 12.9, 21.5 and 60.2%.".

2.21. How is it possible to link the results obtained from 2D figures 5 and S13 to S18 to the ones obtained with the 3D segmentation? Are the results giving the same spatial dissolution rate?

2.21. Author reply: We thank the reviewer for allowing us to elaborate on this important result from the segmentation quantitative analysis point of view. Based on quantitative analysis derived from ML segmentation of the PXCT datasets (for the C_3S/C_2S class, dark brown colour code in the 3D visualization of Fig. 7), it is possible to derive an average spatial dissolution rate. We used mathematical morphology tools to retrieve the outer layer of the 19 h hydration and 47 h hydration segmented grain. Then, we computed the average distance between these outer layers for each grain, giving a mean value of 1.92 pixels (i.e. ~13 nm/h). This value is smaller than that obtained from 2D analysis for alite, 25 nm/h. However, it should be noted that in the segmentation analysis, alite and belite were classified together and therefore, the obtained spatial dissolution rate is underestimated as belite does not dissolve at early ages. Table S5, from the Rietveld analysis, indicates that the amount of belite is approximately half of that of alite during this stage. Therefore, the spatial dissolution rate can be corrected. The value, only for alite, would be close to 13/0.67 or 19 nm/h. This rate agrees relatively well with that obtained from the 2D analysis of 22 measurements, 25 nm/h, given the number of approximations which took place for both calculations. Now in the revised version on page 7: "… Moreover, this spatial dissolution rate can also be estimated from the segmentation results presented in the next subsection. Based on the quantitative analysis derived from Machine Learning (ML) segmentation of the PXCT datasets (for the C_3S/C_2S class, dark brown colour code in the 3D visualization of Fig. 7), it is possible to derive an average spatial dissolution rate. Mathematical morphology tools were used to retrieve the outer layer of the segmented grains at 19 and 47 h. Subsequently, the average distance between these outer layers was computed for each grain, giving a mean value of 1.92 pixels (i.e. ~13 nm/h). This value is smaller than that obtained from the analysis performed in 2D slices for alite, 25 nm/h. However, it should be noted that in the segmentation calculation, alite and belite were classified together and therefore, the obtained spatial dissolution rate is underestimated as belite does not dissolve at early ages. Table S5, Rietveld analysis results, indicates that the amount of belite is half of that of alite during this stage. Therefore, the spatial dissolution rate can be corrected. The alite spatial dissolution rate should be close to 13/0.67 or 19 nm/h. This value agrees relatively well with 25 nm/h, obtained from 22 measurements in 2D slices, given the number of approximations which took place for both calculations....".

2.22. Can you specify what you mean by quantification in this sentence: "Etch-pit growth rate, ~40 nm/h, and coalescence have also been measured but better spatial resolution is required for etch-pit quantification"?

2.22. Author reply: This point is related to that about etch-pit evaluation, 2.15. We acknowledge that the wording was somehow misleading. The etch-pit growth rate was/is an estimation, not an accurate measurement. In fact, due to this, we decided not to report a number in the abstract. Thus, "Etch-pit growth rate, ~40 nm/h, and coalescence have also been measured but better spatial resolution is required for etch-pit quantification" has been replaced by : "… The alite etch-pit growth rate between 19 and 47 h has been estimated as ~40 nm/h, which

decreases to ~7 nm/h in the 47 to 93 h interval. Moreover, etch-pit coalescence, the merging of different branches, has also been visually observed. However, better spatial resolution is required for a thorough etch-pit growth rate quantification."

2.23. At the end of the " implications and outlook" paragraph it is written that " The current spatial resolution of in situ near-field PXCT, ~370 nm, can be improved by increasing the number of projections, without larger acquisition times" which, from my knowledge, is false. While in the supplementary info section it is reported and especially pointed out that "The resolution obtained, see subsection dedicated to the spatial resolution, was limited by the number of projections, which was chosen to have reasonable scan times".

2.23. Author reply: Clearly, as previously stated there was a contradiction. This is very much related to point 1.1 above. The way to have better resolution (acquiring more projections) without increasing the dose too much (to avoid radiation damage) is to decrease the acquisition times. As stated in the answer to point 1.1-c the approach would be to collect data with faster acquisition times (worst signal-to-noise ratio) and to use ML for reconstruction and denoising of datasets. Alternatively, sparsity techniques can be coupled to PXCT, which is being implemented at cSAXS beamline. The text was revised as stated in point 1.1, above.

2.24. Is the sample perfectly stable from one measurement to another? Is there a need to "realign" the volume from one-step to another? Is there a need for volume registration? If yes, how has it be done?

2.24. Author reply: This is an important question that it requires a detailed answer. We acknowledge that the original submission did not contain the requested details. Furthermore, as there are three imaging modalities (ptychography, synchrotron microtomography and laboratory microtomography) the answer depends upon the employed technique. This has been addressed by adding the following information in the S.I. material:

"… Initially, the re-alignment of the data, when needed must be detailed.

For the PXCT, the capillary position was very accurate, as the capillary/holder system was mounted from the tray storage to the sample stage by the flOMNY gripper (robot). Hence, the angular orientation of the sample was maintained. The field of view of the sample was aligned carefully based on features visible in the 2D projections. The scanned regions with time were consistent within a few voxels and therefore no alignment between different acquisitions was required.

For the Syn-µCT, a mark was drawn on the sample holder and sample stage for the incident beam to minimise the initial incidence angular position variability. Before each scan, a projection was acquired as a reference for the next one in order to scan the same region. A minor manual registration was required, mostly rotations around x- and y-axes.

For the Lab-µCT, manual registration was required to align the different acquisitions. The process is described next. The capillary was considered as a cylinder and we manually made the cylinders vertical and centred in the reconstructed volume. The remaining rotation around the z-axis was visually done by superimposing distinguishable landmarks in the corresponding images.

Reviewer #3 (Remarks to the Author):

Major revision is needed.

This paper presents a method to observe the hydration process of cement using 4D nanoimaging. The idea is novel, but there are some problems:

Author reply: Many thanks.

3.1. The literature should be updated, more literature should be in recent three years.

3.1. Author reply: We thank the reviewer for this comment. We have included five new references (2020-2023), just to respect the maximum number of references, which in the guideline for submission is stated as 70. The revised version of this manuscript had already 69 references. Now in the introduction of the revised version "… In the last three years, important advances have been reported including: i) the automated correction for the movement of suspended particles at very early ages[34] which allowed to follow *in situ* PC hydration after water mixing[35]; ii) to follow the fast dissolution of plaster and the precipitation of gypsum[36]; iii) the simultaneous use of neutron and laboratory X-ray tomographies for *in situ* studying the microstructural changes of PC mortars on moderate heating[37]; and iv) the measurement of alite particle dissolution using fast synchrotron nano X-ray computed tomography[38,39]" The new references added are the followings (reference 35 was already included in the original submission):

(34) Vigor, J. E., Bernal, S. A., Xiao, X. & Provis, J. L. Automated correction for the movement of suspended particulate in microtomographic data. *Chem. Eng. Sci.* **223**, 115736 (2020).

(36) Seiller, J. *et al.* 4D in situ monitoring of the setting of α plaster using synchrotron X-ray tomography with

high spatial and temporal resolution. *Constr. Build. Mater.* **304**, 124632 (2021).
(37) Cheikh Sleiman, H., Tengattini, A., Briffaut, M., Huet, B. & Dal Pont, S. Simultaneous x-ray and neutron 4D tomographic study of drying-driven hydro-mechanical behavior of cement-based materials at moderate temperatures. *Cem. Concr. Res.* **147**, 106503 (2021).
(38) Li, X. *et al.* Direct observation of C3S particle dissolution using fast nano X-ray computed tomography. *Cem. Concr. Res.* **166**, 107097 (2023).
(39) Li, X., Hu, Q., Robertson, B., Tyler Ley, M. & Xiao, X. Direct observation of C3S particles greater than 10 μm during early hydration. *Constr. Build. Mater.* **369**, 130548 (2023).

3.2. In the Introduction, the disadvantages of the references should be summarized clearly to emphasize the importance of this work. The difficulties of 4D nanoimaging also need to be summarized.

3.2. Author reply-a: Concerning the disadvantages of the published work, we thank the reviewer since this helps to focus on the work we present in this manuscript. This was already treated in the introduction but we acknowledge that not with the required depth. Now in the revised version: "… In particular, hard X-ray synchrotron microtomography has not the required submicrometer spatial resolution neither sufficient component contrast[35,40], hard X-ray synchrotron nanotomography has not the required contrast between the components to be able to classify the hydrates[38,39] and soft X-ray synchrotron nanotomography has the contrast but it requires very large w/c ratios and very small fields of view which does not allow the hydrates to growth in relevant condition (i.e. confined space with low water-cement ratios)[32].".

3.2. Author reply-b: We think that the difficulties were already detailed in the introduction by stating the four (stringent) requirements that should be met simultaneously. To refer this to 4D imaging in a more obvious way, we have rephrased now this part on page 2: "…. However, none of these 4D imaging works combine the stringent four requirements needed for carrying out relevant contributions to the understanding of the mechanism(s) of Portland cement hydration at early ages: (i) water to cement mass ratio (w/c) close to 0.50, (ii) submicrometer spatial resolution, (iii) good contrast to be able to identify the different evolving components (more than eight), and (iv) relatively large scanned volume to allow hydration to progress with appropriate particle sampling, the particle sizes of commercial PCs have $D_{v,50} \in$ 10-20 μm." We prefer not to reiterate this message.

3.3. In Fig.7, the time selection is very strange."19h","47h","93h". what is the reason. The title of this paper focuses on the early hydration. why not select some early hydration points? for example, Non-contact multiple-frequencies AC impedance instrument for cement hydration based on a high-frequency weak current sensor.

3.3. Author reply: The selection of the hydration time was given by the availability of synchrotron beamtime that was shared with other nanotomographic study. On the other hand, there are several techniques that can help to characterise the overall water porosity evolution with time such as "Non-Contact Multiple-Frequency AC Impedance Instrument for Cement Hydration Based on a High-Frequency Weak Current Sensor; doi: 10.3390/act12010026" but they lack the submicrometer spatial resolution that is the focus of this work.

3.4. This paper is interesting, cement pastes are multi-phase materials. Some phases are overlapped with others in some localized regions. Some nano-scale C-S-H and CH may be mixed together. It is said that the intrinsic size of C-S-H is about 5 nm(doi.org/10.3390/fractalfract5020047). Therefore, in Fig.4 nanoimaging, C-S-H may not be identified in the scale bar 5 μm. Therefore, at least, the typical size of each phase during the cement hydration should be listed out from literature, so that reader can compare comprehensively.

3.4. Author reply: We fully agree with the reviewer's statement. This is also linked to the partial volume effects highlighted by reviewer 2 in his/her remark 2.13. We have clarified this by adding the following set of sentences to the text: "…It should be noted that individual C-S-H nanoparticles have sizes close to 5 nm[12,55] much smaller than the spatial resolution of this work, i.e. ~ 250 nm. Therefore, the C-S-H regions analysed here very likely contain other components like gel and capillary water porosities and interspersed calcium hydroxide. On the other hand, ettringite and portlandite particles have larger sizes, usually ranging 1-5 μm, and they can be imaged in the present work.[3] In any case, partial volume effect (the presence of components contributing below the spatial resolution of the measurements) is always taking place in cement pastes as some hydrates may have quite small particle sizes.[17]" We have also added the suggested reference:
(55) Tang, S. *et al.* Structure, fractality, mechanics and durability of calcium silicate hydrates. *Fractal Fract.* **5**, 47 (2021).

3.5. As we know, some commercial PCs have some mineral admixtures. What about the XRF results of these two commercial PCs in this work.

3.5. Author reply: Indeed, most commercial PCs have limestone in addition to the gypsum used as set regulator, this is also linked to the 3.7 point, below. The employed PCs are type I where only gypsum and limestone are added to the clinker and their contents lower than 5 wt%. The XRF, and the LoI, data were given in Table S1.

3.6. Fig. 3. Left figure is terrible. We can not identify which is which. It is only black and while.

3.6. Author reply: We have made an effort to clarify the message but the bottom-line feature cannot change: the relatively poor spatial resolution and contrast of synchrotron (propagation-based phase-contrast) microtomography when compared to ptychographic nanotomography. When inspecting the fine details at the same (high) magnification, synchrotron microtomography shows the relatively coarse voxel size with limited contrast. Figure 3 caption has been revised to detail the new views. Now in the revised version:

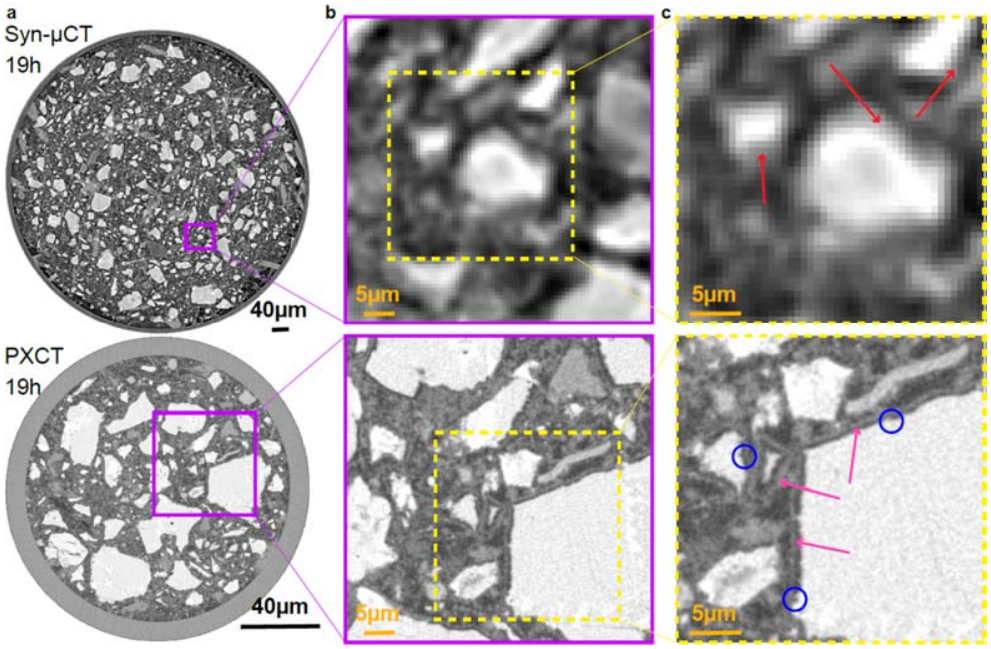

Fig. 3. Comparison of phase-contrast synchrotron tomography and ptychographic X-ray computed tomography. a, Selected orthoslices at 19 h for (top) Syn-µCT [voxel size: 650 nm, total scanned volume: 5.25 10^8 µm^3, overall acquisition time: 5 min], and (bottom) PXCT [voxel size: 186.64 nm, total scanned volume: 8.15 10^5 µm^3, overall acquisition time: 3 h, 55 min]. **b,** enlarged views of the highlighted regions (purple squares) in **a**, in order to illustrate the level of detail that can be observed with these imaging modalities. Every voxel in Syn-µCT image starts to be evident. **c,** Further enlarged views to illustrate the maximum level of detail that can be observed. (Top) The Syn-µCT image shows whitish particles (anhydrous cement particles) surrounded by hydrates (greyish voxels) which are highlighted by red arrows. (Bottom) The PXCT data, at the same magnification, shows a much higher level of detail. The C-S-H gel shells surrounding the alite particles are clearly visible (pink arrows). There is a water gap between the shell and the alite grain due to the inward dissolution of alite. Moreover, etch-pits on the surfaces of the alite particles are also visible (blue circles). The highest spatial resolution and better contrast of PXCT data allow visualizing submicrometre features of the dissolution-precipitation processes which are not visible in propagation-based Syn-µCT. Conversely, propagation-based Syn-µCT permits to scan much larger volumes in much smaller acquisition times, showing the complementary nature of both techniques.

3.7. From Fig.7, the samples used in PXCT have serious carbonation. However, other samples do not have such carbonation. Besides, in Fig.7, how do authors identify the different kinds of C-S-H gels. Is it from AFM test according to porosity or NMR according to silicate calcium chain (doi.org/10.1016/j.conbuildmat.2020.118807 & doi.org/10.1016/j.measurement.2021.110019)

3.7. Author reply-a: Related to carbonation. We do not agree with this statement. The samples have not serious carbonation. It is noted that the employed cements are commercial and these materials have normally 4-5 wt% of limestone addition. This was already shown in the cement mineralogical analyses, see Table S2, where PC-52.5 and PC-42.5 have 2.8 and 3.7 wt% of crystalline calcite, respectively. This is now clarified in the caption of Figure 7 by adding: "… This calcite comes very likely from the limestone addition to the Portland cement as quantified in the anhydrous material, see Table S2."

3.7. Author reply-b: We are aware that there are different C-S-H from the nano-mechanical point of view with different gel pore water contents. Unfortunately, with the spatial resolution and contrast currently available, we cannot distinguish them. From synchrotron microtomography we can distinguish hydrates with high mass/electron densities (portlandite, calcite, high-density C-S-H) from low density compounds (ettringite, AFm-type phases and low-density C-S-H). PXCT allows to distinguish calcite but it does not allow to distinguish high

density and low density C-S-H. This is now clarified in the caption of Figure 7 by adding: "… It is noted that with the quality of the data reported in this study (spatial resolution and electron density contrast), it is not possible to disentangle low-density from high-density C-S-H".

3.8. In Fig.6, authors claim they can monitor the evolution of water porosity (dark-grey) to air porosity (black). Does it mean that water can be distinguished by near field PXCT? As I know, only neutron can examine the presence of water.

3.8. Yes, PXCT can distinguish water from air, if the measurements are done to yield quantitative electron densities. This requires thin specimens surrounded by air. This is known since 2012: "Quantitative x-ray phase nanotomography, doi: 10.1103/PhysRevB.85.020104", where a sensitivity of about 0.02 $e^{-}Å^{-3}$ was demonstrated for the electron density contrast. The electron density of water is 0.33 $e^{-}Å^{-3}$, larger than that of air, i.e. 0.00 $e^{-}Å^{-3}$. This is clarified in the revised version ". It is underlined that PXCT readily distinguishes air and water porosities because of their difference in electron densities, 0 and 0.33 $e^{-}Å^{3}$, respectively; when the phase retrieval is carried out quantitatively[54].".

Obviously, we fully agree that neutron imaging is another technique that can disentangle water from air porosities. The key advantage of neutron imaging is clear, it can scan large volumes. However, it must also be noted that at a much worse spatial resolution compared to PXCT.

We have clarified this in the S.I. by adding "… PXCT provides 3D maps of the electron density of the specimen with quantitative contrast, the sensitivity being about 0.02 $e^{-}Å^{-3}$.[16] For attaining quantitative electron densities, the entire specimen must be included in the field of view, containing some empty space around it, which was the case in our measurements. Therefore, it is possible to easily distinguish air and water regions in the specimen, which have electron densities of 0.00 and 0.33 $e^{-}Å^{-3}$, respectively. Obviously, neutron imaging is the standard technique to disentangle water from air porosities. A key advantage of neutron imaging is its ability to can scan large volumes. However, it must also be noted that at a much worse spatial resolution compared to PXCT."

3.9. In Fig.8, PXCT test results seem that C_4AF content does not change much. It is not reasonable. Common sense tells us that the hydration rate is $C_3A > C_3S > C_4AF > C_2S$.

3.9. Author reply: The reviewer is right to point out a) the well-known hydration rate sequence, $C_3A \sim C_3S > C_4AF > C_2S$; and b) that C_4AF does not change much in our study. However, we do not consider this observation unreasonably for two reasons: i) C_4AF reactivity starts to take place mainly after about 2 days of hydration and our last measurement took place at 4 days (i.e. 93 h); and ii) the w/c ratio in the scanned volume was about 0.40. A low w/c ratio means less water available for the hydration of the phases with the slower kinetics, i.e. C_4AF. We have clarified this by adding the following statement in the figure caption. "… PXCT data shows that C_4AF hydrates little up to 93 h. This is likely due to the low w/c ratio in the scanned volume and its slow hydration rate.".

Reviewer #4 (Remarks to the Author):

A superbly presented, detailed study of cement hydration using various X-ray methods. I would recommend a review by someone expert in the cement hydration field, since I cannot comment on the impact of the results from the point of view of the application. What I can say is that the ptychographic imaging is a significant real-world demonstration of the near-field approach and, to my mind, represents the current state-of-the-art. I have no issue recommending the article for publication, subject only to minor improvement of the English - which although always comprehensible could do with a proof-read.

Author reply: Many thanks

REVIEWERS' COMMENTS

Reviewer #1 (Remarks to the Author):

The author has replied to all the issues and revised the manuscript accordingly. I recommend it for publication.

Reviewer #2 (Remarks to the Author):

First of all, I would like to thank the authors for their very detailed and precise answers. I acknowledge the work they have done to improve the manuscript and precise the methods used for the quantitative analysis of the images. I would recommend adding graphs detailing the large variability in the results of the etch-pit growth rate in the SI. I am happy to reconsider my previous decision and support this work for publication in Nature communications.

Reviewer #3 (Remarks to the Author):

Major revision is needed.
1) In Table S5, the content of Cc increases from 2.0 to 3.6 at 96h. obviously, the serious carbonation occurs, see the review comments 3.7
2) In Table S7, data of AFm and C-A-S-H are missing. As Ca/Si ratio of C-S-H is very close to 1.7, not 1.8. Do authors have data related to C-S-H with Ca/Si 1.7. C-S-H gels are glassy phases so their values are within a certain range in Table S7. What is the range? The electron density of C-S-H and CH are close to each other. In most cases, the hydrating pastes, C-S-H and CH are mixed together with porosity, and hard to be distinguished. Once C-S-H and CH can not be distinguished, 4D nanoimaging of hydration can not be achieved because they are occupied up to 80% volume of hydrates.
3) Some key points should be clarified. Raw clinker of cement is mixture. The microstructure of pastes includes time-evolving multi-phases with different multi-scale(nano-,meso-, and micro). Therefore, if PXCT enables to distinguish the amount and distribution of different phases, these phases should have "distinct" features in electron density derived from PXCT. Obviously, single test or measurement can not achieve this objective. Therefore, other test results and literature results should be carried out and compared to support the evidences in the manuscript. Please the review comment 3.7.

Malaga, 14th of April, 2023

Response to reviewers document. Reference **NCOMMS-22-47460A** (second revision)

Title. "**4D nanoimaging of early age cement hydration**"

Reviewer #1 (Remarks to the Author):

The author has replied to all the issues and revised the manuscript accordingly. I recommend it for publication.

Author reply: Many thanks.

Reviewer #2 (Remarks to the Author):

First of all, I would like to thank the authors for their very detailed and precise answers. I acknowledge the work they have done to improve the manuscript and precise the methods used for the quantitative analysis of the images. I would recommend adding graphs detailing the large variability in the results of the etch-pit growth rate in the SI. I am happy to reconsider my previous decision and support this work for publication in Nature communications.

Author reply-1: Many thanks.

Author reply-2: Concerning the etch-pit growth rate, we can only agree. Therefore, we have prepared a new figure, Fig. S13 with two particles showing the evolution of ten etch-pits. The remaining figures have been renumbered. Figure S13 and its caption are reproduced below.

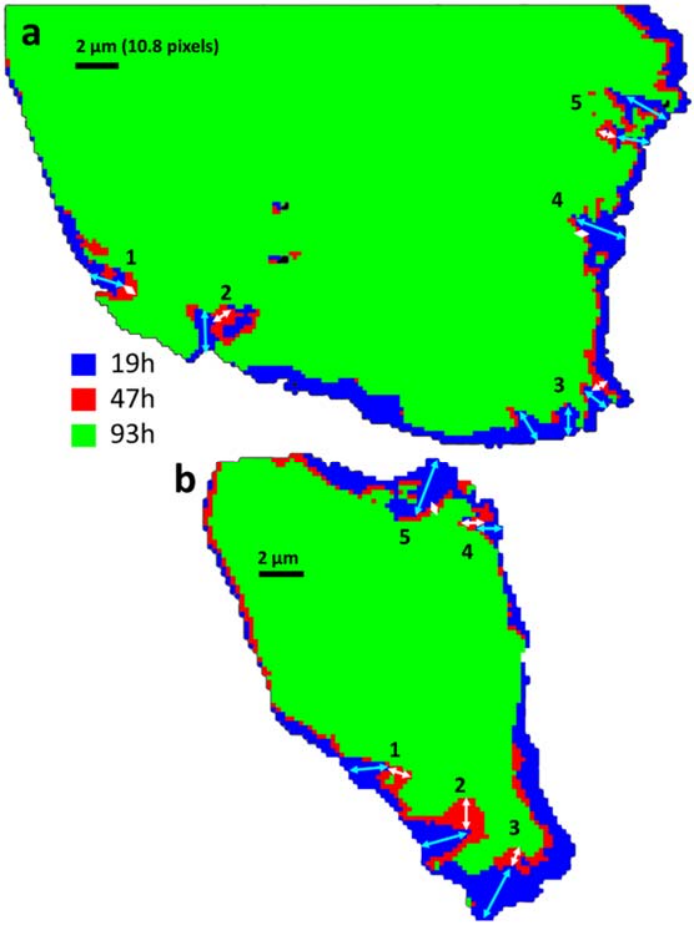

Figure S13. Overlay of the (2D-projected) alite segmented pixels during the hydration process to show the large variability in the growth rates of the etch-pits. **a,** five etch-pits corresponding to Figure 4 of the manuscript. **b,** five etch-pits corresponding to the Figure S11 of this S.I. Pale-blue arrows show size changes from 19h to 47h, meanwhile white arrows display the changes from 47h to 93h.

Reviewer #3 (Remarks to the Author):

Major revision is needed.

3.1. In Table S5, the content of Cc increases from 2.0 to 3.6 at 96h. obviously, the serious carbonation occurs, see the review comments 3.7.

Author reply: The initial PC had an average calcite content of 2.8 wt%, see Table S2, that when diluted with the water resulted in a calcite content of 2.0 wt% (value at t=0). For the large capillary used in the laboratory micro-CT & LXRPD study, ϕ=1.0 mm, the calcite content increased to about 3.6 wt% at 96 h, i.e. the calcite amount increased 1.6 wt%. This is now explicitly acknowledged in the footnote of Table S5. However, the paste within the much thinner capillary, ϕ=0.2 mm, used in the PXCT study did not show a significant carbonation. Now in the revised version of S.I., a footnote of Table S5:

"[#] The calcite content increased from 2.0 wt% at t=0 to 3.6 wt% at 96 h, highlighting a significant carbonation of the paste within this large capillary, i.e. 1 mm of diameter. The thinner capillary used in the PXCT study, i.e. 0.2 mm of diameter, did not show a measurable conversion of CH to Cc, see below. Carbonation of a cement paste has been previously measured by PXCT, when its extension was significant.[22]"

We have added new reference (22) in the S.I.: Trtik, P., Diaz, A., Guizar-Sicairos, M., Menzel, A. & Bunk, O. Density mapping of hardened cement paste using ptychographic X-ray computed tomography. *Cem. Concr. Compos.* **36**, 71–77 (2013)

3.2. In Table S7, data of AFm and C-A-S-H are missing. As Ca/Si ratio of C-S-H is very close to 1.7, not 1.8. Do authors have data related to C-S-H with Ca/Si 1.7. C-S-H gels are glassy phases so their values are within a certain range in Table S7. What is the range? The electron density of C-S-H and CH are close to each other. In most cases, the hydrating pastes, C-S-H and CH are mixed together with porosity, and hard to be distinguished. Once C-S-H and CH can not be distinguished, 4D nanoimaging of hydration can not be achieved because they are occupied up to 80% volume of hydrates.

Author reply-1: We agree that data for AFm and C-A-S-H were missed in Table S7. Thus, the expected data for AFm and hemicarbonate (Hc) phases are now included. We cannot include data for C-A-S-H as this component, with aluminium content larger than ~5 %, mainly forms in the pozzolanic reaction which is not the subject of this investigation.

Author reply-2: Concerning the variable Ca/Si ratio. C-S-H gel from PC hydration, without supplementary materials addition, shows variable Ca/Si ratios close to 1.7-1.8. This is now explicitly stated in the revised version of the manuscript "It should also be noted that the employed stoichiometry for C-S-H gel, i.e. $(CaO)_{1.80}(SiO_2)(H_2O)_{4.0}$,[56,57] is an assumption and slightly smaller Ca/Si ratios, ~1.70, have also been reported.[12,58]". Three new references (56-58) are added: (56) Cuesta, A. *et al.* Local structure and Ca/Si ratio in C-S-H gels from the hydration of blends of tricalcium silicate and silica fume. *Cem. Concr. Res.* **143**, 106405 (2021); (57) Zhu, X. & Richardson, I. G. Morphology-structural change of C-A-S-H gel in blended cements. *Cem. Concr. Res.* **168**, 107156 (2023); (58) Duque-Redondo, E., Bonnaud, P. A. & Manzano, H. A comprehensive review of C-S-H empirical and computational models, their applications, and practical aspects. *Cem. Concr. Res.* **156**, 106784 (2022).

We have calculate the values for $(CaO)_{1.7}(SiO_2)(H_2O)_4$ and compared them with those of $(CaO)_{1.8}(SiO_2)(H_2O)_4$. For the first average stoichiometry, the electron density and μ values would be 0.66 $e^-Å^{-3}$ and 102 cm^{-1}. The corresponding values for the second component are 0.66 $e^-Å^{-3}$ and 104 cm^{-1}. We do not report the values for $(CaO)_{1.7}(SiO_2)(H_2O)_4$ in Table S7 as they are, as expected, very close to those of $(CaO)_{1.8}(SiO_2)(H_2O)_4$.

Author reply-3: Concerning C-S-H and CH electron density values. Indeed, the electron density values of these components are close and in some regions, they are interspersed. We could disentangle these components by nano-imaging in most regions. However, the presence of partial volume effect was explicitly acknowledged in the manuscript and reproduced here: "… In any case, partial volume effect (the presence of components contributing below the spatial resolution of the measurements) is always taking place in cement pastes as some hydrates may have quite small particle sizes.[17]"

3.3. Some key points should be clarified. Raw clinker of cement is mixture. The microstructure of pastes includes time-evolving multi-phases with different multi-scale(nano-,meso-, and micro). Therefore, if PXCT enables to distinguish the amount and distribution of different phases, these phases should have "distinct" features in electron density derived from PXCT. Obviously, single test or measurement can not achieve this objective. Therefore, other test results and literature results should be carried out and compared to support the evidences in the manuscript. Please the review comment 3.7.

Author reply-1: The reviewer is right in pointing out that the cements are mixtures. This was detailed in the S.I. by reporting their mineralogical analyses. However, this is now clarified in the main text by adding: "… As reported in Table S2, the anhydrous cements are mixtures with more than eight crystalline phases."

Author reply-2: PXCT allows distinguishing components within the hydrating cement paste but it has limitations that are detailed in the manuscript. The two main limitations are: (i) the current spatial resolution, i.e. 250 nm. Clearly, component interspersed at smaller length scales cannot be disentangled, leading to partial volume effects. (ii) The electron density contrast is about 0.02-0.04 $e^{-}Å^{-3}$ and components with electron densities closer than ~0.04 $e^{-}Å^{-3}$ cannot be separated. However, to use additional techniques to *in situ* study the hydration of these cements (in addition to the already employed ones: calorimetry, laboratory powder diffraction and laboratory microtomography) will be the subject of further works, but this is not within the scope of the present investigation.

Description of Additional Supplementary Files

- File name: Supplementary Movie 1 - Summary of 4D nanoimaging of cement hydration

  Description: A summarized display of the cement paste hydration evolution as seen by this nanoimaging study. The progress of the different components is displayed after segmentation by Machine-Learning. Moreover, key changes like water porosity evolution or shrinkage development are highlighted on the video by embedded written text.

- File name: Supplementary Movie 2 - C-S-H shell characterization at 19 hours

  Description: A movie revealing the arrangement of the 3D segmented C-S-H shells through the 19 h nanoimaging dataset.

Annex: Other publications

- Cuesta, A.; **Shirani, S.**; De la Torre, A.G.; Santacruz, I.; Morales-Cantero, A.; Koufany, I.; Redondo-Soto, C.; Salcedo, I.R.; León-Reina, L. ; Aranda, M.A.G. "Combined use of laboratory X-ray diffraction and microtomography in early age cement hydration" *The 16th International Congress on the Chemistry of Cement 2023 (ICCC2023)*, **2023**.
- Bernal, I.M.R.; **Shirani, S.**; Cuesta, A.; Santacruz, I.; Aranda, M.A.G. "Phase and microstructure evolutions in limestone calcined clay cements by multi-technique approach including synchrotron micro-tomography" *Construction and Building Materials*, **2021**, 300, 124054. DOI: 10.1016/j.conbuildmat.2021.124054.
- Kakouie, A.; Vatani, A.; Hosseini Moghaddam, S.A. ; **Shirani, S.**; Ferrero, C.; Brun, E.; "Lattice kinetic model of 3D flow characterization in core samples via synchrotron X-ray micro-tomography" *Computers and Geosciences*, **2021**, 156, 104908. DOI: 10.1016/j.cageo.2021.104908.
- Salcedo I. R.; Cuesta, A.; **Shirani, S.**; León-Reina L.; Aranda, M.A.G. "Accuracy in Cement Hydration Investigations: Combined X-ray Microtomography and Powder Diffraction Analyses" *Materials*, **2021**, 14(22), 6953. DOI: 10.3390/ma14226953.
- Morales-Cantero, A.; De la Torre, A.G.; Cuesta, A.; Fraga-Lopez, E; **Shirani, S.**; Aranda, M.A.G. "Belite hydration at high temperature and pressure by in situ synchrotron powder diffraction" *Construction and Building Materials*, **2020**, 137, 106201. DOI: 10.1016/j.conbuildmat.2020.120825.

List of Figures

List of Tables

References

Here are the references in alphabetic order

Adams, Matthew P. and Jason H. Ideker (2017). 'Influence of aggregate type on conversion and strength in calcium aluminate cement concrete'. In: *Cement and Concrete Research* 100, pp. 284–296. DOI: https://doi.org/10.1016/j.cemconres.2017.07.007 (cited on page 37).

Adrien, Jérôme et al. (2016). 'In-situ X-ray tomographic monitoring of gypsum plaster setting'. In: *Cement and Concrete Research* 82, pp. 107–116 (cited on page 64).

Alarcon-Ruiz, Lucia et al. (2005). 'The use of thermal analysis in assessing the effect of temperature on a cement paste'. In: *Cement and Concrete Research* 35.3, pp. 609–613. DOI: https://doi.org/10.1016/j.cemconres.2004.06.015 (cited on page 44).

Awoyera, PO et al. (2017). 'Suitability of mortars produced using laterite and ceramic wastes: Mechanical and microscale analysis'. In: *Construction and Building Materials* 148, pp. 195–203 (cited on page 62).

Bae, Sungchul, Manabu Kanematsu, et al. (2016). 'In situ soft X-ray spectromicroscopy of early tricalcium silicate hydration'. In: *Materials* 9.12, p. 976 (cited on page 65).

Bae, Sungchul, Rae Taylor, et al. (2015). 'Soft X-ray ptychographic imaging and morphological quantification of calcium silicate hydrates (C–S–H)'. In: *Journal of the American Ceramic Society* 98.12, pp. 4090–4095 (cited on page 64).

Banfill, Phillip FG et al. (2003). 'The rheology of fresh cement and concrete-a review'. In: *Proceedings of the 11th international cement chemistry congress*. Vol. 1, pp. 50–62 (cited on page 46).

Barcelo, Laurent et al. (2014). 'Cement and carbon emissions'. In: *Materials and structures* 47.6, pp. 1055–1065 (cited on page 36).

Barrett, Julia F. and Nicholas Keat (Nov. 2004). 'Artifacts in CT: Recognition and Avoidance1'. en. In: *RadioGraphics*. DOI: 10.1148/rg.246045065 (cited on page 52).

Bayoux, JP (1990). 'Acidic Corrosion of High Alumina Cement Calcium Aluminate ements'. In: *E&F. N. SPON*, pp. 230–240 (cited on page 37).

Bernal, S Shirani, et al. (2021). 'Phase and microstructure evolutions in LC3 binders by multi-technique approach including synchrotron microtomography'. In: *Construction and Building Materials* 300, p. 124054 (cited on pages 61, 63).

Bonse, U. and M. Hart (Apr. 1965). 'An x-ray interferometer'. In: *Applied Physics Letters* 6.8, pp. 155–156. DOI: 10.1063/1.1754212 (cited on page 58).

Bossa, Nathan et al. (2015). 'Micro-and nano-X-ray computed-tomography: A step forward in the characterization of the pore network of a leached cement paste'. In: *Cement and Concrete Research* 67, pp. 138–147 (cited on page 62).

Böttcher, B, SA Wynne, and RA Crowther (1997). 'Determination of the fold of the core protein of hepatitis B virus by electron cryomicroscopy'. In: *Nature* 386.6620, pp. 88–91 (cited on page 112).

Bravin, Alberto, Paola Coan, and Pekka Suortti (Jan. 2013). 'X-ray phase-contrast imaging: from pre-clinical applications towards clinics'. eng. In: *Physics in Medicine and Biology* 58.1, R1–35. DOI: 10.1088/0031-9155/58/1/R1 (cited on page 58).

Breiman, Leo (1996). 'Bagging predictors'. In: *Machine learning* 24, pp. 123–140 (cited on page 129).

– (2001). 'Random forests'. In: *Machine learning* 45, pp. 5–32 (cited on page 129).

Brisard, Sebastien et al. (2012). 'Morphological quantification of hierarchical geomaterials by X-ray nano-CT bridges the gap from nano to micro length scales'. In: *American Mineralogist* 97.2-3, pp. 480–483 (cited on page 64).

Browne, J. and A. B. de Pierro (1996). 'A row-action alternative to the EM algorithm for maximizing likelihood in emission tomography'. eng. In: *IEEE transactions on medical imaging* 15.5, pp. 687–699. DOI: 10.1109/42.538946 (cited on page 52).

Chatterjee, A.K. (1996). 'High belite cements—Present status and future technological options: Part I'. In: *Cement and Concrete Research* 26.8, pp. 1213–1225. DOI: https://doi.org/10.1016/0008-8846(96)00099-3 (cited on page 36).

Cloetens, Peter et al. (Jan. 1996). 'Phase objects in synchrotron radiation hard x-ray imaging'. en. In: *Journal of Physics D: Applied Physics* 29.1, p. 133. DOI: 10.1088/0022-3727/29/1/023 (cited on page 58).
Cuesta, A et al. (2019). 'Quantitative disentanglement of nanocrystalline phases in cement pastes by synchrotron ptychographic X-ray tomography'. In: *IUCrJ* 6.3, pp. 473–491 (cited on pages 64, 113, 135).
Cuesta, A, A De la Torre, et al. (2017a). 'Chemistry and mass density of aluminum hydroxide gel in eco-cements by ptychographic X-ray computed tomography'. In: *The Journal of Physical Chemistry C* 121.5, pp. 3044–3054 (cited on page 64).
– (2017b). 'In situ hydration imaging study of a ye'elimite paste by ptychographic X-ray computed tomography'. In: *Proceedings of the 39 International Conference on Cement Microscopy, Toronto, ON, Canada*, pp. 10–13 (cited on page 65).
Cuesta, Ana, Andres Ayuela, and Miguel A.G. Aranda (2021). 'Belite cements and their activation'. In: *Cement and Concrete Research* 140, p. 106319. DOI: https://doi.org/10.1016/j.cemconres.2020.106319 (cited on page 36).
Cuesta, Alejandro Morales-Cantero, et al. (2023). 'Recent Advances in C-S-H Nucleation Seeding for Improving Cement Performances'. In: *Materials* 16.4. DOI: 10.3390/ma16041462 (cited on page 40).
Cuesta, Isabel Santacruz, et al. (2021). 'Local structure and Ca/Si ratio in CSH gels from hydration of blends of tricalcium silicate and silica fume'. In: *Cement and Concrete Research* 143, p. 106405 (cited on page 38).
Cuesta, Jesus D Zea-Garcia, et al. (2018). 'Multiscale understanding of tricalcium silicate hydration reactions'. In: *Scientific reports* 8.1, p. 8544 (cited on page 38).
Das, Sumanta et al. (2015). 'Effective properties of a fly ash geopolymer: Synergistic application of X-ray synchrotron tomography, nanoindentation, and homogenization models'. In: *Cement and Concrete Research* 78, pp. 252–262. DOI: https://doi.org/10.1016/j.cemconres.2015.08.004 (cited on pages 46, 62).
Davis, GR and JC Elliott (2006). 'Artefacts in X-ray microtomography of materials'. In: *Materials science and technology* 22.9, pp. 1011–1018 (cited on page 52).
De La Torre, AG, S Bruque, and Aranda (2001). 'Rietveld quantitative amorphous content analysis'. In: *Journal of Applied Crystallography* 34.2, pp. 196–202 (cited on page 42).
Dempster, A. P., N. M. Laird, and D. B. Rubin Reviewed work(s): (1977). 'Maximum Likelihood from Incomplete Data via the EM Algorithm'. en. In: *Journal of the Royal Statistical Society. Series B (Methodological)* 39.1, pp. 1–38 (cited on page 52).
Dong, Biqin et al. (2017). 'Monitoring reinforcement corrosion and corrosion-induced cracking by X-ray microcomputed tomography method'. In: *Cement and Concrete Research* 100, pp. 311–321 (cited on page 64).
Eldib, Mohamed Elsayed et al. (Feb. 2017). 'A Ring Artifact Correction Method: Validation by Micro-CT Imaging with Flat-Panel Detectors and a 2D Photon-Counting Detector'. en. In: *Sensors* 17.2, p. 269. DOI: 10.3390/s17020269 (cited on page 52).
Feldkamp, L. A., L. C. Davis, and J. W. Kress (June 1984). 'Practical cone-beam algorithm'. EN. In: *JOSA A* 1.6, pp. 612–619. DOI: 10.1364/JOSAA.1.000612 (cited on page 51).
Ferrari, Giorgio et al. (2017). 'Improving the performance of PCE superplasticizers in early stiffening Portland cement'. In: *Construction and Building Materials* 130, pp. 83–91 (cited on page 62).
Fienup, James R (1978). 'Reconstruction of an object from the modulus of its Fourier transform'. In: *Optics letters* 3.1, pp. 27–29 (cited on page 60).
Flatt, R and I Schober (2012). 'Superplasticizers and the rheology of concrete'. In: *Understanding the rheology of concrete*. Elsevier, pp. 144–208 (cited on page 39).
Flatt, Robert J. (2004). 'Dispersion forces in cement suspensions'. In: *Cement and Concrete Research* 34.3, pp. 399–408. DOI: https://doi.org/10.1016/j.cemconres.2003.08.019 (cited on page 39).
Frank, J. and M. van Heel (1982). 'Correspondence analysis of aligned images of biological particles'. In: *Journal of Molecular Biology* 161.1, pp. 134–137. DOI: https://doi.org/10.1016/0022-2836(82)90282-0 (cited on page 112).
Gallucci, E et al. (2007). '3D experimental investigation of the microstructure of cement pastes using synchrotron X-ray microtomography (μCT)'. In: *Cement and Concrete Research* 37.3, pp. 360–368 (cited on page 64).
Garg, Nishant et al. (2019). 'Nanoscale ordering and depolymerization of calcium silicate hydrates in the presence of alkalis'. In: *The Journal of Physical Chemistry C* 123.40, pp. 24873–24883 (cited on page 38).

Geng, Guoqing et al. (2018). 'Synchrotron X-ray nanotomographic and spectromicroscopic study of the tricalcium aluminate hydration in the presence of gypsum'. In: *Cement and Concrete Research* 111, pp. 130–137 (cited on page 65).
Gerchberg, RW (1972). 'Holography without fringes in the electron microscope'. In: *Nature* 240.5381, pp. 404–406 (cited on page 60).
Gilbert, P. (July 1972). 'Iterative methods for the three-dimensional reconstruction of an object from projections'. eng. In: *Journal of Theoretical Biology* 36.1, pp. 105–117. DOI: 10.1016/0022-5193(72)90180-4 (cited on page 52).
Goitein, Michael (Dec. 1971). 'Three-dimensional density reconstruction from a series of two-dimensional projections'. en. In: (cited on page 52).
Gordon, Richard, Robert Bender, and Gabor T. Herman (Dec. 1970). 'Algebraic Reconstruction Techniques (ART) for three-dimensional electron microscopy and X-ray photography'. en. In: *Journal of Theoretical Biology* 29.3, pp. 471–481. DOI: 10.1016/0022-5193(70)90109-8 (cited on page 52).
Grass, M., T. Köhler, and R. Proksa (Feb. 2000). '3D cone-beam CT reconstruction for circular trajectories'. eng. In: *Physics in Medicine and Biology* 45.2, pp. 329–347. DOI: 10.1088/0031-9155/45/2/306 (cited on page 51).
Guizar-Sicairos, Manuel and Pierre Thibault (2021). 'Ptychography: A solution to the phase problem'. In: *Physics Today* 74.9, pp. 42–48 (cited on page 59).
Harauz, George and Marin van Heel (1986). 'Exact filters for general geometry three dimensional reconstruction.' In: *Optik.* 73.4, pp. 146–156 (cited on page 112).
Hemberg, O., M. Otendal, and H. M. Hertz (Aug. 2003). 'Liquid-metal-jet anode electron-impact x-ray source'. en. In: *Applied Physics Letters* 83.7, pp. 1483–1485. DOI: 10.1063/1.1602157 (cited on page 55).
Henke, John W, A Richard Krachenberg, and Thomas F Lyons (1993). 'Perspective: cross-functional teams: good concept, poor implementation!' In: *Journal of product innovation management* 10.3, pp. 216–229 (cited on page 47).
Hoppe, W et al. (1982). 'Trace structure analysis, ptychography, phase tomography'. In: *Ultramicroscopy* 10.3, pp. 187–198 (cited on page 59).
Hoppe, Walter (1969). 'Beugung im inhomogenen primärstrahlwellenfeld. i. prinzip einer phasenmessung von elektronenbeugungsinterferenzen'. In: *Acta Crystallographica Section A: Crystal Physics, Diffraction, Theoretical and General Crystallography* 25.4, pp. 495–501 (cited on page 59).
Hu, Qinang, Mohammed Aboustait, et al. (2016a). 'Direct three-dimensional observation of the microstructure and chemistry of C3S hydration'. In: *Cement and concrete research* 88, pp. 157–169 (cited on page 65).
Hu, Qinang, Mohammed Aboustait, et al. (2016b). 'Direct measurements of 3d structure, chemistry and mass density during the induction period of C3s hydration'. In: *Cement and concrete research* 89, pp. 14–26 (cited on page 65).
Hudson, H. M. and R. S. Larkin (1994). 'Accelerated image reconstruction using ordered subsets of projection data'. eng. In: *IEEE transactions on medical imaging* 13.4, pp. 601–609. DOI: 10.1109/42.363108 (cited on page 52).
Initiative, Cement Sustainability (2009). 'Cement industry energy and CO2 performance: getting the numbers right'. In: *World Business Council for Sustainable Development* (cited on page 36).
Jackson, Marie D et al. (2013). 'Material and elastic properties of Al-tobermorite in ancient Roman seawater concrete'. In: *Journal of the American Ceramic Society* 96.8, pp. 2598–2606 (cited on page 64).
John, Vanderley M. et al. (2018). 'Fillers in cementitious materials — Experience, recent advances and future potential'. In: *Cement and Concrete Research* 114, pp. 65–78. DOI: https://doi.org/10.1016/j.cemconres.2017.09.013 (cited on page 36).
Juenger, Maria C.G. and Rafat Siddique (2015). 'Recent advances in understanding the role of supplementary cementitious materials in concrete'. In: *Cement and Concrete Research* 78, pp. 71–80. DOI: https://doi.org/10.1016/j.cemconres.2015.03.018 (cited on page 36).
Juenger, Maria C.G., Ruben Snellings, and Susan A. Bernal (2019). 'Supplementary cementitious materials: New sources, characterization, and performance insights'. In: *Cement and Concrete Research* 122, pp. 257–273. DOI: https://doi.org/10.1016/j.cemconres.2019.05.008 (cited on page 36).
Kak, Avinash C. and Malcolm Slaney (2001). *Principles of computerized tomographic imaging*. en. Classics in applied mathematics 33. Philadelphia: Society for Industrial and Applied Mathematics (cited on page 51).

Kakouie, Aliakbar et al. (2021). 'Lattice kinetic model of 3D flow characterization in core samples via synchrotron X-ray micro-tomography'. In: *Computers and Geosciences* 156, p. 104908. DOI: https://doi.org/10.1016/j.cageo.2021.104908 (cited on page 61).
Karim, MR and K Krabbenhoft (2010). 'Extraction of effective cement paste diffusivities from X-ray microtomography scans'. In: *Transport in porous media* 84, pp. 371–388 (cited on page 62).
Kashani, Alireza et al. (2017). 'A sustainable application of recycled tyre crumbs as insulator in lightweight cellular concrete'. In: *Journal of cleaner production* 149, pp. 925–935 (cited on page 62).
Katsevich, Alexander (2003). 'Improved Exact FBP Algorithm for Spiral CT'. en. In: (cited on page 51).
Koster, M, J Hannawald, and W Brameshuber (2006). 'Simulation of water permeability and water vapor diffusion through hardened cement paste'. In: *Computational mechanics* 37, pp. 163–172 (cited on page 62).
Kudo, H. and T. Saito (Nov. 1991). 'Helical-scan computed tomography using cone-beam projections'. In: *Conference Record of the 1991 IEEE Nuclear Science Symposium and Medical Imaging Conference*, 1958–1962 vol.3. DOI: 10.1109/NSSMIC.1991.259259 (cited on page 51).
Kupwade-Patil, Kunal et al. (2018). 'Use of silica fume and natural volcanic ash as a replacement to Portland cement: Micro and pore structural investigation using NMR, XRD, FTIR and X-ray microtomography'. In: *Construction and Building Materials* 158, pp. 574–590 (cited on page 62).
Lanzón, Marcos et al. (2012). 'X-ray microtomography (μ-CT) to evaluate microstructure of mortars containing low density additions'. In: *Cement and Concrete Composites* 34.9, pp. 993–1000 (cited on page 62).
– (2015). 'Microstructural examination and potential application of rendering mortars made of tire rubber and expanded polystyrene wastes'. In: *Construction and building materials* 94, pp. 817–825 (cited on page 62).
Lee, WE et al. (2001). 'Castable refractory concretes'. In: *International Materials Reviews* 46.3, pp. 145–167 (cited on page 37).
Lei, Lei, Tsuyoshi Hirata, and Johann Plank (2022). '40 years of PCE superplasticizers - History, current state-of-the-art and an outlook'. In: *Cement and Concrete Research* 157, p. 106826. DOI: https://doi.org/10.1016/j.cemconres.2022.106826 (cited on page 39).
Lei, Lei, Marta Palacios, et al. (2022). 'Interaction between polycarboxylate superplasticizers and non-calcined clays and calcined clays: A review'. In: *Cement and Concrete Research* 154, p. 106717. DOI: https://doi.org/10.1016/j.cemconres.2022.106717 (cited on page 39).
Leite, M.B. and P.J.M. Monteiro (2016). 'Microstructural analysis of recycled concrete using X-ray microtomography'. In: *Cement and Concrete Research* 81, pp. 38–48. DOI: https://doi.org/10.1016/j.cemconres.2015.11.010 (cited on page 62).
Li, Xiaodan, Qinang Hu, Bret Robertson, M Tyler Ley, Vincent Joseph De Andrade, et al. (2023). 'Direct observation of C3S particle dissolution using fast nano X-ray computed tomography'. In: *Cement and Concrete Research* 166, p. 107097 (cited on page 65).
Li, Xiaodan, Qinang Hu, Bret Robertson, M Tyler Ley, and Xianghui Xiao (2023). 'Direct observation of C3S particles greater than 10 μm during early hydration'. In: *Construction and Building Materials* 369, p. 130548 (cited on page 65).
Long, Wu-Jian et al. (2018). 'Micro-and macro-scale characterization of nano-SiO2 reinforced alkali activated slag composites'. In: *Materials Characterization* 136, pp. 111–121 (cited on page 62).
Lothenbach, Barbara, Karen Scrivener, and R.D. Hooton (2011). 'Supplementary cementitious materials'. In: *Cement and Concrete Research* 41.12, pp. 1244–1256. DOI: https://doi.org/10.1016/j.cemconres.2010.12.001 (cited on page 36).
Marinoni, Nicoletta et al. (2015). 'A combined synchrotron radiation micro computed tomography and micro X-ray diffraction study on deleterious alkali-silica reaction'. In: *Journal of materials science* 50, pp. 7985–7997 (cited on page 64).
Mehta, P Kumar (1999). 'Advancements in concrete technology'. In: *Concrete International* 21.6, pp. 69–76 (cited on page 39).
Meier, Roger, Jennifer Anderson, and Sabine Verryn (2012). 'Industrial X-ray diffraction analysis of building materials'. In: *reviews in mineralogy and geochemistry* 74.1, pp. 147–165 (cited on page 42).
Melo, Javier Pinilla, Alberto Sepulcre Aguilar, and Francisco Hernández Olivares (2014). 'Rheological properties of aerated cement pastes with fly ash, metakaolin and sepiolite additions'. In: *Construction and Building Materials* 65, pp. 566–573 (cited on page 62).

Miao, Jianwei et al. (1999). 'Extending the methodology of X-ray crystallography to allow imaging of micrometre-sized non-crystalline specimens'. In: *Nature* 400.6742, pp. 342–344 (cited on page 61).
Michel, Alexander et al. (2011). 'Monitoring reinforcement corrosion and corrosion-induced cracking using non-destructive x-ray attenuation measurements'. In: *Cement and Concrete Research* 41.11, pp. 1085–1094 (cited on page 64).
Miller, Sabbie A and Frances C Moore (2020). 'Climate and health damages from global concrete production'. In: *Nature Climate Change* 10.5, pp. 439–443 (cited on page 36).
Miller, Sabbie A and Rupert J Myers (2019). 'Environmental impacts of alternative cement binders'. In: *Environmental science & technology* 54.2, pp. 677–686 (cited on page 36).
Mindess, Sidney (2019). *Developments in the Formulation and Reinforcement of Concrete*. Woodhead Publishing (cited on page 37).
Mobilio, Settimio and Carlo Meneghini (2015). *Synchrotron radiation Basics, methods and applications*. Germany: Springer (cited on page 56).
Moradian, Masoud et al. (2019). 'Multi-scale observations of structure and chemical composition changes of portland cement systems during hydration'. In: *Construction and Building Materials* 212, pp. 486–499 (cited on page 65).
Moradian, Masoud et al. (2017). 'Direct observation of void evolution during cement hydration'. In: *Materials & Design* 136, pp. 137–149 (cited on page 65).
Morgan, IL et al. (1979). 'Examination of steel and concrete by computerized tomography'. In: *RILEM* 2, pp. 115–123 (cited on page 61).
– (1980). 'Examination of concrete by computerized tomography'. In: *Journal Proceedings*. Vol. 77. 1, pp. 23–27 (cited on page 61).
Murugan, M et al. (2016). 'Influence of 2D rGO nanosheets on the properties of OPC paste'. In: *Cement and Concrete Composites* 70, pp. 48–59 (cited on page 62).
Niewiadomski, Paweł, Damian Stefaniuk, and Jerzy Hoła (2017). 'Microstructural analysis of self-compacting concrete modified with the addition of nanoparticles'. In: *Procedia Engineering* 172, pp. 776–783 (cited on page 62).
Olawuyi, Babatunde J and William P Boshoff (2017). 'Influence of SAP content and curing age on air void distribution of high performance concrete using 3D volume analysis'. In: *Construction and Building Materials* 135, pp. 580–589 (cited on page 62).
Paganin, David et al. (2002). 'Simultaneous phase and amplitude extraction from a single defocused image of a homogeneous object'. In: *Journal of microscopy* 206.1, pp. 33–40 (cited on pages 59, 117).
Parisatto, Matteo et al. (2015). 'Examining microstructural evolution of Portland cements by in-situ synchrotron micro-tomography'. In: *Journal of Materials Science* 50, pp. 1805–1817 (cited on page 65).
Pilehvar, Shima et al. (2017). 'Mechanical properties and microscale changes of geopolymer concrete and Portland cement concrete containing micro-encapsulated phase change materials'. In: *Cement and Concrete Research* 100, pp. 341–349 (cited on page 62).
Poirier, Mathilde et al. (2022). 'Synchrotron X-ray micro-tomography investigation of the early hydration of blended cements: A case study on CaCl2-accelerated slag-based blended cements'. In: *Construction and Building Materials* 321, p. 126412 (cited on page 65).
Pöllmann, Herbert (2012). 'Calcium aluminate cements–raw materials, differences, hydration and properties'. In: *Reviews in Mineralogy and Geochemistry* 74.1, pp. 1–82 (cited on page 37).
Prade, Friedrich et al. (2016). 'Time resolved X-ray dark-field tomography revealing water transport in a fresh cement sample'. In: *Scientific reports* 6.1, pp. 1–7 (cited on page 65).
Promentilla, Michael Angelo B, T Sugiyama, et al. (2009). 'Quantification of tortuosity in hardened cement pastes using synchrotron-based X-ray computed microtomography'. In: *Cement and Concrete Research* 39.6, pp. 548–557 (cited on page 62).
Promentilla, Michael Angelo B, Takafumi Sugiyama, et al. (2008). 'Characterizing the 3D pore structure of hardened cement paste with synchrotron microtomography'. In: *Journal of Advanced Concrete Technology* 6.2, pp. 273–286 (cited on page 62).
Provis, John L, Rupert J Myers, et al. (2012). 'X-ray microtomography shows pore structure and tortuosity in alkali-activated binders'. In: *Cement and concrete research* 42.6, pp. 855–864 (cited on page 62).

Provis, John L, Volker Rose, et al. (2011). 'Hard X-ray nanotomography of amorphous aluminosilicate cements'. In: *Scripta Materialia* 65.4, pp. 316–319 (cited on page 64).
Pyatina, Tatiana et al. (2016). 'Effect of tartaric acid on hydration of a sodium-metasilicate-activated blend of calcium aluminate cement and fly ash F'. In: *Materials* 9.6, p. 422 (cited on page 62).
Rattanasak, Ubolluk and Kevin Kendall (2005). 'Pore structure of cement/pozzolan composites by X-ray microtomography'. In: *Cement and concrete research* 35.4, pp. 637–640 (cited on page 62).
Reid, John K (1971). 'On the method of conjugate gradients for the solution of large sparse systems of linear equations'. In: *Conf. on Large Sparse Set of Linear Equations*. Academic Press (cited on page 52).
Rifai, H. et al. (2018). 'In-situ pore size investigations of loaded porous concrete with non-destructive methods'. In: *Cement and Concrete Research* 111, pp. 72–80. DOI: https://doi.org/10.1016/j.cemconres.2018.06.008 (cited on page 62).
Rodenburg, JM and RHT Bates (1992). 'The theory of super-resolution electron microscopy via Wigner-distribution deconvolution'. In: *Philosophical Transactions of the Royal Society of London. Series A: Physical and Engineering Sciences* 339.1655, pp. 521–553 (cited on page 60).
Rosenthal, Peter B and Richard Henderson (2003). 'Optimal determination of particle orientation, absolute hand, and contrast loss in single-particle electron cryomicroscopy'. In: *Journal of molecular biology* 333.4, pp. 721–745 (cited on page 112).
Šavija, Branko et al. (2015). 'Corrosion induced cover cracking studied by X-ray computed tomography, nanoindentation, and energy dispersive X-ray spectrometry (EDS)'. In: *Materials and Structures* 48, pp. 2043–2062 (cited on page 64).
Saxton, WO and W_ Baumeister (1982). 'The correlation averaging of a regularly arranged bacterial cell envelope protein'. In: *Journal of microscopy* 127.2, pp. 127–138 (cited on page 112).
Schabowicz, Krzysztof et al. (2016). 'Application of X-ray microtomography to quality assessment of fibre cement boards'. In: *Construction and Building Materials* 110, pp. 182–188 (cited on page 62).
Schaefer, Carolyn E et al. (2018). 'Irradiated recycled plastic as a concrete additive for improved chemo-mechanical properties and lower carbon footprint'. In: *Waste management* 71, pp. 426–439 (cited on page 62).
Schock, J et al. (2016). 'Obtaining the spacing factor of microporous concrete using high-resolution Dual Energy X-ray Micro CT'. In: *Cement and Concrete Research* 89, pp. 200–205 (cited on page 62).
Scrivener, Karen, François Avet, et al. (2018). 'Impacting factors and properties of limestone calcined clay cements (LC3)'. In: *Green Materials* 7.1, pp. 3–14 (cited on page 36).
Scrivener, Karen and A Capmas (2003). 'Calcium aluminate cements'. In: *Advanced concrete technology* 3, pp. 1–31 (cited on page 37).
Scrivener, Karen, Fernando Martirena, et al. (2018). 'Calcined clay limestone cements (LC3)'. In: *Cement and Concrete Research* 114, pp. 49–56. DOI: https://doi.org/10.1016/j.cemconres.2017.08.017 (cited on page 36).
Scrivener, Karen L., Jean-Louis Cabiron, and Roger Letourneux (1999). 'High-performance concretes from calcium aluminate cements'. In: *Cement and Concrete Research* 29.8, pp. 1215–1223. DOI: https://doi.org/10.1016/S0008-8846(99)00103-9 (cited on page 37).
Scrivener, Karen L., Vanderley M. John, and Ellis M. Gartner (2018). 'Eco-efficient cements: Potential economically viable solutions for a low-CO2 cement-based materials industry'. In: *Cement and Concrete Research* 114, pp. 2–26. DOI: https://doi.org/10.1016/j.cemconres.2018.03.015 (cited on pages 35, 36).
Seiller, J et al. (2021). '4D in situ monitoring of the setting of α plaster using synchrotron X-ray tomography with high spatial and temporal resolution'. In: *Construction and Building Materials* 304, p. 124632 (cited on page 65).
Sha, Shengnan et al. (2020). 'Influence of the structures of polycarboxylate superplasticizer on its performance in cement-based materials-A review'. In: *Construction and Building Materials* 233, p. 117257. DOI: https://doi.org/10.1016/j.conbuildmat.2019.117257 (cited on page 39).
She, Wei et al. (2018). 'Application of organic-and nanoparticle-modified foams in foamed concrete: Reinforcement and stabilization mechanisms'. In: *Cement and Concrete Research* 106, pp. 12–22 (cited on page 62).
Shirani, Shiva et al. (2023). '4D nanoimaging of early age cement hydration'. In: *Nature Communications* 14.1, p. 2652. DOI: https://doi.org/10.1038/s41467-023-38380-1 (cited on pages 136, 140).

Silva, Julio C da et al. (2015). 'Mass density and water content of saturated never-dried calcium silicate hydrates'. In: *Langmuir* 31.13, pp. 3779–3783 (cited on page 64).
Skibsted, Jørgen and Ruben Snellings (2019). 'Reactivity of supplementary cementitious materials (SCMs) in cement blends'. In: *Cement and Concrete Research* 124, p. 105799. DOI: https://doi.org/10.1016/j.cemconres.2019.105799 (cited on page 36).
Sleiman, Hani Cheikh et al. (2021). 'Simultaneous x-ray and neutron 4D tomographic study of drying-driven hydro-mechanical behavior of cement-based materials at moderate temperatures'. In: *Cement and Concrete Research* 147, p. 106503 (cited on page 65).
Tanaka, Eiichi and Hiroyuki Kudo (May 2003). 'Subset-dependent relaxation in block-iterative algorithms for image reconstruction in emission tomography'. en. In: *Physics in Medicine & Biology* 48.10, p. 1405. DOI: 10.1088/0031-9155/48/10/312 (cited on page 52).
Taylor, Harry FW et al. (1997). *Cement chemistry*. Vol. 2. Thomas Telford London (cited on page 35).
Trtik, Pavel et al. (2013). 'Density mapping of hardened cement paste using ptychographic X-ray computed tomography'. In: *Cement and Concrete Composites* 36, pp. 71–77 (cited on page 64).
Van Heel, Marin and Michael Schatz (2005). 'Fourier shell correlation threshold criteria'. In: *Journal of structural biology* 151.3, pp. 250–262 (cited on page 112).
Van Vliet, Krystyn et al. (2012). 'Set in stone? A perspective on the concrete sustainability challenge'. In: *MRS bulletin* 37.4, pp. 395–402 (cited on page 36).
Viejo, Ismael et al. (2016). 'Numerical modelling of porous cement-based materials by superabsorbent polymers'. In: *Cement and Concrete Research* 90, pp. 184–193 (cited on page 62).
Vigor, James E et al. (2020). 'Automated correction for the movement of suspended particulate in microtomographic data'. In: *Chemical Engineering Science* 223, p. 115736 (cited on page 65).
– (2022). 'Time-resolved 3D characterisation of early-age microstructural development of Portland cement'. In: *Journal of Materials Science* 57.8, pp. 4952–4969 (cited on page 65).
Von Dreele, RB and AC Larson (2004). 'General structure analysis system (GSAS)'. In: *Los Alamos Natl. Lab. Rep. LAUR* 748, pp. 86–748 (cited on page 42).
Wan, KeShu and Qiong Xu (2014). 'Local porosity distribution of cement paste characterized by X-ray micro-tomography'. In: *Science China Technological Sciences* 57, pp. 953–961 (cited on page 62).
Wang, G. et al. (1993). 'A general cone-beam reconstruction algorithm'. eng. In: *IEEE transactions on medical imaging* 12.3, pp. 486–496. DOI: 10.1109/42.241876 (cited on page 51).
Wang, Lin et al. (2014). 'Construction of dynamic three-dimensional microstructure for the hydration of cement using 3D image registration'. In: *Pattern Analysis and Applications* 17, pp. 655–665 (cited on page 65).
Wei, She et al. (2013). 'Characterization and simulation of microstructure and thermal properties of foamed concrete'. In: *Construction and building materials* 47, pp. 1278–1291 (cited on page 62).
Winslow, Douglas Nathaniel and SJJM Diamond (1970). 'A mercury porosimetry study of the porosity in Portland cement'. In: *Journal of Materials* (cited on page 45).
Withers, Philip J et al. (2021). 'X-ray computed tomography'. In: *Nature Reviews Methods Primers* 1.1, p. 18 (cited on page 116).
Yan, X. and R. M. Leahy (Mar. 1992). 'Cone beam tomography with circular, elliptical and spiral orbits'. en. In: *Physics in Medicine & Biology* 37.3, p. 493. DOI: 10.1088/0031-9155/37/3/001 (cited on page 51).
Zhu, Xiaohong et al. (2018). 'Characterisation of pore structure development of alkali-activated slag cement during early hydration using electrical responses'. In: *Cement and Concrete Composites* 89, pp. 139–149 (cited on page 64).
Zunino, Franco and Karen Scrivener (2021). 'The reaction between metakaolin and limestone and its effect in porosity refinement and mechanical properties'. In: *Cement and Concrete Research* 140, p. 106307. DOI: https://doi.org/10.1016/j.cemconres.2020.106307 (cited on page 36).